# Collective dynamics of self-propelled particles : waves, vortex, swarm, braiding

Jean-Baptiste Caussin

ENS DE LYON

Lab PHYS ENS de LYON

ED 52 - PHAST
Physique & Astrophysique de Lyon
Ecole doctorale

UNIVERSITÉ DE LYON

**THÈSE**

en vue de l'obtention du grade de

**Docteur de l'Université de Lyon,**
délivré par l'École Normale Supérieure de Lyon

Discipline : PHYSIQUE

Laboratoire de Physique de l'ENS de LYON

École Doctorale de Physique et d'Astrophysique de Lyon

---

# Dynamique collective de particules auto-propulsées : ondes, vortex, essaim, tressage

## Collective dynamics of self-propelled particles: waves, vortex, swarm, braiding

---


Présentée par

**Jean-Baptiste CAUSSIN**

Directeur de thèse : Denis BARTOLO


**Présentée et soutenue publiquement le 24 juin 2015**

**Après avis de:** M. Eric BERTIN
M. Luca GIOMI

**Devant la commission d'examen formée de:**

| | |
|---|---|
| M. Jean-Louis BARRAT | Examinateur |
| M. Denis BARTOLO | Directeur de thèse |
| M. Eric BERTIN | Rapporteur |
| M. Luca GIOMI | Rapporteur |
| M. Emmanuel TRIZAC | Examinateur |

# Table of contents

# Introduction

Some of the most spectacular examples of collective motion are provided by animal populations that self-assemble into coherently-moving groups. The spontaneous emergence of coordinated motion at large scale is observed in systems as diverse as bird flocks, fish shoal or locust swarms (see Fig. 1). From a physical perspective, this robust observation has raised an intense interest over the past 20 years. Such ensembles of motile individuals were shown to display rich physical properties, which strongly differ from all equilibrium systems. A variety of theoretical models are now available, together with a number of experimental realizations. They unveiled a large diversity of phenomenologies, and define the field of "active matter" [136, 216].

In this introduction, we situate more precisely this thesis in the broad area of active matter. In the first section, we specify the subclass of systems which we consider: populations displaying polar structures, i.e. directed motion at large scale. We then introduce, in section 2, the paradigmatic framework of active matter, which we refer to as "Vicsek-like models". In section 3, we recall the standard hydrodynamic approaches used to describe the large-scale dynamics of active populations. Section 4 is devoted to the connection between theoretical models and actual experimental systems. Finally, we conclude in section 5 with a general outline of the thesis.

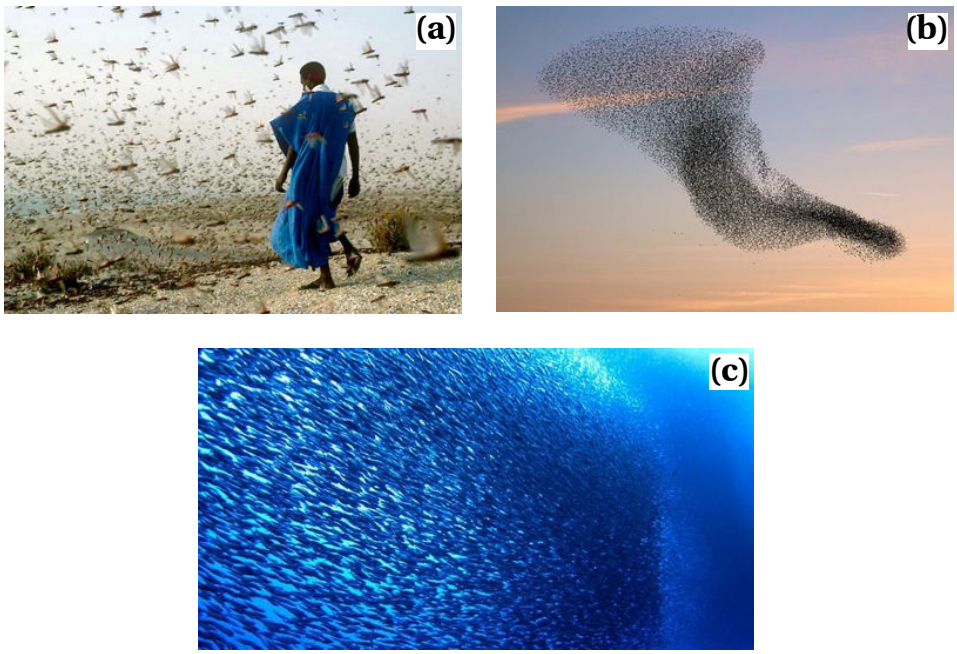


**Figure 1** – Coherent motion in animal groups. **(a)** Populations of locusts form swarms that cover hundreds of km$^2$. **(b)** Thousands of starlings move coherently within a flock. **(c)** Millions of sardines migrate collectively by forming large shoals [218].

# 1 Polar active matter

Before we describe the theoretical background of this thesis, it is useful to specify the subclass of active systems that we have in mind. In a physical perspective, the motile individuals that we mentioned in Fig. 1 are examples of *self-propelled particles*. Irrespective of the mechanisms they use to achieve their motion, they share two main features [168].

(i) Each individual converts energy, which is stored or homogeneously supplied to the system, into net translational motion. The local spend or injection of energy keeps the population out of equilibrium.

(ii) Each individual propels itself along its own direction. Self-propelled bodies are *polar* particles which carry an orientation (although their geometric shape can be isotropic).

As a matter of fact, this general definition encompasses a variety of systems. A number of biological situations involve active elements to generate motion, from animal flocks to the internal dynamics of cells [30, 121, 187, 223]. In addition, much effort has been devoted over the past 8 years to building synthetic systems in the lab. Several strategies are now available to prepare self-propelled particles, either extracted from biological materials or purely artificial. All the fundamental components of soft-matter have been motorized: polymers [115, 188, 190, 201], emulsions [52, 102, 110, 209, 210, 213], colloids [39, 105, 112, 149–151, 204], and grains [68, 120, 122, 144]. Synthetic active populations are then obtained by assembling these self-propelled units.

As an illustration of the diversity of recent active materials, three examples of experimental systems are shown in Fig. 2: bacteria swimming in thin films of liquid [227], colloids propelled by self-phoretic effects [151], and microtubule filaments driven by molecular motors [188]. We will not enter the details of the propulsion and interaction mechanisms. However, comparing the experimental pictures (Fig. 2) to the initial flocking problem (Fig. 1) yields a striking remark: none of these examples display coherent flocks akin to those observed in animal populations. In controlled experiments, more complex spatio-temporal patterns have been systematically reported, such as clustering [151, 204], swirling [68, 73], nematic organization with dynamical defects [115, 188, 201] etc. Stable directed motion is not observed at the entire population scale.

This rich phenomenology shows that the terms “collective motion” and “active matter” encompass very diverse behaviors. We have to be more precise in specifying the class of systems we study. More specifically, in this thesis we focus on *polar active matter*. We are interested in active populations which display stable directed motion, akin to the animal groups shown in Fig. 1. Locally, the individuals align their orientations and move coherently along the same local direction. Until recently, the physical descriptions of this subclass of systems were mostly restricted to theo-

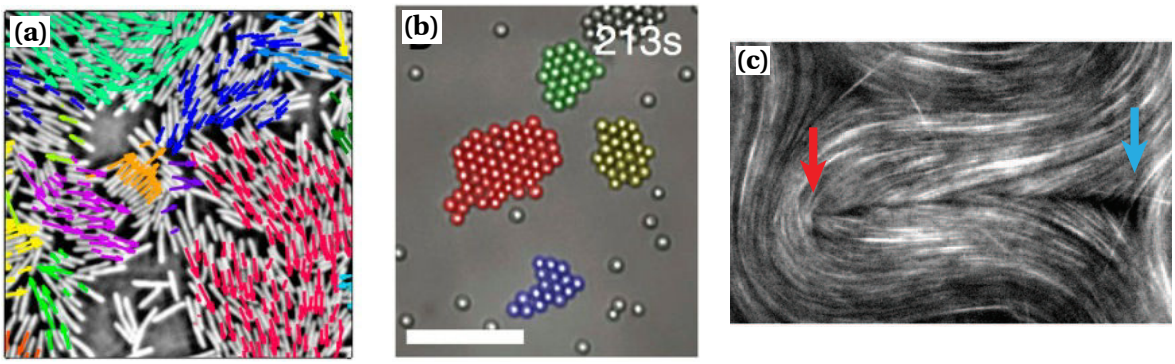


**Figure 2** – Illustration of the diversity of active patterns. **(a)** Moving clusters in suspensions of motile bacteria (reproduced from [227]). **(b)** Dynamical crystals in a suspension of self-propelled colloids (reproduced from [151]). **(c)** Nematic order in a suspension of microtubules driven by molecular motors, confined at an oil-water interface. The arrows denote disclination defects (reproduced from [188]).

retical and numerical approaches. From this perspective, the emergence of polar structures is well accounted for by a simple numerical framework, that we now describe.

## 2 The paradigmatic numerical framework: Vicsek-like models

### 2.1 The Vicsek model: aligning self-propelled spins

The physics of active matter was initiated by the seminal work of Vicsek *et al.* in 1995 [215]. The numerical model that they proposed can be introduced from a simple remark. The emergence of directed motion is observed in a variety of living systems, which obviously involve very different interaction mechanisms, see Fig. 1. This observation suggests that simple physical rules may be sufficient to account for the flocking behavior, irrespective of the details of the communication between the individuals. The Vicsek model identifies three minimal ingredients which are sufficient to explain the emergence of directed motion. (i) The motile individuals are viewed as self-propelled spins moving at a constant speed. (ii) In analogy with magnetic systems, where ferromagnetic phases arise from alignment couplings between neighboring spins, neighboring particles are assumed to align their directions of motion. (iii)These interactions compete with rotational noise, which randomizes the orientations (as does thermal noise in spin systems at equilibrium).

More precisely, the previous ingredients are implemented in a 2D agent-based model, with discrete time [215]. N point particles, located at positions $\mathbf{r}_i(t)$, move at the constant speed $v_0$. Their directions of motion are set by unit vectors $\hat{\mathbf{p}}_i(t)$. At each time step $\Delta t$, the particle positions evolve according to:

$$\mathbf{r}_i(t+\Delta t) = \mathbf{r}_i(t) + v_0 \hat{\mathbf{p}}_i(t)\,\Delta t. \tag{1}$$

This equation is complemented by an alignment rule for the particle orientations. We denote by $\theta_i$ the angle between $\hat{\mathbf{p}}_i$ and the $\hat{\mathbf{x}}$-axis. Identifying vectors and complex numbers, it is convenient to write $\hat{\mathbf{p}}_i \equiv \exp(i\theta_i)$ and $\theta_i = \arg\left(\hat{\mathbf{p}}_i\right)$ [25]. With these notations, the particles rotate their orientations as follows. At each time step, particle $i$ interacts with the $\mathrm{N}_i$ neighbors lying in the circle $\mathscr{A}_i$ of radius R, centered at $\mathbf{r}_i$ (Fig. 4(a)). Within this interaction range, the mean orientation of the neighbors is given by the angle:

$$\bar{\theta}_i = \arg\left(\frac{1}{\mathrm{N}_i}\sum_{j\in\mathscr{A}_i}\hat{\mathbf{p}}_j\right). \tag{2}$$

The particle instantaneously changes its orientation and aligns in the direction $\bar{\theta}_i$, up to a noise term (see Fig. 3). Its direction of motion becomes:

$$\theta_i(t+\Delta t) = \bar{\theta}_i(t) + \xi_i(t), \tag{3}$$

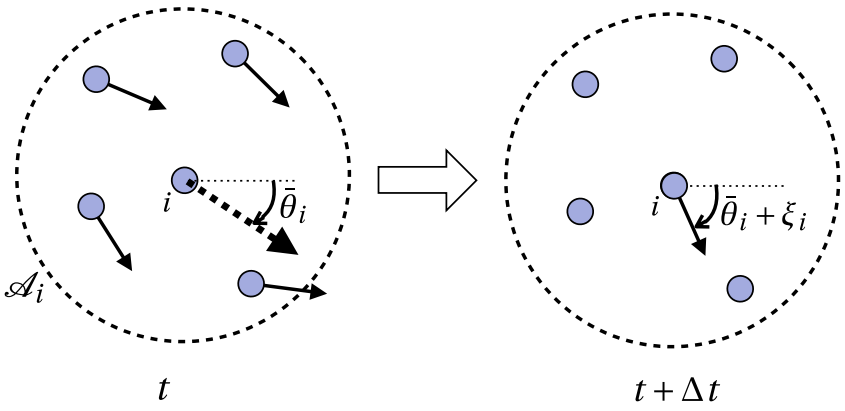


**Figure 3** – Alignment rule in the Vicsek model. To pick up its new orientation, particle $i$ computes the mean orientation $\bar{\theta}_i$ of the neighbors lying in the domain $\mathscr{A}_i$, and makes an error $\xi_i$.

where the rotational noise $\xi_i$ is uniformly distributed in the interval $[-\pi D, \pi D]$. The dynamics is simulated in periodic boundary conditions. As both the time step $\Delta t$ and the interaction radius R can be set to one, without loss of generality, the dynamics is controlled by three parameters: the particle speed $v_0$, the amplitude of the noise D, and the averaged density of particles in the simulation box.

***Transition to collective motion*** In order to characterize the emergence of polar order, we need an order parameter which quantifies the degree of alignment between the flying spins. The average polarization is defined as the modulus of the mean particle orientation:

$$\Pi_0 \equiv \left| \frac{1}{N} \sum_i \hat{\mathbf{p}}_i \right|. \tag{4}$$

We clearly find $\Pi_0 \approx 0$ when the particle orientations are random, and $\Pi_0 = 1$ when they are all perfectly aligned. Upon decreasing the noise amplitude at fixed density, the population undergoes a non-equilibrium phase transition from isotropic to polar states. The bifurcation curve is shown in Fig. 4(a). At high noise amplitudes, the system forms an homogeneous, disordered gas: $\Pi_0 \approx 0$. All directions of motion are equally distributed, as shown in Fig. 5(a). Decreasing D below a threshold value, the population self-organizes into polar phases: $\Pi_0 \neq 0$. This spontaneous symmetry breaking was expected from the alignment interactions, in analogy with the ferro-para transition in spin systems. However, the interplay with self-propulsion makes the phenomenology more subtle. As a matter of fact, two types of polar phases are successively observed.

***Onset of collective motion: heterogeneous polar phase*** In a range of noise amplitudes below the transition point, at the onset of collective motion, the system becomes spatially heterogeneous. At a first glance, the population looks phase-separated, as exemplified in Fig. 5(b): dense polar bands propagate in a dilute isotropic gas. The bands move along one of the axis of the periodic box, and are invariant along the transverse direction. When several bands are observed, they organize into periodic patterns [198]. The emergence of such spatial patterns strongly impacts the order of the transition to polar states. In contrast with the ferro-para transition at equilibrium, here the transition to collective motion is first-order. Although this question remains controversial in some limits [1, 9, 216], this feature of the transition was clearly demonstrated by the finite-size scaling analysis carried out by Chaté *et al.* [49]. They showed that the bifurcation curve, $\Pi_0$ versus D, displays a sharp jump at the transition and becomes discontinuous in the limit of large system sizes. This result is also supported by the sharp drop of the Binder cumulant, $G = 1 - \langle \Pi_0^4 \rangle / \left(3 \langle \Pi_0^2 \rangle^2\right)$, which is a signature of a discontinuous transition, see Fig. 4(b) [49]. Another evidence is the observation of hysteresis close to the transition, as shown in Fig. 4(c). This latter finding is another

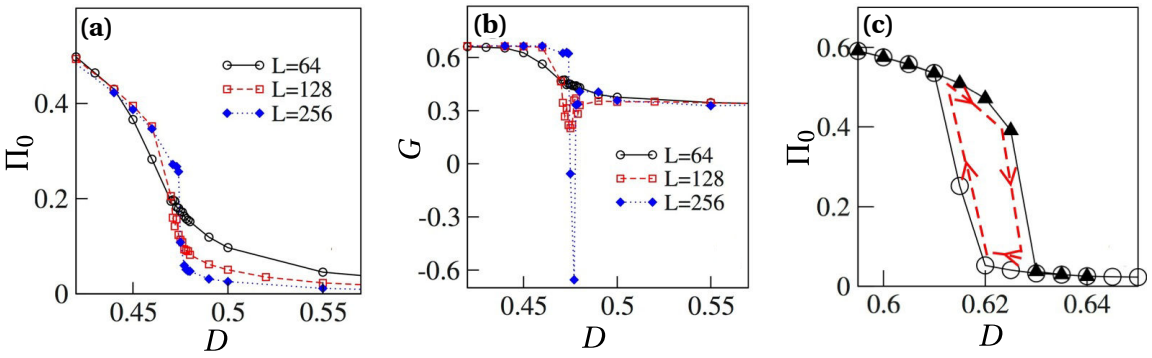


**Figure 4** – Transition to polar states in the Vicsek model (reproduced from [49]). **(a)** Average polarization $\Pi_0$ plotted versus the noise amplitude D. The different curves correspond to different system sizes. **(b)** Binder cumulant, $G = 1 - \langle \Pi_0^4 \rangle / \left(3 \langle \Pi_0^2 \rangle^2\right)$, plotted versus the noise amplitude. **(c)** Hysteresis loop in the transition curve (obtained here for a 3D version of the Vicsek model).

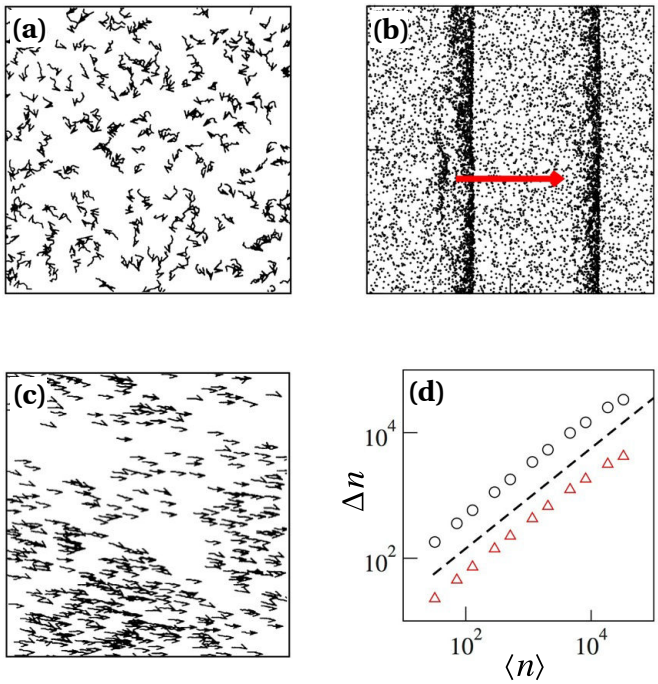


**Figure 5** – Phase diagram of the Vicsek model. **(a)** Isotropic gas (reproduced from [215]). **(b)** Heterogeneous polar phase: propagating bands (reproduced from [49]). **(c)** Homogeneous polar phase (reproduced from [215]). **(d)** Standard deviation of the particle number, $\Delta n$, plotted versus the mean number, $\langle n \rangle$, in the homogeneous polar phase (log scale). Dashed line: slope 0.8 (reproduced from [49]).

signature of first-order transitions and echoes, e.g., the nucleation of a gas bubble in a metastable liquid. It suggests that the emergence of polar states may result from the nucleation of polar patterns from a stable isotropic gas.

***Homogeneous polar phase: giant density fluctuations*** At lower noise amplitudes, far from the transition, the population forms a highly-polarized phase. A typical snapshot is shown in Fig. 5(c). In contrast with the band phase observed close to the transition, here the system is spatially homogeneous on average. This second type of polar states displays two remarkable features. (i) The polar order is truly long-ranged, in 2D. This result contrasts with equilibrium systems, in which the Mermin-Wagner theorem forbids long-range order when a continuous symmetry is spontaneously broken due to short-range interactions. (ii) Although this polar phase is globally homogeneous, it exhibits anomalously large density fluctuations. We count the number $n$ of particles lying in an arbitrary domain. Figure 5(d) shows the standard deviation $\Delta n$ plotted versus the mean particle number in the domain, $\langle n \rangle$. The number fluctuations scale as $\Delta n \propto \langle n \rangle^a$, where $a \approx 0.8$ in the limit of large domain sizes [49]. This scaling shows that density correlations are long-ranged: in any system with short-ranged correlations, the central limit theorem imposes the exponent $a = \frac{1}{2}$. Density fluctuations are enhanced in the polar phase.

## 2.2 The hallmarks of polar active matter

A number of variants of the Vicsek model have been proposed. They rely on slightly different implementations of the three fundamental ingredients identified above: self-propulsion, alignment interactions and rotational noise. These "Vicsek-like" models include e.g. various definitions of the noise [1, 9, 49, 92], metric-free interaction rules (each individual interacts with its nearest-neighbors, irrespective of the distance) [83, 160], continuous-time equations of motion [79, 156], and 1D implementations on periodic lattices [147, 197]. Without entering the details of the differences between these models, let us mention one specific example which will be of great impor-

tance in this thesis. A couple of works have considered an active analog of the classical XY model, referred to as the "flying XY model" and defined by [79, 156]:

$$\frac{\mathrm{d}}{\mathrm{d}t}\mathbf{r}_i = v_0\hat{\mathbf{p}}_i, \tag{5}$$

$$\frac{\mathrm{d}}{\mathrm{d}t}\theta_i = -\frac{1}{\tau}\sum_{j\in\mathscr{A}_i}\sin(\theta_i-\theta_j)+\xi_i, \tag{6}$$

where $\xi_i$ is the rotational noise and $\tau$ the typical alignment time. The first term of Eq. (6) takes the form of an effective potential for the particle orientation: $\frac{\mathrm{d}}{\mathrm{d}t}\theta_i = -\frac{\partial}{\partial\theta_i}\sum_j \mathscr{H}_{\mathrm{eff}}(\theta_i-\theta_j)+\xi_i$, where $\mathscr{H}_{\mathrm{eff}}(\theta_i,\theta_j) = -\tau^{-1}\cos(\theta_i-\theta_j)$ promotes alignment between particles in a typical timescale $\tau$. In this model, the alignment couplings are pairwise-additive: the more neighbors in the interaction range, the stronger the alignment. This property, which is expected for a number of physical interactions, contrasts with the non-additive behavioral rules introduced in the Vicsek approach.

The variants of the Vicsek model make it possible to test the robustness of the macroscopic phenomenology to the specific forms of the alignment interactions and rotational noise. Three distinctive features of polar active matter have been identified.

***Transition to collective motion*** In all models, the competition between alignment interactions and rotational noise gives rise to a transition to polar phases, upon decreasing the noise amplitude. Apart from metric-free models (in which the particle density is not relevant), we stress that the transition can also be reached by increasing the mean density, at fixed noise amplitude. The latter control parameter can be easily varied in experimental systems: the existence of a transition has been also confirmed in experiments, as we will discuss it later [38, 68, 122, 190].

***Onset of collective motion: heterogeneous polar phase*** The emergence of spatial patterns at the onset of collective motion is a very robust observation. Apart from metric-free models, it has been observed in a wealth of numerical simulations and experiments [36, 49, 92, 175, 190, 197, 219], irrespective of the symmetry of the order parameter [198]. Heterogeneous polar structures, akin to the bands shown in Fig. 5(b), propagate in a dilute, weakly-polarized background. However, beyond this generic qualitative feature, the precise shape of the band pattern depends on the specifics of the model. The exact structure of the heterogeneous polar phase is not universal, and remains difficult to understand theoretically. We will come back to the numerical and experimental phenomenology in Chapter 2, in which we consider this question in more details.

***Homogeneous polar phase: giant density fluctuations*** The existence of giant density fluctuations is also a robust feature of homogeneous polar phases. The standard deviation of the number fluctuations scales as $\Delta n \sim \langle n\rangle^a$, where $a > \frac{1}{2}$. Theoretical and experimental approaches demonstrated that this abnormal behavior arises from the interplay between self-propulsion and splay fluctuations [136, 144, 169, 189, 214]. Due to the particle motion, any splay disturbance of the particle orientations yields density fluctuations, as sketched in Fig. 6. Although the splay modes are

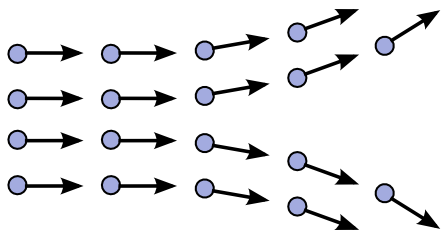

**Figure 6** – In polar phases, splay disturbances of the particle orientations are coupled to density fluctuations (here, a diverging splay perturbation yields a local depletion of particles).

damped diffusively, they are advected over long distances by the particle propulsion. The resulting density correlations are long-ranged. When counting the number fluctuations in a large domain, the central limit theorem does not apply and the density fluctuations are anomalously large. This scenario is confirmed by the absence of giant number fluctuations in one-dimensional models.

We stress that the homogeneous polar phase remains linearly stable. The splay mode, which is responsible for the density fluctuations, is diffusively damped. By contrast, a number of experimental and numerical works have also reported giant fluctuations in a different context, in systems displaying spatio-temporal patterns such as dynamical clusters [68, 151, 227]. When the homogeneous polar state is unstable and gives rise to heterogeneous structures, the origin of the enhanced number fluctuations and their scaling exponent may be different. All in all, regardless of their origin, large density fluctuations were found in all polar systems. Conversely, we will study in this thesis an experimental system displaying a homogeneous polar state with very few density fluctuations $\left(a = \frac{1}{2}\right)$. This observation suggests that the giant fluctuations can be suppressed by additional mechanisms, which we will try to identify.

The three previous properties are the hallmarks of polar active systems, governed by alignment interactions. They have been firmly established by a number of numerical studies, and are robust to the specifics of the interaction rules. We now describe the analytical approaches which were proposed to explain these observations.

# 3 Hydrodynamic description of active populations

## 3.1 Active populations as self-flowing fluids

In addition to the numerical models, the theoretical study of active matter was initiated by Toner and Tu in 1995 [211]. They adopted the basic idea of hydrodynamics: the coupled dynamics of all particles cannot be solved at the microscopic level, however the macroscopic properties of the system are well accounted for by a coarse-grained continuum description. Al large scale, the population is viewed as an effective material, a fluid capable of flowing by itself. The hydrodynamics of this active fluid is described by two slowly-varying fields: the local density $\rho(\mathbf{r}, t)$, and the local velocity $\mathbf{u}(\mathbf{r}, t)$.

Toner and Tu derived evolution equations for these hydrodynamic fields from conservation laws and symmetry arguments. First, the particle-number conservation imposes the usual continuity equation:

$$\partial_t \rho + \nabla \cdot (\rho \mathbf{u}) = 0. \tag{7}$$

Second, the equivalent of the Navier-Stokes equation is obtained by keeping all the terms allowed by symmetry. As the hydrodynamic description is meant to account for slow spatial variations, the equation is truncated at second order in gradients [211, 214]:

$$\partial_t \mathbf{u} + \xi_1 (\mathbf{u} \cdot \nabla)\mathbf{u} = \left(a_2 - a_4 |\mathbf{u}|^2\right)\mathbf{u} - \nabla P + \xi_2 (\nabla \cdot \mathbf{u})\mathbf{v} + D_1 \nabla^2 \mathbf{u} + D_2 \nabla (\nabla \cdot \mathbf{u}) + D_3 (\mathbf{u} \cdot \nabla)^2 \mathbf{u}. \tag{8}$$

Random forces can be added as well to account for fluctuations at the hydrodynamic level.

Three important comments are in order.

(i) The first term in Eq. (8) allows a spontaneous breaking of the rotational symmetry, when $a_2 > 0$. Indeed, looking at spatially-homogeneous states, this equation reduces to $\partial_t \mathbf{u} = \left(a_2 - a_4 |\mathbf{u}|^2\right)\mathbf{u}$. When $a_2 < 0$, the velocity relaxes to zero. This situation corresponds to an isotropic phase: a vanishing mean velocity is found when the motile particles move in random directions. Conversely, when $a_2 > 0$ the disordered state is linearly unstable and the population forms a polar state with non-zero mean velocity. Assuming $a_4 > 0$, the corresponding solution is $u = \sqrt{a_2 / a_4}$. Note that a negative $a_4$ coefficient would require to include higher-order terms in the expansions, such as $a_6 |\mathbf{u}|^4 \mathbf{u}$, in order to prevent the divergence of the velocity. Hence the form of

Eq. (8) captures the spontaneous breaking of the rotational symmetry by the selection of a random direction.

(ii) The above equations have been deduced from generic symmetry arguments. They apply to all polar systems, irrespective of the form of the interactions at the microscopic level. However, the generality of this approach implies that the eight coefficients $a_2$, $a_4$, P, $\xi_1$, $\xi_2$, $D_1$, $D_2$, $D_3$ are unknown. Importantly, they are not scalar coefficients, *a priori*, but functionals of the two scalar fields $\rho$ and $|\mathbf{u}|^2$. Both their signs and their functional dependences are related to the details of the microscopic dynamics. They cannot be predicted by this general approach.

(iii) The gradient expansion used to derive Eq. (8) holds when the interactions are short-ranged. In this thesis, we will show that long-ranged interactions add non-local terms which impact the large-scale properties of the active fluid.

The previous hydrodynamic framework was successfully used to explain the large-scale properties of homogeneous polar phases. The Toner and Tu equations predict the propagation of linear waves having anisotropic propagation speeds [212, 214]. They also explain the emergence of long-range order in polar phases, which was elucidated from a renormalization-group analysis of Eqs. (7)–(8) [211, 212]. In addition, the giant density fluctuations are well captured by this hydrodynamic description (we will come back to this specific point in Chapter 1) [136, 212]. We also note that similar phenomenological approaches were applied to many other active systems, including active gels [113, 117, 118, 163], bacterial suspensions [222, 223] or active nematics [85–87, 169, 192].

However, important numerical findings cannot be explained within this general framework. First, the value of the scaling exponent of the density fluctuations is still debated. Second and more important, generic symmetry arguments are not sufficient to predict the existence of a phase transition when varying microscopic parameters, nor the emergence of spatial patterns at the onset of collective motion. The expressions of the 8 unknown functional are crucial to answer these questions. In order to make further progress, we have to discuss the connection between the Toner-Tu theory at large scale, and the equations of motion at the one-particle level.

## 3.2 Connection with the microscopic dynamics: kinetic-theory approaches

Over the past few years, significant effort has been devoted to establishing hydrodynamic theories, akin to the Toner-Tu equations, from microscopic models. The hydrodynamic fields are explicitly built from the degrees of freedom of the particles. The density field is inferred from the distribution of the particle positions:

$$\rho(\mathbf{r},t) = \left\langle \sum_i \delta\left(\mathbf{r}-\mathbf{r}_i(t)\right) \right\rangle, \tag{9}$$

where the brackets $\langle\cdot\rangle$ denote the average over the realizations of the stochastic microscopic dynamics. Similarly, the local average of the particle orientations defines the polarization field:

$$\mathbf{\Pi}(\mathbf{r},t) = \frac{1}{\rho(\mathbf{r},t)} \left\langle \sum_i \hat{\mathbf{p}}_i \delta\left(\mathbf{r}-\mathbf{r}_i(t)\right) \right\rangle, \tag{10}$$

which, for particles moving at a constant speed $v_0$, readily sets the velocity field $\mathbf{u}(\mathbf{r},t) = v_0\mathbf{\Pi}(\mathbf{r},t)$.

The evolution equations for the density and velocity fields are established from the microscopic dynamics using kinetic-theory methods. The equations of motion of the particles are coarse-grained and lead to Toner-Tu-like hydrodynamic equations, focusing on slow time and space variations. Such approaches have been implemented for a large number of microscopic models, in the literature [11–13, 23–25, 79, 108, 131, 139, 158–160, 207, 208]. In particular, E. Bertin *et al.* considered a variant of the Vicsek model, in which particle alignment occurs during binary collisions. They used a Boltzmann-like approach to derive the resulting hydrodynamic equations.

These coarse-graining methods have been much useful for our work: we will review their technical implementations in Chapter 1.

The kinetic-theory approaches lead to hydrodynamic equations having the form predicted by Toner and Tu. In addition, they provide the functional dependences of all coefficients as a function of $\rho$ and $|\mathbf{v}|^2$, and relate them to the parameters of the microscopic dynamics. Importantly, these results account for the existence of a transition to collective motion. As we discussed it above, the transition between isotropic and polar states is triggered by the sign change of the coefficient $a_2$. In Vicsek-like models assuming finite-ranged (metric) interactions, it takes the form: $a_2 = \alpha(\rho - \rho_c)$, where $\alpha$ and $\rho_c$ depend on the noise amplitude [23, 25, 79]. Hydrodynamic descriptions therefore account for the emergence of collective motion when the density reaches a critical value $\rho_c$, in agreement with the numerical findings. A more detailed analysis of the expressions of $\alpha$ and $\rho_c$ shows that the transition is also reached by decreasing the noise amplitude, at fixed density.

In spite of this qualitative success of hydrodynamic theories, two numerical observations remain poorly understood.

(i) It was numerically shown, in the Vicsek model, that the transition to collective motion is first-order. In the canonical Landau description of phase transitions, this result would be readily explained by a negative $a_4$ coefficient. Conversely, the kinetic theories demonstrate that $a_4$ is positive. Looking at spatially-homogeneous states, Eq. (8) therefore predicts a *continuous* transition from the isotropic to the polar phase. When the density reaches $\rho_c$, the velocity continuously bifurcates from $u = 0$ to $u = \sqrt{\alpha(\rho - \rho_c)/a_4}$. In other words, a (meta-)stable disordered phase never coexists with a (meta-)stable polar phase. The existence of hysteresis at the transition, Fig. 4(c), has no simple explanation.

(ii) The origin of the spatial patterns observed at the onset of collective motion is still debated. Two scenarios have been proposed. In a first scenario, the spatial structures result from the (still unexplained) first-order nature of transition. The spatial structures would correspond to a phase separation: polar droplets would coexist with the isotropic gas. In a second scenario, the polar patterns emerge from an instability of the polar phase. For short-ranged (metric) interactions, the hydrodynamic theories indeed predict that the homogeneous polar phase is linearly unstable against finite-wavelength perturbations [25, 136, 141]. The shape of the spatial patterns is then set by the non-linearities of the hydrodynamic equations. Consistently, propagating solitonic solutions have been demonstrated numerically in specific models [25, 88, 91, 141].

As a matter of fact, these questions are the two sides of the same coin: the formation of localized structures is related to the first-order nature of the transition [49, 109]. However, it does not reduce to a simple coexistence scenario at the mean-field level: there is no domain where both the isotropic gas and the homogeneous polar phase are linearly stable. Conversely, it is the formation of spatial patterns which makes the transition discontinuous. We shall note that the importance of spatial fluctuations was already stressed in equilibrium systems: fluctuations can make first-order a transition which is second-order at the mean field level [35, 104, 202]. However, we will show that the transition to collective motion follows a very different mechanism from these equilibrium scenarios. To gain more insight, we will have to study the non-linear excitations of polar active matter. This is the purpose of Chapter 2.

To close this section, we stress that continuum descriptions are the standard theoretical framework used to study active populations. Lagrangian descriptions have been scarcely explored. Yet, the individual motions are known to display non-trivial behaviors in polar phases, such as anomalous transverse diffusion [43, 49, 211]. In complement to the usual hydrodynamic approaches, we will also consider the dynamics of interacting particles in a Lagrangian description, see Chapter 3.

# 4 From theoretical models to actual systems

In the previous sections, we have recalled the two basis of active-matter theory: minimal interaction rules at the microscopic level (Vicsek-like models), and generic hydrodynamic descriptions at the macroscopic level (Toner-Tu theory). Kinetic theories connect these two approaches. The next step is to come back to experiments and test the relevance of this theoretical framework to the description of actual systems: does it accurately accounts for the origin and the properties of polar structures in real populations? This question is one of the main issues of this thesis. It can be tackled by considering two types of systems: living populations, or synthetic active particles.

## 4.1 Inferring behavioral rules from living populations

Up to now, the only examples of *polar* active systems that we mentioned are animal groups. It is natural to confront the theoretical descriptions to these living systems, which have inspired the first works on active matter. A number of experiments have studied animal populations, either in the wild or in the lab. For instance, Bialek *et al.* have derived a microscopic theory from experimental data on starling flocks [27]. Measuring the velocities all bird in the flock, they showed that the orientational correlations are reproduced by a probability distribution of the form:

$$\mathrm{P}\left(\{\hat{\mathbf{p}}_i\}\right) = \frac{1}{\mathrm{Z}} \exp\left[-\sum_{i,j} \mathrm{J}_{ij}\, \hat{\mathbf{p}}_i \cdot \hat{\mathbf{p}}_j\right], \tag{11}$$

where $\hat{\mathbf{p}}_i$ is the direction of motion of the $i^{\text{th}}$ bird. The latter distribution satisfies the maximum entropy principle: it is the simplest distribution which reproduces the experimental correlations. It is analogous to a thermal equilibrium distribution, for which the effective Hamiltonian $\mathscr{H}_{\text{eff}}(\hat{\mathbf{p}}_i, \hat{\mathbf{p}}_j) = \mathrm{J}_{ij}\, \hat{\mathbf{p}}_i \cdot \hat{\mathbf{p}}_j$ has exactly the form defining the "flying XY model", Eq. (6) above (although birds interact with a fixed number of nearest neighbors, rather via metric alignment rules [10]). This approach has been refined to also describe velocity fluctuations and rapid information transfers in the flock [6, 8, 26, 46]. It confirms, on a rigorous basis, the relevance of alignment interactions between birds viewed as flying spins. Consistent quantitative results have also been obtained in animal populations as diverse as fish schools [132], locust swarms [38] or midge groups [7].

However, although alignment interactions correctly capture the emergence of directed motion, they are not sufficient to fully reproduce the behaviors displayed by animal populations. In particular, they do not lead to compact flocks. Attractive and repulsive couplings are also required to ensure the cohesion of the group at long distance, and to prevent collisions between individuals at short range [50, 57, 172]. As a result, quantitative data analysis on living populations clearly validate the Vicsek ideas, but also show that basic alignment couplings are entangled with

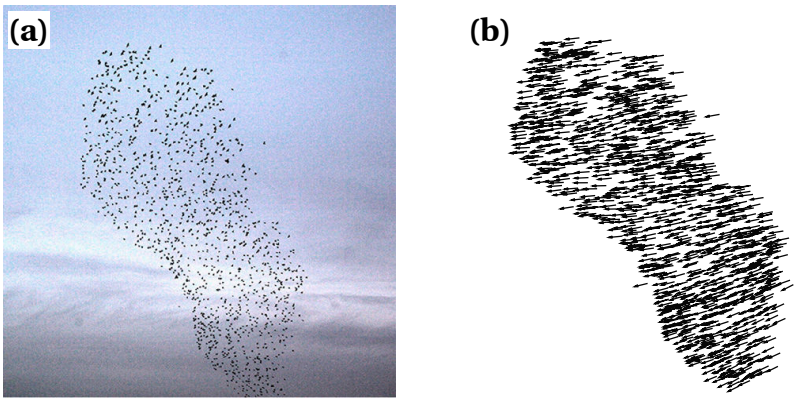


**Figure 7** – Relevance of the Vicsek ideas to the description of animal groups. **(a)** A starling flock can be described as **(b)** a population of flying spins endowed with ferromagnetic alignment couplings (reproduced from [27]).

more complex behavioral rules. This finding highlights the limitation of the approaches based on animal populations: the models rely on effective interaction rules, which must be inferred *a posteriori* from experimental measurements [26, 27, 40, 114, 132]. In living systems, the real interaction mechanisms are obviously much more complex. The communication between individuals involves elaborate biological processes which cannot be modeled from first physical principles. Hence it is very difficult to identity and vary the control parameters in experiments. The formation of polar flocks results from a combination of environmental factors, and the transition to collective motion cannot be triggered by tuning a simple experimental parameter.

## 4.2 Modeling experimental systems

In order to circumvent the intrinsic limitations of experiments on living populations, significant effort has been devoted to designing artificial systems. Such experiments aim at controlling all parameters of the dynamics, in order to understand the very origin of collective motion. An optimal model system fulfills three requirements: (i) all parameters are controlled or measured, (ii) polar structures form at large scale, (iii) the interactions between particles are physically understood from first principles. Satisfying these conditions requires a combination of experimental work to build large populations of self-propelled bodies, and theoretical effort to model the microscopic dynamics and make the connection with the standard numerical and hydrodynamic approaches. At the beginning of this PhD, these three requirements were not met in any experimental system. As we already stressed it at the beginning of this introduction, a number of controlled experimental systems are now available. However, only few of them display polar structures. A first realization consists in populations of robots: collective behaviors were indeed observed and modeled, however it is difficult to reach large particle numbers [84]. Two other experimental systems exhibit polar order in larger populations.

***Actin filaments driven by molecular motors*** Schaller *et al.* devised an active system by assembling biological materials [190]. The motile objects are actin filaments – elongated proteins which compose the cell cytoskeleton. They are set in motion by molecular motors (myosin proteins) fixed on a 2D surface, as sketched in Fig. 8(a). The main advantage of this molecular system is that large particle numbers are easily reached. Varying the actin concentration, a transition to collective motion has been observed. At low concentrations, the filaments move in random directions and form an isotropic phase. Upon increasing the filament density, it self-organizes into coherent polar structures which take the form of moving clusters (Fig. 8(b)), bands (Fig. 8(c)) and swirls (Fig. 8(d)). In dense systems, giant density fluctuations were measured. Their origin was clearly related to splay fluctuations, in qualitative agreement with the theoretical predictions [189].

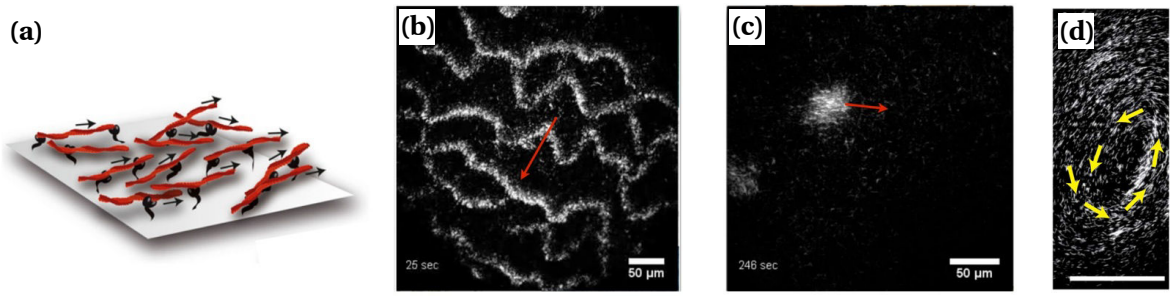


**Figure 8** – Actin filaments driven by molecular motors. **(a)** Sketch of the experimental system (reproduced from [189]). **(b)** Polar bands (reproduced from [190]). **(c)** Polar cluster (reproduced from [190]). **(d)** Swirling pattern (reproduced from [190]).

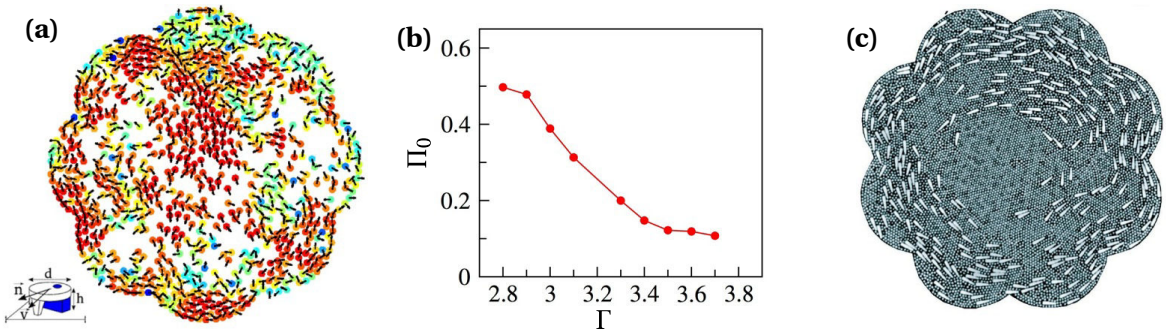


**Figure 9** – Vibrated polar grains. **(a)** Polar disks moving on a vibrating surface. Red colors denote polar clusters of aligned disks (reproduced from [68]). **(b)** Average polarization plotted versus the amplitude of the surface vibration (adapted from [68]). **(c)** Polar rods (white color) surrounded by passive beads (grey color) (reproduced from [122]).

***Vibrated polar grains*** Another class of systems consists is grains shaken on a vibrating surface. When the grains are polar, more precisely when the friction with the surface is asymmetric, the repeated collisions with the vibrating plane results in a net motion of the particles [120]. Using polar disks, J. Deseigne and O. Dauchot demonstrated the existence of a transition to polarized phases, as shown in Figs. 9(a) and 9(b) [68]. Reducing the amplitude of vibration makes it possible to decrease the rotational diffusivity of the disks, and to trigger a transition akin to that observed in Vicsek-like models. In this system, the alignment results from contact interactions between the motile disks. Another possibility was recently proposed by Kumar *et al.*: the interactions between pointy rods are mediated by non-motile, isotropic beads [122]. The motion of the active rods induces a flow of passive beads, as would an active swimmer in a fluid: the polar rods interact at a distance via the displacement of the beads. At high enough density, the rods coherently circulate in the confining box as shown in Fig. 9(c).

The experimental systems mentioned above partially validate the theoretical framework of polar active matter: a transition to collective motion is observed, it is associated with heterogeneous spatial structures, and giant density fluctuations have been measured. However, they do not significantly increase our knowledge of the origin of directed motion. Indeed, the interactions between the motile bodies are very difficult to describe. They mostly arise from short-range collisions and remain challenging to describe from first physical principles. In the actin motility assays, the emergence of polar order from contact interactions between elongated filament is far from obvious. At a first glance, excluded-volume interactions between hard rods have rather a nematic symmetry, as sketched in Fig. 10 [11, 13]. It is not much easier to understand how alignment arises from collisions between circular grains. Up to now, the theoretical descriptions have been restricted to phenomenological approaches, based on numerical simulations of simplified microscopic models [94, 122, 219]. They showed that polar states emerge from very subtle mechanisms, which do not reduce to effective alignment torques as assumed in all Vicsek-like models. As a result, it is difficult to unambiguously identify and model the physical ingredients which rule, at the

**Figure 10** – At a first glance, the repulsion between slender motile bodies seems to promote nematic ordering. When the initial angle between the rods is closer to $\frac{\pi}{2}$, this naive picture does not hold and polar collisions are actually favored.

one-particle level, the formation and the shape of the observed patterns.

In this thesis, we will study another experimental system in which the microscopic dynamics can be modeled from first physical principles. The physical origin of collective motion can be clearly identify, and put into the simple form of Vicsek-like alignment torques. Hence the large-scale behavior of the population can be explicitly linked to the microscopic dynamics, following the standard hydrodynamic approaches. This is the purpose of Chapter 1.

### 4.3 A diversity of polar patterns

Finally, we compare the previous experimental observations and the standard theories of active matter. It is worth noting that none of the systems described above fully reproduce the phenomenology of Vicsek-like models. In particular, none of them displays the homogeneous polar state found numerically at large density and small noise. More complex patterns have been systematically observed, such as clustering and swirling motions. From a theoretical perspective, it is important to understand the discrepancies between paradigmatic theories and model experiments. Two explanations can be proposed.

- First, most of the numerical simulations have been performed in periodic boundary conditions. By contrast, experimental systems are confined in closed boxes. The emergence of homogeneous polar phases is therefore frustrated: the particles are forced to change their direction when reaching the boundaries. This simple remark highlights the role of the boundary conditions in setting the shape of the polar patterns.

- Second, in real systems the alignment rules are entangled with more complex interactions. A very large number of numerical models, which we will not describe here, have demonstrated that including additional interactions to the microscopic models dramatically impacts the large-scale structure of the population. The diversity of experimental patterns echoes the variety of numerical behaviors obtained from different interaction rules, see e.g. [50, 55, 57, 92, 95, 128, 134, 140, 176].

We will obviously have to consider these two points more carefully when modeling our experimental system.

## 5 Goals and organization of this thesis

The previous sections have highlighted three main issues of active-matter theories: microscopic models, large-scale descriptions, and connection with experimental systems. They are obviously closely related, and this thesis aims at establishing links between these various aspects. It is based on three entry points, which compose the three main chapters of this manuscript.

***Chapter 1:*** **Emergence of macroscopic polar phases in a model colloidal system**
The first part of this thesis is devoted to the theoretical description of a model experimental system: a population of motile colloids. We quantitatively confront active-matter theories and experiments.

- We explicitly link the macroscopic properties of the system to the microscopic dynamics. We establish and coarse-grain the equations of motion of the colloidal population. This approach makes it possible to identify the microscopic interactions responsible for the patterns observed at large scale.

- As opposed to the other available experiments, this system displays homogeneous polar states at high densities. Yet giant density fluctuations are not observed. We propose a mechanism to explain this discrepancy with the previous theoretical predictions.

- We investigate the influence of the boundary conditions on the structure of the polar patterns. We show that rigid confinement leads to the formation of an heterogeneous vortex phase.
- Beyond the specifics of this system, we discuss the generality of our results. In particular, we classify the possible interactions between self-propelled bodies.

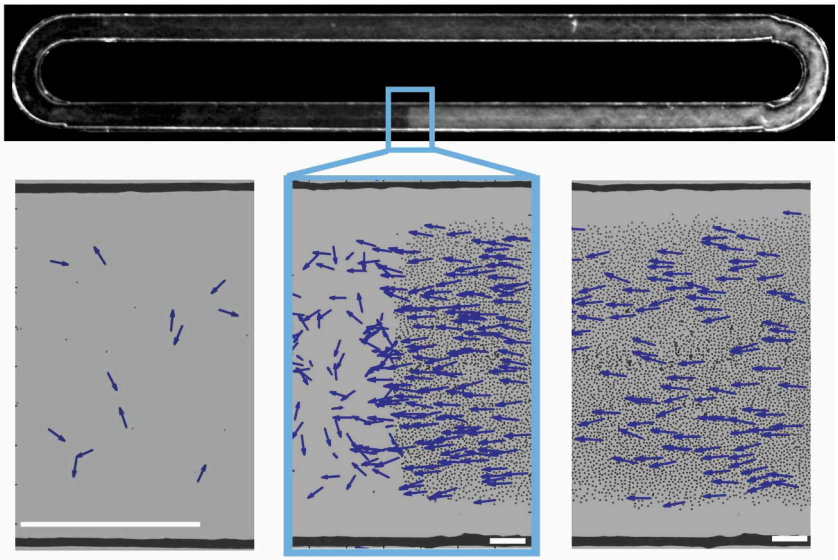

**Figure 11** – We study a population of colloidal rollers which reproduce the Vicsek phenomenology. Top: a macroscopic polar band forms at the onset of collective motion. Bottom: close view on the three phases of the system – isotropic gas, polar band and homogeneous polar liquid.

***Chapter 2:*** **Emergent spatial structures in flocking models**
The second chapter deals with the heterogeneous polar patterns which generically form at the transition to collective motion. We introduce a dynamical-system framework to analyze the shape of these non-linear excitations. We show that the conventional hydrodynamic theories possess traveling solutions which exactly correspond to the patterns observed in simulations and experiments. The results also provide further insight into the first-order nature of the transition to collective motion.

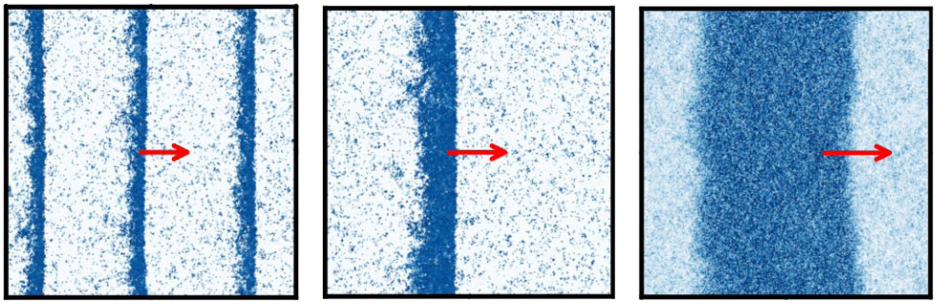

**Figure 12** – Simulations and experiments display three types of spatial patterns, which correspond to three classes of non-linear solutions of the hydrodynamic equations of active matter.

***Chapter 3:*** **Geometry of interacting trajectories in a flock**
Finally, we propose another description of active systems. Combining analytical and numerical results, we adopt a geometric approach to characterize the particle trajectories in standard flocking models.

- We show that the non-equilibrium dynamics of interacting active particles can be mapped onto the conformations of semi-flexible polymer chains at equilibrium. Building on this analogy, we study the statistics of the curvature and the writhe of the trajectories. These quantities provide information on the microscopic dynamics, in a Lagrangian approach.

- In a geometric perspective, the motion of a compact flock defines a braid of entangled trajectories. We characterize the winding between the particle trajectories, which measures the mixing dynamics within the flock. We show that it is predominantly set by the global twist which arises from a spontaneous symmetry breaking.

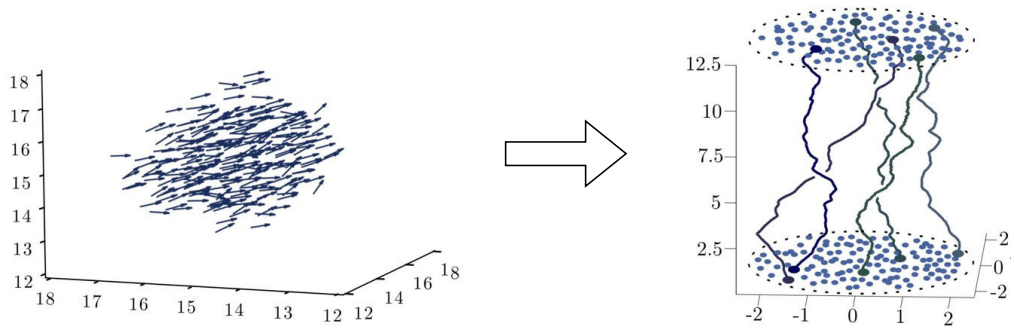


**Figure 13** – A compact polar flock (left) can be seen as a braid of entangled individual trajectories (right).

***Appendix:* Non-equilibrium dynamics of confined suspensions**

In the appendix, we reproduce two articles devoted to a closely-related problem. They study the collective dynamics of suspensions of particles confined in thin liquid films. Two situations are considered: (i) *passive* particles driven by an external flow (e.g. droplets advected in a microfluidic channel), and (ii) *active* particles which propel themselves (e.g. swimming bacteria in thin films). The motion of the particles induces a flow field in the liquid. It turns out that, in both cases, the resulting hydrodynamic interactions have the same symmetry: they correspond to long-ranged, unscreened dipolar flows. In the passive case, we demonstrate the propagation of density waves. The theoretical dispersion relation is in agreement with a model microfluidic experiment. In the active case, we investigate the large-scale hydrodynamics of isotropic suspensions, and show that the phase behavior solely depends on the shape of the swimmers.

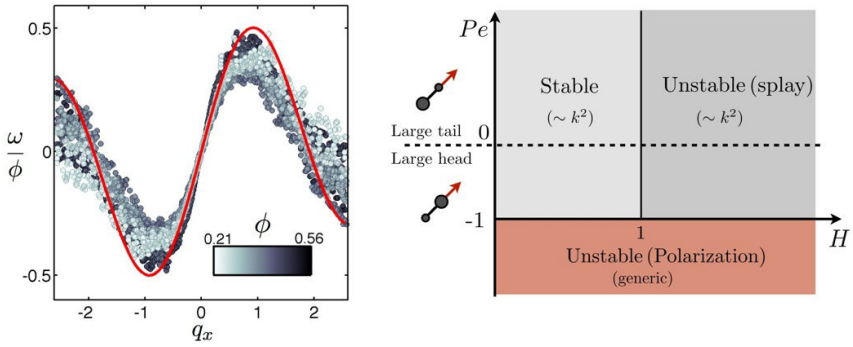


**Figure 14** – Left: propagation of density waves in advected confined emulsions. The dispersion relation is studied experimentally (grey dots) and theoretically (red curve). Right: phase diagram of a confined suspension of active particles. The linear stability of disordered states depends on the strength of the hydrodynamic interactions and on the shape of the swimmers.

CHAPTER 1

# Emergence of macroscopic polar phases in a model colloidal system

Although polar active matter has motivated a large number of theoretical works, only few experiments display polar structures in fully controlled systems. Comparing theories to controlled experiments therefore remains a challenging issue. On the theoretical side, numerical and analytical models have identified simple interaction rules that account for the emergence of polar structures: self-propelled spins endowed with alignment interactions undergo a transition from disordered to polar states [136, 216]. However, the relevance of this standard framework to the description of real systems is difficult to assess. In living populations, the communication between individuals involves biological mechanisms, e.g. visual and cognitive processes, that are not set by physical laws and cannot be modeled *a priori*. Identifying the parameters that chiefly rule the collective dynamics, and controlling their values in experiments, is a difficult challenge. To gain more insight into the physical mechanisms that trigger collective motion, we rather turn to synthetic systems in which all parameters can be controlled.

Until 2013, only two artificial systems displayed polar structures in large populations: actin filaments propelled by molecular motors [190], and polar grains shaken on a vibrating surface [68]. However, in these two experiments the interactions mostly arise from collisions between the particles, which are utterly difficult to describe theoretically [13]. Analytical descriptions were therefore restricted to simplified collision rules introduced semi-phenomenologically. In addition, none of these experimental setups displayed the homogeneous polar phase found in simulations of the Vicsek-like models. We therefore need another system, experimentally controlled, which would make it possible to fully model the dynamics from first physical principles. It would thereby allow a quantitative comparison between theory and experiments.

In the group of Denis Bartolo, we have studied a population of rolling colloids that fulfills these requirements. In strong connection with the experiments, we have modeled the dynamics from the microscopic to the macroscopic level.

Hereafter, I briefly outline our approach and our main results, putting emphasis on the theoretical part. This summary does not aim at providing thorough explanations about the calculations, it merely highlights the main steps that we have followed. All details can be found in the articles reproduced at the end of the chapter. More precisely, most of the theoretical results are derived in the Supplementary Document of the article "Emergence of macroscopic directed motion in population of motile colloids", which is reproduced p. 43. We will also refer to the two articles "Emergent vortices in populations of colloidal rollers" and "Tailoring the interactions between self-propelled bodies", p. 66 and 79, that focus on more specific points.

This chapter is organized as follows.

1) In the first section, we show how to design a model active system. We theoretically introduce the propulsion mechanism, based on the Quincke rotation of colloidal spheres near a surface, and compare with experimental results.

2) We then model the interactions between rolling colloids from the Stokes and Maxwell equations. We also discuss the validity and the generality of the resulting equations of motion.

3) Finally, we coarse-grain the microscopic model and study the large-scale behavior of the population. We theoretically explain the macroscopic phenomenology observed experimentally.

# 1 Designing a population of self-propelled colloids

In this section, we show how to design a synthetic population of self-propelled particles. The propulsion of colloidal spheres is achieved by combining two effects, that we briefly introduce in the first subsections:

1) a net rotation of the particles is produced by an electro-hydrodynamical instability known as the Quincke rotation,

2) this rotational motion is then converted to translational motion by letting the sphere roll on a solid surface.

We then validate our theoretical description by comparing to experiments. We finally exploit this active system to probe the emergence of polar order, and briefly describe the collective behaviors observed experimentally.

## 1.1 Powering an insulating particle in a conducting liquid: the Quincke rotation

To produce the mechanical motion of spherical particles, we take advantage of an electro-hydrodynamic effect that converts electrostatic energy supplied to the system into mechanical motion. Let us consider an insulating sphere of radius $a$, located at $\mathbf{r} = \mathbf{0}$ and immersed in a conducting fluid (an ionic solution). A uniform electric field $\mathbf{E}_0$ is applied in the direction $\hat{\mathbf{z}}$, as sketched in Fig. 1.1. Above a critical magnitude of the electric field, the particle spontaneously rotates around an axis perpendicular to $\mathbf{E}_0$. This effect was first reported by Quincke in 1896 [165] and is known as the Quincke rotation. A complete theoretical explanation was proposed by Melcher and Taylor in 1969 [138]. More recent studies have mostly focused on the impact on the rheology and the conductivity of suspensions [62, 72, 106, 126, 152, 153].

We briefly recall the physical origin of this instability. As an external electric field is applied, a surface-charge distribution arises at the interface between the spherical particle and the liquid.

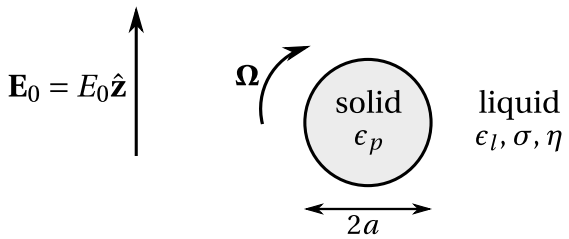


**Figure 1.1** – An insulating sphere is embedded in a conducting liquid, and a uniform DC electric field $\mathbf{E}_0$ is applied. The particle undergoes the Quincke rotation when the amplitude of the field exceeds a threshold value.


**Figure 1.2** – Emergence of the Quincke rotation. **(a)** Electric charges accumulate at the particle-liquid interface and result in a dipolar surface distribution. **(b)** When a small rotational perturbation tilts the dipole $\mathbf{P}$, a net electric torque $\mathbf{T}^e$ amplifies the initial perturbation.

It has two origins. (i) The particle and the liquid have different dielectric permittivities; in the external field, their dielectric polarization gives rise to a net charge-density at the interface. (ii) Ions are transported in the conducting liquid from one electrode to the other, and accumulate at the interface with the insulating particle. The resulting charge distribution induces an electric field that superimposes to $\mathbf{E}_0$. It in turn impacts the dielectric polarization and the transport of ions in the liquid: a steady state is reached when the net flux of charges vanishes at the interface. The particle then carries a dipolar charge distribution. Its dipole moment $\mathbf{P}$ is opposite to the applied field $\mathbf{E}_0$, as sketched in Fig. 1.2(a).

A naive analysis readily suggests that this steady state is mechanically unstable. Let us consider a small rotational perturbation. When the particle rotates, the ions that have accumulated at the interface are advected by the particle motion. The rotational disturbance therefore tilts the dipole moment, as depicted in Fig. 1.2(b). The particle experiences an electrostatic torque, $\mathbf{T}^e = \frac{\epsilon_l}{\epsilon_0}\mathbf{P}\times\mathbf{E}_0$, which amplifies the initial rotation and makes the non-rotating state unstable. However, the conduction of charges in the liquid makes the situation more complex: ions are continuously transported between the electrodes. They reach or leave the interface in order to restore the initial state, in which $\mathbf{P}$ is opposite to $\mathbf{E}_0$ and $\mathbf{T}^e = \mathbf{0}$. The latter mechanism enhances the stability of the non-rotating state. Hence the steady state of the system is set by the competition between two effects: the advection of charges at the interface increases the electrostatic torque, while the transport of ions in the solution makes it relax to zero. As a result, the non-rotating state remains stable for low amplitudes of the electric field. The rotational instability arises when $\mathrm{E}_0$ exceeds a threshold value $\mathrm{E}_\mathrm{Q}$.

More quantitatively, the evolution of the dipole moment is ruled by the charge-conservation equation at the interface:

$$\frac{\mathrm{d}\mathbf{P}}{\mathrm{d}t} = -\frac{1}{\tau}\left(\mathbf{P} + 2\pi\epsilon_0 a^3\mathbf{E}_0\right) + \boldsymbol{\Omega}\times\left(\mathbf{P} - 4\pi\epsilon_0 a^3\chi^\infty\mathbf{E}_0\right), \tag{1.1}$$

where $\boldsymbol{\Omega}$ is the angular velocity of the particle. The first term in the right-hand side accounts for the transport of charges by conduction in the liquid. If the particle does not rotate, the dipole moment relaxes to $\mathbf{P} = -2\pi\epsilon_0 a^3\mathbf{E}_0$, which is opposite to the applied field, Fig. 1.2(a). The relaxation time is the so-called Maxwell-Wagner time $\tau \equiv \frac{\epsilon_p+2\epsilon_l}{2\sigma_l}$. The second term corresponds to the advection of charges at the interface: the dipole moment rotates as the particle rotates (the component $4\pi\epsilon_0 a^3\chi^\infty\mathbf{E}_0$ accounts for the dielectric polarization, which adjusts quasi-instantaneously: it is not advected by the particle rotation).

The electrodynamical equation (1.1) is complemented by a mechanical equation. The electrostatic torque is balanced by the viscous drag: $\mathbf{T}^e = \mu_r^{-1}\boldsymbol{\Omega}$, where $\mu_r = (8\pi\eta a^3)^{-1}$ and $\eta$ is the viscosity of the liquid. As a consequence, it can be shown that the non-rotating state is unstable when the external field $\mathrm{E}_0$ exceeds $\mathrm{E}_\mathrm{Q} = \left[4\pi\epsilon_l a^3(\chi^\infty + \frac{1}{2})\mu_r\tau\right]^{-1/2}$. The stable state corresponds to a steady rotation at the rate:

$$\Omega = \frac{1}{\tau}\sqrt{\left(\frac{\mathrm{E}_0}{\mathrm{E}_\mathrm{Q}}\right)^2 - 1}. \tag{1.2}$$

Importantly, the rotation axis can be any direction perpendicular to $\mathbf{E}_0$. It is set by the random

direction of the initial rotational perturbation. In other words, the Quincke rotation spontaneously breaks the rotational symmetry in the plane orthogonal to $\mathbf{E}_0$.

## 1.2 From rotational to translational motion

The Quincke effect provides a mechanism that drives the rotation of the particles. In order to devise a system of self-propelled bodies, we have to convert this rotational motion into net translation. The basic idea is simple: we let the spherical particles roll on a surface, Fig. 1.3(a).

The presence of a surface makes the above theory more complex. First, experimentally the surface is also the lower electrode used to induce $\mathbf{E}_0$. It therefore *a priori* impacts the electrodynamic equation (1.1). We have shown that taking account of this effect only yields subdominant corrections, within the experimental conditions. Second, the rotating particle now exchanges momentum with the surface, which impacts the mechanical equation relating the electrostatic torque to the rotation rate. More precisely, the contact between the particle and the surface is lubricated by the viscous liquid, and the sphere both rolls and slides. Its motion is described by a mobility matrix $\mathscr{M}$ that links the electrostatic force and torque, $\mathbf{F}^{\mathrm{e}}$ and $\mathbf{T}^{\mathrm{e}}$, to the translational and rotational velocities, $\mathbf{v}$ and $\mathbf{\Omega}$:

$$\begin{pmatrix} \frac{1}{a}\mathbf{v} \\ \mathbf{\Omega}_{\parallel} \\ \Omega_z \end{pmatrix} = \mathscr{M} \cdot \begin{pmatrix} a\mathbf{F}^{\mathrm{e}}_{\parallel} \\ \mathbf{T}^{\mathrm{e}}_{\parallel} \\ \mathrm{T}^{\mathrm{e}}_z \end{pmatrix}, \tag{1.3}$$

where we have distinguished between the in-plane and the $z$-components of the vectors, Fig. 1.3(b).

In an unbounded fluid, the mobility matrix is diagonal and the electrostatic torque induces no net force. Close to a no-slip wall, $\mathscr{M}$ has non-diagonal components that couple translational and rotational motion: the sphere rolls. All these mobility factors are deduced from the friction coefficients calculated in the literature [89, 90, 130, 148], in the lubrication regime. In particular, the electrostatic torque induces a net translation of the particle: $\mathbf{v} = a\tilde{\mu}_t \mathbf{T}^{\mathrm{e}} \times \hat{\mathbf{e}}_z$, where $\tilde{\mu}_t$ is an off-diagonal term of the matrix $\mathscr{M}$.

Combining Eq. (1.3) with the electrodynamic equation (1.1), we obtain the equation of motion of an isolated roller. After a relaxation time $\sim \tau$, we find that the sphere steadily rolls on the surface in the direction opposite to the in-plane component of the polarization:

$$\mathbf{v} = -\frac{\epsilon_l}{\epsilon_0} a\tilde{\mu}_t \mathrm{E}_0 \mathbf{P}_{\parallel}, \tag{1.4}$$

At this stage, our theoretical description gives two predictions for the motion of an isolated particle.

(i) The Quincke mechanism corresponds to a spontaneous symmetry breaking: in the plane of the surface, all directions of motion are equivalent.

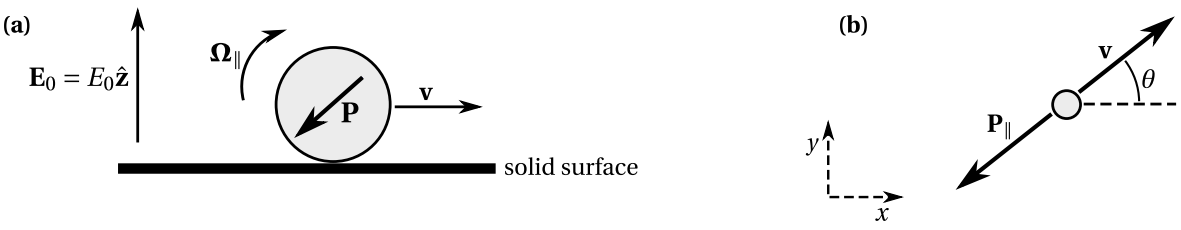


**Figure 1.3** – **(a)** When rotating close to a surface, a spherical particle rolls and propels itself. **(b)** The direction of motion is set by the angle $\theta$ in the plane of the surface.

(ii) The rolling speed is controlled by the amplitude of the external electric field $E_0$, as:

$$v_0 = \frac{a\tilde{\mu}_t}{\mu_r \tau}\sqrt{\left(\frac{E_0}{E_Q}\right)^2 - 1}, \tag{1.5}$$

where $E_Q$ is the threshold of the Quincke rotation.

The first prediction has a clear consequence on the equations of motion: as there is no privileged direction in the plane of the surface, the propulsion mechanism cannot change the direction of motion. The rotation of the particle is solely triggered by the noise acting on it. An isolated roller therefore undergoes a persistent random walk at constant speed. Its motion is described by:

$$\dot{\mathbf{r}} = v_0\hat{\mathbf{p}} = v_0(\cos\theta, \sin\theta), \tag{1.6}$$

$$\dot{\theta} = \sqrt{2D_r}\xi(t), \tag{1.7}$$

where $\xi(t)$ is a Gaussian white noise with zero mean and variance $\langle\xi(t)\xi(t')\rangle = \delta(t-t')$. The rotational diffusivity $D_r$ is the typical rate at which the particle orientation changes.

## 1.3 Experimental realization

The propulsion mechanism analyzed above was used to build an experimental population of motile colloids. The experiments were carried out by Antoine Bricard and Nicolas Desreumaux, in parallel with the theoretical work. PMMA colloids of radius $a = 2.4\,\mu$m are immersed in an AOT/hexadecane solution. The suspension is first injected between two conducting glass slides in a microfluidic device, and the colloids sediment on the bottom slide, Fig. 1.4(a). When an electric field $E_0 \sim 3\times10^6\,\mathrm{V\cdot m^{-1}}$ is then applied, the colloids rotate due to the Quincke mechanism. They roll on the electrode.

Fig. 1.4(b) shows the superposition of successive snapshots of the colloidal population. In this dilute regime, the rollers undergo very few interactions and behave as persistent random walkers. We can therefore test our theoretical predictions for the one-particle dynamics.

First, the probability distribution of the velocity vector is plotted in Fig. 1.5(a). The distribution is clearly isotropic: the direction of motion is random, which confirms that the propulsion corresponds to a spontaneous symmetry breaking.

Second, the distribution of the velocity is sharply peaked on a circle. The rollers therefore move at a constant speed $v_0$ (in contrast with brownian particles), in agreement with the equation of motion (1.6). More precisely, the roller speed is tuned by the applied electric field $E_0$, as shown in Fig. 1.5(b). The variations of $v_0$ with the applied electric field are well fitted by the theoretical formula (1.5). As our model does not involve any phenomenological parameter except the noise amplitude, we can compare the experimental values of the fitting parameters to the orders

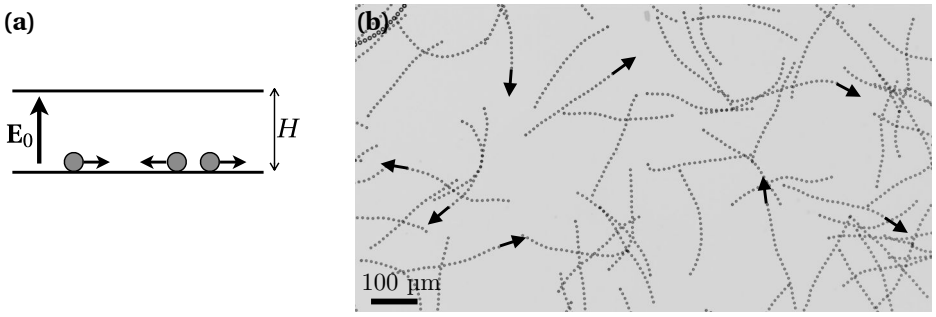


**Figure 1.4** – **(a)** Sketch of the experimental setup. **(b)** Trajectories of colloids rolling on the surface. The rollers undergo persistent random walks with long persistence times.

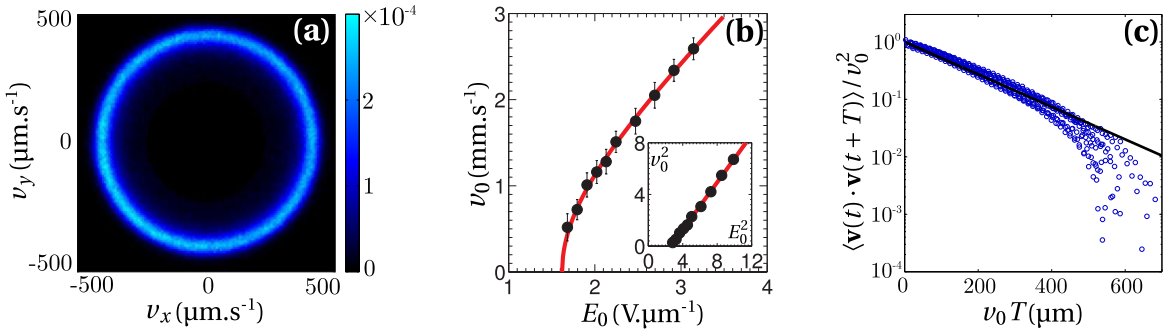


**Figure 1.5** – **(a)** Probability distribution of the roller velocity. **(b)** Speed of a colloid as a function of the applied electric field. **(c)** Autocorrelation of the roller direction, $\langle \mathbf{v}(t)\cdot\mathbf{v}(t+\mathrm{T})\rangle / v_0^2$, plotted versus the traveled distance $v_0\mathrm{T}$.

of magnitudes expected from the theory. Using typical values for the microscopic parameters (liquid viscosity and conductivity, colloid radius, dielectric permittivities...), we expect $\mathrm{E_Q} \sim 10^6\,\mathrm{V\cdot m^{-1}}$ for the threshold of the Quincke rotation, and $(a\tilde{\mu}_t)/(\mu_r \tau) \sim 2\,\mathrm{mm\cdot s^{-1}}$ for the typical velocity of the particle. These orders of magnitude are compatible with the experimental measurements. Note the high speed of the colloids, which travel more than 100 times their size during 1s. All these results unambiguously validate our theoretical description of the propulsion mechanism.

Finally, we use the experimental data to measure our sole phenomenological parameter, the amplitude of the noise $\mathrm{D}_r$. From Eq. (1.7), we deduce that the autocorrelation of the roller velocity decays as $\langle \mathbf{v}(t)\cdot\mathbf{v}(t+\mathrm{T})\rangle = v_0^2 \exp(-\mathrm{D}_r\mathrm{T})$. This quantity is plotted in Fig. 1.5(c) and indeed displays an exponential decay at short times (the sharp drop of the autocorrelation at longer times originates from collisions with the boundaries). The rotational diffusion time is $\mathrm{D}_r^{-1} = 0.31 \pm 0.02$ s, which corresponds to a persistence length $v_0/\mathrm{D}_r = 160$ µm.

## 1.4 Towards collective motion

Having devised a population of self-propelled colloids, we can now investigate the emergence of collective motion. To do so, we increase the density of rollers in order to make them interact. Before we go any further in the theoretical modeling, let us summarize the phenomenology observed experimentally. The large-scale patterns displayed by the populations of rollers fall in three main classes.

***Transition to directed motion: propagating band in periodic boundaries*** The motion of the rollers is first confined to a racetrack. This geometry, which is periodic in the direction of the closed track, is compatible with the emergence of steady polar phases (as in simulations of Vicsek-like models). The experimental control parameter is the mean area fraction $\phi_0$, which is the fraction of the racetrack area occupied by the rollers. At low $\phi_0$, the population forms an isotropic gas, the directions of the rollers are random. Upon increasing the area fraction above a critical value $\phi_b$, the system self-organizes into polar phases. This transition is quantified by the averaged polarization $\Pi_0 \equiv |\langle \hat{\mathbf{p}}_i \rangle_i|$, plotted versus $\phi_0$ in Fig. 1.6(a). The rise of the order parameter to non-zero values unveils the emergence of coherent polar phases at $\phi_0 > \phi_b$.

Close to the transition, the stationary state takes the form of a single band cruising along the track, as shown in Fig. 1.6(b) and 1.6(c). A macroscopic fraction of the rollers form a coherent structure having a sharp front and a long tail, which propagates in a sea of disordered particles. Remarkably, the band has no intrinsic length: its size is proportional to the total length of the track, for a given area fraction. In other words, the fraction of the racetrack area that is occupied by the band does not depend on the system size, it solely increases with $\phi_0$.

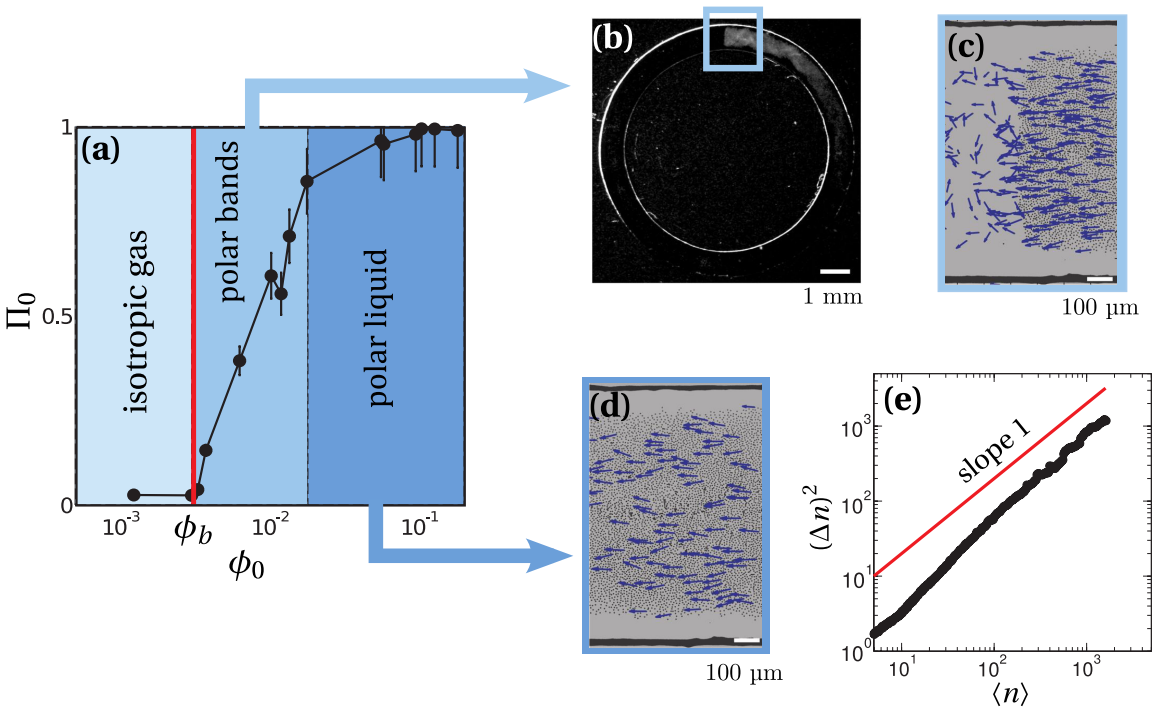


**Figure 1.6** – Polar phases in periodic boundaries (racetrack). **(a)** Transition to collective motion: averaged polarization versus the mean area fraction. Above the critical area fraction $\phi_b$, the population self-organizes into polar phases. **(b)** A macroscopic band propagates along the racetrack. **(c)** Close-up on the front of the band: the polar band propagates in a disordered sea. **(d)** Close-up view of the polar liquid phase. **(e)** Variance of the particle number, $(\Delta n)^2$, versus the mean number of particles, $\langle n \rangle$, in the polar liquid. The density fluctuations are normal.

***Polar liquid in periodic boundaries*** Further increasing the area fraction in a periodic confinement, the length of the band reaches the length of the track. After a transient regime in which a band nucleates and catches up with itself, the population forms a homogeneous polar phase with high polarization, $\Pi_0 \approx 1$. All the colloids move in the same direction with very little spatial heterogeneities, as exemplified in Fig. 1.6(d). We emphasize that this phase diagram is strikingly similar to the Vicsek model, which also displays propagating bands close to the transition and homogeneous polar states at high densities. The Quincke rollers provide the first experimental realization of an homogeneous polar phase, which had never been observed before.

However, the structure of the polar liquid is qualitatively different from all theories of active matter. In all flocking models, it has been shown numerically and analytically that the homogeneous polar state displays giant density fluctuations: the standard deviation of the particle number increases as $\Delta n \sim \langle n \rangle^a$, where $\langle n \rangle$ is the mean particle number and $a \approx 1$ [136, 211, 212]. This behavior was believed to be a hallmark of active polar systems. In Fig. 1.6(e) we plot the variance of the number fluctuations measured in our experimental system, in strongly polarized phases. Unexpectedly, we find that density fluctuations are *normal*: $\Delta n \sim \sqrt{\langle n \rangle}$. This observation is a major difference between our system and all the available models.

***Polar vortex in confining boundaries*** We finally change the boundaries and confine the rollers in a circular box. In non-periodic geometries, the emergence of a uniform polarization is frustrated. Instead, the population forms a steadily-rotating vortex that spans the entire box, see Fig. 1.7(a). This behavior arises from a non-equilibrium phase transition, demonstrated in Fig. 1.7(b) by plotting the azimuthal polarization versus the mean area fraction $\phi_0$. The vortex corresponds to a spatially-heterogeneous structure. The local density of particles increases from the center to the edge of the confining box, as shown by the radial density profile plotted in Fig. 1.7(c).

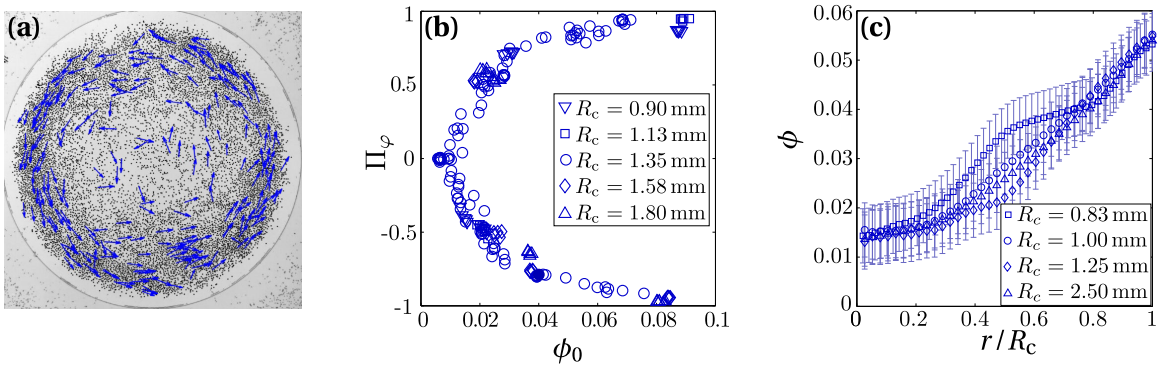


**Figure 1.7** – Vortex structure observed in confining boundaries (disk). **(a)** The roller population self-organizes into a macroscopic vortex. **(b)** Azimuthal polarization, $\Pi_\varphi \equiv \langle \hat{\mathbf{p}}_i \cdot \hat{\mathbf{e}}_\varphi \rangle_i$, plotted versus the area fraction for different confinement radii $R_c$. **(c)** Radial density profile plotted versus the rescaled distance to the center, $r/R_c$, for different confinement radii.

Remarkably, this structure has no intrinsic length-scale: all density profiles, obtained for different box sizes, collapse on a single master curve when the distance to the center is rescaled by the radius of the confining box. Hence the vortex is not a finite-size effect; it defines a genuine macroscopic – yet heterogeneous – phase of polar active matter in confinement.

In a word, the population of Quincke rollers spontaneously self-organizes into macroscopic polar patterns involving thousands of colloids. In what follows, we aim at explaining theoretically the large-scale patterns reported above from a microscopic description of the interactions. We have to elucidate:

- the transition to directed motion associated with the emergence of propagating bands,
- the absence of giant density fluctuations in the polar liquid,
- the structure of the heterogeneous vortex observed in confining boundaries.

As a first step, in the next section we describe the microscopic dynamics of interacting rollers and establish their equations of motion.

## 2 Microscopic dynamics of a population of rollers

We now build a microscopic model which describes the dynamics of the system. We first investigate the interaction mechanisms, and show how the rollers reorient in the electrostatic and hydrodynamic fields induced by their neighbors. We then derive the equations of motion for the population of rollers. We discuss their accuracy by comparing numerical simulations of the model to the experimental measurements. Finally, we show that the form of the equations of motion is not specific to the Quincke rollers and can be extended to a whole class of systems.

### 2.1 Origin of the roller-roller interactions

In the population of Quincke rollers, the interactions arise from physical mechanisms that can be easily identified, in the far-field limit. They have two origins. First, a motile colloid carries a surface electric charge. It therefore disturbs the electric field around it, and induces electrostatic interactions. Second, the rolling motion gives rise to a flow field in the liquid, and induces hydrodynamic interactions. We consider the dynamics of a test particle and denote by $\delta\mathbf{E}(\mathbf{r},t)$ and $\mathbf{u}(\mathbf{r},t)$ the electrostatic and hydrodynamic fields created by the neighboring colloids. Although

the individual propulsion does not promote any direction in the plane of the surface, the in-plane components of the fields $\delta\mathbf{E}(\mathbf{r},t)$ and $\mathbf{u}(\mathbf{r},t)$ now define privileged directions. The interactions *explicitly* break the rotational symmetry around the $\hat{\mathbf{z}}$-axis and give rise to a nontrivial orientational dynamics, as we show it now.

We focus on dilute populations and treat the interactions perturbatively. We assume that $|\delta\mathbf{E}|/\mathrm{E}_0 = \mathscr{O}(\epsilon)$ and $\tau\left|\partial_z \mathbf{u}_\parallel\right| = \mathscr{O}(\epsilon)$ are small quantities. The electrostatic and hydrodynamic equations describing the Quincke rotation near a surface, Eqs. (1.1) and (1.3), are impacted by the disturbance fields $\delta\mathbf{E}$ and $\mathbf{u}$. Without entering the details of the calculation, the dynamics of the particle can be described by three parameters: the $z$-component of its dipole moment, $\mathrm{P}_z$; the norm of its velocity, $v$; its in-plane direction of motion, set by the angle $\theta$. In the absence of noise, we showed that the coupled evolution equations have the following structure:

$$\dot{\mathrm{P}}_z = \frac{1}{\tau} f_{10}(\mathrm{P}_z, v) + \frac{\epsilon}{\tau} f_{11}(\mathrm{P}_z, v, \theta), \tag{1.8}$$

$$\dot{v} = \frac{1}{\tau} f_{20}(\mathrm{P}_z, v) + \frac{\epsilon}{\tau} f_{21}(\mathrm{P}_z, v, \theta), \tag{1.9}$$

$$\dot{\theta} = 0 + \frac{\epsilon}{\tau} f_{31}(\mathrm{P}_z, v, \theta). \tag{1.10}$$

The latter equations display two well-separated time-scales. In the right-hand side, the first terms describe the individual propulsion due to the Quincke mechanism, and involve the Maxwell-Wagner time $\tau$. The second terms correspond to the interactions with the neighboring rollers, which take place on a much longer time-scale $\sim \tau/\epsilon$.

The separation between fast and slow variables makes it simple to obtain the solution at lowest order in $\epsilon$ (in a direct multi-scale analysis).

- Neglecting the corrections of order $\mathscr{O}(\epsilon)$ in Eqs. (1.8) and (1.9), we find that $\mathrm{P}_z$ and $v$ relax towards their unperturbed value over a time $\sim \tau$. In particular, the particle speed quickly relaxes towards $v_0$, the value set by the Quincke rotation in the absence of interactions.

- By contrast, the direction of motion does *not* evolve at order $\mathscr{O}(\epsilon^0)$, as we already discussed it previously. The orientational dynamics is set by the interactions, which explicitly break the rotational symmetry. As a result, the direction of motion rotates on a time-scale $\tau/\epsilon$ which is much longer than $\tau$.

In view of building a large-scale description of the population of rollers, valid for long observation times, we average over the fast relaxation of the particle speed and only retain the slow orientational dynamics. We arrive at our first main result regarding the motion of interacting rollers: in this approximation, the particles move at a *constant speed* and only change their orientations due to interactions. This prediction is compatible with the experimental findings: the colloid velocity only increases by $\sim 10\%$ when the averaged area fraction varies from 0.01 to 0.04 (note that, in principle, this moderate increase should be accounted for by the terms of order $\mathscr{O}(\epsilon)$).

We deduce the equations of motion of particle $i$, in the absence of noise. Replacing the function $f_{31}$ by its explicit expression, we obtain:

$$\dot{\mathbf{r}}_i = v_0 \hat{\mathbf{p}}_i = v_0(\cos\theta_i, \sin\theta_i), \tag{1.11}$$

$$\dot{\theta}_i = -\frac{\partial}{\partial\theta_i}\left[-\mu_1 \hat{\mathbf{p}}_i \cdot \partial_z \mathbf{u}_\parallel(\mathbf{r}_i) + \mu_2 \hat{\mathbf{p}}_i \cdot \delta\mathbf{E}_\parallel(\mathbf{r}_i)\right], \tag{1.12}$$

where $\mu_1$ and $\mu_2$ are positive coefficients that depend on $a$, $\tau$, $v_0$ and the mobility factors. These equations have a clear meaning. The particle reorients, at constant speed, along the local flow direction and opposite to the electric field induced by its neighbors.

## 2.2 Equations of motion

We now use the previous result to derive the equations of motion of a dilute population of rollers. To do so, we have explicitly calculated the fields $\delta\mathbf{E}_{\parallel}^{(j)}(\mathbf{r}_i)$ and $\mathbf{u}_{\parallel}^{(j)}(\mathbf{r}_i)$ induced at the position $\mathbf{r}_i$ by a neighboring particle $j$, in the far-field limit. The electrostatic field is deduced from the dipolar charge distribution at the surface of particle $j$. We also take account for the lower electrode on which the particles roll, by considering a fictive image-charge distribution below the electrode. The flow field is calculated in a similar manner using hydrodynamic singularities. Taking advantage of the linearity of the Stokes equation, we introduce a fictive distribution of force-sources and mass-sources, that are the Green functions of the hydrodynamic equations [56, 199]. In the far-field limit, the flow field can be decomposed as the sum of the elementary flows created by force and source multipoles, that are combined to fulfill the boundaries conditions at the particle-liquid interface. The additional no-flux and no-slip constraints on the upper and lower surfaces are accounted for by complex image-singularity distributions. In the present case, the hydrodynamic field induced by a rolling colloid amounts to the flow created by a rotlet singularity, i.e. a pointwise torque exerted on the fluid and located on the particle. The flow induced by a rotlet near a rigid wall (resp. confined between two walls) has been calculated by Blake and Chwang [29] (resp. Hackborn [98]). We have used these available results to deduce the hydrodynamic couplings between two rollers.

Assuming that both electrostatic and hydrodynamic interactions are pairwise-additive, we finally obtain the equations of motion for the population of rollers. The particle $i$ moves at a constant velocity $v_0$, and changes its direction of motion due to interactions and noise:

$$\dot{\mathbf{r}}_i = v_0\hat{\mathbf{p}}_\mathbf{i}, \tag{1.13}$$

$$\dot{\theta}_i = -\frac{1}{\tau}\frac{\partial}{\partial\theta_i}\sum_{j\neq i}\mathscr{H}_{\text{eff}}(\mathbf{r}_i-\mathbf{r}_j,\hat{\mathbf{p}}_i,\hat{\mathbf{p}}_j) + \sqrt{2D_r}\,\xi_i(t). \tag{1.14}$$

$\xi_i(t)$ is a Gaussian white noise with zero mean and variance $\langle\xi_i(t)\xi_j(t')\rangle = \delta(t-t')\delta_{ij}$, it accounts for the rotational diffusion of the rollers. The effective potential $\mathscr{H}_{\text{eff}}$ describes both electrostatic and hydrodynamic couplings. It can be written in the following form:

$$\mathscr{H}_{\text{eff}}(\mathbf{r},\hat{\mathbf{p}}_i,\hat{\mathbf{p}}_j) = -\text{A}(r)\,\hat{\mathbf{p}}_j\cdot\hat{\mathbf{p}}_i - \text{B}(r)\,\hat{\mathbf{r}}\cdot\hat{\mathbf{p}}_i - \text{C}(r)\,\hat{\mathbf{p}}_j\cdot(2\hat{\mathbf{r}}\hat{\mathbf{r}}-\mathbf{I})\cdot\hat{\mathbf{p}}_i, \tag{1.15}$$

where $\hat{\mathbf{r}}\equiv\mathbf{r}/r$. The explicit expressions of the functions $\text{A}(r)$, $\text{B}(r)$ and $\text{C}(r)$ are provided in the Supplementary Document of the article "Emergence of macroscopic directed motion in population of motile colloids", p. 55 of the present manuscript. They only involve well-identified microscopic quantities, with no phenomenological parameter.

(i) The first term, $-\text{A}(r)\,\hat{\mathbf{p}}_j\cdot\hat{\mathbf{p}}_i$, promotes the alignment of particle $i$ with the direction of particle $j$. It is analogous to the spin-spin alignment interactions defining the standard XY model. In the absence of the B- and C-terms, the above equations would therefore reduce to the so-called "flying XY model" [79, 156]. In the experimental conditions, this alignment term is dominated by hydrodynamic couplings that are exponentially screened over a distance $\sim \text{H}/\pi$, where H is the gap between the two horizontal surfaces (Fig. 1.4(a)).

(ii) The second term, $-\text{B}(r)\,\hat{\mathbf{r}}\cdot\hat{\mathbf{p}}_i$, corresponds to repulsive interactions, as $\text{B}(r)>0$. Particle $i$ rotates its direction of motion in order to align along $-(\mathbf{r}_i-\mathbf{r}_j)$ and moves away from particle $j$. This term is a purely electrostatic effect, that is also screened over a distance $\sim \text{H}/\pi$.

(iii) The last term, $-\text{C}(r)\,\hat{\mathbf{p}}_j\cdot(2\hat{\mathbf{r}}\hat{\mathbf{r}}-\mathbf{I})\cdot\hat{\mathbf{p}}_i$, has a dipolar symmetry. As opposed to the previous terms, it includes an hydrodynamic contribution which is not screened over the channel height, and algebraically decays like $r^{-2}$ at long distance. This interaction is therefore truly long-ranged in 2D, and arises from mass conservation in the liquid. Its strength is small compared to the short-ranged hydrodynamic terms, yet we will show that it significantly

impacts the properties of polar phases. A more detailed discussion on the origin and the features of this long-range coupling is provided in the Appendix.

## 2.3 How accurate is our microscopic model?

Before we link the microscopic model with the macroscopic behavior of the population, we discuss its accuracy and its robustness. We first test the validity of the model by comparing numerical simulations of the equations of motion with the experimental results.

Remarkably, all coefficients involved in the model can be measured or estimated. The particle speed and the rotational diffusion have been deduced from the isolated-roller dynamics, as explained in section 1.3. The threshold electric field $E_Q$ is measured experimentally as the critical field at which the colloids start moving. We use typical values for the dielectric constants and the conductivity of the liquid, and we assume the distance between the particle and the surface to be $\sim 50$ µm (although this parameter is not controlled precisely, it only yields logarithmic corrections to the mobility coefficients when this gap is small compared to the particle diameter).

The equations of motion (1.13)–(1.15) have been simulated numerically by Charles Savoie, Debasish Das and David Saintillan. A short-range force was added to prevent the overlap between colloids. This steric repulsion is not accounted for by our far-field description, its range is the only free parameter of the model. Obviously, we do not expect a perfect quantitative agreement between numerical and experiments result. However, we hope that the orders of magnitudes are correctly predicted by the theory.

The microscopic model, solved numerically, reproduces all the macroscopic behaviors observed experimentally. Qualitatively, both the steady states and the transient regimes look strikingly similar. In order to perform a more quantitative comparison, we focus on confining boundaries: the rollers are confined in a circular box. Above a critical area fraction $\phi_v$, the numerical model leads to the emergence of a macroscopic vortex akin to the experimental pattern, see Fig. 1.8(a). Both the bifurcation curve, showing the azimuthal polarization as a function of the mean density, and the radial density profiles are in good qualitative agreement with the experiments, as shown in Fig. 1.8(b) and 1.8(c). The main discrepancy is the precise position of the transition point $\phi_v$. The numerical value is underestimated by a factor of $\sim 3$. Given the large number of approximations required to establish the model and the uncertainties in the estimation of the parameters, the agreement is very convincing. In addition, we note that $\phi_v$ can be tuned to the experimental value by increasing the range of the steric repulsion, our only free parameter.

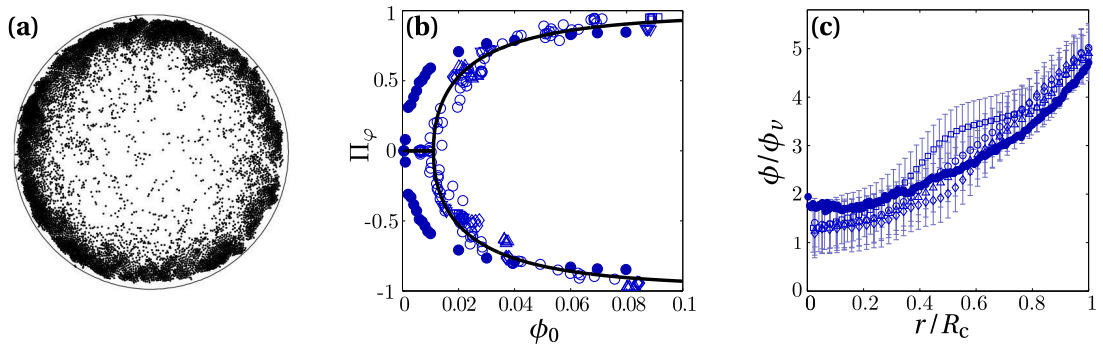


**Figure 1.8** – Numerical simulation of the microscopic model in a circular box of radius $R_c$. **(a)** Snapshot of the vortex phase. **(b)** Azimuthal polarization, $\Pi_\varphi \equiv \langle \hat{\mathbf{p}}_i \cdot \hat{\mathbf{e}}_\varphi \rangle_i$, plotted versus the area fraction. The vortex forms above a critical area fraction $\phi_v$. Open symbols: experiments. Filled disks: numerical data. **(c)** Radial area fraction, $\phi(r)/\phi_v$, plotted versus the rescaled distance to the center, $r/R_c$. Open symbols: experiments. Filled disks: numerical data.

The agreement between numerical and experimental results validates our model. It proves that all the fundamental ingredients which rule the macroscopic phenomenology have been correctly identified. To go beyond, we mention three elements that could be considered in more details for future improvements of the model.

- The short-range interactions are not described in our theory: a non-phenomenological description of collisions between colloids in contact is difficult to achieve. Yet, steric repulsion is a necessary ingredient for a realistic description of the system. Numerically, it was added phenomenologically and only impacts the dynamics at the quantitative level.

- We have modeled all electrostatic effects using the Maxwell-Wagner framework, which neglects all electro-osmosis phenomenon occurring at the interfaces, inside the polarization layers. This approximation is justified given the small value of the Debye length, $\ell_D \sim 10^{-10}$ m, which is very small compared to the colloid size. Nevertheless, it has been shown that any heterogeneity on an electrode, such a particle lying on it, induces an electrohydrodynamic flow [174]. This effect also contributes to the repulsion between colloids and should increase the coefficient $B(r)$ in Eq. (1.15). However, it does not change the functional form of the potential, as we justify it in the next section.

- Rotational noise has been included phenomenologically in the simplest possible form: it was supposed to be uncorrelated with a Gaussian statistics. It would be interesting to go beyond this minimal assumption by studying how fluctuations in the Quincke electro-rotation yield rotational diffusion. In addition, in systems of interacting colloids the rotational diffusivity is renormalized by particle collisions and fluctuations in the interactions. This remark is compatible with the numerical observations: the model underestimates the area fraction $\phi_v$ at which the system self-organizes into a vortex, i.e. underestimates the amplitude of the noise.

## 2.4 How robust is our microscopic model?

We now would like to place the microscopic model in a broader perspective. Is it fully specific to our experimental system, or can we generalize to other active populations?

To answer this question, we have classified the possible interactions between self-propelled particles according to their symmetries. The results are thoroughly explained in the article "Tailoring the interactions between self-propelled bodies", reproduced p. 79. Here, we introduce the main idea by generalizing the special case of the Quincke rollers. We show that the structure and the symmetries of the equations of motion are not specific to this model, and can be extended to a whole class of systems. Coming back to the derivation of the equations of motion, we stress that the model is based on two fundamental ingredients, irrespective of the specifics of the interactions.

***Propulsion at constant speed*** The first ingredient is that the particles move at a constant speed (section 2.1). This result comes from the following assumption: the interactions yield small perturbations to the propulsion mechanism. In order to stress the generality of this result, we consider a standard model, which describes the propulsion by a simple non-linear force [74, 128]:

$$\partial_t \mathbf{r}_i = \mathbf{v}_i, \tag{1.16}$$

$$\partial_t \mathbf{v}_i = \frac{1}{\tau}\left(1 - \frac{|\mathbf{v}_i|}{v_0}\right)\mathbf{v}_i + \sum_{j\neq i} \mathbf{F}_{j\to i} + \sqrt{2D}\boldsymbol{\xi}_i(t). \tag{1.17}$$

The first term in the right-hand side of Eq. (1.17) accounts for the propulsion and the friction forces experienced by a particle of unit mass. In the absence of interactions and noise, the speed relaxes to $|\mathbf{v}| = v_0$ in a typical time $\tau$ and the particle steadily moves in a random direction. The

second and third terms describe respectively the interactions between particles, and the noise. We assume that they only yield small perturbations to the propulsion mechanism: $\mathrm{F}_{j\to i}, \mathrm{D} \ll v_0/\tau$. We observe the dynamics on long time-scales and do not pay attention to the fast variations of the particle speed $|\mathbf{v}|$. Averaging the stochastic equations Eqs. (1.16) and (1.17) over time-scales larger than $\tau$, we arrive at:

$$\partial_t \mathbf{r}_i = v_0 \hat{\mathbf{p}}_i, \tag{1.18}$$

$$\partial_t \hat{\mathbf{p}}_i = \frac{1}{v_0}(\mathbb{I} - \hat{\mathbf{p}}_i\hat{\mathbf{p}}_i)\cdot\left[\sum_{j\neq i}\mathbf{F}_{j\to i}(t) + \sqrt{2\mathrm{D}}\boldsymbol{\xi}_i(t)\right] \tag{1.19}$$

(keeping only the dominant terms). In this limit, the particle moves at a constant speed and undergoes a slow orientational dynamics due to interactions and noise. The projection operator $(\mathbb{I} - \hat{\mathbf{p}}_i\hat{\mathbf{p}}_i)$ ensures that the norm of the orientation $\hat{\mathbf{p}}_i$ remains constant. Remarkably, the equations of motion obtained from this simple model have the same form as those of Quincke rollers.

***Symmetries of the interactions*** The second main ingredient of our model is that the rollers interact through (electrostatic and hydrodynamic) fields (section 2.2). In the effective potential that rules the orientational dynamics, Eq. (1.15), we have grouped the different terms according to their symmetries. The resulting expression corresponds to a multipolar expansion of the interaction fields: the particle reorients in the homogeneous, monopolar and dipolar fields created by its neighbors. Again, the form of this equation is not specific to the Quincke rollers: it could have been deduced from generic symmetry arguments.

In a more general perspective, the interaction force $\mathbf{F}_{j\to i}$ exerted by particle $j$ on particle $i$, in Eq. (1.19), can be Fourier expanded with respect to the angular position. It is recast into a generic multipolar series:

$$\mathbf{F}_{j\to i} = \mathbf{f}_0 + f_1^{\mathrm{div}}\hat{\mathbf{r}}_{ij} + f_1^{\mathrm{rot}}\hat{\mathbf{r}}_{ij}\times\hat{\mathbf{z}} + f_{-1}\left(2\frac{\mathbf{f}_{-1}\mathbf{f}_{-1}}{f_{-1}^2} - \mathbb{I}\right)\cdot\hat{\mathbf{r}}_{ij} + \mathbf{f}_2\cdot(2\hat{\mathbf{r}}_{ij}\hat{\mathbf{r}}_{ij} - \mathbb{I}) + \dots \tag{1.20}$$

The $\mathbf{f}_k$s are coefficients which only depend on the orientations $\hat{\mathbf{p}}_i$ and $\hat{\mathbf{p}}_j$, and on the distance $r_{ij}$ between the two particles. The symmetries of the first terms are sketched in Fig. 1.9. They correspond to homogeneous, monopolar, vortical, elongational, and dipolar force fields.

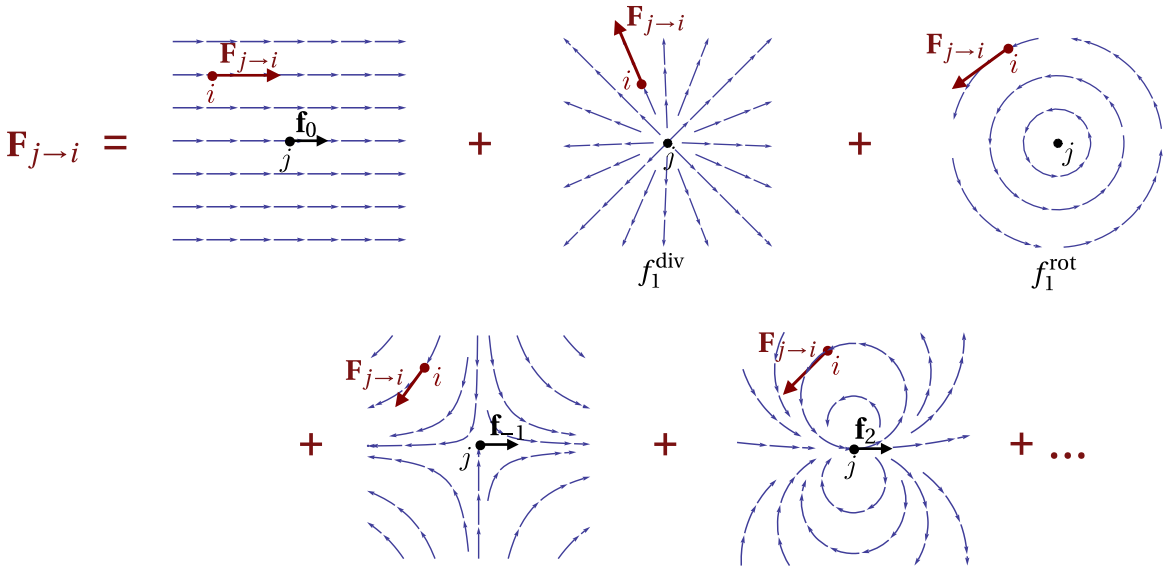


**Figure 1.9** – Sketch of the first Fourier modes of the force $\mathbf{F}_{j\to i}$ exerted by particle $j$ on particle $i$.

Importantly, this decomposition only requires translational invariance. It applies to all active systems, irrespective of the specifics of the interactions. Additional information about the interaction mechanism further constrains the form of the Fourier coefficients $\mathbf{f}_k$. Different cases are analyzed in the article. For instance, potential forces necessary take the form $\mathbf{F}_{j\to i} = f_1^{\mathrm{div}}(r_{ij})\hat{\mathbf{r}}_{ij}$ and result in attractive or repulsive couplings (see e.g. [55, 74, 128] for typical examples considering Morse potentials). Inelastic collisions, satisfying Galilean invariance, impose $\mathbf{f}_k = f_k(r_{ab}, |\hat{\mathbf{p}}_a - \hat{\mathbf{p}}_b|)\,(\hat{\mathbf{p}}_a - \hat{\mathbf{p}}_b)$ (see e.g. the numerical model of shaken grains studied in [219]). The Quincke rollers belong to a third class: individuals rotating their orientations in the field created by their neighbors. This class also includes, e.g., the experimental system of Kumar *et al.* made of pointy rods lying on a shaken bed of isotropic rods, biofilaments in plant cytoskeleton, and all agent-based models for collective motion involving pairwise-additive interactions. The coefficients then take the form $\mathbf{f}_k = f_k(r_{ab})\hat{\mathbf{p}}_b$. In addition, all components $\mathbf{f}_k$ having negative topological charges, $k < 0$, are forbidden for Laplacian fields.

This general analysis answers our initial question: the microscopic model for the Quincke rollers *is* robust. Any error in modeling of the electrostatic or hydrodynamic interactions would impact the amplitudes of the prefactors $A(r)$, $B(r)$, $C(r)$ and their dependence in the distance $r$, but would not change the form of the equations of motion. It also suggests a last remark: in this framework, the existence of alignment effects in polar systems is not surprising. It emerges naturally as the lowest-order component of an angular Fourier expansion.

# 3 From microscopic to macroscopic dynamics

In the last part of this chapter, we use the microscopic model that we derived above to elucidate the large-scale phenomenology observed experimentally. We coarse-grain the equations of motion to establish an hydrodynamic description of the population. We then exploit this approach to explain the experimental phase diagram: (i) the transition to collective motion, (ii) the structure of the polar liquid, (iii) the vortex phase found in confining boundaries.

## 3.1 Hydrodynamic description

We aim at understanding the macroscopic behaviors of the population of rollers from the microscopic model. To do so, we view the population as an active fluid. We describe its large-scale dynamics in terms of hydrodynamic fields that are easily measurable, such as density and velocity fields. Over the past 6 years, a large number of articles have been devoted to building hydrodynamic theories from microscopic models [11–13, 23–25, 79, 108, 139, 158–160, 207, 208]. Most of them are based on the same kinetic-theory framework but use slightly different approximation schemes. We discuss and adapt these methods to our model.

In order to define the hydrodynamic variables, we introduce the one-body distribution function, $\Psi^{(1)}(\mathbf{r},\theta,t)$, that is the probability density of finding a particle at position $\mathbf{r}$, moving in the direction $\theta$, at time $t$. The hydrodynamic fields are the successive moments of $\Psi^{(1)}$.

- The density field is given by $\rho(\mathbf{r},t) \equiv \int \mathrm{d}\theta\ \Psi^{(1)}(\mathbf{r},\theta,t)$. To make the comparison with the experiments easier, we multiply by the particle area and consider the local area fraction (Fig. 1.10(a)):
$$\phi(\mathbf{r},t) \equiv \pi a^2 \int \mathrm{d}\theta\ \Psi^{(1)}(\mathbf{r},\theta,t). \tag{1.21}$$
- The first-order moment defines the polarization field, that is the averaged orientation of the particles at position $\mathbf{r}$:
$$\mathbf{\Pi}(\mathbf{r},t) \equiv \frac{\pi a^2}{\phi} \int \mathrm{d}\theta\ \hat{\mathbf{p}}\Psi^{(1)}(\mathbf{r},\theta,t). \tag{1.22}$$

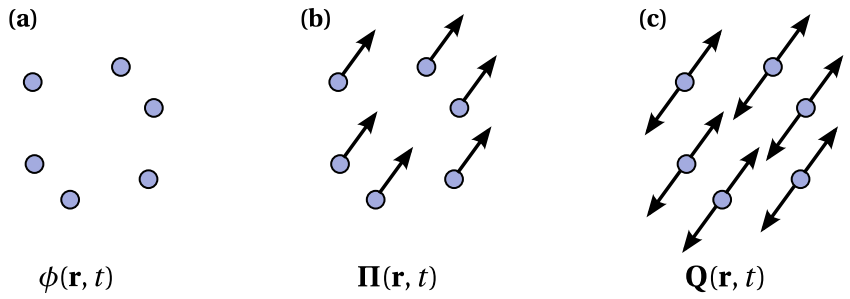


**Figure 1.10** – The angular moments of the one-particle distribution function describe the local orientational order. **(a)** The area fraction gives the local density of particles. **(b)** The polarization reflects the alignment of the particle directions of motion, i.e. the polar order. **(c)** The nematic-order tensor reflects the alignment of the particle axis irrespective of their direction, i.e. the nematic order.

$\mathbf{\Pi}(\mathbf{r},t)$ characterizes the local polar order. Its norm quantifies the degree of alignment of the particle orientations (Fig. 1.10(b)). Its direction is the direction of motion of the active population.

- The second-order moment of $\Psi^{(1)}$ is the nematic-order tensor, defined as:

$$\mathbf{Q}(\mathbf{r},t) \equiv \frac{\pi a^2}{\phi}\int \mathrm{d}\theta \left(\hat{\mathbf{p}}\hat{\mathbf{p}} - \frac{1}{2}\mathbf{I}\right)\Psi^{(1)}(\mathbf{r},\theta,t). \tag{1.23}$$

$\mathbf{Q}(\mathbf{r},t)$ characterizes the local nematic order (Fig. 1.10(c)). Its largest eigenvalue quantifies the degree of alignment of the particle axis, irrespective of the directions of motion. The correspondig eigenvector gives the direction of the nematic order.

We now coarse-grain the microscopic model to establish evolution equations for the hydrodynamic variables $\phi$, $\mathbf{\Pi}$, $\mathbf{Q}$. We start from the coupled equations of motion that rule the dynamics of the N rollers. The state of the system is set by the N positions $\mathbf{r}_1,...,\mathbf{r}_\mathrm{N}$ and orientations $\theta_1,...,\theta_\mathrm{N}$ of all particles. It is fully encoded by the N-particle distribution function $\Psi^{(\mathrm{N})}(\mathbf{r}_1...,\mathbf{r}_\mathrm{N},\theta_1,...,\theta_\mathrm{N},t)$. Using standard kinetic theory methods [173], we transform the 2N coupled Langevin equations (1.13) and (1.14) into a Fokker-Planck equation for $\Psi^{(\mathrm{N})}$:

$$\frac{\partial\Psi^{(\mathrm{N})}}{\partial t} + \sum_i \nabla_i\cdot\left(v_0\hat{\mathbf{p}}_i\Psi^{(\mathrm{N})}\right) + \sum_i \frac{\partial}{\partial\theta_i}\left(\frac{1}{\tau}\sum_{j\neq i}\frac{\partial\mathscr{H}_\mathrm{eff}(\mathbf{r}_i-\mathbf{r}_j,\theta_i,\theta_j)}{\partial\theta_i}\Psi^{(\mathrm{N})}\right) - \mathrm{D}_r\sum_i\frac{\partial^2}{\partial\theta_i^2}\Psi^{(\mathrm{N})} = 0. \tag{1.24}$$

This equation contains all information on the dynamics of the system. However, we aim at describing the population in terms of hydrodynamic fields that only involve the one-body distribution $\Psi^{(1)}$. When moving from the full phase-space to this reduced one-body representation, information is lost. Coarse-graining the equations of motion therefore requires simplifying assumptions, that are known as *closure relations*.

***First closure approximation: two-body correlations*** We first establish the evolution equation for the one-particle distribution. $\Psi^{(1)}$ is inferred from the total distribution function $\Psi^{(\mathrm{N})}$ by integrating over the degrees of freedom of all particles but one: $\Psi^{(1)}(\mathbf{r},\theta,t) = \frac{1}{(\mathrm{N}-1)!}\int \mathrm{d}^2\mathbf{r}_2...\mathrm{d}^2\mathbf{r}_\mathrm{N}\mathrm{d}\theta_2...\mathrm{d}\theta_\mathrm{N}\,\Psi^{(\mathrm{N})}(\mathbf{r},\mathbf{r}_2,...\mathbf{r}_\mathrm{N},\theta,\theta_2,...,\theta_\mathrm{N},t)$. After integration, the Fokker-Planck equation (1.24) yields:

$$\partial_t\Psi^{(1)} + v_0\,\hat{\mathbf{p}}\cdot\nabla\Psi^{(1)} + \frac{1}{\tau}\partial_\theta\int d^2\mathbf{r}'\mathrm{d}\theta'\,\frac{\partial\mathscr{H}_\mathrm{eff}(\mathbf{r}-\mathbf{r}',\theta,\theta')}{\partial\theta}\Psi^{(2)}(\mathbf{r},\mathbf{r}',\theta,\theta',t) - \mathrm{D}_r\,\partial_\theta^2\Psi^{(1)} = 0. \tag{1.25}$$

The evolution of the one-body density involves the two-body correlation function $\Psi^{(2)}(\mathbf{r},\mathbf{r}',\theta,\theta',t) \equiv \frac{1}{(\mathrm{N}-2)!}\int \mathrm{d}^2\mathbf{r}_3...\mathrm{d}^2\mathbf{r}_\mathrm{N}\mathrm{d}\theta_3...\mathrm{d}\theta_\mathrm{N}\,\Psi^{(\mathrm{N})}(\mathbf{r},\mathbf{r}',\mathbf{r}_2,...\mathbf{r}_\mathrm{N},\theta,\theta',\theta_3,...,\theta_\mathrm{N},t)$, that gives the probability of finding

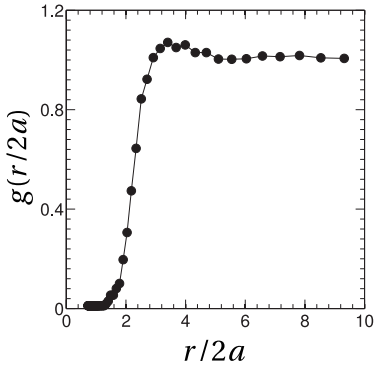


**Figure 1.11** – Experimental measurement of the radial pair distribution function, defined as the pair distribution $\Psi^{(2)}$ averaged over the particle orientations and normalized by $\Psi^{(1)}\Psi^{(1)}$: $g\left(|\mathbf{r}_i-\mathbf{r}_j|\right) = \Psi^{(2)}(\mathbf{r}_i,\mathbf{r}_j)/\left[\Psi^{(1)}(\mathbf{r}_i)\Psi^{(1)}(\mathbf{r}_j)\right]$. The distance has been normalized by the particle diameter.

two particles at positions $\mathbf{r}$ and $\mathbf{r}'$ with orientations $\theta$ and $\theta'$. $\Psi^{(2)}$ therefore accounts for the two-body correlations. Similarly, the evolution equation of $\Psi^{(2)}$ involves the three-particle correlations, etc. We end up with a hierarchy of N evolution equations that couple the dynamics of the $n$-body distribution $\Psi^{(n)}$ to $\Psi^{(n+1)}$.

In order to close this hierarchy and obtain an evolution equation for $\Psi^{(1)}$ only, we have to postulate an extra relation between $\Psi^{(2)}$ and $\Psi^{(1)}$. All available models use a mean-field approximation (akin to the "molecular-chaos" assumption in Boltzmann-like approaches), and neglect correlations at all distances. Here, we assume that the correlations vanish over a distance as small as one particle diameter. However, we also account for the two-body correlations arising at short range from the steric repulsion between colloids. In a crude approximation, we therefore introduce the steric repulsion *a posteriori* by writing that two particles cannot be closer than one colloid diameter. We postulate a modified mean-field closure relation:

$$\Psi^{(2)}(\mathbf{r},\mathbf{r}',\theta,\theta',t) = \begin{cases} 0 & \text{if } |\mathbf{r}-\mathbf{r}'|<2a \\ \Psi^{(1)}(\mathbf{r},\theta,t)\Psi^{(1)}(\mathbf{r}',\theta',t) & \text{if } |\mathbf{r}-\mathbf{r}'|\geq 2a \end{cases}. \tag{1.26}$$

This ansatz is supported by two observations. First, the radial structure factor measured experimentally is plotted in Fig. 1.11. Even at high densities in the polar phase, it is well approximated by a Heaviside function, which confirms that the positional correlations are very weak beyond a distance of a few particle radii. Second, we have used the same ansatz to study the density waves that propagate in driven suspensions of confined particles, see the Appendix. We have shown that the short-ranged correlations induced by local collisions are a key ingredient, which captures very well the experimental dispersion relation at small wavelengths.

As a last remark, we note that this coarse-graining approach is valid when the distance between particles is small compared to the interaction radius. The colloids then experience interaction fields induced by their neighbors at all times [54]. This approximation is compatible with our microscopic model, which describes the interactions at long distance. Here, the range of the interactions is set by the channel height, $H \sim 200\,\mu m$ in the experimental conditions. The interparticle distance being $\sim a/\sqrt{\phi}$, this approximation is fully justified in the range of area fractions in which collective motion emerges, $\phi \gg (a/H)^2 \sim 10^{-4}$. In the opposite limit of interactions occuring during sparse collision events, one should rather use a Boltzmann-like approach which quantifies the collision rate between individuals [12, 25].

***Second closure approximation: orientational structure*** From the evolution of the one-particle distribution $\Psi^{(1)}$, we deduce the dynamics of the hydrodynamic fields.

Integrating Eq. (1.25) over $\theta$, we recover the particle-conservation law:

$$\partial_t \phi + v_0 \nabla\cdot(\phi\mathbf{\Pi}) = 0. \tag{1.27}$$

Taking the first-order moment of Eq. (1.25), we find the evolution of the polarization field:

$$\partial_t(\phi\mathbf{\Pi}) + v_0\nabla\cdot\left(\phi\mathbf{Q} + \frac{\phi}{2}\mathbb{I}\right) = \mathscr{F}[\phi,\mathbf{\Pi},\mathbf{Q}], \tag{1.28}$$

where the right-hand side is an effective force field arising from the interactions and the noise. At first order in a gradient expansion, it is given by:

$$\mathscr{F} = -D_r\,\phi\mathbf{\Pi} + \frac{\alpha}{\tau}\phi^2(\mathbb{I}-2\mathbf{Q})\cdot\mathbf{\Pi} - \frac{a\beta}{2\tau}\phi(\mathbb{I}-2\mathbf{Q})\cdot\nabla\phi + \frac{\kappa}{\tau}\phi(\mathbb{I}-2\mathbf{Q})\cdot\mathbf{M}*\phi\mathbf{\Pi} + \mathscr{O}(a\mathrm{H}\nabla^2). \tag{1.29}$$

Importantly, all coefficients are explicitly related to the microscopic parameters involved in the model, Eq. (1.15). The first term reflects the rotational diffusion that damps the local polarization. The second term stems from the alignment rule at the microscopic level, with amplitude $\alpha = \int_{r\geq 2a} \mathrm{d}r\, r\mathrm{A}(r)/a^2$. The third term, with strength $\beta = \int_{r\geq 2a} \mathrm{d}r\, r^2\mathrm{B}(r)/a^3$, is related to the electrostatic repulsion. The last term arises from the non-screened hydrodynamic interactions having a dipolar symmetry; it involves a non-local kernel $\mathbf{M}$ that we will discuss later.

Similarly, taking the second-order moment of Eq. (1.25) provides the evolution of the nematic-order tensor $\mathbf{Q}$ etc. However, this procedure produces an infinite hierarchy of equations: the evolution of $\phi$ involves the first-order moment $\mathbf{\Pi}$, the dynamics of which depends on the second-order moment $\mathbf{Q}$, which is coupled to the third-order one etc. Hence we have to make a second approximation to close the hierarchy and find evolution equations for $\phi$ and $\mathbf{\Pi}$ only. We need an additional closure relation between $\phi$, $\mathbf{\Pi}$ and $\mathbf{Q}$.

The closure problem has been thoroughly studied in the context of the hydrodynamics of anisotropic fluids, see e.g. [71, 103]. However, the relations that were obtained are not compatible with the polar symmetry and cannot be used directly. More recently, several articles have tackled the question in the case of self-propelled particles endowed with alignment interactions [12, 25, 160]. It turns out that there is no rigorous closure method holding for all magnitudes of the polarization. Different assumptions are required in weakly- and strongly-polarized phases.

### 3.2 Transition to collective motion

We first investigate the transition from disordered to polar states. In the literature, two types of closure approximations have been systematically used to relate $\phi$, $\mathbf{\Pi}$ and $\mathbf{Q}$. Both of them are valid for weakly-polarized phases, they are therefore well-suited for studying the emergence of collective motion.

- Most of the available theories use the closure scheme first introduced by Bertin, Droz and Grégoire [25]. They note that the hydrodynamic fields correspond to the first angular Fourier modes of the distribution function $\Psi^{(1)}$. Defining these modes as $\Psi^{(1)}(\mathbf{r},\theta,t) \equiv \frac{1}{2\pi}\sum_{k\in\mathbb{Z}} \hat{\Psi}^{(1)}_k(\mathbf{r},t)\,\mathrm{e}^{-ik\theta}$, we readily find from Eqs. (1.21) and (1.22) that $\phi = \pi a^2\hat{\Psi}^{(1)}_0$ and $(\Pi_x,\Pi_y) = (\mathrm{Re}\,\hat{\Psi}^{(1)}_1, \mathrm{Im}\,\hat{\Psi}^{(1)}_1)/\phi$. As we noted it above, the evolution equation for $\Psi^{(1)}$, Eq. (1.25), turns into an infinite hierarchy of equations which couple all Fourier components.
  In weakly-polarized states, the angular probability distribution is very flat. Hence its Fourier series is sharply peaked around the zeroth-order mode $\hat{\Psi}^{(1)}_0$. From this remark, Bertin *et al.* proposed the following scaling ansatz: $\hat{\Psi}^{(1)}_k = \mathscr{O}\left(|\epsilon|^k\right)$, where $\epsilon \ll 1$. Looking at long time- and space-variations, they also assume $\partial_t, \nabla = \mathscr{O}(\epsilon)$ [160]. These hypothesis make it possible to truncate the infinite hierarchy in a controlled manner – for instance by neglecting all terms of order $\mathscr{O}(\epsilon^3)$.

- Baskaran and Marchetti use a slightly different approach [13]. They also truncate the high-order Fourier modes of the distribution function, but at a different level. Rather than neglecting terms in the final equations, they immediately specify the form of the one-body

distribution: $\Psi^{(1)} = \phi\left(1 + 2\hat{\mathbf{p}}\cdot\mathbf{\Pi} + 4\hat{\mathbf{p}}\hat{\mathbf{p}} : \mathbf{Q}\right)/(2\pi^2 a^2)$. A closed set of equations for $\phi$ and $\mathbf{\Pi}$ is then obtained by assuming that the nematic order relaxes much faster than the local polarization.

For the colloidal rollers, we have checked that both approaches are strictly equivalent. Note that this would not be the case, however, for more complex interaction rules.

Using these methods, after lengthy algebra and at leading order in $a/\mathrm{H} \ll 1$, we obtain the following hydrodynamic equations:

$$\partial_t \phi + v_0 \nabla\cdot(\phi\mathbf{\Pi}) = 0, \tag{1.30}$$

$$\begin{aligned}\partial_t(\phi\mathbf{\Pi}) + \frac{3v_0\alpha}{8\tau \mathrm{D}_r}(\phi\mathbf{\Pi}\cdot\nabla)\phi\mathbf{\Pi} = &\left[\frac{\alpha}{\tau}\phi - \mathrm{D}_r - \frac{\alpha^2}{2\tau^2\mathrm{D}_r}(\phi^2\Pi^2)\right]\phi\mathbf{\Pi} - \frac{1}{2\tau}\left(\tau v_0 + \beta a\phi\right)\nabla\phi \\ &+ \frac{\kappa}{\tau}\phi\mathbf{M} * \phi\mathbf{\Pi} - \frac{5v_0\alpha}{8\tau\mathrm{D}_r}(\nabla\cdot\phi\mathbf{\Pi})\phi\mathbf{\Pi} + \frac{5v_0\alpha}{16\tau\mathrm{D}_r}\nabla(\phi^2\Pi^2) + \frac{\alpha\beta}{2\tau^2\mathrm{D}_r}a(\nabla\phi\cdot\phi\mathbf{\Pi})\phi\mathbf{\Pi} + \mathcal{O}(\nabla^2).\end{aligned} \tag{1.31}$$

The coefficients $\alpha$, $\beta$, $\kappa$ and the non-local kernel $\mathbf{M}$ are given in the Supplementary Document of the article, p. 58. Apart from the non-local term, the recover the terms obtained phenomenologically by Toner and Tu [211, 214]. In addition, we now know the density-dependence of all scalar coefficients, as well as their explicit expressions as a function of the microscopic parameters.

***Homogeneous states*** We look for homogeneous solutions of the previous equations. Eqs. (1.30) reduces to $\phi(\mathbf{r}, t) = \phi_0$ and Eq. (1.31) implies:

$$\partial_t\mathbf{\Pi} = \left(\frac{\alpha}{\tau}\phi_0 - \mathrm{D}_r\right)\mathbf{\Pi} - \frac{\alpha^2}{2\tau^2\mathrm{D}_r}(\phi_0^2\Pi^2)\mathbf{\Pi}. \tag{1.32}$$

The term $(\alpha/\tau\phi_0)\mathbf{\Pi}$ arises from alignment interactions at the microscopic level, and favors the emergence of polar order. It competes with the rotational diffusion, $-\mathrm{D}_r\mathbf{\Pi}$, which destroys the polarization, and gives rise to a non-equilibrium phase transition. The isotropic phase becomes unstable and the system forms a polar phase above the critical area fraction

$$\phi_c = \frac{\tau\mathrm{D}_r}{\alpha}. \tag{1.33}$$

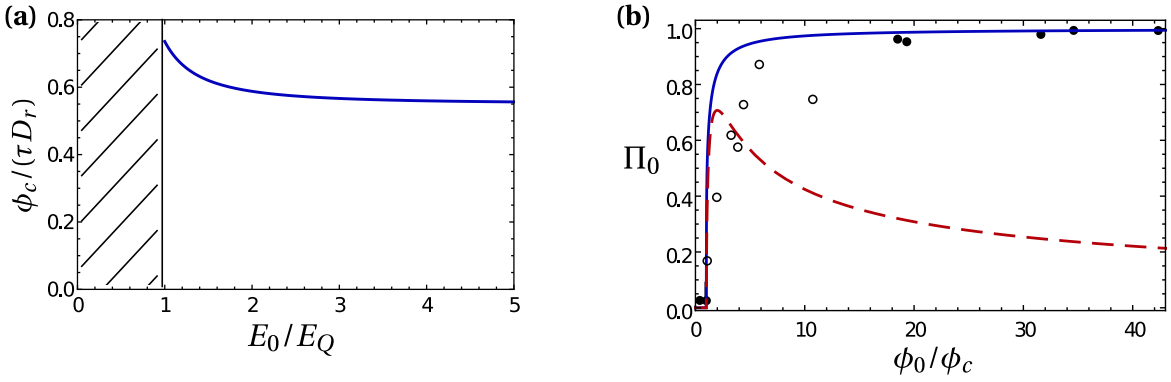


**Figure 1.12** – **(a)** Critical area fraction (rescaled by $\tau\mathrm{D}_r$) plotted versus the external electric field $\mathrm{E}_0/\mathrm{E}_Q$ (we used typical values of the microscopic parameters that correspond to the experimental conditions, as explained in section 2.3). In the density-external field plane, polar states are found above this transition line. **(b)** Orientation–density relation in homogeneous phases. Red dashed line: bifurcation curve given by Eq. (1.34), valid when $\phi_0/\phi_c$ is close to 1. Blue full line: prediction from Eq. (1.38), accurate for strongly polar phases. These two asymptotic models predict a phase transition to a polar state at $\phi_0 = \phi_c$. Dot symbols: experimental data. At the onset of collective motion, the experimental values correspond to polar bands propagating in an isotropic gas. This spatially-heterogeneous state is not accounted for by Eqs. (1.34) and (1.38), which hold for spatially-homogeneous phases only.

The last cubic term, in Eq. (1.32), prevents the divergence of the polarization. Neglecting all gradient terms, we find the following bifurcation for the polarization (see also Fig. 1.12(b)):

$$\Pi_0(\phi_0) = \begin{cases} \sqrt{2\frac{\phi_c}{\phi_0}\left(1-\frac{\phi_c}{\phi_0}\right)} & \text{if } \phi_0 > \phi_c \\ 0 & \text{if } \phi_0 \leq \phi_c \end{cases}. \tag{1.34}$$

This simple result shows that our model correctly reproduces a transition to collective motion. Polar order originates from alignment interactions, as postulated in Vicsek-like models. Here the physical origin of the alignment interactions can be clearly identified: given the experimental orders of magnitudes, the main contribution to the coefficient $\alpha$ arises from hydrodynamic couplings. More quantitatively, we find that the critical area fraction $\phi_c$ weakly depends on the applied electric field $E_0$, as shown in Fig. 1.12(a). This prediction is in agreement with the experimental data, which showed no notable influence of $E_0$ on the threshold density at which polar phases form.

***Onset of collective motion*** To gain more insight into the transition to collective motion, we investigate the linear stability of the homogenous states against spatial fluctuations. We consider plane-wave perturbations: $\phi(\mathbf{r},t) = \phi_0 + \delta\tilde{\phi}\, e^{i(\mathbf{q}\cdot\mathbf{r}-\omega t)}$ and $\mathbf{\Pi}(\mathbf{r},t) = \Pi_0\hat{\mathbf{x}} + \delta\tilde{\mathbf{\Pi}}\, e^{i(\mathbf{q}\cdot\mathbf{r}-\omega t)}$. We linearize Eqs. (1.30) and (1.31) in the perturbations, and calculate the eigenvalues $\omega(\mathbf{q})$. The imaginary part $\mathrm{Im}(\omega)$ is the growth rate of the corresponding eigenmode.

We find that the isotropic state, $\Pi_0 = 0$, is stable for $\phi_0 < \phi_c$. Conversely, above the critical area fraction $\phi_c$, both the isotropic state and the homogeneous polar phase given by Eq. (1.34) are linearly unstable. Starting from the isotropic phase, we note that the most unstable mode corresponds to compression waves that couple density and orientational perturbations in the longitudinal direction. This instability arises from the alignment couplings. Its growth rate, $\mathrm{Im}(\omega)_{\max} = \frac{\alpha}{2\tau}(\phi_0-\phi_c)\left[1+\sqrt{1-\frac{2\tau v_0(\tau v_0+\beta a\phi_0)}{\alpha^2(\phi_0-\phi_c)^2}q^2}\right]$, is maximum for small-$q$ perturbations. These findings are consistent with all the available models describing the transition to polar states [25, 136]. They also agree with the experimental observations: at the onset of collective motion, the disordered phase destabilizes in the form of bands, which consist in coupled density and polarization heterogeneities in the longitudinal direction, occurring at the entire-system size. These spatial structures stem from small-$q$ compression fluctuations that have been amplified.

The latter results have an important consequence on the nature of the transition to collective motion, as we already stressed it in the Introduction. A the onset of polar order, the system is spatially heterogeneous. Hence the transition cannot be correctly described by the spatially-homogeneous theory, Eq. (1.32). We cannot expect Eq. (1.32) to fit the experimental data at $\phi_0 > \phi_c$. A reliable theory should account for the structure of the band phase: it should go beyond the linear analysis performed above, and deal with the non-linearities that set the shape of the bands. This problem is the purpose of Chapter 2, and will be considered in a more general and more formal framework. Here, we only mention that the existence of spatial patterns makes the transition first-order. Hence the critical area fraction $\phi_c$ arising in the theory is *a priori* different from the experimental value $\phi_b$ at which polar bands form.

## 3.3 Structure of the homogeneous polar liquid

In the previous section, we have followed the closure scheme that is widely used in active-matter theories. However, deep in the polar phase this approximation is not valid any more and yields non-physical results. For instance, Eq. (1.34) would predict that the polarization decays at large densities (see Fig. 1.12(b)), which is obviously not expected from the interplay between pairwise-additive alignment couplings and rotational diffusion. We therefore have to use another closure relation to investigate the properties of strongly-polarized phases.

Deep in the polar phase, the closure problem has been overlooked so far. The simplest ansatz consists in assuming that the polar order is perfect. The distribution function then takes the form $\Psi^{(1)}(\mathbf{r},\hat{\mathbf{p}},t) = \phi(\mathbf{r},t)\,\delta\left[\hat{\mathbf{p}} - \hat{\mathbf{\Pi}}(\mathbf{r},t)\right]$, which imposes $\mathbf{Q} = \hat{\mathbf{\Pi}}\hat{\mathbf{\Pi}} - \frac{1}{2}\mathbb{I}$ [71, 184, 223]. However, this ansatz does not account for the possible melting of the polarization, due to rotational noise or interactions that would destroy alignment. We therefore propose another closure relation which also allows fluctuations of the magnitude of the polarization. In strongly-polarized states, the angular distribution $\Psi^{(1)}(\mathbf{r},\theta,t)$ is sharply peaked around the local mean direction $\bar{\theta}(\mathbf{r},t)$, with variance $\sigma^2(\mathbf{r},t) \ll (2\pi)^2$. We neglect the high-order cumulants and approximate the characteristic function by $\hat{\Psi}^{(1)}_k = \phi\exp\left(i\bar{\theta}k - \sigma^2 k^2/2\right)$. The angular distribution is approximated by a wrapped normal distribution (a Gaussian on the unit circle). The mean $\bar{\theta}$ gives the direction of the local polarization, and the variance is related to its magnitude as $\Pi^2 = \exp(-\sigma^2/2)$. This "Gaussian"ansatz constrains the second-order moment: $\hat{\Psi}_2 = |\hat{\Psi}_1|^2\hat{\Psi}_1\hat{\Psi}_1/\hat{\Psi}_0^3$. In real space, it leads to the following expression for the nematic-order tensor:

$$\mathbf{Q} = \Pi^4\left(\hat{\mathbf{\Pi}}\hat{\mathbf{\Pi}} - \frac{1}{2}\mathbb{I}\right). \tag{1.35}$$

We use this new closure relation to obtain the evolution equation of the polarization field from Eq. (1.28). At second order in a gradient expansion and neglecting higher-order terms in $a/\mathrm{H}$, we arrive at:

$$\partial_t\phi + v_0\nabla\cdot(\phi\mathbf{\Pi}) = 0, \tag{1.36}$$

$$\begin{aligned}\partial_t\mathbf{\Pi} + v_0\Pi^2(\Pi\cdot\nabla)\mathbf{\Pi} = &\left[\frac{\alpha}{\tau}(1-\Pi^4)\phi - D_r\right]\mathbf{\Pi} + \frac{\kappa}{\tau}\left[(1+\Pi^4)\mathbb{I} - 2\Pi^2\mathbf{\Pi}\mathbf{\Pi}\right]\cdot\mathbf{M} * \phi\mathbf{\Pi} \\ &- \frac{v_0}{2\phi}(1-\Pi^4)\nabla\phi + \frac{v_0}{\phi}(1-\Pi^2)(\mathbf{\Pi}\cdot\nabla\phi)\mathbf{\Pi} + v_0(1-\Pi^2)(\nabla\cdot\mathbf{\Pi})\mathbf{\Pi} + v_0(\Pi^2\mathbb{I} - \mathbf{\Pi}\mathbf{\Pi})\cdot\nabla(\Pi^2) \\ &- \frac{\beta a}{2\tau}\left[(1+\Pi^4)\mathbb{I} - 2\Pi^2\mathbf{\Pi}\mathbf{\Pi}\right]\cdot\nabla\phi + \frac{\gamma a^2}{2\tau}\left[(1+\Pi^4)\mathbb{I} - 2\Pi^2\mathbf{\Pi}\mathbf{\Pi}\right]\cdot\nabla^2(2\mathbb{I} - \mathbf{M})\cdot\phi\mathbf{\Pi} + \mathscr{O}(\nabla^3).\end{aligned} \tag{1.37}$$

***Homogeneous polar state*** As we did it before, we first look for spatially-homogeneous solutions of Eqs. (1.36) and (1.37). The polarization is readily obtained as a function of the area fraction $\phi_0$:

$$\Pi_0(\phi_0) = \left(1 - \frac{\phi_c}{\phi_0}\right)^{1/4}. \tag{1.38}$$

As expected, $\Pi_0$ plateaus to 1 in the limit of highly-concentrated populations, as plotted in Fig. 1.12(b). Although this expression is only valid for large polarizations, we note that it also predicts a transition to collective motion at the same critical density $\phi_c$, which suggests that it might be qualitatively reliable in a wide range of polarizations.

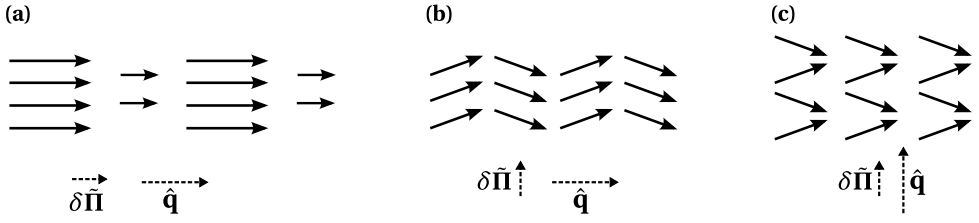


**Figure 1.13** – Three asymptotic orientational modes. **(a)** Compression mode: fluctuations of the modulus of the polarization field along the mean direction of motion. **(b)** Bending modes: fluctuations of the orientation of the polarization along the mean direction of motion. **(c)** Splay modes: fluctuations of the orientation of the polarization perpendicularly to the mean direction of motion. Both compression and splay modes couple orientation and density fluctuations.

***Linear stability*** We now study the stability of the homogeneous polar state against small plane-wave perturbations: $\phi(\mathbf{r},t)=\phi_0+\delta\tilde{\phi}\,e^{i(\mathbf{q}\cdot\mathbf{r}-\omega t)}$ and $\mathbf{\Pi}(\mathbf{r},t)=\Pi_0\hat{\mathbf{x}}+\delta\tilde{\mathbf{\Pi}}\,e^{i(\mathbf{q}\cdot\mathbf{r}-\omega t)}$. The results can be summarized by discussing three special modes.
*Compression waves:* the compression mode couples density fluctuations to variations of the magnitude of the polarization (Fig. 1.13(a)). It was found to be unstable at the onset of collective motion. Here, we indeed find that this mode is unstable below a critical area fraction ($\sim 10\phi_c$). However, it is re-stabilized at higher densities due to the repulsive interactions which clearly disfavor density heterogeneities (β-term in Eq. (1.37)).
*Bending modes:* orientational bending fluctuations, $\hat{\mathbf{q}}\perp\mathbf{\Pi}_0$ (Fig. 1.13(b)), are unstable due to the non-screened hydrodynamic coupling. This result was obtained in an isotropic geometry. However, the dipolar hydrodynamic interactions are are sensitive to the shape of the boundaries, due to their long-ranged nature (see the Appendix for more explanations). Experimentally, the rollers are confined in a track. In such anisotropic boundaries, the bending instability is suppressed by the transverse confinement.
*Splay modes:* splay perturbations, $\hat{\mathbf{q}}\parallel\mathbf{\Pi}_0$, couple density and orientation fluctuations (Fig. 1.13(c)). They are damped due to the long-ranged dipolar hydrodynamic couplings. We note that, in all populations of hydrodynamically-coupled particles, splay and bend fluctuations have dual behaviors. A bending (resp. splay) instability is associated with the damping of the splay (resp. bending) mode, as it was found for suspensions of extensile (resp. contractile) swimmers [183, 184]. Here, the damping of splay fluctuations, due to the dipolar couplings, can be understood as follows. In strongly-polarized states, $\Pi\sim 1$, the long-range interactions rotate the local polarization due to the effective torque $(\mathbb{I}-\mathbf{\Pi}\mathbf{\Pi})\cdot\mathbf{F}_{\rm dip}$, where $\mathbf{F}_{\rm dip}=(2\kappa/\tau)\mathbf{M}*\phi\mathbf{\Pi}$ has a dipolar symmetry. More precisely, $\mathbf{F}_{\rm dip}$ arises from the flow field induced by a distribution of source dipoles $\propto\phi\mathbf{\Pi}$, and satisfies $\nabla\cdot\mathbf{F}_{\rm dip}=-(2\kappa/\tau)\nabla\cdot\phi\mathbf{\Pi}$. For splay fluctuations, $\hat{\mathbf{q}}=\hat{\mathbf{y}}$, we readily see that $\mathbf{F}_{\rm dip}=-(2\kappa/\tau)\,\phi\,\delta\Pi_y\,\hat{\mathbf{y}}$ is opposite to the local disturbance of the polarization field, $\delta\Pi_y\hat{\mathbf{y}}$. The dipolar field damps the splay mode. In addition, it is worth noting that $\mathbf{F}_{\rm dip}$ does *not* depend on the amplitude of the wave-vector, $q$. The damping of splay fluctuations is *generic*: the damping rate does not depend on the wave-length.

***Density fluctuations*** We finally consider the unexpected experimental finding: density fluctuations are not giant, but normal in the polar liquid. We show that giant density fluctuations, that were generically found in polar phases, are suppressed by the long-range dipolar couplings.

Briefly, in the standard theories of active matter, giant density fluctuations emerge from two ingredients: (i) due to the propulsion of the particles, the splay mode couples the density and polarization fields; (ii) the splay fluctuations are damped *diffusively*, at a rate proportional to $q^2$: larger-scale fluctuations (that involve larger particle numbers) are damped slower [136, 212]. As a result, although the homogeneous polar phase is linearly stable, the standard deviation of the particle number, $\Delta n$, scales with the particle number $\langle n\rangle$ as $\Delta n\sim\langle n\rangle$ in 2D [211]. By contrast, here the splay fluctuations are damped *generically*: their damping rate is independent of $q$. This peculiar behavior stems from the interplay between the dipolar symmetry and the $r^{-2}$ decay of the long-ranged hydrodynamic couplings, in 2D. We now show that it suppresses the giant fluctuations in the polar liquid.

To do so, we follow the standard framework introduced by Toner, Tu and Ramaswamy [212]. We add a conserved white noise term $\nabla\cdot\boldsymbol{\xi}_\phi$ to Eq. (1.36) and a non-conserved Gaussian noise $\xi_\Pi\hat{\mathbf{y}}$ to Eq. (1.37), with zero mean and correlations $\left\langle\xi_{\phi_m}(\mathbf{r},t)\xi_{\phi_n}(\mathbf{r}',t')\right\rangle\equiv 2D_\phi\,\delta_{m,n}\delta(\mathbf{r}-\mathbf{r}')\delta(t-t')$, $\left\langle\xi_\Pi(\mathbf{r},t)\xi_\Pi(\mathbf{r}',t')\right\rangle\equiv 2D_\Pi\,\delta(\mathbf{r}-\mathbf{r}')\delta(t-t')$, $\left\langle\xi_{\phi_m}(\mathbf{r},t)\xi_\Pi(\mathbf{r}',t')\right\rangle\equiv 0$. We calculate the correlation function, $\left\langle|\delta\phi_{\mathbf{q},\omega}|^2\right\rangle$, in Fourier space within a linear-response approximation. For rollers enclosed in a region of area $\mathscr{A}$, the static structure factor is deduced as:

$$S(\mathbf{q})\equiv\frac{\left\langle|\delta\phi_{\mathbf{q}}(t)|^2\right\rangle}{\pi a^2\phi_0\mathscr{A}}=\frac{1}{\pi a^2\phi_0\mathscr{A}}\int_{-\infty}^{+\infty}\frac{d\omega}{2\pi}\left\langle|\delta\phi_{\mathbf{q},\omega}|^2\right\rangle. \tag{1.39}$$

This lengthy calculation yields complex expressions that are provided in the Supplementary Document of the article. The structure factor has a clear interpretation. Fluctuations of the number of

particles lying in a domain of size L are described by the Fourier mode $q \sim 2\pi/\mathrm{L}$. From Eq. (1.39), they are readily related to the structure factor by $\mathrm{S}(q \sim 2\pi/\mathrm{L}) \sim (\Delta \mathrm{N})^2/\langle \mathrm{N} \rangle$. In the limit of large domains, $\mathrm{L} \to \infty$, we therefore have to study the structure factor at vanishing $q$. We find that it saturates to a constant value, $\mathrm{S}(q) = \mathcal{O}\left((qa)^0\right)$, due to the generic stabilization of splay fluctuations by the long-range hydrodynamic interactions. As a result, the density fluctuations are normal:

$$\frac{\Delta n}{\langle n \rangle} \sim \frac{1}{\sqrt{\langle n \rangle}}, \tag{1.40}$$

in agreement with the experimental finding (Fig. 1.6(e))

Our theoretical model therefore provides a mechanism that suppresses the giant density fluctuations. Note that the long-ranged hydrodynamic interactions that are responsible for this behavior are not specific to Quincke rollers; they generically occur in all suspensions of self-propelled bodies confined in a thin layer of liquid, as we explain it in the Appendix.

### 3.4 Polar phases in confinement: rotating vortices

We now turn to the last pattern observed experimentally: in confining disk, the population of rollers displays a transition from a disordered gas to a steadily rotating vortex. This state of the system has been studied by combining experiments (carried out by A. Bricard and V. Chikkadi), numerical simulations (performed by C. Savoie, D. Dash and D. Saintillan), and theory. The results are reported in the article "Emergent vortices in populations of colloidal rollers", that can be found p. 66.

***Experimental and numerical findings*** Let us first have a more detailed look at the experimental and numerical phenomenology. Experimentally, a population of colloidal rollers is confined in a disk of radius $\mathrm{R_c}$. Numerically, the equations of motion that we established above, Eqs. (1.13)–(1.15), have been simulated in a circular box with reflecting boundaries.

Above the critical area fraction $\phi_v$, the population forms a steady axisymmetric vortex that spans the entire disk, as illustrated by the density and polarization fields in Figs. 1.14(a) and 1.14(b). This bifurcation is quantified by the polarization field projected along the azimuthal direction, $\Pi_\varphi = \mathbf{\Pi} \cdot \hat{\mathbf{e}}_\varphi$, plotted versus the mean area fraction $\phi_0$ in Fig. 1.14(c). Remarkably, the vortex is spatially heterogeneous. At a first glance, Figs. 1.14(a) and 1.14(b) suggest that the system is phase separated: a dense polar-liquid ring encloses a dilute and disordered gas at the center. This picture is supported by the variations of the area occupied by the polar ring, $\mathrm{A_{ring}}$ (defined as the region where $\Pi_\varphi > 0.5$), as a function of $\phi_0$ for different confinement radii $\mathrm{R_c}$. All curves collapse on a single master curve when rescaling $\mathrm{A_{ring}}$ by the overall confinement area $\pi \mathrm{R_c^2}$, as shown in Fig. 1.14(d). The polarized ring therefore occupies the same area fraction, irrespective of the system size, as would a liquid coexisting with its vapor at equilibrium. However, this phase-separation scenario is not consistent with the spatial variations of the density field. If two phases were coexisting, they would be separated by an interface having an intrinsic width. Here, the radial density profiles plotted in Fig. 1.14(e) do not display any clear interface. More importantly, they all collapse on a single master curve when rescaling the distance to the center by $\mathrm{R_c}$. The confinement radius is the only characteristic length-scale of the vortex.

***Hydrodynamic description*** We now use the theoretical model to elucidate the vortex pattern. We start from the hydrodynamic equations Eqs. (1.27) and (1.28) that couple $\phi$, $\mathbf{\Pi}$ and $\mathbf{Q}$. We look for steady axisymmetric solutions of the form $\phi = \phi(r)$, $\mathbf{\Pi} = \Pi_\varphi(r)\hat{\mathbf{e}}_\varphi$ and $\mathbf{Q} = \mathrm{Q}(r)(\hat{\mathbf{e}}_\varphi\hat{\mathbf{e}}_\varphi - \hat{\mathbf{e}}_r\hat{\mathbf{e}}_r)$, where $\mathrm{Q}(r) > 0$. As we discussed it above, we *a priori* need a closure relation to link these three hydrodynamic fields. Remarkably, this extra approximation is not needed to establish the existence and the spatial structure of the vortex pattern.

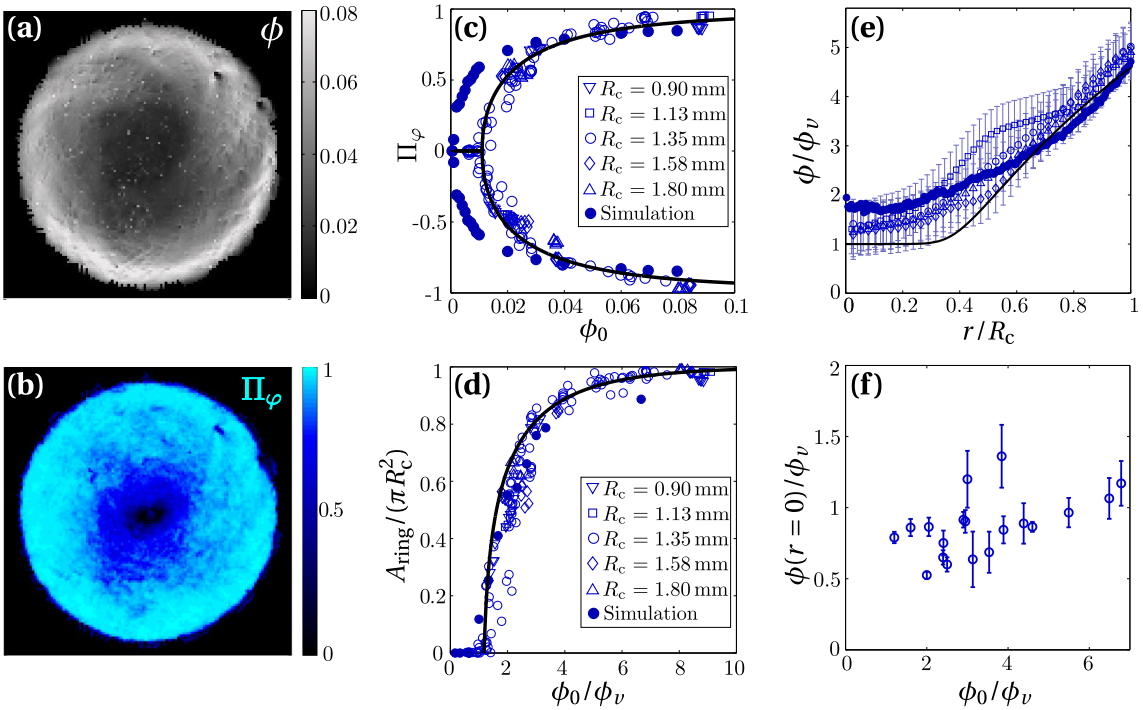


**Figure 1.14** – **(a)** Time-averaged of the local area fraction measured experimentally ($R_c = 1.35\,\mathrm{mm}$, $\phi_0 = 0.05$). **(b)** Time-averaged polarization field. **(c)** Averaged azimuthal polarization plotted versus the mean area fraction $\phi_0$. A polar vortex forms at $\phi_0 > \phi_v$. Open symbols: experiments. Filled circles: numerical simulations (see section 2.3). Full line: best fit from the theory. **(d)** Area fraction occupied by the polar ring, defined as the region where $\Pi_\varphi > 0.5$, plotted as a function of the mean area fraction $\phi_0$. Open symbols: experiments. Filled circles: numerical simulations. Full line: theoretical prediction with no free fitting parameter. **(e)** Radial density profiles rescaled by $\phi_v$, plotted versus the rescaled distance to the center $r/R_c$. Open symbols: experiments performed for different confinement radii. Filled circles: numerical simulations. Full line: theoretical prediction. **(f)** Time-averaged packing fraction at the center of the disk normalized by $\phi_v$ and plotted versus the averaged area fraction (experimental measurement).

First, we project the momentum equation, Eq. (1.28), on the azimuthal direction. With the axisymmetric ansatz, we find:

$$0 = \left[\frac{\alpha}{\tau}\phi(1-2Q) - D_r\right]\phi\Pi_\varphi. \tag{1.41}$$

For the sake of simplicity, we have neglected the non-local term (it can be calculated exactly and only yields a small correction to the first term, as $\kappa/\alpha \sim a/H \ll 1$). Eq. (1.41) accounts for the competition between alignment and rotational diffusion, it again leads to a dynamical phase transition. Increasing the mean area fraction above the critical value $\phi_c = \tau D_r/\alpha$, the system bifurcates from an isotropic state with $\Pi_\varphi = 0$, to a polarized vortex with $\Pi_\varphi \neq 0$ and $Q = \frac{1}{2}\left(1-\phi_c/\phi\right)$. The bifurcation from the disordered gas to the polar vortex occurs at the mean-field critical density: $\phi_v = \phi_c$.

Second, we project Eq. (1.28) on the radial direction. We obtain:

$$-2\frac{v_0}{r}Q = -\frac{\beta a}{2\tau}(1+2Q)\partial_r\phi, \tag{1.42}$$

with $Q = \frac{1}{2}\left(1-\phi_c/\phi\right)$. The left-hand side corresponds to the advection of momentum due to the propulsion of the particles. In the rotating frame, it amounts to a centrifugal force: in the absence of any interaction, self-propulsion drives the particles away from the center of their circular trajectories. This kinematic effects competes with the repulsive interactions between the rollers, right-hand side of Eq. (1.42). When density heterogeneities form, the repulsive couplings result in

a net force that is oriented against the local density gradient. A radial density profile forms and adjusts so that the centrifugal force is exactly balanced by the repulsion. This stationary profile is deduced from Eq. (1.42) and satisfies by the implicit relation:

$$r = r^\star \exp\left[\Lambda \frac{\phi}{\phi_c} + \frac{\Lambda}{2}\log\left(\frac{\phi}{\phi_c} - 1\right)\right], \tag{1.43}$$

where $\Lambda \equiv \phi_c \beta a/(\tau v_0)$ and $r^\star$ is an integration constant. The density plateaus at $\phi = \phi_c$ at the center of the box, and grows significantly as $r > r^\star$, where $r^\star$ therefore sets the typical core radius of the vortex. Importantly, the vortex has no intrinsic length-scale. Its only characteristic length is the constant $r^\star$ , which is set by the total particle number in the box: $\pi R_c^2 \phi_0 = 2\pi \int_0^{R_c} r\,dr\,\phi(r)$. As a consequence, we readily find that $r^\star$ scales with the confinement radius, for fixed $\phi_0$. As $\phi$ only depends on $r/r^\star$, Eq. (1.43), all density profiles obtained for different box sizes $R_c$ collapse on a single curve, in agreement with the experimental data.

***Comparison with the experiments*** To further check the theoretical description, we quantitatively compare the analytical results to the experimental data. First, the model predicts that the density at the center exactly corresponds to the critical density at which the vortex emerges: $\phi(r = 0) = \phi_c = \phi_v$. This relation holds for any confinement radius and total particle number. It is validated by the experiments, see Fig. 1.14(f). Second, we can use the theoretical expressions to fit the experimental data. To do so, we also need the polarization field. At this point we have to specify a closure relation to deduce $\Pi_\varphi$ from $\phi$ and Q. Here, the vortex corresponds to large spatial variations of the polarization, from 0 at the center to $\sim 1$ close to the boundary, in dense populations. We therefore need an assumption that reproduces the basic physical behaviors expected both in the isotropic phase ($Q = 0$) and in the strongly-polarized regime ($Q = 1/2$). We take a simple relation which neglects the correlations in the orientational fluctuations: $Q = \Pi_\varphi^2/2$ [223]. This choice leads to:

$$\Pi_\varphi(r) = \sqrt{1 - \frac{\phi_c}{\phi(r)}}. \tag{1.44}$$

We use this relation, together with Eq. (1.43), to fit the experimental polarization curve, Fig. 1.14(c). The best fit is obtained for values of $\phi_c$ and $\beta$ that are respectively five and two times larger than those deduced from the microscopic parameters. Given the number of simplifications needed to establish the model, the agreement is very convincing. Keeping the exact same values of the fitting parameters, we also calculate the area fraction of the outer polarized ring and the density profile, Figs. 1.14(d) and 1.14(e). Again, the agreement with the experimental very good.

The hydrodynamic theory therefore demonstrates that the vortex observed experimentally does not correspond to a coexistence between two phases. Such a phase-separation would be obtained if the area fraction in the vortex core were smaller, $\phi(r = 0) < \phi_c$: a bubble of isotropic gas would then nucleate in the polar liquid. Here, the density at the center self-regulates to $\phi(r = 0) = \phi_c$. The vortex consists in *one* spatially-heterogeneous phase which lies on the verge of a phase separation. The azimuthal polarization is produced by the alignment interactions; the spatial structure of the vortex is set by the competition between repulsive interactions and the centrifugal force induced by self-propulsion.

Finally, we again stress on the generality of our result and emphasize that the latter scenario is not specific to the Quincke rollers. Indeed, the hydrodynamic equations have the form predicted by the Toner and Tu theory [211, 214], which applies to all polar systems (irrespective of the microscopic origin of the hydrodynamic forces). More generally, this mechanism is not even restricted to interactions having a polar symmetry, since the existence of a centrifugal force solely relies on self-propulsion. The same large-scale behavior is also expected for self-propelled bodies experiencing nematic alignment rules, e.g. shaken elongated rods, concentrated bacterial suspensions or motile biofilaments.

## Conclusion and perspectives

To close this chapter, we very briefly outline the steps that we followed and the main results. We have theoretically studied the emergence of collective behaviors in a controlled experimental system. To do so, we have explicitly modeled the microscopic dynamics from first physical principles (the Maxwell's and Stokes' equations), and made the connection with the large-scale behavior of the population in a hydrodynamic description. This approach has made it possible to demonstrate the physical origin of the large-scale phenomenology observed experimentally.

- Alignment interactions mostly originate from hydrodynamic couplings between the colloids. They compete with the rotational noise and give rise to a dynamical phase transition to polar states.
- Repulsion between particles plays an important role in stabilizing homogeneous polar phases at high densities, as well as heterogeneous polar vortices in non-periodic geometries.
- Additional long-ranged dipolar couplings, that are not present in standard active-matter models, provide a possible mechanism for the suppression of the giant density fluctuations in the polar phase.

The macroscopic behavior of the system also highlights the importance of the geometry of the boundaries. In this non-equilibrium system, several stationary states can be found (e.g. propagating bands or rotating vortices). The boundary conditions play a key role in selecting a pattern among all possible solutions.

In addition, apart from the long-range interactions, the symmetries of both microscopic and hydrodynamic equations are not specific to the Quincke rollers. The latter remark makes this system a good candidate for studying new properties of active matter (e.g. in more complex geometries) on a model experimental population which is fully modeled theoretically.

To conclude, we mention a few open questions and suggest possible extensions of this work.

- We noted that the boundary conditions play an important role in selecting the steady state. However, we have merely rationalized the experimental phenomenology *a posteriori*: for instance, in circular boundaries we have explicitly focused on axisymmetric states. The mechanisms which select a macroscopic phase, after a transient regime, are not understood. As

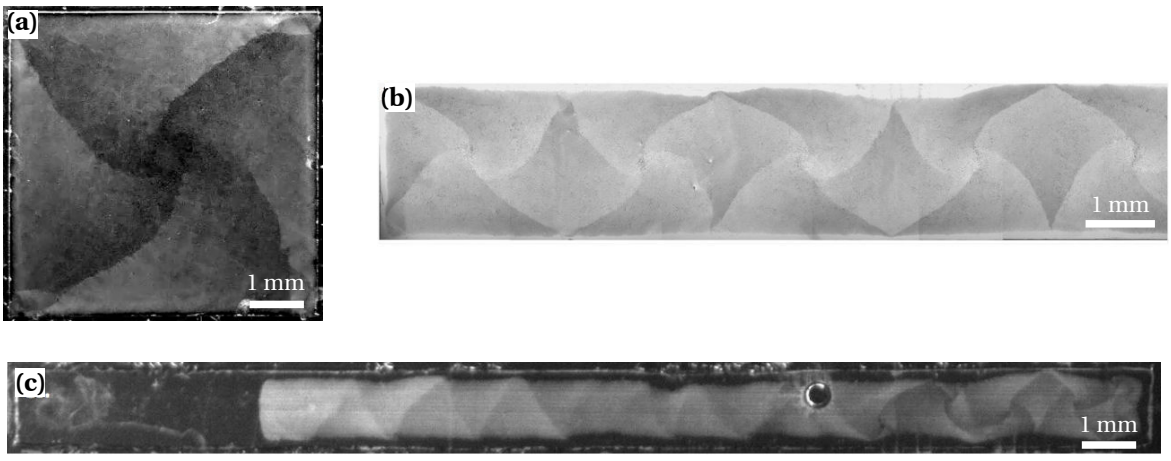


**Figure 1.15** – Large-scale patterns in rectangular boxes. **(a)** A vortex. **(b)** An array of counter-rotating vortices. **(c)** A band bouncing against the walls.

a matter of fact, predicting the final state of the system in an arbitrary geometry is a complex problem. Let us e.g. consider a rectangular confining box and vary its aspect ratio. In squared boxes, the population self-organizes into complex vortex patterns that we did not describe theoretically, see Fig. 1.15(a). In rectangular boxes, we find an array of counter-rotating vortices, Fig. 1.15(b). Further increasing the aspect ratio, the population forms a moving band which bounces endlessly against the box, Fig. 1.15(c). These experimental results show that the final state cannot be readily deduced from the topology of the confining area: bands are found both in periodic racetracks and in rectangular boxes. Although an analytical study might be difficult to achieve, this open problem could be studied experimentally and numerically.

- The boundary conditions play another important role: they impact the nature of the transition to collective motion. (i) In a confining disk, we have shown that the transition towards vortex states is well described by a continuous (second-order) bifurcation. Upon increasing the mean density, the maximum polarization in the vortex continuously increases from 0 (at the transition) to 1 (at very high density). (ii) By contrast, in periodic boundaries the population forms propagating bands. Even at the onset of collective motion, the polarization at the front is very high; increasing the density chiefly increases the width of the band. The emergence of such propagating structures is associated with a first-order transition, see [49, 109] for numerical evidences on the Vicsek model and Chapter 2. The formation of vortices and bands therefore correspond to very different scenarios. These two situations highlight the the impact of the boundary conditions on the nature of the transition to collective motion, which could be further investigated both experimentally and theoretically.

- In order to make the comparison between theory and experiments more quantitative, the dispersion relation of linear waves could be measured experimentally.

- Experimentally, the tail of the band clearly displays a bending motion. In order to theoretically account for this observation, one should study small perturbations of the non-linear band structure. In a more naive approach, two explanations can be advanced. (i) We mentioned that the long-ranged dipolar interactions result in a bending instability of the polar liquid, that is reduced by the confinement but could remain noticeable in the band phase. (ii) In a density gradient, repulsive couplings may favor the bending of the polarized phase. A numerical study may easily identify the very origin of this experimental finding.

- For large values of the applied electric field, it was experimentally found that the colloids stop rolling. This effect is not explained by the Quincke theory. Studying the chemical processes which occur at the interfaces might be required to get a more thorough understanding of the system.

- Our theory holds for dilute populations of rollers. In the high-density limit, contact interactions may play a predominant role and lead to different behaviors, allowing e.g. significant variations of the roller speed with the local density and polarization.

# Article: *Emergence of macroscopic directed motion in populations of motile colloids*

A. Bricard, J.-B. Caussin, N. Desreumaux, O. Dauchot and D. Bartolo, *Nature* **503**, 95 (2013) doi:10.1038/nature12673

**From the formation of animal flocks to the emergence of coordinate motion in bacterial swarms, at all scales, populations of motile organisms display coherent collective motion. This consistent behavior strongly contrasts with the difference in communication abilities between the individuals. Guided by this universal feature, physicists have proposed that solely alignment rules at the individual level could account for the emergence of unidirectional motion at the group level** [136, 212, 215, 216]**. This hypothesis has been supported by agent-based simulations** [38, 92, 215]**. However, more complex collective behaviors have been systematically found in experiments including the formation of vortices** [190, 201, 222]**, fluctuating swarms** [190, 227]**, clustering** [151, 204]**, and swirling** [68, 73, 120, 188]**. All these (living and man-made) model systems (bacteria** [73, 222, 227]**, biofilaments and molecular motors** [188, 190, 201]**, shaken grains** [68, 120] **and reactive colloids** [151, 204]**) predominantly rely on actual collisions to display collective motion. As a result, the potential local alignment rules are entangled with more complex, and often unknown, interactions. The large-scale behaviour of the populations therefore strongly depends on these uncontrolled microscopic couplings that are extremely challenging to measure and describe theoretically.**

**Here, we demonstrate a new phase of active matter. We reveal that dilute populations of millions of colloidal rollers self-organize to achieve coherent motion along a unique direction, with very few density and velocity fluctuations. Identifying, quantitatively, the microscopic interactions between the rollers allows a theoretical description of this polar-liquid state. Comparison of the theory with experiment suggests that hydrodynamic interactions promote the emergence of collective motion either in the form of a single macroscopic flock at low densities, or in that of a homogenous polar phase at higher densities. Furthermore, hydrodynamics protects the polar-liquid state from the giant density fluctuations, which were hitherto considered as the hallmark of populations of self-propelled particles** [136, 194, 212]**. Our experiments demonstrate that genuine physical interactions at the individual level are sufficient to set homogeneous active populations into stable directed motion.**

Our system consists of large populations of colloids capable of self-propulsion and of sensing the orientation of their neighbors solely by means of physical mechanisms. We take advantage of an overlooked electrohydrodynamic phenomenon referred to as the Quincke rotation [138, 165] (Fig. 1.16a). When an electric field $\mathbf{E_0}$ is applied to an insulating sphere immersed in a conducting fluid, above a critical field amplitude $E_Q$, the charge distribution at the sphere's surface is unstable to infinitesimal fluctuations. This spontaneous symmetry breaking results in a net electrostatic torque, which causes the sphere to rotate at a constant speed around a random direction transverse to $\mathbf{E_0}$ [165]. We exploit this instability to engineer self-propelled colloidal rollers. We use PMMA beads of radius $a = 2.4\,\mu$m diluted in an hexadecane solution filling the gap between two conducting glass slides. Once the particles have sedimented on the bottom electrode, we apply an homogeneous electric field, and indeed observe their high-speed rolling motion (Fig. 1.16a). Iso-

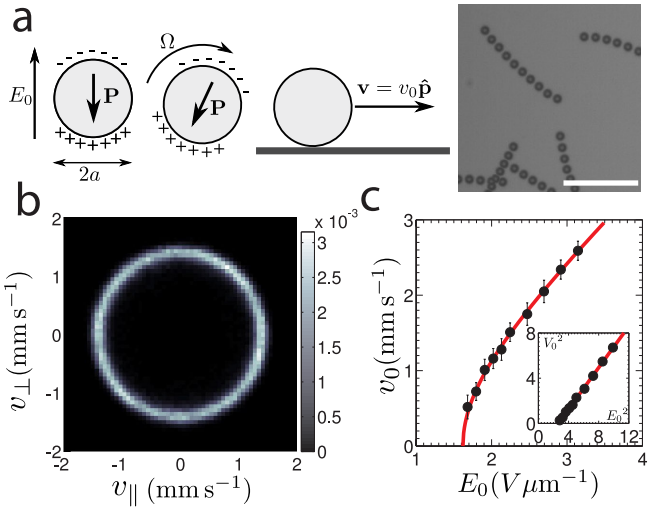


**Figure 1.16 – Single-roller dynamics.** **a**– Sketch of the Quincke rotation and of the self-propulsion mechanisms, and superposition of ten successive snapshots of rolling colloids. Time interval: 5.6 ms. Scale bar 50 µm. **b**– Probability distribution of the velocity vector ($v_\parallel$, $v_\perp$) for isolated rollers. e$v_\parallel$ corresponds to the projection of the velocity on the direction tangent to the racetrack-shaped confinement, see Fig.2. $v_\perp$ is normal to $v_{//}$. The probability distribution involves more than $1.4 \times 10^5$ instantaneous-speed measurements. **c**– Modulus of the individual velocity $v_0$ with respect to the electrostatic field amplitude $E_0$. Inset : $v_0^2$ versus ${E_0}^2$. The black dots represent the maximum of the probability distribution, and the error bars are defined from the standard deviation.

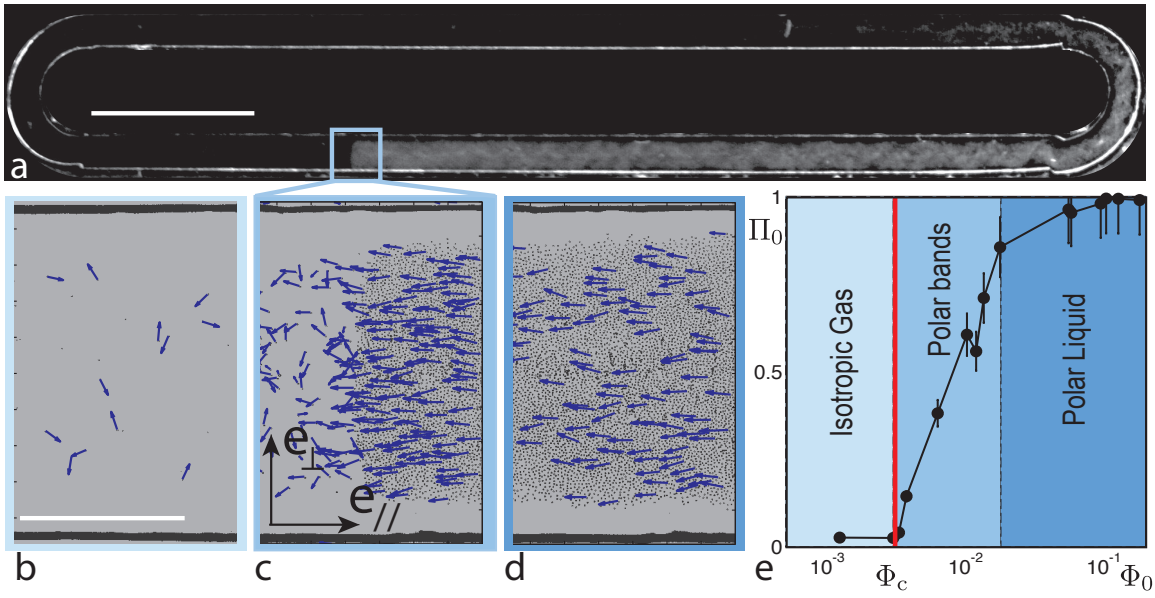


**Figure 1.17 – Transition to directed collective motion.** **a**– Dark field pictures of a roller population that spontaneously forms a macroscopic band propagating along the racetrack, $E_0/E_Q = 1.39$ and $\phi_0 = 10^{-2}$. Scale bar 5 mm. **b, c, d**– Close views on the roller populations. The arrows correspond to the roller displacement between two subsequent movie frames (180 fps).Three distinct regimes are observed when varying $\phi_0$. **b**– Isotropic gas, $\phi_0 = 6 \times 10^{-4}$. **c**– Propagating band, $\phi_0 = 10^{-2}$. **d**– Homogeneous polar liquid $\phi_0 = 1.8 \times 10^{-1}$. Scale bar 500 µm. (Note that the apparent size of the particles is twice larger than $2a = 4.8\,\mu$m, due to light diffraction). **e**– The modulus of the average polarization, $\Pi_0$, increases sharply from zero when the average area fraction $\Phi_0$ exceeds $\Phi_c = 3\,10^{-3}$ and reaches $\Pi_0 \sim 1$ for the largest area fraction. $\Phi_c$ is independent of $E_0$. The error bars correspond to the standard deviations.

lated rollers propel along random directions (Fig. 1.16b). Their velocity $v_0$ is set by $E_0$ and scales as $\left[(E_0/E_Q)^2-1\right]^{\frac{1}{2}}$ (Fig. 1.16c and Supplementary Materials).

In view of questioning the emergence of collective unidirectional motion, we electrically confine the roller populations in racetracks periodic in the curvilinear coordinate $s$. Their width is $500\,\mu m < W < 5\,mm$ (Fig. 1.17a and Methods). During a typical 10-minute-long experiment, millions of rollers travel over distances as large as $10^5-10^6$ particle radii, which makes it possible to investigate exceptionally large-scale dynamics. At low area fraction, $\phi_0$, the rollers form an isotropic gaseous phase. They all move at the same velocity along random directions as would an isolated particle (Fig. 1.17b). Increasing $\phi_0$ above a critical value $\phi_c$, we observe a clear transition to collective motion. A macroscopic fraction of the rollers self-organizes and cruises coherently along the same direction (Figs. 1.17c and 1.17d). More quantitatively, we define a polarization order parameter $\Pi_0$ as the modulus of the time and ensemble average of the particle-velocity orientation. $\Pi_0$ increases sharply with $\phi_0$ and displays a clear slope discontinuity at $\phi_c = 3\times10^{-3}$, revealing the strongly collective nature of the transition (Fig. 1.17e). Remarkably, $\phi_c$ is a material constant: it is independent of the electric-field amplitude.

For area fractions higher than but close to $\phi_c$, small density excitations nucleate from an unstable isotropic state and propagate along random directions. After complex collisions and coalescence events, the system phase separates to form a single macroscopic band that propagates at a constant velocity $c_{band}$ through an isotropic gaseous phase (Figs. 1.17a, 1.17c and 1.18a). No stationary state involving more than a single band was observed even in the largest systems (10 cm long). The velocity $c_{band}$ is found to be very close to the single particle velocity $v_0$ at the front of the band. The bands are coupled to a net particle flux: they are colloidal flocks traveling through an isotropic phase. Their density profile is strongly asymmetric, unlike the slender bands observed in dense motility assays [190]. This marked asymmetry is akin to that found in 1D agent-based mod-

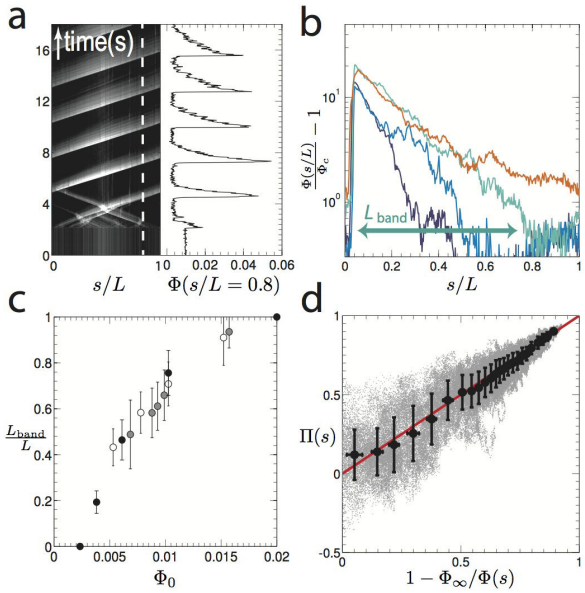


**Figure 1.18 – Propagating-band state.** **a**– Left: spatiotemporal diagram of the area fraction recorded along the curvilinear coordinate $s$. Right: temporal variations of the area fraction measured at the curvilinear coordinate $s = 0.8L$ (white dotted line on left panel), where L is the overall length of the racetrack. **b**– Shape of the band for four different area fractions $\Phi_0 = 5.3\,10^{-3}, 7.8\,10^{-3}, 1.0\,10^{-2}$, and $1.5\,10^{-2}$. The local area fraction is plotted as a function of $s/L$. Inside the band $\phi(s)$ decreases exponentially towards $\Phi_\infty \simeq \Phi_c$. **c**– The band length rescaled by the stadium length $L_{band}/L$ increases with the area fraction $\Phi_0$ and is independent of the racetrack length (L = 28 mm, (white dots): L = 50 mm (grey dots), L = 73mm (black dots). The error bars represent the estimated error associated with the measurements $L_{band}$ from the plots shown in **b**. **d**– Modulus of the local polarization $\Pi(s)$ plotted versus $1-\Phi(s)/\Phi_\infty$. The black dots correspond to averages over 5000 local measurements (grey dots). The error bars correspond to the standard deviations. The red curve is the theoretical prediction.

els [147]. It might be promoted by the high aspect ratio of the confinement. The local area fraction $\phi(s,t)$, at curvilinear coordinate $s$, and time $t$, increases sharply and then decays exponentially to a constant value $\phi_\infty$, which is very close to the critical volume fraction $\phi_c$ (Fig. 1.18b). This shape is similar to the one found in numerical simulations of the celebrated 2D Vicsek model [25, 51]. Remarkably, the bands have no intrinsic scale and their length, $L_{band}$, is set by the particle-number conservation only. This result is readily inferred from Fig. 1.18c, which shows that the bands span a fraction of the racetrack which merely increases with $\phi_0$ regardless of the overall curvilinear length L.

Looking now at the local polarization, we observe that the colloidal flock loses its internal coherence away from the band front as $\Pi(s,t)$ decays continuously to zero along the band. Quantitatively $\phi(s,t)$ and $\Pi(s,t)$ are related in a universal manner irrespective of the particle velocity, and of the mean volume fraction (Fig. 1.18d). All our data collapse on a single master curve solely parametrized by the particle fraction $\phi_\infty$ away from the band: $\Pi(s,t) = \left(1 - \frac{\phi_\infty}{\phi(s,t)}\right)$. As it turns out, this relation corresponds to particle-number conservation in a system where density and polarization waves propagate steadily at a velocity $v_0$ (see [25] and Supplementary Methods). This robust observation unambiguously demonstrates that the band state corresponds to a genuine *stationary* flocking phase of colloidal active matter.

Further increasing the area fraction above $\phi_0 \sim 2\times10^{-2}$, transient bands eventually catch-up with themselves along the periodic direction and form a homogeneous polar phase (Fig. 1.17d) where the velocity distribution condenses on a single orientation of motion (Fig. 1.19a, to be contrasted with the perfectly isotropic distribution below $\phi_c$ in Fig. 1.16b). Conversely the roller positions are weakly correlated as evidenced by the shape of the pair-distribution function, which is similar to that found in low-density molecular liquids (Fig. 1.19b). We also emphasize that the density fluctuations are normal at all scales (Fig. 1.19c). This is the first experimental observation of a polar-liquid phase of active matter. The existence of a polar-liquid phase was theoretically established yet had never been observed in any prior experiment involving active materials. Until now, collective motion has been found to occur in the form of patterns with marked density and/or orientational heterogeneities [68, 73, 188, 190, 227]. Furthermore, in contrast with the present observations, giant density fluctuations are considered to be a generic feature of the uniaxially-ordered states of self-propelled-particle liquids [136, 194, 212]. We solve this apparent contradiction below and explain quantitatively our experimental observations.

From a theoretical perspective, the main advantage offered by the rollers is that their interactions are clearly identified. We show in the Supplementary Methods how to establish the equations of motion of Quincke rollers interacting via electrostatic and far-field hydrodynamic interactions.

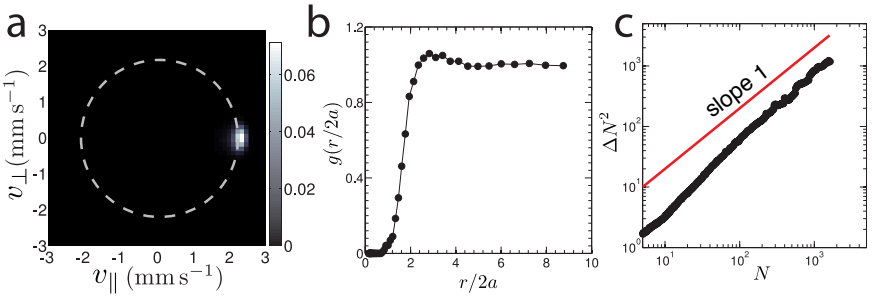


**Figure 1.19 – Polar-liquid state.** **a**– Probability distribution of the velocity vector ($v_{//}$, $v_\perp$) in the the polar-liquid state, where $v_\parallel$ corresponds to the projection of the velocity on the direction tangent to the racetrack shown in Fig.2. $v_\perp$ is normal to $v_{//}$. The probability distribution involves more than $3.2\times10^7$ instantaneous-speed measurements. **b**– Pair correlation function of the particle position in the polar liquid state. **c**– Variance of the number of colloids $\Delta N^2$ scales linearly with the average number of colloids N counted inside boxes of increasing size. $E_0/E_Q = 1.39$ and $\phi_0 = 9.5\times10^{-2}$.

They take a compact form both for the position $\mathbf{r_i}$, and the orientation $\hat{\mathbf{p}}_i$ of the $i^{\text{th}}$ particle:

$$\dot{\mathbf{r}}_i = v_0\hat{\mathbf{p}}_i \tag{1.45}$$

$$\dot{\theta}_i = \tau^{-1}\sum_{i\neq j}\partial_{\theta_i}\mathscr{H}_{\text{eff}}(\mathbf{r}_i-\mathbf{r}_j,\hat{\mathbf{p}}_i,\hat{\mathbf{p}}_j) \tag{1.46}$$

where $\hat{\mathbf{p}}_i$ makes an angle $\theta_i$ with the $x$-axis. In dilute systems, the particle interactions do not affect their propulsion speed, yet the electric field and flow field compete to align the $\hat{\mathbf{p}}_i$s with them. This competition takes the form of an effective potential $\mathscr{H}_{\text{eff}}$ for the local orientations $\hat{\mathbf{p}}_i$. At leading order in $a/r$, $\mathscr{H}_{\text{eff}}(\mathbf{r},\mathbf{p}_i,\mathbf{p}_j) = \mathrm{A}(r)\hat{\mathbf{p}}_i\cdot\hat{\mathbf{p}}_j + \mathrm{B}(r)\hat{\mathbf{p}}_i\cdot\hat{\mathbf{r}} + \mathrm{C}(r)\hat{\mathbf{p}}_j\cdot(2\hat{\mathbf{r}}\hat{\mathbf{r}}-\mathrm{I})\cdot\hat{\mathbf{p}}_\mathrm{j}$, where $\mathrm{A}(r)$ is a positive function, and thus promotes the alignment of the neighboring rollers. Importantly, A is dominated by a hydrodynamic interaction, which arises from a hydrodynamic singularity screened over distances of the order of the chamber height [98]. $\mathrm{B}(r)$ is also short ranged and accounts for a dipolar repulsion. Conversely, $\mathrm{C}(r)$ is long ranged and decays algebraically as $r^{-2}$ due to unscreened potential-dipole flows induced by the roller motion in confinement [37]. Neither B nor C yield any net alignment interaction. Neglecting these two terms, our model built from the actual microscopic interactions would amount to the so-called flying $xy$-model introduced phenomenologically in [79]. We emphasize that $\mathscr{H}_{\text{eff}}$ is independent of $v_0$ and $\mathrm{E}_0$, and that it is *not* specific to the Quincke mechanism. Its expression could have been deduced from generic arguments based on global rotational invariance. We then use a conventional kinetic-theory framework à la Boltzmann to derive the large-scale equation of motion for the density, and the polarization fields [25, 79]. In the present case, this approximation was fully supported by the weak positional correlations in all the three phases, as exemplified in Fig. 1.19b. The resulting hydrodynamic equations are shown in the Supplementary Methods. At the onset of collective motion, the magnitude of the terms arising from the long-range hydrodynamic interactions are negligible. We are therefore left with equations for $\phi$ and $\Pi$ akin to the Toner and Tu model [136, 212]. However, we provide explicitly the functional form of the transport coefficients phenomenologically introduced in [212]. Accordingly, we find that the competition between the polar ordering (induced by the short-range hydrodynamic interactions) and rotational diffusion yields a mean-field phase transition between an isotropic and a macroscopically ordered state (see Supplementary Methods). The phase transition occurs above a critical fraction $\phi_c$ that does not depend on the particle velocity (i.e. on $\mathrm{E}_0$), in agreement with our experiments: collective motion chiefly stems from hydrodynamic interactions between the electrically powered rollers. However, at the onset of collective motion (i.e. for $\phi_0 > \phi_\mathrm{c}$), the homogeneous polar state is linearly unstable to spatial heterogeneities. Moreover, for $\phi_0 > \phi_\mathrm{c}$, the compression modes are unstable eigenmodes of the isotropic state, in agreement with the emergence of density bands observed in the experiments, all starting from an homogeneous state and an isotropic velocity distribution.

We also rigorously establish a kinetic theory for the strongly polarized state reached for $\phi_0 \gg \phi_c$ (Supplementary Methods). In this regime, the short range electrostatic repulsion matters, causing the density fluctuations to relax and stabilizes the polar-liquid state. In addition, the long-range hydrodynamic interactions further stabilize the system by damping the splay modes of $\mathbf{\Pi}$ [37], thereby suppressing the giant density fluctuations [189], in agreement with our unanticipated experimental findings (Fig. 1.19c and Supplementary Methods). We stress here that theses long-range hydrodynamic interactions do not depend at all on the propulsion mechanism at the individual level. They solely arise from from the confinement of the fluid in the $z$-direction [37]. They are therefore *not* specific to the Quincke propulsion mechanism. The only way to destroy the robust polar-liquid phase is to forbid it geometrically by eliminating the angular periodicity of the confinement in the curvilinear coordinate. In rectangular geometries with large enough aspect ratio, we observe that the bands never relax but rather bounce endlessly against the confining box. In confinement with an aspect ratio of order one, the band state is replaced by a single macroscopic spiral.

We have engineered large-scale populations of self-propelled particles from which collective macroscopic polar motion emerges from hydrodynamic interactions at exceptionally small densi-

ties. In addition, we believe that control over their interactions, and the ease with which they can be confined in custom geometries, will extend the current paradigm of active matter to collective motion in more complex environments relevant to biological, robotic and social systems.

**METHODS**

We use commercial PMMA colloids (Thermo scientific G0500, 2.4µm radius), dispersed in a 0.15 mol.$L^{-1}$ AOT/hexadecane solution. The suspension is injected in a wide microfluidic chamber made of double-sided scotch tapes. The tape is sandwiched between two ITO-coated glass slides (Solems, ITOSOL30, 80 nm thick). To achieve electric confinement an additional layer of scotch tape including a hole having the desired geometry is added to the upper ITO-coated slide. The holes are made with a precision plotting cutter (Graphtec robo CE 5000). The gap between the two ITO electrode is constant over the entire chamber H = 220µm. The electric field is applied by means of a voltage amplifier (Trek 606E-6). The colloids are observed with a Nikon AMZ1500 stereomicroscope (1X magnification) equipped with a dark-field illuminator, and with a Zeiss axiovert microscope (10X objective) for local measurements. In both case, high speed movies are taken with CMOS camera (Basler A CE) at frame rates comprised between 70 and 900 fps.The particles are detected to a 1 pixel accuracy by locating the intensity maxima on the experimental pictures. The particle trajectories are reconstructed using a conventional tracking code[58].

**Acknowledgements** We acknowledge support from Paris emergence program (DB), C'Nano IdF (DB), and Institut Universitaire de France (DB).

**Author Contributions** A.B. and J.-B. C. have equal contributions. A.B. and N.D. performed the experiments. A. B., N. D., O. D. and D. B. analyzed the experimental results. D.B. conceived and designed the experiments. J.-B. C. and D. B. performed the theory and wrote the Supplementary Methods. J.-B. C., O. D. and D.B. wrote the paper.

# Supplementary Information

Here, we provide a comprehensive description of the theoretical model outlined in the main text, which accounts of the large-scale properties of a population of colloidal rollers. For sake of clarity, this document is written in a self-consistent fashion, all the notations and definitions of the main text are explicitly re-defined. It is organized as follows: In section 1 we introduce a microscopic model that accounts for the motion of a single colloidal roller moving on a solid surface. Then, in section 2 we model the two-body interactions between colloidal rollers. We show that the combination of the electrostatic and the hydrodynamic couplings take the form of an effective potential $\mathscr{H}_{\text{eff}}$ that couples the orientation of the rollers. In section 3, the latter microscopic model is coarse-grained following a kinetic theory framework. We focus first on weakly polarized states, for which we establish the dynamics of the local density $\phi(\mathbf{r}, t)$, and of the local polarization field $\mathbf{\Pi}(\mathbf{r}, t)$ in section 4. This model accounts for a mean-field transition to collective motion. The linear stability of the homogeneous polar phase is questioned, and the existence of unstable compression modes is shown to be consistent with the formation of a band state. This stationary band state is characterized by the constitutive relation between the local density and the local polarization. Finally, we consider the large-scale dynamics of the polar-liquid phases in section 5. Our main result is the explanation for the suppression of the giant density fluctuations by long-ranged hydrodynamic interactions.

# 1 From Quincke rotation to self-propulsion: the single roller dynamics

## 1.1 Quincke rotation: uniform electric field, quiescent fluid

Before discussing the key role played by the solid surface, we briefly recall the main ingredients which originate the Quincke rotation of an isolated particle embedded in a quiescent and unbounded liquid [138].

This electro-hydrodynamic effect arises from the interplay between interfacial electrodynamics and the particle motion in a viscous fluid. Let us consider an insulating sphere of radius $a$ located at $\mathbf{r} = \mathbf{0}$, possibly rotating at the angular velocity $\Omega$. We note $\epsilon_p$ the dielectric permittivity of the particle. It is surrounded by a conducting liquid with a conductivity $\sigma$ and a permittivity $\epsilon_l$. The solid particle is assumed to be impermeable. As the charge carriers in the liquid are ions, the sphere is a perfect insulator. A uniform DC electric field $\mathrm{E}_0\,\hat{\mathbf{z}}$ is applied along the $z$-direction as sketched in Fig. 1.20A. After a transient regime, the electric charge relaxes to zero in the bulk. However, the charge distribution is not uniform at the the liquid-particle interface. Due to the conductivity and permittivity discontinuity, a non-uniform charge distribution arises close to the interface. The thickness of the charge layer is assumed to be much smaller than the particle radius $a$. Therefore it can be modeled by a surface-charge distribution deduced from the continuity relation: $q_s = (\epsilon_l \mathbf{E}^l - \epsilon_p \mathbf{E}^p)\cdot\hat{\mathbf{r}}|_{r=a}$, where $\mathbf{E}^l$ (resp. $\mathbf{E}^p$) stands for the electrostatic field inside the liquid (resp. the particle). Using the Maxwell's equations, it can be readily shown that the surface charge distribution is dipolar. It is thus described by its first moment $\mathbf{P} \equiv \int \mathrm{d}^2 s\; q_s \hat{\mathbf{r}}_s$. To establish how $\mathbf{P}$ depends on $\mathbf{E}_0$, we use the surface-charge conservation equation $\partial_t q_s + \nabla_s \cdot \mathbf{j}_s = 0$, where $\nabla_s \equiv (\mathbf{I} - \hat{\mathbf{r}}\hat{\mathbf{r}})\cdot\nabla$ is the surface divergence operator, and $\mathbf{j}_s$ is the surface current. Due to the possible rotation of the particle, both ohmic conduction and charge advection contribute to the surface current: $\mathbf{j}_s = \sigma\mathbf{E} + q_s\,\Omega \times a\hat{\mathbf{r}}$. After some elementary algebra, the charge-conservation equation can be recast into a dynamical equation for the dipole moment $\mathbf{P}$ [138, 153]:

$$\frac{\mathrm{d}\mathbf{P}}{\mathrm{d}t} + \frac{1}{\tau}\mathbf{P} = -\frac{1}{\tau} 2\pi\epsilon_0 a^3 \mathbf{E}_0 + \Omega \times \left(\mathbf{P} - 4\pi\epsilon_0 a^3 \chi^\infty \mathbf{E}_0\right) \tag{1.47}$$

where $\chi^\infty \equiv \frac{\epsilon_p - \epsilon_l}{\epsilon_p + 2\epsilon_l}$ and $\tau$ is the so-called Maxwell-Wagner time. It is convenient to distinguish two contributions to the overall polarization vector: $\mathbf{P} \equiv \mathbf{P}^\epsilon + \mathbf{P}^\sigma$. The "static" contribution, $\mathbf{P}^\epsilon \equiv 4\pi\epsilon_0 a^3 \chi^\infty \mathbf{E}_0$ arises from the dielectric polarization, due to the permittivity discontinuity at the interface. The dynamic contribution $\mathbf{P}^\sigma$ results from the transport of the charges in the solution. When no rotation occurs, the dipole $\mathbf{P}$ relaxes towards a stationary value and orients along $-\mathbf{E}_0$ in a time $\tau$ due to the finite conductivity of the solution. However, as the particle rotates, charge advection competes with the spontaneous relaxation, and could in principle result in a dipole orientation making a finite angle with the external field $\mathbf{E}_0$.

More quantitatively, we now show that the surface charge distribution can spontaneously break a rotational symmetry and therefore induce the steady rotation of the insulating sphere. In order to do so, we need an extra equation that is the angular momentum conservation. Since the particle carries surface charges, it may experience a net electric force $\mathbf{F}^\mathrm{e}$ and an electric torque $\mathbf{T}^\mathrm{e}$. The net interfacial electric stress is the jump of the Maxwell stress tensor across the interface:

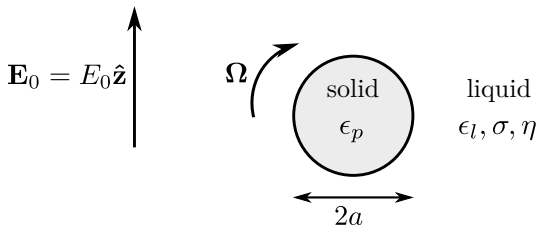


**Figure 1.20** – An isolated solid sphere in an unbounded conducting liquid. When an external electric field $\mathbf{E}_0$ is applied, the particle can undergo Quincke rotation.


**Figure 1.21** – Emergence of Quincke rotation. **A**– Electric charges accumulate at the particle-liquid interface and result in a dipolar surface distribution. **B**– A small rotational perturbation tilts the dipole $\mathbf{P}$, thereby inducing a net electric torque $\mathbf{T}^e$ which amplifies the initial perturbation.

$\hat{\mathbf{r}}\cdot\left[\mathcal{T}_{\mathbf{M}}{}^{l}-\mathcal{T}_{\mathbf{M}}{}^{p}\right]_{r=a}$, where $\mathcal{T}_{\mathbf{M}}\equiv\epsilon\mathbf{E}\mathbf{E}-\frac{1}{2}\epsilon E^2\mathbf{I}$. Integrating over the surface, we obtain the torque $\mathbf{T}^e=\frac{\epsilon_l}{\epsilon_0}\mathbf{P}\times\mathbf{E}_0$ and the net force $\mathbf{F}^e=\frac{\epsilon_l}{\epsilon_0}(\mathbf{P}\cdot\nabla)\mathbf{E}_0$, which vanishes in a uniform external field. Having colloidal systems in mind, we ignore the inertia of the sphere. Therefore the translation velocity $\mathbf{v}$ and the rotation speed $\Omega$ are linearly related to $\mathbf{F}^e$ and $\mathbf{T}^e$ through a mobility matrix $\mathscr{M}$:

$$\begin{pmatrix}\frac{1}{a}\mathbf{v}\\ \Omega\end{pmatrix}\equiv\mathscr{M}\cdot\begin{pmatrix}a\mathbf{F}^e\\ \mathbf{T}^e\end{pmatrix} \tag{1.48}$$

In an unbounded fluid, $\mathscr{M}$ is diagonal and has the form $\mathscr{M}=\begin{pmatrix}\mu_t\mathbf{I} & 0\\ 0 & \mu_r\mathbf{I}\end{pmatrix}$, where $\mu_t=(6\pi\eta a^3)^{-1}$ in a liquid of viscosity $\eta$. Eqs. (1.47) and (1.48) together fully capture the particle dynamics. When $\chi^\infty+\frac{1}{2}>0$ and when the external field $\mathbf{E}_0$ exceeds the threshold value $E_Q=\left[4\pi\epsilon_l a^3(\chi^\infty+\frac{1}{2})\mu_r\tau\right]^{-1/2}$, two stationary states are found from Eqs. (1.47) and (1.48). A first non-rotating solution is unstable against rotational perturbations. The second solution is stable and corresponds to a steady rotation at angular velocity

$$\Omega=\frac{1}{\tau}\sqrt{\left(\frac{E_0}{E_Q}\right)^2-1} \tag{1.49}$$

The rotation axis can be any direction perpendicular to $\mathbf{E}_0$ as the symmetry is spontaneously broken. Such a stationary rotating state is conditioned by the competition between two opposite effects, that can be easily read from Eq. (1.47). On the one hand, the charge relaxation promotes the alignment of the dipole $\mathbf{P}$ in the direction $-\mathbf{E}_0$, thereby canceling the electric torque $\mathbf{T}^e$. On the other hand, any small rotational perturbation advects the surface charge distribution and tilts the dipole $\mathbf{P}^\sigma$. This gives rise to a net electric torque $\mathbf{T}^e$ which tends to amplify the initial disturbance, until it is balanced by the viscous torque, see Fig. 1.21A.

The Quincke-electro-rotation mechanism can be summarized as follows: when the external field exceeds a threshold value $E_Q$, any infinitesimal perturbation results in an electrostatic torque which is large enough to advect the charges despite the stabilizing mechanism provided by the finite conductivity of the solution. The advection amplifies the initial perturbation until the viscous torque balances the electric torque. When the stationary state is reached, the particle steadily rotates at $\Omega$ around an axis perpendicular to $\mathbf{E}_0$, the direction of which is set by the initial perturbation only.

## 1.2 Self-propulsion of a Quincke roller

In an unbounded fluid and a uniform electric field, the particle experiences no net force and thus have no translational velocity. To achieve propulsion of the spheric particle, the basic idea is to let it roll on a plane surface that is one of the two electrodes used to induce $\mathbf{E}_0$. In order to establish the equations of motion of a Quincke roller, we have to modify both the mechanical and the electrostatic equations introduced above.

First we note that contact between the sphere and the planar electrode is lubricated by the surrounded liquid. A priori, the sphere both rolls and slides on the surface. This is accounted for

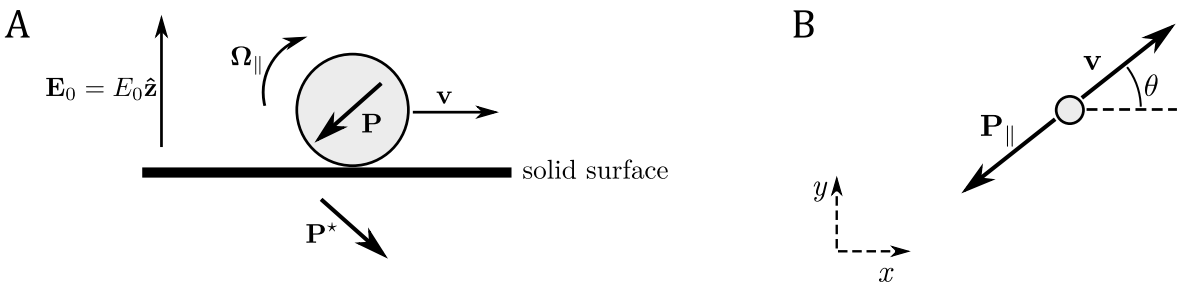


**Figure 1.22** – Quincke rotating particle rolling on a plane conducting surface. **A**– The surface couples rotational and translational motion, allowing propulsion. It also disturbs the electric field. The dominant contribution to the image charge distribution is the symmetric dipole $\mathbf{P}^\star$. **B**– In the plane of the surface, the direction of the translation velocity is defined by the angle $\theta$.

by a modified mobility matrix $\mathscr{M}$:

$$\begin{pmatrix} \frac{1}{a}\mathbf{v} \\ \Omega_\parallel \\ \Omega_z \end{pmatrix} = \mathscr{M} \cdot \begin{pmatrix} a\mathbf{F}^{\mathrm{e}}_\parallel \\ \mathbf{T}^{\mathrm{e}}_\parallel \\ \mathrm{T}^{\mathrm{e}}_z \end{pmatrix} \tag{1.50}$$

where we now have to distinguish between the in-plane components and the $z$-component of the vectors, see Fig. 1.22A. The mobility matrix is non-diagonal and can be written as

$$\mathscr{M} = \begin{pmatrix} \mu_t\mathbf{I} & \tilde{\mu}_t\boldsymbol{\Lambda} & 0 \\ -\tilde{\mu}_r\boldsymbol{\Lambda} & \mu_r\mathbf{I} & 0 \\ 0 & 0 & \mu_\perp \end{pmatrix}, \tag{1.51}$$

where $\boldsymbol{\Lambda} = \begin{pmatrix} 0 & 1 \\ -1 & 0 \end{pmatrix}$. The off-diagonal blocks of $\mathscr{M}$ couple rotational and translational motion: they are responsible for the rolling motion. For instance $\tilde{\mu}_t$ relies the electric torque to the translational propulsion speed. The mobility factors are easily inferred from the friction coefficients which were calculated in [89, 90, 130, 148], in the lubrication regime. They depend only logarithmically on the distance between the particle and the surface, which was assumed to be small compared to the particle radius. Although we do not precisely control this gap, the numerical values of the mobility coefficients are weakly affected by this logarithmic dependence.

The surface at $z = 0$ does not only modify the hydrodynamics of the fluid, but also disturbs the electric field. Indeed, the particle lies on the lower electrode, which is an equipotential surface. We take it into account by considering an electric image charge distribution in the region $z < 0$, which is dominated by a dipole $\mathbf{P}^\star = \mathrm{P}_z\hat{\mathbf{z}} - \mathbf{P}_\parallel$ at $z = -a$, as sketched in Fig. 1.22A. As opposed to the case considered in the previous section, where we considered the classical Quincke setup, the particle experiences an external electric field which is *not* uniform. It includes here a correction $\delta\mathbf{E}^\star$ induced by the image charges. From the steady solution of the Quincke rotation in an infinite fluid, we can calculate the unperturbed dipole $\mathbf{P}$ in the absence of the surface, and then evaluate the disturbance field due to the surface. Whithin our experimental conditions, $\mathrm{E}_0 < 3\mathrm{E}_\mathrm{Q}$ and $\chi^\infty \ll \frac{1}{2}$ [153]. Therefore, the correction $\delta\mathbf{E}^\star$ is much smaller that the magnitude of the unperturbed field: $|\delta\mathbf{E}^\star|/\mathrm{E}_0 \sim 0.01$. At leading order in $|\delta\mathbf{E}^\star|/\mathrm{E}_0$, the dynamics of the electric polarization is written in a form that is more complex than Eq. (1.47):

$$\frac{\mathrm{d}\mathrm{P}^\sigma_z}{\mathrm{d}t} + \frac{1}{\tau}\mathrm{P}^\sigma_z = \frac{\epsilon_l}{\epsilon_0}\mu_r\mathrm{E}_0\mathrm{P}^{\sigma\,2}_\parallel - \frac{1}{\tau}4\pi\epsilon_0 a^3\left(\chi^\infty + \frac{1}{2}\right)\mathrm{E}_0 \tag{1.52}$$

$$\frac{\mathrm{d}\mathrm{P}^\sigma_\parallel}{\mathrm{d}t} + \frac{1}{\tau}\mathrm{P}^\sigma_\parallel = -\frac{\epsilon_l}{\epsilon_0}\mu_r\mathrm{E}_0\mathrm{P}^\sigma_z\mathrm{P}^\sigma_\parallel \tag{1.53}$$

$$\frac{\mathrm{d}\theta}{\mathrm{d}t} = 0 \tag{1.54}$$

where θ defines the direction of the in-plane component of the polarization, Fig. 1.22B. The relation between the polarization, the electric torque and the electric force is not affected by the substrate. In addition, it is worth noting that the surface induces no tangential force $\mathbf{F}^{\mathrm{e}}_{\parallel}$, and no perpendicular torque $\mathrm{T}^{\mathrm{e}}_{z} = 0$ on the sphere. This is a rigorous results that does not depend on the specifics of the experiments. It holds at all order in $|\delta\mathbf{E}^{\star}|/\mathrm{E}_0$ as it only follows from the symmetry of the real charges and of the image charges with respect to the equipotential plane. Combing now Eqs. (1.47) and (1.50) we infer the equations of motion of an isolated sphere lying on a planar electrode:

$$\mathbf{v} = -\frac{\epsilon_l}{\epsilon_0} a\tilde{\mu}_t \mathrm{E}_0 \mathbf{P}^{\sigma}_{\parallel} \tag{1.55}$$

This is the first main result of this supplementary document: The particle steadily rolls on the electrode at a velocity $\mathbf{v}$, which points in the direction opposite to the electric polarization. When $\mathrm{E}_0 > \mathrm{E}_{\mathrm{Q}}$, the rolling speed $v_0 \equiv |\mathbf{v}|$ is proportional to the in-plane component of $\mathbf{P}$, and is given by

$$v_0 = \frac{a\tilde{\mu}_t}{\mu_r \tau}\sqrt{\left(\frac{\mathrm{E}_0}{\mathrm{E}_{\mathrm{Q}}}\right)^2 - 1} \tag{1.56}$$

The variations of the roller velocity that we measured are in excellent agreement with the above prediction as shown in Fig. 1.16c main text. As our theory does not involve any phenomenological parameter, we can provide an estimate of both the Quincke threshold and the intrinsic velocity scale of the rollers. We have $a = 2.4\,\mu\mathrm{m}$, $\eta \sim 2\,\mathrm{mPa}\cdot\mathrm{s}^{-1}$, $\epsilon_l \sim 2\epsilon_0$ and $\tau \sim 1\,\mathrm{ms}$ [153]. So using the expressions below Eq. (1.48), we find $\mathrm{E}_{\mathrm{Q}} \sim 10^6\,\mathrm{V}\cdot\mathrm{m}^{-1}$ which is consistent with the value deduced from the best fit which yields $\mathrm{E}_{\mathrm{Q}} = 1.6\,10^6\,\mathrm{V}\cdot\mathrm{m}^{-1}$. The mobility coefficients weakly depends on the thickness of the lubrication layer underneath the roller, which is assumed to be here of the order of 10-100 nm. Hence we find $\frac{a\tilde{\mu}_t}{\mu_r\tau} \sim 2\,\mathrm{mm}\cdot\mathrm{s}^{-1}$, which again agrees well with the value deduced from our measurements $\sim 1.5\,\mathrm{mm}\cdot\mathrm{s}^{-1}$. These results unambiguously confirm that the fast motion of the colloids results from the Quincke rotation of the colloids that in turn roll on the planar electrode, and that we have now a quantitative understanding of this novel self-propulsion mechanism.

## 2 Roller-roller interactions

The one-particle dynamics does not explicitly break the rotational invariance around the $\hat{\mathbf{z}}$-axis, as Eq. (1.54) shows. When there are no inter-particle interactions, the system undergoes a spontaneous symmetry breaking, and all the rolling directions θ have the same probability. In this section we show how this invariance is destroyed by the roller-roller interactions, and establish the equations of motion of a population of interacting active colloids.

The rollers are *a priori* coupled by electrostatic and hydrodynamic interactions as well. Their surface-charge distribution induces a field disturbance $\delta\mathbf{E}(\mathbf{r}, t)$ which may alter the polarization, and the velocity, of the surrounding particles. Moreover, as it moves a roller induces a nontrivial fluid motion around it. Therefore, all the rollers are advected by a flow field $\mathbf{u}_{\parallel}(\mathbf{r}, t)$ resulting from the motion of their neighbors. Generically, for a given distribution of roller position, both $\delta\mathbf{E}_{\parallel}$ and $\mathbf{u}_{\parallel}$ break the rotational invariance around $\hat{\mathbf{z}}$ thereby yielding orientational couplings between the active colloids.

### 2.1 A roller in heterogeneous fields

Let us first consider the simpler problem of a single roller in a non-uniform electric field. Its charge distribution has other multipolar components on top of the dipole that we considered so far. However, it can be shown that the dynamics of $\mathbf{P}^{\sigma}$ is not coupled to the other multipoles, see

e.g. [62], and obeys

$$\frac{\mathrm{d}\mathbf{P}^{\sigma}}{\mathrm{d}t}+\frac{1}{\tau}\mathbf{P}^{\sigma}=-\frac{1}{\tau}4\pi\epsilon_0 a^3\left(\chi^{\infty}+\frac{1}{2}\right)(\mathbf{E}_0+\delta\mathbf{E})+\Omega\times\mathbf{P}^{\sigma} \tag{1.57}$$

This modified equation for the in-plane electric dipole is again complemented by a mechanical equation that relates the velocity of the particle to the forces and torques acting on it. Considering that the roller is driven both by the Quincke mechanism and by an external fluid-flow field $\mathbf{u}$, we need to introduce two additional mobility coefficients to generalize Eq. (1.50) [90]:

$$\begin{pmatrix}\frac{1}{a}\mathbf{v}\\ \Omega_{\parallel}\\ \Omega_z\end{pmatrix}=\mathscr{M}\cdot\begin{pmatrix}a\mathbf{F}^e_{\parallel}\\ \mathbf{T}^e_{\parallel}\\ \mathrm{T}^e_z\end{pmatrix}+\begin{pmatrix}\mu_s\,\partial_z\mathbf{u}_{\parallel}\big|_{z=0}\\ \tilde{\mu}_s\,\hat{\mathbf{z}}\times\partial_z\mathbf{u}_{\parallel}\big|_{z=0}\\ 0\end{pmatrix} \tag{1.58}$$

We now proceed to a perturbative analysis of Eqs. (1.57) and (1.58). Having dilute systems in mind, we assume that $|\delta\mathbf{E}|/\mathrm{E}_0=\mathscr{O}(\epsilon)$ and $\tau\left|\partial_z\mathbf{u}_{\parallel}\right|=\mathscr{O}(\epsilon)$ are small parameters. We will further justify this approximation scheme at the end of this section. At leading order in $\epsilon$, Eqs. (1.53)–(1.52) remain valid despite the interactions. $\mathrm{P}_z$, $\mathrm{P}_{\parallel}$ and the norm of the velocity relax towards their unperturbed value over the timescale $\tau$. However, as anticipated the orientations of the particles are now coupled, and evolve on much longer timescales $\sim\tau/\epsilon$. After some tedious algebra, at leading order in $\epsilon$ this slow orientational dynamics takes a rather simple form

$$\frac{\mathrm{d}\theta}{\mathrm{d}t}=\frac{a}{\tau v_0}\frac{\tilde{\mu}_s\tilde{\mu}_t}{\mu_r}\hat{\mathbf{p}}^{\perp}\cdot\partial_z\mathbf{u}_{\parallel}\big|_{z=0}-\frac{v_0}{a}\frac{\mu_r}{\tilde{\mu}_t}\left(\frac{\mu_{\perp}}{\mu_r}-1\right)\hat{\mathbf{p}}^{\perp}\cdot\frac{\delta\mathbf{E}_{\parallel}}{\mathrm{E}_0}+\frac{a\tilde{\mu}_r}{\tau\mu_r}\hat{\mathbf{p}}^{\perp}\cdot(\mathbf{P}\cdot\nabla)\frac{\delta\mathbf{E}_{\parallel}}{\mathrm{E}_0} \tag{1.59}$$

where $\hat{\mathbf{p}}^{\perp}=-\sin\theta\hat{\mathbf{x}}+\cos\theta\hat{\mathbf{y}}$. The three terms on the right-hand-side have a clear physical meaning. First term: when the direction of motion is perpendicular to the flow field, the particle experiences a torque which promotes the reorientation along the local flow direction. The direction $\hat{\mathbf{p}}$ thus rotates until aligning with $\mathbf{u}_{\parallel}$. Similarly, the second term accounts for the electrostatic coupling: it causes the dipole $\mathbf{P}^{\sigma}_{\parallel}$ to align with $\delta\mathbf{E}_{\parallel}$, and therefore aligns $\mathbf{v}$ in the opposite direction, since $(\frac{\mu_{\perp}}{\mu_r}-1)>0$. The last term stems from the field inhomogeneity. Within our experimental conditions, it can be checked from the numerical values of the prefactors, that this last term is subdominant, and we henceforth neglect its contribution.

We have just shown that when a roller feels weak heterogeneities in the electric field and in the flow field, its propulsion speed is unchanged. Conversely, the slow orientational dynamics of the particles now explicitly breaks rotational invariance. The roller is prone to align its velocity with the reverse local electric field and with the local fluid velocity past the planar surface.

## 2.2 Equation of motion of a population of interacting rollers

We now exploit the above results to establish the equations of motion of a population of interacting rollers. Eq. (1.59) is correct regardless of the origin of the fields' heterogeneities. Let us begin with a first important remark: If one now consider a test particle moving in an electric and a flow field perturbed by its neighbors, we readily infer that the speed of the test particle is unchanged. In a dilute population of interacting rollers all the particles propel themselves at the same speed, which is again confirmed by the narrow velocity distributions found experimentally both in the isotropic and in the polar-liquid phases, Fig. 1.16b and 1.19a in the main text.

To go beyond this result, we derive explicitly the forms of the electrostatic and of the hydrodynamic interactions between the active colloids. We note $\mathbf{r}_i(t)$ (resp. $\hat{\mathbf{p}}_i(t)$) the position (resp. the orientation) of particle $i$.

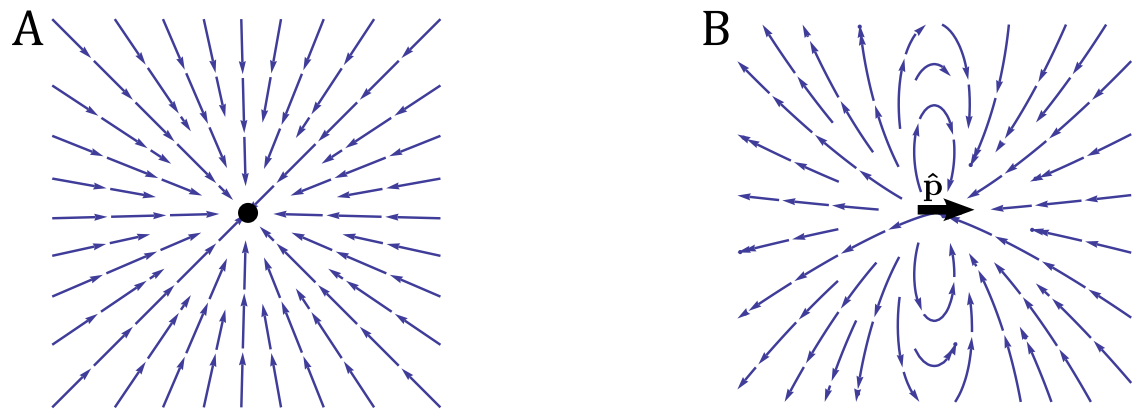


**Figure 1.23** – Electrostatic interactions: a particle rolling in direction $\hat{\mathbf{p}}$ creates a perturbative electric field. The field lines are plotted in the plane containing all the other particles, which tend to align in the opposite direction. **A**– A radial part (proportional to $P_z$) results in a repulsive effect, which does not depend on the orientation of the particle. **B**– An additional contribution (proportional to $P_\parallel$) breaks the rotational symmetry and yields a position-dependent interaction.

#### a) Electrostatic interactions

We calculate the disturbance fields $\delta\mathbf{E}_\parallel(\mathbf{r}_i,t)$ and $\mathbf{u}_\parallel(\mathbf{r}_i,t)$ induced by all the other rollers $j\neq i$. The electric field induced by the particle $j$ originates from the dipole $\mathbf{P}_j$ and its electrostatic image $\mathbf{P}_j^\star$ (Fig. 1.22A). Summing these two contributions in a far-field expansion, we find

$$\delta\mathbf{E}_\parallel^{(j)}(\mathbf{r}_i,t)=\frac{3}{2\pi\epsilon_0 r_{ij}^3}\left[\frac{a}{r_{ij}}P_z\hat{\mathbf{r}}_{ij}-\frac{a^2}{r_{ij}^2}P_\parallel\hat{\mathbf{p}}_j\cdot\left(5\hat{\mathbf{r}}_{ij}\hat{\mathbf{r}}_{ij}-\mathbf{I}\right)+\mathcal{O}\left(\frac{a^3}{r_{ij}^3}\right)\right] \tag{1.60}$$

where $\mathbf{r}_{ij}=\mathbf{r}_i-\mathbf{r}_j=r_{ij}\hat{\mathbf{r}}_{ij}$, and where $P_z$ and $P_\parallel$ are the components of the total polarization at order $\epsilon^0$. We recall that in an heterogeneous field, the dipolar fouling to the local field causes the roller to align its velocity in a direction opposite to $\delta\mathbf{E}_\parallel$. Hence we infer from Eq. (1.60) that the two-body electrostatic interactions combine two contributions. The first term in Eq. (1.60) is proportional to $P_z$. Since $P_z<0$, this first term corresponds to a repulsive interaction: it favors a roller velocity $\mathbf{v}_i$ pointing in the direction opposite to $\hat{\mathbf{r}}_{ij}$ The second term on the r.h.s of Eq. (1.60) is proportional to $P_\parallel$, and it possibly results in alignment or anti-alignment with $\hat{\mathbf{p}}_j$, depending on the relative positions between the two rollers. The symmetry of these two electrostatic couplings is better understood by inspecting the electric-vector field plotted in Fig. 1.23A. So far, we have implicitly neglected the influence of the upper electrode, which is also a conducting equipotential surface. The former results are therefore valid only at distance smaller than the separation distance H between the two electrodes. Experimentally, the channel height is $H=200\,\mu m\gg a$. At larger scales, all the electrostatic couplings are exponentially screened over a characteristic length $H/\pi$.

As a last comment about electrostatic interactions, we note that Eqs. (1.60) and (1.61) confirm that the perturbative treatment $|\delta\mathbf{E}|/E_0=\mathcal{O}(\epsilon)$, $\tau\left|\partial_z\mathbf{u}_\parallel\right|=\mathcal{O}(\epsilon)$ is self-consistent for dilute systems as the algebraic electrostatic repulsion prevents the formation of concentrated clusters in a population of rollers.

#### b) Hydrodynamic interactions

A similar approach is used to deal with the hydrodynamic interactions in dilute systems. The flow field created by the particles is expressed in terms of pointwise hydrodynamic singularities. $r_{ij}<H$: Over distances smaller than the channel height H, a Quincke roller is akin to a rotlet near a no-slip wall. The particle is a pointwise torque-source which induces a complex flow field. This flow was computed by Blake and Chwang using the image singularity method [29]. $r_{ij}>H$:

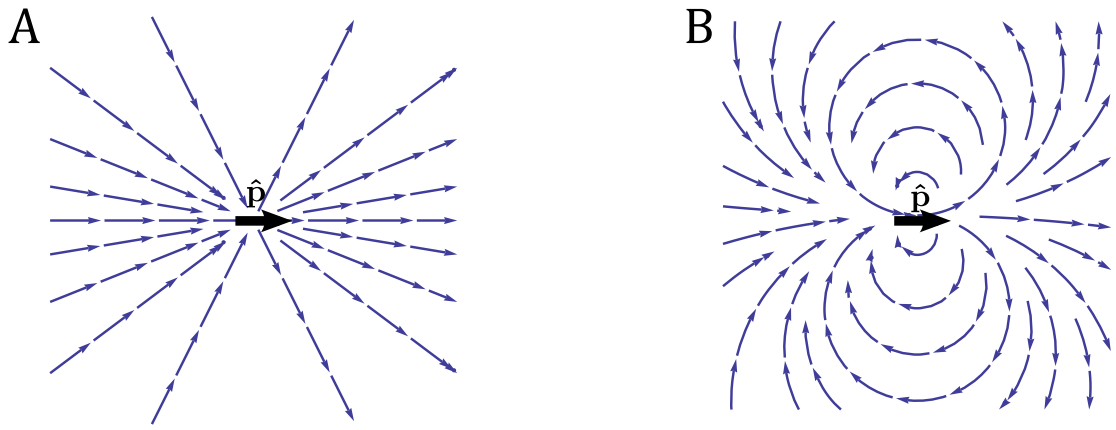


**Figure 1.24** – Hydrodynamic interactions: a particle rolling in direction $\hat{\mathbf{p}}$ creates a flow field. The streamlines are plotted in the plane containing all the other particles, which tend to align in flow. **A**– At distances smaller than the channel height, the central roller induces a radial shear with anisotropic amplitude, which globally promotes alignment. **B**– At distances much larger than the channel height, the non-screened resulting flow has a dipolar symmetry.

At long distances, unlike electrostatic screening, mass conservation gives rise to a non-vanishing flow having the form of a two-dimensional source dipole, as it was derived by Hackborn for a rotlet located between two rigid walls [98]. These results provide the shear rate induced by particle $j$ at the location of the particle $i$. Keeping only the leading order terms in a $a/r_{ij}$ expansion, we obtain

$$\partial_z \mathbf{u}_\parallel^{(j)}\Big|_{z=0}(\mathbf{r}_i,t) = \begin{cases} \frac{6\mu_r}{a\tilde{\mu}_t} v_0 \frac{a^3}{r_{ij}^3}(\hat{\mathbf{p}}_j\cdot\hat{\mathbf{r}}_{ij})\hat{\mathbf{r}}_{ij} & \text{if } r_{ij} < \frac{\mathrm{H}}{\pi} \\ \frac{6\mu_r}{\mathrm{H}\tilde{\mu}_t} v_0 \frac{a^2}{r_{ij}^2}\hat{\mathbf{p}}_j\cdot(2\hat{\mathbf{r}}_{ij}\hat{\mathbf{r}}_{ij}-\mathbf{I}) & \text{at long distance } r_{ij} \gg \frac{\mathrm{H}}{\pi} \end{cases} \tag{1.61}$$

The corresponding streamlines are plotted in Fig. 1.24. We showed that the particle velocity reorients along the local direction of $\partial_z \mathbf{u}_\parallel$. Therefore, we deduce from Eq. (1.61) and Fig. 1.24A that, at short distances ($r_{ij} \ll \mathrm{H}$) the hydrodynamic interactions promote the alignment of the roller velocities. In addition, for $r_{ij} > \mathrm{H}$, long-range hydrodynamic interactions that algebraically decay as $r^{-2}$ have a dipolar symmetry. They can either cause alignment or anti-alignment, depending on the relative positions between the rollers, Fig. 1.24B.

### c) Equations of motion

Assuming that both electrostatic and hydrodynamic interactions are pairwise additive, the above results can be summarized in a compact form. The particle $i$ moves at constant velocity $v_0$ on the surface, and undergoes a slow orientational dynamics:

$$\dot{\mathbf{r}}_i = v_0\hat{\mathbf{p}}_\mathbf{i} \tag{1.62}$$

$$\dot{\theta}_i = \frac{1}{\tau}\frac{\partial}{\partial\theta_i}\sum_{j\neq i}\mathscr{H}_{\mathrm{eff}}(\mathbf{r}_i-\mathbf{r}_j,\hat{\mathbf{p}}_i,\hat{\mathbf{p}}_j) + \sqrt{2\mathrm{D}_r}\,\xi_i(t) \tag{1.63}$$

The global interaction potential $\mathscr{H}_{\mathrm{eff}}$ accounts for all the possible interactions between the rollers that we have established above. It takes the generic form:

$$\mathscr{H}_{\mathrm{eff}}(\mathbf{r},\hat{\mathbf{p}}_i,\hat{\mathbf{p}}_j) = \mathrm{A}(r)\,\hat{\mathbf{p}}_j\cdot\hat{\mathbf{p}}_i + \mathrm{B}(r)\,\hat{\mathbf{r}}\cdot\hat{\mathbf{p}}_i + \mathrm{C}(r)\,\hat{\mathbf{p}}_j\cdot(2\hat{\mathbf{r}}\hat{\mathbf{r}}-\mathbf{I})\cdot\hat{\mathbf{p}}_i \tag{1.64}$$

where the coefficients have complex expressions, deduced from well identified microscopic parameters:

$$A(r) = 3\tilde{\mu}_s \frac{a^3}{r^3}\Theta(r) + 9\left(\frac{\mu_\perp}{\mu_r} - 1\right)\left(\chi^\infty + \frac{1}{2}\right)\left(1 - \frac{E_Q^2}{E_0^2}\right)\frac{a^5}{r^5}\Theta(r) \tag{1.65}$$

$$B(r) = 6\left(\frac{\mu_\perp}{\mu_r} - 1\right)\sqrt{\frac{E_0^2}{E_Q^2} - 1}\left[\left(\chi^\infty + \frac{1}{2}\right)\frac{E_Q^2}{E_0^2} - \chi^\infty\right]\frac{a^4}{r^4}\Theta(r) \tag{1.66}$$

$$C(r) = 6\tilde{\mu}_s \frac{a}{H}\frac{a^2}{r^2} + 3\tilde{\mu}_s \frac{a^3}{r^3}\Theta(r) + 15\left(\frac{\mu_\perp}{\mu_r} - 1\right)\left(\chi^\infty + \frac{1}{2}\right)\left(1 - \frac{E_Q^2}{E_0^2}\right)\frac{a^5}{r^5}\Theta(r) \tag{1.67}$$

Here, $\mathbf{r}$ reduces to a two-dimensional vector parallel to the surface, and $\Theta$ accounts for the screening of finite-range interactions. For sake of simplicity, we henceforth approximate the screening function by a step function: $\Theta(r) = 1$ if $r \leq H/\pi$, and $\Theta(r) = 0$ otherwise. We have also introduced a noise term in Eq. (1.63) to account for rotational diffusion. $\xi_i(t)$ is a Gaussian white noise with zero mean and unit variance $\langle \xi_i(t)\xi_j(t')\rangle = \delta(t-t')\delta_{ij}$. Remarkably, the rotational diffusivity $D_r$ is the only phenomenological coefficient of our theory.

Several comments are in order:

(i) The term $A(r)\,\hat{\mathbf{p}}_j \cdot \hat{\mathbf{p}}_i$ is an alignment interaction. It arises both from the short-distance hydrodynamic interactions and from part of the electrostatic couplings. They correspond respectively to the first and the second terms in (1.65).

(ii) In the absence of the B and C terms, our model would reduce to the so-called "flying XY model" introduced phenomenologically in [79]. Nevertheless, additional terms have been obtained from the microscopic analysis.

(iii) The coefficient $B(r)$ is positive, since $\chi^\infty + \frac{1}{2} > 0$ and $\chi^\infty < 0$ in our experimental system. It corresponds to the electrostatic repulsive coupling. The last term $C(r)$ combines electric and hydrodynamic interactions. Contrary to $A(r)$, theses additional terms in Eq. (1.64) do not yield any net alignment interaction in an isotropic population.

(iv) $A(r)$ and $B(r)$ are finite-range interactions, being screened on a distance set by the channel height. Conversely, $C(r)$ contains the unscreened dipolar hydrodynamic coupling. It is truly long-ranged since it algebraically decays like $r^{-2}$ in two dimensions. Note however, that its strength is small compared to the short-range hydrodynamic effect, since it is proportional to $a/H \ll 1$.

(v) The hydrodynamic interactions yield no dependence on $E_0$ for the effective potential $\mathscr{H}_{\text{eff}}$, as the first terms in Eqs. (1.65) and (1.67) show. Although the induced flow field is proportional to the particle velocity, the norm of the velocity vector $v_0\hat{\mathbf{p}}$ is constant. As a consequence, the resulting orientation rate does not depend on $v_0$, it is thus independent of the external electric field.

(vi) Finally we note, as we did it in the main text, that the generic relation (1.64) is not specific to the Quincke rollers. Indeed, this effective potential is expected whenever particles move at constant velocity, and experience short-range polar alignment. The slow angular variations of the two-body interactions are described by the first terms of a generic Fourier-expansion in $\theta$. Imposing global rotational invariance, the resulting effective potential can be recast into a function of $\hat{\mathbf{p}}$, leading to the generic equation (1.64). In this approach, the first term accounts for alignment in a uniform field. The repulsive term proportional to $B(r)$ corresponds to a local alignment in a monopolar field, while the last term corresponds to a local alignment in a dipolar field. We stress that no other lower-order moment is allowed, due to symmetry considerations. Within this framework, the flow induced by model swimmers referred to as pushers and pullers would be coupled via a higher order quadrupolar term reflecting the symmetry of the flow lines induced by force dipoles [47].

## 3 From microscopic interactions to macroscopic hydrodynamic equations

In the following, we link the microscopic interaction rules to the large-scale properties of the roller population. The microscopic equations of motion have to be coarse-grained, in order to derive kinetic equations for hydrodynamic fields such as the particle density and the orientation field. We sumarize here the main steps of this procedure. Using standard kinetic theory methods (see e.g. [139, 173]), the 2N coupled Langevin equations (1.62)–(1.63) can be transformed into a Fokker-Planck equation for the N-particle distribution function $\Psi^{(\mathrm{N})}(\mathbf{r}_1...,\mathbf{r}_\mathrm{N},\theta_1,...,\theta_\mathrm{N},t)$:

$$\frac{\partial\Psi^{(\mathrm{N})}}{\partial t}+\sum_i\nabla_i\cdot\left(v_0\hat{\mathbf{p}}_i\Psi^{(\mathrm{N})}\right)+\sum_i\frac{\partial}{\partial\theta_i}\left(\frac{1}{\tau}\sum_{j\neq i}\frac{\partial\mathscr{H}_{\mathrm{eff}}(\mathbf{r}_i-\mathbf{r}_j,\theta_i,\theta_j)}{\partial\theta_i}\Psi^{(\mathrm{N})}\right)-\mathrm{D}_r\sum_i\frac{\partial^2}{\partial\theta_i^2}\Psi^{(\mathrm{N})}=0 \tag{1.68}$$

By integrating over N−1 particle positions and directions, we obtain the time evolution of the one-particle density $\Psi^{(1)}(\mathbf{r},\theta,t)\equiv\frac{1}{(\mathrm{N}-1)!}\int\mathrm{d}^2\mathbf{r}_2...\mathrm{d}^2\mathbf{r}_\mathrm{N}\mathrm{d}\theta_2...\mathrm{d}\theta_\mathrm{N}\ \Psi^{(\mathrm{N})}(\mathbf{r},\mathbf{r}_2,...\mathbf{r}_\mathrm{N},\theta,\theta_2,...,\theta_\mathrm{N},t)$. It is coupled to the two-point distribution function $\Psi^{(2)}(\mathbf{r},\mathbf{r}',\theta,\theta',t)\equiv\frac{1}{(\mathrm{N}-2)!}\int\mathrm{d}^2\mathbf{r}_3...\mathrm{d}^2\mathbf{r}_\mathrm{N}\mathrm{d}\theta_3...\mathrm{d}\theta_\mathrm{N}\ \Psi^{(\mathrm{N})}(\mathbf{r},\mathbf{r}',\mathbf{r}_2,...\mathbf{r}_\mathrm{N},\theta,\theta',\theta_3,...,\theta_\mathrm{N},t)$, and obeys:

$$\partial_t\Psi^{(1)}+v_0\,\hat{\mathbf{p}}\cdot\nabla\Psi^{(1)}+\frac{1}{\tau}\partial_\theta\int d^2\mathbf{r}'\mathrm{d}\theta'\,\frac{\partial\mathscr{H}_{\mathrm{eff}}(\mathbf{r}-\mathbf{r}',\theta,\theta')}{\partial\theta}\Psi^{(2)}(\mathbf{r},\mathbf{r}',\theta,\theta',t)-\mathrm{D}_r\,\partial_\theta^2\Psi^{(1)}=0 \tag{1.69}$$

The latter expression is the first equation of an infinite hierarchy, which couples the $n$-point distribution $\Psi^{(n)}$ to the $(n+1)$-point distribution $\Psi^{(n+1)}$. To close this hierarchy of equations, we postulate a relation between $\Psi^{(2)}$ and $\Psi^{(1)}$, and introduce a generalized mean-field (i.e. Boltzmann-like) approximation. We assume that the two-body correlations cancel over a distance as small as one particle diameter. We also include steric exclusion effects between the colloids:

$$\Psi^{(2)}(\mathbf{r},\mathbf{r}',\theta,\theta',t)=\begin{cases}0 & \text{if } |\mathbf{r}-\mathbf{r}'|<2a\\ \Psi^{(1)}(\mathbf{r},\theta,t)\Psi^{(1)}(\mathbf{r}',\theta',t) & \text{if } |\mathbf{r}-\mathbf{r}'|\geq 2a\end{cases} \tag{1.70}$$

This ansatz is supported by the absence of positional correlation in the three phases (gas, bands and polar liquid). Even at the high densities, in the polar-liquid phase, the radial distribution function of the colloids is very well approximated by a Heaviside function. In addition, we note that this approximation was successfully used to describe the large scale behavior of driven confined suspensions [69]. We then derive from Eqs. (1.69) and (1.70) a closed equation for the one-particle distribution function. The hydrodynamic fields that characterize the structure of the population are defined by the angular Fourier modes of $\Psi^{(1)}$. Defining these modes as $\Psi^{(1)}(\mathbf{r},\theta,t)=\frac{1}{2\pi}\sum_{k\in\mathbb{Z}}\hat{\Psi}_k^{(1)}(\mathbf{r},t)\,\mathrm{e}^{-ik\theta}$, the three hydrodynamic field that we consider are:

Area fraction:
$$\phi(\mathbf{r},t)\equiv\pi a^2\int\mathrm{d}\theta\,\Psi^{(1)}(\mathbf{r},\theta,t)=\frac{1}{\pi a^2}\hat{\Psi}_0^{(1)} \tag{1.71}$$

Velocity polarization:
$$\Pi(\mathbf{r},t)\equiv\frac{\pi a^2}{\phi}\int\mathrm{d}\theta\,\hat{\mathbf{p}}\Psi^{(1)}(\mathbf{r},\theta,t)=\frac{1}{\hat{\Psi}_0^{(1)}}\begin{pmatrix}\mathrm{Re}\,\hat{\Psi}_1^{(1)}\\ \mathrm{Im}\,\hat{\Psi}_1^{(1)}\end{pmatrix} \tag{1.72}$$

Nematic order tensor:
$$\mathbf{Q}(\mathbf{r},t)\equiv\frac{\pi a^2}{\phi}\int\mathrm{d}\theta\left(\hat{\mathbf{p}}\hat{\mathbf{p}}-\frac{1}{2}\mathbf{I}\right)\Psi^{(1)}(\mathbf{r},\theta,t)=\frac{1}{2\hat{\Psi}_0^{(1)}}\begin{pmatrix}\mathrm{Re}\,\hat{\Psi}_2^{(1)} & \mathrm{Im}\,\hat{\Psi}_2^{(1)}\\ \mathrm{Im}\,\hat{\Psi}_2^{(1)} & -\mathrm{Re}\,\hat{\Psi}_2^{(1)}\end{pmatrix} \tag{1.73}$$

In all that follows and in the main text we do not refer anymore to the electrostatic properties of the colloids. Therefore, for sake of simplicity $\mathbf{\Pi}$ will be simply referred to as the polarization field.

By integrating Eq. (1.69) over θ, we immediately recover the particle-number conservation law:

$$\partial_t\phi+v_0\nabla\cdot(\phi\mathbf{\Pi})=0 \tag{1.74}$$

Taking the first angular moment of Eq. (1.69) similarly couples the time evolution of $\mathbf{\Pi}$ to the nematic order tensor $\mathbf{Q}$. We thereby generate a new hierarchy of equations which couples each moment of the distribution function to higher-order moments [13, 103, 223]. One more closure assumption is required, and it should be carefully defined for each phase that we want to describe as we will show it below.

## 4 Transition to collective motion

We first focus on the transition to collective motion. For weakly-polarized phases, two possible closure schemes have been used in the context of active fluids. Bertin *et al.* [25, 160] introduced a scaling ansatz for the amplitude of the angular Fourier components of the one-point function. This ansatz is expected to be relevant for nearly-isotropic states with small and slow variations of the hydrodynamic field. Baskaran and Marchetti [13] assume the distribution function to be a linear functional of its first three moments. This ansatz is obviously exact in the limit of purely isotropic states. Coming back to our model for the population of rollers, (1.62)–(1.64), we have checked that these two closure methods lead to the same kinetic equations, and are therefore strictly equivalent. We also assume that $\mathbf{Q}$ is a fast-relaxing variable, following again [25] and [103] in a fluid mechanics context. Within this approximation scheme, after lengthy algebra, and at leading order in $a/\mathrm{H} \ll 1$, we obtain the following equation for the evolution of the orientation field:

$$\tau\partial_t(\phi\mathbf{\Pi}) + \frac{3v_0\alpha}{8D_r}(\phi\mathbf{\Pi}\cdot\nabla)\,\phi\mathbf{\Pi} = \left[\alpha\phi - \tau D_r - \frac{\alpha^2}{2\tau D_r}(\phi^2\Pi^2)\right]\phi\mathbf{\Pi} + \kappa\phi\,\mathbf{M}*\phi\mathbf{\Pi} - \frac{1}{2}\left(\tau v_0 + a\beta\phi\right)\nabla\phi \tag{1.75}$$
$$- \frac{5v_0\alpha}{8D_r}(\nabla\cdot\phi\mathbf{\Pi})\,\phi\mathbf{\Pi} + \frac{5v_0\alpha}{16D_r}\nabla(\phi^2\Pi^2) + \frac{\alpha\beta}{2\tau D_r}a(\nabla\phi\cdot\phi\mathbf{\Pi})\,\phi\mathbf{\Pi} + \mathcal{O}(\nabla^2)$$

where

$$\alpha \equiv \int_{r\geq 2a} \mathrm{d}r\ \mathrm{A}(r)\frac{r}{a^2} = \frac{3}{2}\tilde{\mu}_s + \frac{3}{8}\left(\frac{\mu_\perp}{\mu_r} - 1\right)\left(\chi^\infty + \frac{1}{2}\right)\left(1 - \frac{E_Q^2}{E_0^2}\right) \tag{1.76}$$

$$\beta \equiv \int_{r\geq 2a} \mathrm{d}r\ \mathrm{B}(r)\frac{r^2}{a^3} = 3\left(\frac{\mu_\perp}{\mu_r} - 1\right)\sqrt{\frac{E_0^2}{E_Q^2} - 1}\left[\left(\chi^\infty + \frac{1}{2}\right)\frac{E_Q^2}{E_0^2} - \chi^\infty\right] \tag{1.77}$$

$$\kappa \equiv 3\tilde{\mu}_s\frac{a}{\mathrm{H}} \ll \alpha \tag{1.78}$$

$$\mathbf{M}*\phi\mathbf{\Pi}(\mathbf{r},t) \equiv \frac{1}{\pi}\int_{|\mathbf{r}-\mathbf{r}'|\geq 2a} \mathrm{d}^2\mathbf{r}'\ \frac{1}{|\mathbf{r}-\mathbf{r}'|^2}\left(2\frac{(\mathbf{r}-\mathbf{r}')(\mathbf{r}-\mathbf{r}')}{|\mathbf{r}-\mathbf{r}'|^2} - \mathbf{I}\right)\cdot\phi(\mathbf{r}',t)\mathbf{\Pi}(\mathbf{r}',t) \tag{1.79}$$

We stress that all the coefficients involved in the above non-local equation have been inferred from a well controlled microscopic model introduced in the first section of this document. We only briefly recall their physical origin:

- $\alpha > 0$ accounts for the alignment interactions, which favor the emergence of polar order. It is chiefly set by the local hydrodynamic interactions between the rollers (first term on the r.h.s of Eq. 1.76). It yields the same generic terms as those found in [25] or [79] (when the particle velocity is constant), which are known to lead to large-scale coherent motion.
- $\beta > 0$ stems from the repulsive electrostatic couplings.
- $\kappa$ gives the strength of the long-range dipolar hydrodynamic interactions, which result in a non-local operator $\mathbf{M}$. We studied the impact of these truly long-range interactions in [37, 69].

### 4.1 Homogeneous states: A Curie-Weiss description of collective motion

Looking for homogeneous phases, i.e. dropping space derivatives, Eq. (1.74) reduces to $\phi(\mathbf{r},t)=\phi_0$, and Eq. (1.75) takes the simple form:

$$\tau\partial_t\mathbf{\Pi}=\left(\alpha\phi_0-\tau D_r\right)\mathbf{\Pi}-\frac{\alpha^2}{2\tau D_r}(\phi_0^2\Pi^2)\mathbf{\Pi} \tag{1.80}$$

Hence, it readily follows from the cubic form of the r.h.s that the system undergoes a mean-field phase transition to a polar state as $\phi_0$ exceeds the critical area fraction:

$$\phi_c=\frac{\tau D_r}{\alpha} \tag{1.81}$$

At small density $\phi_0\leq\phi_c$, the only stationary state is an isotropic phase with zero mean orientation: $\Pi_0=0$. The disordered solution becomes unstable above $\phi_c$, and the system forms a polar ordered phase with $\Pi_0\neq 0$. At the onset of collective motion, the following bifurcation is expected, see also Fig. 1.25B:

$$\Pi_0(\phi_0)=\begin{cases}\sqrt{2\frac{\phi_c}{\phi_0}\left(1-\frac{\phi_c}{\phi_0}\right)} & \text{if } \phi_0>\phi_c\\ 0 & \text{if } \phi_0\leq\phi_c\end{cases} \tag{1.82}$$

Starting from a realistic and accurate microscopic description of the Quincke mechanism at the single-roller level, we have established the existence of a genuine phase transition to collective motion in populations of such active colloids. This is one of our main theoretical results.

To further stress on the importance of the hydrodynamic interactions in this collective phenomena, we plot the variations of $\phi_c$ as a function of $E_0$ in Fig. 1.25A. Using microscopic parameters corresponding to our experimental setup, we indeed observe that the transition line weakly depends on the magnitude of external field. As we discussed above, the hydrodynamic polar interactions result in an orientation rate which does not depend on the particle velocity, and thus does not yield any dependence on $E_0$ for $\phi_c$. The qualitative agreement with the experimental

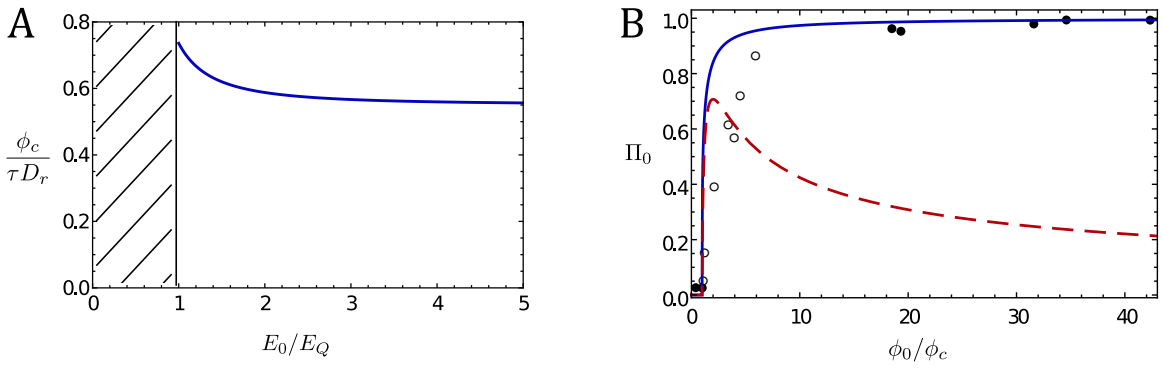


**Figure 1.25** – Homogeneous steady states. **A**– Transition line in the plane of density and external applied electric field. The variations of the critical area fraction (rescaled by $\tau D_r$) are plotted as a function of $E_0/E_Q$. (The distance between the particle and the surface was set to $0.01a$, mobility coefficients were deduced from [89, 90, 130, 148] and dielectric constants were taken from [153]). **B**– t The symbols denote the experimental values of the average polarization. The data show a transition to collective motion at a critical area fraction, as expected from both theoretical curves. They also unveil the formation of polar-liquid phases (filled symbols) at high area fractions, in agreement with Eq. (1.86). However, for intermediate densities (open symbols), the experimental data correspond to phase-separated states consisting in bands propagative in a gaseous apolar phase. The band state is obviously not accounted for by the theoretical expressions (1.82) and (1.86), which hold for spatially homogeneous systems only. As a consequence, the theoretical curves are quantitatively relevant for isotropic phases and polar-liquid phases only. However we stress that the two asymptotic models correctly predict a phase transition to a macroscopically polar state.

data, which showed no dependence of $\phi_c$ on $E_0$, strengthens the relevance of our theory, further confirms the central role of the hydrodynamic interactions in the transition to collective motion.

## 4.2 Linear stability analysis

We now investigate the stability of the isotropic and of the polar homogeneous phases against spatial fluctuations. We consider plane-wave perturbations: $\phi(\mathbf{r},t) = \phi_0 + \delta\hat{\phi}\, e^{i(\mathbf{q}\cdot\mathbf{r}-\omega t)}$ and $\mathbf{\Pi}(\mathbf{r},t) = \Pi_0\hat{\mathbf{x}} + \delta\hat{\Pi}\, e^{i(\mathbf{q}\cdot\mathbf{r}-\omega t)}$. In the following, we define the wave-vector direction as $\mathbf{q} \equiv q\cos\varphi_{\mathbf{q}}\hat{\mathbf{x}} + q\sin\varphi_{\mathbf{q}}\hat{\mathbf{y}}$.

***Weakly-polarized phases*** We linearize Eqs. (1.74) and (1.75) around a uniform polar state with density $\phi_0 > \phi_c$ and orientation $\Pi_0 = \sqrt{2\frac{\phi_c}{\phi_0}\left(1-\frac{\phi_c}{\phi_0}\right)}$. The eigenvalues $\omega(\mathbf{q})$ cancel a cubic equation which is solved numerically. We found that the growth rates $\mathrm{Im}(\omega)$ are invariant upon the transformations $\varphi_{\mathbf{q}} \to -\varphi_{\mathbf{q}}$ and $\varphi_{\mathbf{q}} \to \varphi_{\mathbf{q}} + \pi$. Without loss of generality, we focus on $\varphi_{\mathbf{q}} \in \left[0, \frac{\pi}{2}\right]$. The growth rates are plotted in Fig. 1.26A as a function of the wave vector direction $\varphi_{\mathbf{q}}$. The uniform polar states are unstable for all wave-vector directions: no homogeneous polar phase exists at the onset of collective motion. This result is consistent with all the available models that were used so far to account for the emergence of collective dynamics in active polar matter [136]. The compression modes are eigenmodes of the linear stability problems. They are exponentially amplified in the polar phase. This mode of destabilization is consistent with the formation of propagative bands in our experiments for $\phi_0$ close but above $\phi_c$.

***Isotropic phases*** A similar stability analysis is carried out around a uniform and isotropic state $\Pi_0 = 0$. Two modes couple the density fluctuations and the orientational perturbations in the longitudinal direction. The corresponding eigenvalues are $\omega_\pm = i\frac{\alpha}{2\tau}(\phi_0-\phi_c)\left[1 \pm \sqrt{1-\frac{2\tau v_0(\tau v_0+\beta a\phi_0)}{\alpha^2(\phi_0-\phi_c)^2}q^2}\right]$. We also find a pure transverse orientational mode, with the pulsation $\omega_\perp = i\frac{\alpha}{\tau}(\phi_0-\phi_c)$. We find that the isotropic state is linearly stable below the critical density $\phi_c$. However, it is unstable against both orientation and compression fluctuations when $\phi_0 > \phi_c$. Again, the fact that compression modes are unstable is consistent with the formation of bands from isotropic phases, which is observed experimentally when $\phi_0 > \phi_c$.

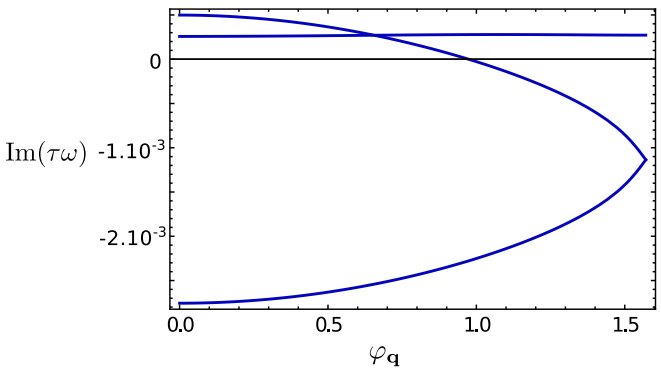


**Figure 1.26** – Stability of weakly-polar states against linear fluctuations. The growth rates of the three eigenmodes modes are plotted as a function of the wave-vector direction $\varphi_{\mathbf{q}}$, for $E_0 = 2E_Q$, $\phi_0 = 1.1\phi_c$ and $qa = \frac{1}{500}$. The values of the other parameters are the same as in Fig. 1.25A. Instabilities were observed for all values of $E_0$, $\phi_0$, and $qa$.

### 4.3 Constitutive density-polarization relation in band phases

At the onset of collective motion, homogeneous states are linearly unstable. The experiments show that large density excitations (bands) steadily propagate in the system. It is difficult to derive analytically the shape of band-density profiles. However, the particle-number conservation provides a relation between the local density and the local polarization field when density excitations propagate steadily. Looking for propagative solutions of the form $\phi = \phi(x - c_{\rm band}\, t)$, $\Pi = \Pi(x - c_{\rm band}\, t)\hat{\mathbf{x}}$ and integrating Eq. (1.74) over the transverse direction leads to the relation

$$\Pi(s) = \frac{c_{\rm band}}{v_0}\left(1 - \frac{\phi_\infty}{\phi(s)}\right) \tag{1.83}$$

where the integration constant $\phi_\infty$ is the area fraction far away from the band. Note that this expression does not depend on any closure scheme at the hydrodynamic level. The latter relation was used to fit the data, Fig. 1.18d in the main text. The agreement with our theoretical prediction is a direct proof that the bands are stationary structures as it was also demonstrated in [25] for the numerical Vicsek model. Band states are genuine phases of colloidal active matter.

## 5 Polar liquid phase

The closure scheme we followed above (a scaling ansatz for the magnitude of the Fourier modes of $\Psi$) was widely implemented in the previous studies on active matter. We stress that this scheme is not relevant any more for strongly polarized phases. In particular, it results in an unexpected decay of the mean orientation $\Pi_0$ with the density, as shown in Fig. 1.25B (dashed line). This approximation does not support the observation of stable homogeneous polar liquids, in strong contrast with our experimental findings. This may not be surprising, since the link it provides between $\mathbf{Q}$, $\phi$, and $\mathbf{\Pi}$ was devised for weakly-organized phases, an approximation which obviously breaks down in the polar-liquid phase.

In order to investigate the properties of the polar liquids, we introduce a new closure approximation. When the angular probability distribution $\Psi(\mathbf{r}, \theta, t)$ is peaked, the high-order cumulants of the generating function can be neglected. Then a simple assumption, which becomes exact in the limit of perfectly polar order, is to approximate the angular distribution by the wrapped normal distribution, the mean and the variance of which is determined in a self-consistent fashion. The "Gaussian" ansatz imposes the following relation between the angular Fourier components $\hat{\Psi}_k$ of the distribution function: $\hat{\Psi}_2 = |\hat{\Psi}_1|^2\hat{\Psi}_1\hat{\Psi}_1/\hat{\Psi}_0^3$. Equivalently, it can also be written as $\mathbf{Q} = \Pi^2\,\mathbf{\Pi}\,\mathbf{\Pi} - \frac{1}{2}\Pi^4\,\mathbf{I}$, where we have dropped the implicit dependence in $\mathbf{r}, t$. With this new closure relation, neglecting higher-order terms in $\frac{a}{\mathrm{H}}$, the dynamics of the orientation field is obtained from Eqs. (1.69)–(1.70). Again after some lengthy algebra we obtain:

$$\begin{aligned}
\tau\partial_t\,\mathbf{\Pi} + \tau v_0\Pi^2(\mathbf{\Pi}\cdot\nabla)\mathbf{\Pi} = {} & \left[\alpha(1-\Pi^4)\phi - \tau D_r\right]\mathbf{\Pi} + \kappa\left[(1+\Pi^4)\mathbf{I} - 2\Pi^2\,\mathbf{\Pi}\,\mathbf{\Pi}\right]\cdot\mathbf{M} * \phi\mathbf{\Pi} \\
& - \frac{\tau v_0}{2\phi}(1-\Pi^4)\nabla\phi + \frac{\tau v_0}{\phi}(1-\Pi^2)(\mathbf{\Pi}\cdot\nabla\phi)\mathbf{\Pi} + \tau v_0(1-\Pi^2)(\nabla\cdot\mathbf{\Pi})\mathbf{\Pi} \\
& + \tau v_0(\Pi^2\mathbf{I} - \mathbf{\Pi}\,\mathbf{\Pi})\cdot\nabla(\Pi^2) - \frac{1}{2}\beta a\left[(1+\Pi^4)\mathbf{I} - 2\Pi^2\,\mathbf{\Pi}\,\mathbf{\Pi}\right]\cdot\nabla\phi \\
& + \frac{1}{2}\gamma a^2\left[(1+\Pi^4)\mathbf{I} - 2\Pi^2\,\mathbf{\Pi}\,\mathbf{\Pi}\right]\cdot\nabla^2(2\mathbf{I} - \mathbf{M})\cdot\phi\mathbf{\Pi} + \mathscr{O}(\nabla^3)
\end{aligned} \tag{1.84}$$

where

$$\gamma \equiv \tilde{\mu}_s\frac{3\mathrm{H}}{4\pi a} \tag{1.85}$$

### 5.1 Transition to collective motion: Curie-Weiss description

Even though we built this novel closure scheme to address the properties of the polar liquid, it is worth noting that Eq. (1.84) also accounts for the transition to collective motion. Looking again at homogeneous phases, the relation between the average polarization $\Pi_0$ and the average area fraction $\phi_0$ follows from Eq. (1.84):

$$\Pi_0(\phi_0) = \left(1 - \frac{\phi_c}{\phi_0}\right)^{1/4} \tag{1.86}$$

These variations are plotted in Fig. 1.25B (full line). As expected, $\Pi_0$ plateaus to 1 in the limit of highly concentrated suspensions. More surprisingly, even though the closure scheme is *a priori* valid only for ordered phases, the above relation predicts a transition to collective motion at the same critical value $\phi_c$ as the one found in Eq. (1.80). Therefore, we can reasonably expect Eq. (1.84) to be accurate over a wide range of area fractions. However, the $1/4$ scaling at the onset of collective motion is not expected to be valid. Firstly, the usual closure relation, that we used in the previous section, to account for weakly polarized states is not compatible with the Gaussian fluctuation hypothesis. In addition, and more importantly, we know from the experiments that this scaling inferred from a Curie-Weiss approximation cannot be probed as the system phase separates so that extended ordered bands cruise through an isotropic gaseous phase. This phase separation is reflected by a mere qualitative agreement between the theory and the measure of the polarization curve shown in Fig. 1.25B.

### 5.2 Linear stability analysis

Following the same approach as in section IV 4.2, we now investigate the linear stability of homogeneous polar phases, with respect to spatial fluctuations, for densities $\phi_0 \gg \phi_c$. The mean polarization $\Pi_0$ is given by Eq. (1.86). We consider plane-wave perturbations of the form $\phi(\mathbf{r},t) = \phi_0 + \delta\hat{\phi}\, e^{i(\mathbf{q}\cdot\mathbf{r}-\omega t)}$ and $\mathbf{\Pi}(\mathbf{r},t) = \Pi_0\hat{\mathbf{x}} + \delta\hat{\Pi}\, e^{i(\mathbf{q}\cdot\mathbf{r}-\omega t)}$. The wave-vector direction is defined as $\mathbf{q} \equiv q\cos\varphi_{\mathbf{q}}\,\hat{\mathbf{x}} + q\sin\varphi_{\mathbf{q}}\,\hat{\mathbf{y}}$. Performing a conventional linear stability analysis of Eqs. (1.74) and (1.84), and restraining ourselves to terms at zeroth order in $\frac{\phi_0}{\phi_c}$, we find that the dispersions take the form $\omega_\pm(\mathbf{q}) \equiv \omega'_\pm(\mathbf{q}) + i\,\omega''(\mathbf{q})$. Their explicit expressions are:

$$\tau\omega'_\pm = \tau v_0 q\cos\varphi_{\mathbf{q}} \pm \sqrt{\sqrt{F_1^2+F_2^2}+F_1} \tag{1.87}$$

$$\tau\omega''_\pm = F_0 \pm \sqrt{\sqrt{F_1^2+F_2^2}-F_1} \tag{1.88}$$

where $F_0 = \kappa\phi_0\cos(2\varphi_{\mathbf{q}}) - \frac{\Upsilon}{2}a^2\phi_0\left(2-\cos(2\varphi_{\mathbf{q}})\right)q^2$, $F_1 = \frac{\beta}{2}a\tau v_0\phi_0 q^2\sin^2\varphi_{\mathbf{q}} - \frac{1}{2}F_0^2$ and $F_2 = -2\tau v_0\phi_0 q\left[\kappa + \frac{\Upsilon}{2}a^2q^2\right]\sin^2\varphi_{\mathbf{q}}\cos\varphi_{\mathbf{q}}$. We note again that the above eigenvalues are invariant upon the transformations $\varphi_{\mathbf{q}} \to -\varphi_{\mathbf{q}}$ and $\varphi_{\mathbf{q}} \to \varphi_{\mathbf{q}} + \pi$. Without loss of generality, we focus on $\varphi_{\mathbf{q}} \in \left[0, \frac{\pi}{2}\right]$. The growth rates are plotted in Fig. 1.27A. Depending on the direction $\varphi_{\mathbf{q}}$, we find positive or negative growth rates, leading to unstable or stable eigenmodes, respectively.

- *Splay modes* To further clarify the stabilization/destabilization mechanisms, we expand Eqs. (1.87) and (1.88) in the small wave-vector limit. For $\varphi_{\mathbf{q}} > \pi/4$, the eigenvalues follow simple scaling laws: $\tau\omega'_\pm = \mathcal{O}(qa)$, $\tau\omega''_+ = \mathcal{O}(q^2a^2)$ and $\tau\omega''_- = 2\kappa\phi_0\cos(2\varphi_{\mathbf{q}}) + \mathcal{O}(q^2a^2)$. Importantly, we find that the fastest rate $\tau\omega''_-$ scales as $\tau\omega''_- = -2\kappa\phi_0 + \mathcal{O}((qa)^2)$. It corresponds to a pure splay mode ($\varphi_{\mathbf{q}} = \pi/2$). Since $\omega''_-$ is proportional to $\kappa$ and negative, splay fluctuations are stabilized by the long-range hydrodynamic interactions. We also emphasize that at leading order in $qa$ the relaxation rate $|\omega''_-|$ does not depend on the wave-vector, i.e. the stabilization of the corresponding splay mode is generic, for the very same reason as the one we discussed in [37]. This important observation plays a central role in the suppression of giant density fluctuations, as we discuss it in the next section.

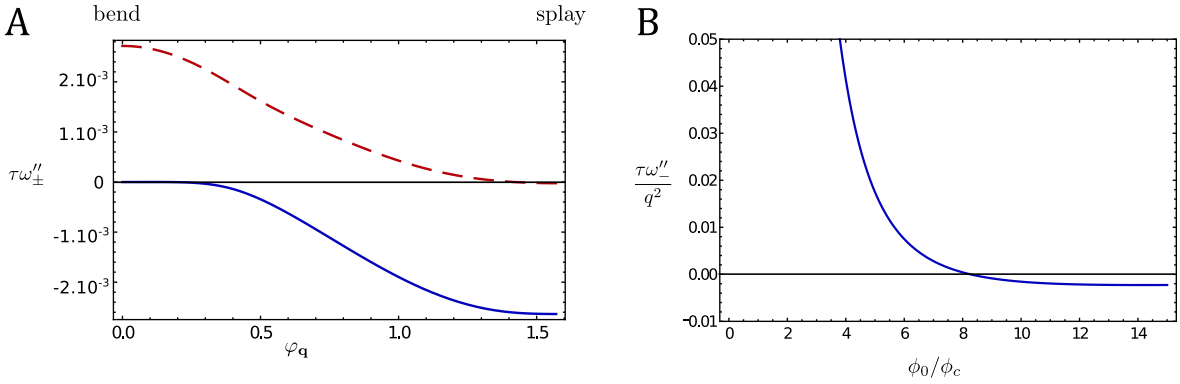


**Figure 1.27** – Stability of strongly polarized states. **A–** The growth rates $\omega''_{\pm}$ are plotted as a function of the wave-vector direction $\varphi_{\mathbf{q}}$ Blue line: $\tau\omega''_{-}$, red dashed line: $\tau\omega''_{+}$ ($\phi_0 = 10\phi_c$, $qa = \frac{1}{500}$, $E_0 = 2E_Q$, the values of the other parameters are the same as in Fig. 1.25A). **B–** Magnitude of the pure compression mode $\varphi_{\mathbf{q}} = 0$ plotted versus the average area fraction of rollers. The repulsive electrostatic interactions result in a restabilization of the compression waves at high area fractions.

- *Bending modes* For $\varphi_{\mathbf{q}} < \pi/4$, a similar small-$q$ expansion yields $\tau\omega'_{\pm} = \mathcal{O}(qa)$, $\tau\omega''_{+} = 2\kappa\phi_0\cos(2\varphi_{\mathbf{q}}) + \mathcal{O}(q^2a^2)$ and $\tau\omega''_{-} = \mathcal{O}(q^2a^2)$. Fluctuations having the form of bend modes ($\varphi_{\mathbf{q}} = 0$) are exponentially amplified. However, as obviously expected transverse confinement eliminates this instability. More details about confinement-induced stabilization will be provided in a forthcoming detailed paper.

- *Compression mode* At leading order in $\left(\frac{\phi_0}{\phi_c}\right)$, the pure-compression mode corresponding to $\varphi_{\mathbf{q}} = 0$, and $\delta\Pi_x \neq 0$ is marginally stable, i.e. compression fluctuations are merely advected at a velocity $v_0$. Investigating their linear stability requires to expand the equations of motion up to order $\left(\frac{\phi_0}{\phi_c}\right)^2$. This yields the following growth rate:

$$\tau\omega''_{-} = \frac{3(\tau v_0)^2}{64\alpha\phi_0}\left(\frac{\phi_c}{\phi_0}\right)^2 q^2 - \frac{\beta}{8\alpha}a\tau v_0\frac{\phi_c}{\phi_0}\left[1+\frac{\phi_c}{\phi_0}\right]q^2 + o(q^2a^2) \tag{1.89}$$

  It is plotted as a function of $\phi_0$ in Fig. 1.27B. The compression mode is unstable below a critical area fraction, and becomes stable at higher densities. To gain more physical insight into this bifurcation mechanism, we propose the following qualitative explanation. Below a critical area fraction ($\sim 10\,\phi_c$ within our experimental conditions) the first term of the above expression leads to a positive growth rate. It originates from the alignment interactions, which destabilize the compression fluctuations. When the density locally increases, alignment is enhanced and the local polar order increases accordingly: $\delta\Pi_x > 0$. As a consequence, concentrated regions move coherently as a "rigid body" through a less concentrated background. As a result this "coherent pack "captures even more particles due to the alignment interactions with the particles that collide it. The initial density fluctuations are thus amplified. This is consistent with the weakly polarized state being unstable near the transition to collective motion, as we found in section 4. However, the electrostatic repulsion, proportional to $\beta$, impedes the formation of concentrated regions. It results in a second term which stabilizes polar liquid phases above a critical density, see Fig. 1.27B. Again this prediction is in good agreement with our experimental observations. We find that the band phase evolves into an homogeneous polar-liquid state as the roller density is sufficiently increased, see Fig. 1.17e in the main text.

To close this section, it is worth noting that hydrodynamics was shown to destroy polar ordering in several models of active suspensions [136, 183, 184]. These papers focus on 3D suspensions of microswimers. The flow disturbance induced by the swimmer on the surrounding fluid is modeled as a force dipole singularity (in the far field). Moreover, the swimmers reorient along the

principal direction of the local elongation of the flow, and rotate due to the local vorticity (Jeffery's orbits). The resulting equations of motion for the density and the polarization fields are linearly unstable around a homogeneous polar state. The hydrodynamic dipoles result in a generic suppression of polar ordering (the growth rate of the instability does not depend on the wavelength at long-enougth wavelengths) [183, 184]. However, in our system the propulsion mechanism, the rolling of the colloids, strongly involve the lower surface. As they roll, the colloids induce far-field perturbations that have the symmetry of a mirrored rotlet. The magnitude of this singular perturbation to the flow can have a non-zero value because momentum is continuously exchanged between the fluid and the confining walls. In addition, the coupling to the local flow field also differs from the one considered for unbounded suspensions. As shown in the previous sections, the rollers align with the local flow on the bottom-surface. Both the symmetry of the far-field flow, and the local coupling to the fluid flow result in an alignment interaction between the colloidal rollers. The emergence of polar order from an isotropic population is a direct consequence of this microscopic polar interaction. Therefore the qualitative consequences of hydrodynamic interactions on the large-scale behavior of active fluids strongly depend on the microscopic mechanism responsible for self-propulsion.

### 5.3 Density fluctuations

We now turn to the question of density-density correlations in the polar liquid phase. Most of all the previous theoretical studies on polar active matter have reported the emergence of "giant density fluctuations" in polar liquids. Giant density fluctuations were believed to be a robust and generic feature of active polar liquids [136, 212]. Although our model includes classical alignment interactions, it also contains additional repulsive and dipolar couplings: among them, the long-range hydrodynamic interactions destroy the giant density fluctuations, as we show below.

To account for the density fluctuations, we employ a fluctuating-hydrodynamic description. We add a conserved white noise term $\nabla\cdot\boldsymbol{\xi}_\phi$ to Eq. (1.74) and a non-conserved Gaussian noise $\xi_\Pi\hat{\mathbf{y}}$ to Eq. (1.84), with zero mean and correlations $\langle\xi_{\phi_m}(\mathbf{r},t)\xi_{\phi_n}(\mathbf{r}',t')\rangle \equiv 2D_\phi\,\delta_{m,n}\delta(\mathbf{r}-\mathbf{r}')\delta(t-t')$, $\langle\xi_\Pi(\mathbf{r},t)\xi_\Pi(\mathbf{r}',t')\rangle \equiv 2D_\Pi\,\delta(\mathbf{r}-\mathbf{r}')\delta(t-t')$, $\langle\xi_{\phi_m}(\mathbf{r},t)\xi_\Pi(\mathbf{r}',t')\rangle \equiv 0$. The correlation function $\langle|\delta\phi_{\mathbf{q},\omega}|^2\rangle$ is calculated in Fourier space within a linear response approximation. The static structure factor for rollers enclosed in a region of area $\mathscr{A}$ is defined as:

$$S(\mathbf{q}) \equiv \frac{1}{\pi a^2\phi_0\mathscr{A}}\int_{-\infty}^{+\infty}\frac{d\omega}{2\pi}\langle|\delta\phi_{\mathbf{q},\omega}|^2\rangle \tag{1.90}$$

Computing the field amplitude that linearly responds to the noise sources, and averaging over the noise realizations we obtain a rather complex expression for the static structure factor of the polar liquid:

$$S(\mathbf{q}) = \frac{16\pi^2\tau}{a^2\phi_0\mathscr{A}}\left[\left(v_0^2\phi_0^2\sin^2\varphi_{\mathbf{q}}D_\Pi + 4\kappa^2\phi_0^2\cos^2(2\varphi_{\mathbf{q}})D_\phi\right)q^2I_1(\mathbf{q}) + D_\phi q^2 I_2(\mathbf{q})\right] \tag{1.91}$$

where

$$I_1(\mathbf{q}) = \frac{|\omega_+''| + |\omega_-''|}{2\tau^3|\omega_+''\omega_-''|\left[(\omega_+' - \omega_-')^2 + (|\omega_+''| + |\omega_-''|)^2\right]} \tag{1.92}$$

$$I_2(\mathbf{q}) = \frac{|\omega_+''|\omega_-'^2 + |\omega_-''|\omega_+'^2 + |\omega_+''\omega_-''|(|\omega_+''| + |\omega_-''|)}{2\tau|\omega_+''\omega_-''|\left[(\omega_+' - \omega_-')^2 + (|\omega_+''| + |\omega_-''|)^2\right]} \tag{1.93}$$

where $\omega_\pm'$ and $\omega_\pm''$ are given by Eqs. (1.87) and (1.88). In the small $q$ limit, at leading order we readily find that the structure factor behaves as $S(q) = \mathscr{O}((qa)^0)$. The density fluctuations saturate as $q\to 0$. In this limit, the structure factor quantifies the large-scale density fluctuations: $S(q\to 0) = \frac{(\Delta N)^2}{\langle N\rangle}$, where $\langle N\rangle$ is the mean particle number and $(\Delta N)^2$ is the variance of the particle number

N. It then follows from the saturation of S that the density fluctuations are normal

$$\frac{\Delta N}{\langle N\rangle} \sim \frac{1}{\sqrt{\langle N\rangle}} \tag{1.94}$$

In a suspension of Quincke rolling particles, the large-scale number fluctuations follow the same scaling law as in equilibrium systems. Contrary to most of active systems, there are *no* giant density fluctuations. This unusual behavior stems from the generic stabilization of splay disturbances $\omega_-''(q) = \mathcal{O}(1)$ by the long-range dipolar hydrodynamic interactions, which decay like $r^{-2}$ in two dimensions [37].

Importantly, the previous asymptotic expansions are valid in the limit of small wave vectors $qH \ll 1$ (we recall that H is the channel height). The long-range dipolar interactions, that govern the density fluctuations at large scales, are subdominant at distances smaller than H (see section 2). As a consequence, deviations from the above prediction are expected below a crossover length of order H. In the case of splay fluctuations, i.e. $\varphi_{\mathbf{q}} = \pi/2$, the small-$q$ expansion yields a simple analytic expression for the structure factor at all $q$s:

$$S(q\hat{\mathbf{y}}) = S_0\left(1+\zeta q^2\right) + \mathcal{O}(q^3 a^3) \tag{1.95}$$

where $S_0 = \frac{8\pi^2 v_0}{\mathscr{A}\beta a^3}\left(D_\Pi + \frac{4\kappa^2}{v_0^2}D_\phi\right)$ and $\zeta = \frac{\beta a \tau v_0}{4\kappa^2\phi_0^2}\left(\phi_0 + \frac{2\kappa D_\phi}{4\kappa^2 D_\phi + v_0^2 D_\Pi}\right) - \frac{3\gamma}{2\kappa}a^2$. The structure factor therefore deviates from its large-scale behavior when $q \gtrsim |\zeta|^{-1/2}$. From the expressions of the coefficients $\beta$, $\kappa$, $\gamma$ that we deduced from the microscopic model of the roller propulsion and interaction mechanisms, Eqs. (1.77), (1.78) and (1.85), we indeed find that $S(\mathbf{q})$ deviates from a constant value and decays algebraically as $q$ exceeds $H^{-1}$.

A direct comparison with the experimental data is difficult to obtain in stadium-shape potentials due to the small size of our ITO coated slides which prevent the exploration of very small $q$ modes. However, we were able to quantify the particle-number fluctuations in real space. The data unambiguously show that the number fluctuations are normal $\Delta N \sim \sqrt{\langle N\rangle}$, as expected from Eq. (1.94).

As a final remark we stress that the hydrodynamic interactions between the rollers play a curtail role in determining the large-scale behavior of the populations of active colloids. They provide the very mechanism that allows the rollers to sense the orientation of their neighbors and to promote local alignment of their velocities. This microscopic alignment interaction was shown to yield very large-scale orientational order. Furthermore the hydrodynamic couplings also stabilize the density fluctuations of these unique active polar liquids by suppressing the splay fluctuations of the local polarization field that are generically responsible for the usual giant density fluctuations of active matter [189].

# Article: *Emergent vortices in populations of colloidal rollers*

A. Bricard, J.-B. Caussin, D. Das, C. Savoie, V. Chikkadi, K. Shitara, O. Chepizhko, F. Peruani, D. Saintillan and D. Bartolo, *submitted to Nat. Comm.* (2015)

Coherent vortical motion has been reported in a wide variety of populations including living organisms (bacteria, fishes, human crowds) and synthetic active matter (shaken grains, mixtures of biopolymers), yet a unified description of the formation and structure of this pattern remains lacking. In this article we report the self-organization of motile colloids into a macroscopic steadily rotating vortex. Combining physical experiments and numerical simulations, we elucidate this collective behavior. We demonstrate that the emergent-vortex structure lives on the verge of a phase separation, and single out the very ingredient responsible for this state of polar active matter. Building on this observation, we establish a continuum theory and lay out a strong foundation for the description of vortical collective motion in a broad class of motile populations constrained by geometrical boundaries.

Building upon the pioneering work of Vicsek et al. [215], physicists, mathematicians and biologists have contemplated the self-organization of living-organism groups into flocks as an emergent process stemming from simple interaction rules at the individual level [136, 212, 216]. This idea has been supported by quantitative trajectory analysis in animal groups [20, 44, 82], together with a vast number of numerical and theoretical models [136, 216], and more recently by the observations of flocking behavior in ensembles of non-living motile particles such as shaken grains, active colloids, and mixtures of biofilaments and molecular motors [36, 67, 122, 190]. From a physicist's perspective, these various systems are considered as different instances of polar active matter, which encompasses any ensemble of motile bodies endowed with local velocity-alignment interactions. The current paradigm for flocking physics is the following. Active particles are persistent random walkers, which when dilute form a homogeneous isotropic gas. Upon increasing density, collective motion emerges in the form of spatially localized swarms that may cruise in a sea of randomly moving particles; further increasing density, a homogeneous polar liquid forms and spontaneously flows along a well-defined direction [92, 211, 215]. This picture is the outcome of experiments, simulations and theories mostly performed in unbounded or periodic domains.

Beyond this picture, significant attention has been devoted over the last five years to confined active matter [60, 67, 84, 94, 115, 120, 122, 133, 145, 193, 216, 217, 222, 225]. Confined active particles have consistently, yet not systematically, been reported to self-organize into vortex-like structures. However, unlike for our understanding of flocking, we are still lacking a unified picture to account for the emergence and structure of such vortex patterns. This situation is mostly due to the extreme diversity in the nature and symmetries of the interactions between the active particles that have been hitherto considered. Do active vortices exist only in finite-size systems as in the case of bacterial suspensions [222], which lose this beautiful order and display intermittent turbulent dynamics [220] when unconfined? What are the necessary interactions required to observe and/or engineer bona fide stationary swirling states of active matter?

In this paper, we answer these questions by considering the impact of geometrical boundaries on the collective behavior of motile particles endowed with velocity-alignment interactions. Combining quantitative experiments on motile colloids, numerical simulations and analytical theory, we elucidate the phase behavior of *polar* active matter restrained by geometrical boundaries. We use colloidal rollers which, unlike most of the available biological self-propelled bodies, interact via well established dynamical interactions [36]. We first exploit this unique model system to show that above a critical concentration populations of motile colloids undergo a non-equilibrium phase transition from an isotropic gaseous state to a novel ordered state where the entire population self-organizes into a single heterogeneous steadily rotating vortex. This self-organization is *not* the consequence of the finite system size. Rather, this emergent vortex is a genuine state of polar active matter lying on the verge of a macroscopic phase separation. This novel state is the only ordered phase found when unidirectional directed motion is hindered by convex isotropic boundaries. We then demonstrate theoretically that a competition between alignment, repulsive interactions and confinement is necessary to yield large-scale vortical motion in ensembles of motile particles interacting via alignment interactions, thereby extending the relevance of our findings to a broad class of active materials.

## 1 Experiments

The experimental setup is fully described in the *Materials and Methods* section and in Figs. 1.28a and 1.28b. Briefly, we use colloidal rollers powered by the Quincke1896 electrorotation mechanism as thoroughly explained in [36]. An electric field $\mathbf{E_0}$ is applied to insulating colloidal beads immersed in a conducting fluid. Above a critical field amplitude $E_Q$, the symmetry of the electric charge distribution at the bead surface is spontaneously broken. As a result, a net electric torque acts on the beads causing them to rotate at a constant rate around a random axis transverse to the electric field [138, 153, 165]. When the colloids sediment, or are electrophoretically driven, onto one of the two electrodes, rotation is converted into a net rolling motion along a random direction. Here, we use PMMA spheres of radius $a = 2.4\,\mu$m immersed in a hexadecane solution.

As sketched in Fig. 1.28a, the colloids are handled and observed in a microfluidic device made of double-sided scotch tape and of two ITO-coated glass slides. The ITO layers are used to apply a uniform DC field $\mathbf{E}_0 = E_0\hat{\mathbf{z}}$ in the $z$-direction, with $E_0 = 1.6\,\mathrm{V}/\mu\mathrm{m}$ ($E_0 = 1.1E_Q$). Importantly, the

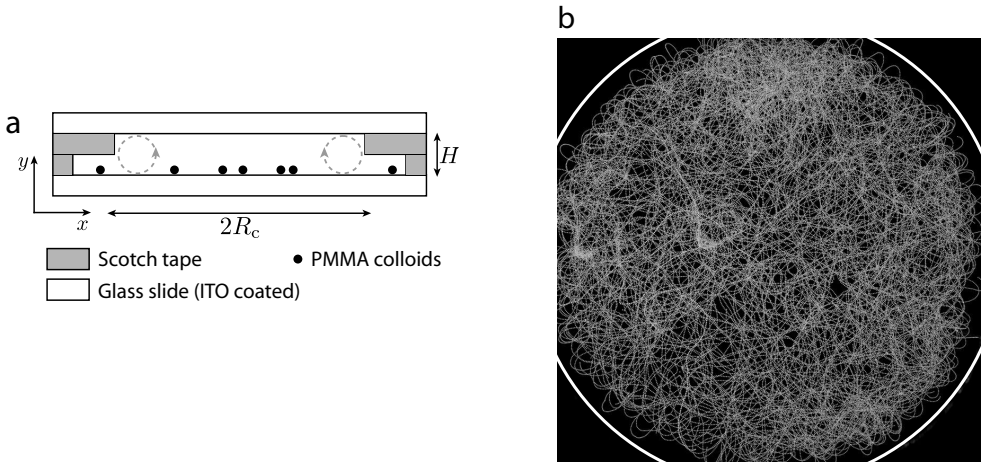


**Figure 1.28 – Experimental setup. a**– Sketch of the setup. 5-micron PMMA colloids roll in a microchannel made of two ITO-coated glass slides assembled with double-sided scotch tape. An electrokinetic flow confines the rollers at the center of the device in a circular chamber of radius $R_c$. **b**– Superimposed fluorescence pictures of a dilute ensemble of rollers ($E_0/E_Q = 1.1$, $\phi_0 = 6\times10^{-3}$). The colloids propel only inside a circular disc of radius $R_c = 1\,$mm and follow persistent random walks.

electric current is nonzero solely in a disc-shaped chamber at the center of the main channel. As exemplified by the trajectories shown in Fig. 1.28b, Quincke1896 rotation is hence restrained to this circular region in which the rollers are trapped. We henceforth characterize the collective dynamics of the roller population for increasing values of the colloid packing fraction $\phi_0$.

## 1.1 Individual self-propulsion in confinement

For area fractions smaller than $\phi^\star = 10^{-2}$, the ensemble of rollers uniformly explores the circular confinement as illustrated by the flat profile of the local packing fraction averaged along the azimuthal direction $\phi(r)$ in Fig. 1.29a. The rollers undergo uncorrelated persistent random walks as demonstrated in Figs. 1.29b and 1.29c. The probability distribution of the roller velocities is isotropic and sharply peaked on the typical speed $v_0 = 493 \pm 17\,\mu\text{m.s}^{-1}$. In addition, the velocity autocorrelation function decays exponentially at short time as expected from a simple model of self-propelled particles having a constant speed $v_0$ and undergoing rotational diffusion with a rotational diffusivity $D^{-1} = 0.31 \pm 0.02\,\text{s}$ that hardly depends on the area fraction (see the Supplementary Information). These quantities correspond to a persistence length of $\ell_p = v_0/D = 160\,\mu\text{m}$ that is about a decade smaller than the confinement radius $R_c$ used in our experiments: $0.9\,\text{mm} < R_c < 1.8\,\text{mm}$.

At long time, due to the collisions on the disc boundary, the velocity autocorrelation function sharply drops to 0 as seen in Fig. 1.29c. Unlike swimming cells [22, 217], self-propelled grains [67, 84, 120] or autophoretic colloids [203], dilute ensembles of rollers do not accumulate at the boundary. Instead, they bounce off the walls of this virtual box as shown in a close-up of a typical roller trajectory in Fig. 1.29d. As a result, the outer region of the circular chamber is depleted, and the local packing fraction vanishes as $r$ goes to $R_c$, Fig. 1.29a. The repulsion from the edges of the circular hole in the microchannel stems from another electrohydrodynamic phenomenon [226]. When an electric field is applied, a toroidal flow sketched in Fig. 1.28a is osmotically induced by the transport of the electric charges at the surface of the insulating adhesive films. Consequently, a net inward flow sets in at the vicinity of the bottom electrode. As the colloidal rollers are prone to reorient in the direction of the local fluid velocity [36], this vortical flow repels the rollers at a distance typically set by the channel height H while leaving unchanged the colloid trajectories in the center of the disc. This electrokinetic flow will be thoroughly characterized elsewhere.

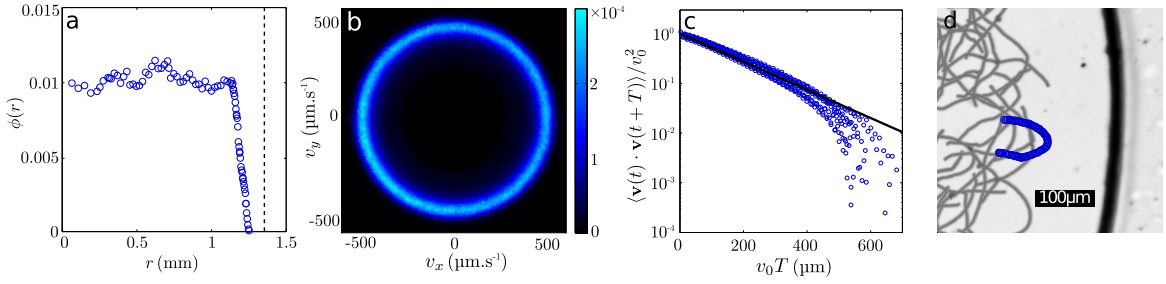


**Figure 1.29 – Dynamics of an isolated colloidal roller.** **a**– Local packing fraction $\phi(r)$, averaged over the azimuthal angle $\phi$, plotted as a function of the radial distance. The dashed line indicates the radius of the circular chamber. **b**– Probability distribution function of the roller velocities measured from the individual tracking of the trajectories. **c**– Autocorrelation of the roller velocity $\langle \mathbf{v}_i(t)\cdot\mathbf{v}_i(t+T)\rangle$ plotted as a function of $v_0T$ for packing fractions ranging from $\phi_0 = 6\times10^{-3}$ to $\phi_0 = 10^{-2}$. Full line: best exponential fit. **d**– Superimposed trajectories of colloidal rollers bouncing off the edge of the confining circle. Time interval: 5.3 ms. ($E_0/E_Q = 1.1$, $\phi_0 = 6\times10^{-3}$). Same parameters for the four panels: $R_c = 1.4\,\text{mm}$, $E_0/E_Q = 1.1$, $\phi_0 = 6\times10^{-3}$.

## 1.2 Collective motion in confinement

As the area fraction is increased above $\phi^\star$, collective motion emerges spontaneously at the entire population level. When the electric field is applied, large groups of rollers akin to the band-shaped swarms reported in [36] form and collide. However, unlike what was observed in periodic geometries, the colloidal swarms are merely transient and ultimately self-organize into a single vortex pattern spanning the entire confining disc as shown in Fig. 1.30a. Once formed, the vortex is very robust, rotates steadily and retains an axisymmetric shape. In order to go beyond this qualitative picture, we measured the local colloid velocity field $\mathbf{v}(\mathbf{r},t)$ and use it to define the polarization field $\Pi(\mathbf{r},t) \equiv \mathbf{v}/v_0$, which quantifies local orientational ordering. The spatial average of $\Pi$ vanishes when a coherent vortex forms, therefore we use its projection $\Pi_\varphi \equiv \langle \Pi \cdot \hat{\mathbf{e}}_\varphi \rangle_{\mathbf{r},t}$ along the azimuthal direction as a macroscopic order parameter to probe the transition from an isotropic gas to a polar-vortex state. As illustrated in Fig. 1.30b, $\Pi_\varphi(\phi_0)$ displays a sharp bifurcation from an isotropic state with $\Pi_\varphi = 0$ to a globally ordered state with equal probability for left- and right-handed vortices above $\phi_0 = \phi^\star$. Furthermore, Fig. 1.30b demonstrates that this bifurcation curve does not depend on the confinement radius $R_c$. The vortex pattern is spatially heterogeneous. The order parameter and density fields averaged over time are displayed in Figs. 1.30c and 1.30d, respectively. At first glance, the system looks phase-separated: a dense and ordered polar-liquid ring where all the colloids cruise along the azimuthal direction encloses a dilute and weakly ordered core at the center of the disc. We shall also stress that regardless of the average packing fraction, the packing fraction in the vortex core is measured to be very close to $\phi^\star$, the average concen-

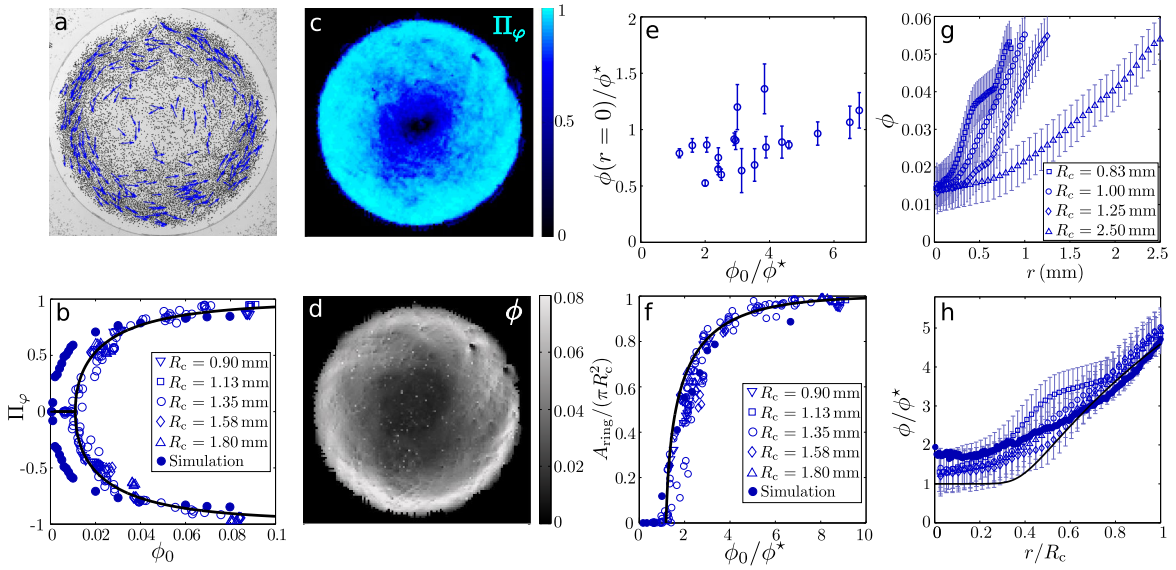


**Figure 1.30 – Collective dynamics: experiments. a**– Snapshot of a vortex of rollers. The dark dots show the position of one half of the ensemble of rollers. The blue vectors represent their instantaneous speed ($R_c$ = 1.35 mm, $\phi_0 = 5\times10^{-2}$). **b**– Average polarization plotted versus the average packing fraction for different confinement radii. Open symbols: experiments. Full line: best fit from the theory. Filled circles: numerical simulations ($b = 3a$, $R_c$ = 1 mm). **c**– Time-averaged polarization field ($R_c$ = 1.35 mm, $\phi_0 = 5\times10^{-2}$). **d**– Time average of the local packing fraction ($R_c$ = 1.35 mm, $\phi_0 = 5\times10^{-2}$). **e**– Time-averaged packing fraction at the center of the disc, normalized by $\phi^\star$ and plotted versus the average packing fraction. Error bars: 1SD. **f**– Fraction of the disc where $\Pi_\varphi > 0.5$ versus the average packing fraction. Open symbols: experiments. Full line: theoretical prediction with no free fitting parameter. Filled circles: numerical simulations ($b = 3a$, $R_c$ = 1 mm). **g**– Radial density profiles plotted as a function of the distance to the disc center $r$. All the experiments correspond to $\phi_0 = 0.032 \pm 0.002$, error bars: $1\sigma$. **h**– Open symbols: same data as in **g**. The radial density profiles are rescaled by $\phi^\star$ and plotted versus the rescaled distance to the center $r/R_c$. All the profiles are seen to collapse on a single master curve. Filled symbols: Numerical simulations. Solid line: theoretical prediction. All the data correspond to $E_0/E_Q = 1.1$.

tration below which the population is in a gaseous state, see Fig. 1.30e. This phase-separation picture is consistent with the variations of the area occupied by the ordered outer ring, $A_{ring}$, for different confinement radii $R_c$, as shown in Fig. 1.30e. We define $A_{ring}$ as the area of the region where the order parameter exceeds 0.5, and none of the results reported below depend on this arbitrary choice for the definition of the outer-ring region. $A_{ring}$ also bifurcates as $\phi_0$ exceeds $\phi^\star$, and increases with $R_c$. Remarkably, all the bifurcation curves collapse on a single master curve when $A_{ring}$ is rescaled by the overall confinement area $\pi R_c^2$, Fig. 1.30f. In other words, the strongly polarized outer ring always occupies the same area fraction irrespective of the system size, as would a molecular liquid coexisting with a vapor phase at equilibrium. However, if the system were genuinely phase-separated, one should be able to define an interface between the dense outer ring and the dilute inner core, and this interface should have a constant width. This requirement is not borne out by our measurements. The shape of the radial density profiles of the rollers in Fig. 1.30g indeed makes it difficult to unambiguously define two homogeneous phases separated by a clear interface. Repeating the same experiments in discs of increasing radii, we found that the density profiles are self-similar, Fig. 1.30h. The width of the region separating the strongly polarized outer ring from the inner core scales with the system size, which is the only characteristic scale of the vortex patterns. The colloidal vortices therefore correspond to a monophasic yet spatially heterogeneous liquid state.

In order to elucidate the physical mechanisms responsible for this intriguing structure, we now introduce a theoretical model that we solve both numerically and analytically.

## 2 Numerical simulations

The Quincke1896 rollers are electrically powered and move in a viscous fluid, and hence interact at a distance both hydrodynamically and electrostatically. In [36], starting from the Stokes and Maxwell equations, we established the equations of motion of a dilute ensemble of Quincke1896 rollers within a pairwise additive approximation. When isolated, the $i$th roller located at $\mathbf{r}_i$ moves at a speed $v_0$ along the direction $\hat{\mathbf{p}}_i = (\cos\theta_i, \sin\theta_i)$ opposite to the in-plane component of the electrostatic dipole responsible for Quincke1896 rotation [36]. When interacting via contact and electrostatic repulsive forces, the roller velocity and orientation are related by:

$$\partial_t \mathbf{r}_i = v_0 \hat{\mathbf{p}}_i - \partial_{\mathbf{r}_i} \sum_{j \neq i} \mathscr{H}_{\text{rep}}(\mathbf{r}_i - \mathbf{r}_j). \tag{1.96}$$

Inertia is obviously ignored, and for the sake of simplicity we model all the central forces acting on the colloids as an effective hard-disc exclusion $\mathscr{H}_{\text{rep}}$ of range $b$. In addition, $\theta_i$ follows an overdamped dynamics in an effective angular potential capturing both the electrostatic and hydrodynamic torques acting on the colloids [36]:

$$\partial_t \theta_i(t) = \partial_{\theta_i} \sum_{j \neq i} \mathscr{H}(\mathbf{r}_i - \mathbf{r}_j; \hat{\mathbf{p}}_i, \hat{\mathbf{p}}_j) + \xi_i. \tag{1.97}$$

The $\xi_i$'s account for rotational diffusion of the rollers. They are uncorrelated white noise variables with zero mean and variance $\langle \xi_i(t)\xi_j(t')\rangle = 2D\delta(t-t')\delta_{ij}$. The effective potential in Eq. (1.97) is composed of three terms with clear physical interpretations:

$$\begin{aligned} \mathscr{H}(\mathbf{r}, \hat{\mathbf{p}}_i, \hat{\mathbf{p}}_j) = {} & A(r)\, \hat{\mathbf{p}}_j \cdot \hat{\mathbf{p}}_i + B(r)\, \hat{\mathbf{r}} \cdot \hat{\mathbf{p}}_i \\ & + C(r)\, \hat{\mathbf{p}}_j \cdot (2\hat{\mathbf{r}}\hat{\mathbf{r}} - \mathbb{I}) \cdot \hat{\mathbf{p}}_i, \end{aligned} \tag{1.98}$$

where $\hat{\mathbf{r}} = \mathbf{r}/r$. The symmetry of these interactions is not specific to colloidal rollers and could have been anticipated phenomenologically exploiting both the translational invariance and the polar symmetry of the surface-charge distribution of the colloids [42]. The first term promotes alignment and is such that the effective potential is minimized when interacting rollers propel

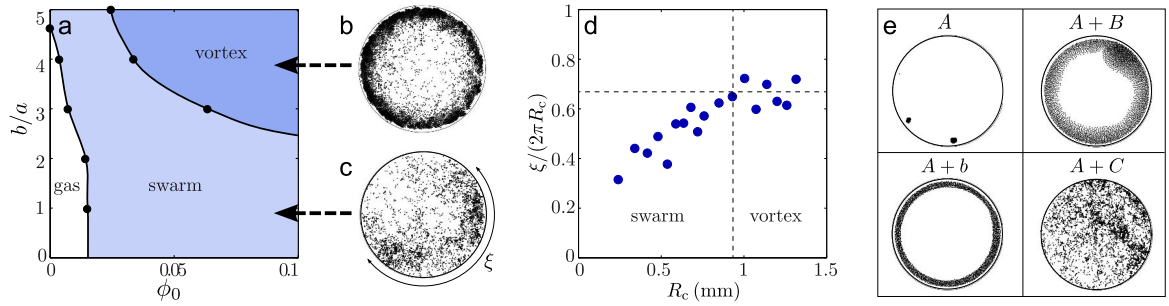


**Figure 1.31 – Collective dynamics: numerical simulations.** **a**– The numerical phase diagram of the confined population is composed of three regions: isotropic gas (low $\phi_0$, small $b$), swarm coexisting with a gaseous phase (intermediate $\phi_0$ and $b$), and vortex state (high $\phi_0$ and $b$). $R_c = 0.5$ mm. **b**– Snapshot of a vortex state. Numerical simulation for $\phi_0 = 0.1$, and $b = 5a$. **c**– Snapshot of a swarm. Numerical simulation for $\phi_0 = 4.5 \times 10^{-2}$, and $b = 2a$. **d**– Variation of the density correlation length as a function of $R_c$. Above $R_c = 1$ mm, $\xi$ plateaus and a vortex is reached ($\phi_0 = 3 \times 10^{-2}$, $b = 3a$). **e**– Four numerical snapshots of rollers interacting via: alignment interactions only (A), alignment interactions and repulsive torques (A + B, where the magnitude of B is 5 times the experimental value), alignment and excluded volume interactions (A + $b$, where the repulsion distance is $b = 5a$), alignment and the C-term in Eq. (1.98) (A + C). Polarized vortices emerge solely when repulsive couplings exist (A + B and A + $b$).

along the same direction. A($r$) is positive, decays exponentially with $r$/H, and results both from hydrodynamic and electrostatic interactions. The second term gives rise to repulsive *torques*, and is minimized when the roller orientation points away from its interacting neighbor. B($r$) also decays exponentially with $r$/H but solely stems from electrostatics. The third term has a less intuitive meaning, and promotes the alignment of $\hat{\mathbf{p}}_i$ along a dipolar field oriented along $\hat{\mathbf{p}}_j$. This term is a combination of hydrodynamic and electrostatic interactions, and includes a long-ranged contribution.

The functions A($r$), B($r$), and C($r$) are provided in the Supplementary Information As it turns out, all the physical parameters (roller velocity, field amplitude, fluid viscosity, etc.) that are needed to compute their exact expressions have been measured, or estimated up to logarithmic corrections, see the Supplementary Information. We are then left with a model having a single free parameter that is the range, $b$, of the repulsive *forces* between colloids. We numerically solved this model in circular simulation boxes of radius $R_c$ with reflecting boundary conditions using an explicit Euler scheme with adaptive time-stepping. All the numerical results are discussed using the same units as in the experiments to facilitate quantitative comparisons.

The simulations revealed a richer phenomenology than the experiments, as captured by the phase diagram in Fig. 1.31a corresponding to $R_c = 0.5$ mm. By systematically varying the range of the repulsive forces and the particle concentration, we found that the ($\phi_0$, $b$) plane is typically divided into three regions. At small packing fractions, the particles hardly interact and form an isotropic gaseous phase. At high fractions, after transient dynamics strikingly similar to that observed in the experiments, the rollers self-organize into a macroscopic vortex pattern, Fig. 1.31b. However, at intermediate densities, we found that collective motion emerges in the form of a macroscopic swarm cruising around the circular box through an ensemble of randomly moving particles, Fig. 1.31c. These swarms are akin to the band patterns consistently reported for polar active particles at the onset of collective motion in periodic domains [36, 92]. This seeming conflict between our experimental and numerical findings is solved by looking at the variations of the swarm length $\xi_s$ with the confinement radius $R_c$ in Fig. 1.31d. We define $\xi_s$ as the correlation length of the density fluctuations in the azimuthal direction. The angular extension of the swarms $\xi_s/R_c$ increases linearly with the box radius. Therefore, for a given value of the interaction parameters, there exists a critical box size above which the population undergoes a direct transition from a gaseous to an axisymmetric vortex state. For $b = 3a$, which was measured to be the typical in-

terparticle distance in the polar liquid state [36], this critical confinement is $R_c = 1\,\mathrm{mm}$. This value is close to the smallest radius accessible in our experiments where localized swarms were never observed, thereby solving the apparent discrepancy with the experimental phenomenology.

More quantitatively, we systematically compare our numerical and experimental measurements in Figs. 1.30b and 1.30c for $R_c = 1\,\mathrm{mm}$. Even though a number of simplifications were needed to establish Eqs. (1.96), (1.97) and (1.98) [36], the simulations account very well for the sharp bifurcation yielding the vortex patterns as well as their self-similar structure. This last point is proven quantitatively in Fig. 1.30h, which demonstrates that the concentration increases away from the vortex core, where $\phi(r=0) = \phi^\star$, over a scale that is solely set by the confinement radius. We shall note however that the numerical simulations underestimate the critical packing fraction $\phi^\star$ at which collective motion occurs, which is not really surprising given the number of approximations required to establish the interaction parameters in the equations of motion Eq. (1.98). We unambiguously conclude from this set of results that Eqs. (1.96), (1.97) and (1.98) include all the physical ingredients that chiefly dictate the collective dynamics of the colloidal rollers. We now exploit the opportunity offered by the numerics to turn on and off the four roller-roller interactions one at a time, namely the alignment torque, A, the repulsion torque B and force $b$, and the dipolar coupling C. Snapshots of the resulting particle distributions are reported in Fig. 1.31e. None of these four interactions alone yields a coherent macroscopic vortex. We stress that when the particles solely interact via pairwise-additive alignment torques, $B = C = b = 0$, the population condenses into a single compact polarized swarm. Potential velocity-alignment interactions are *not* sufficient to yield macroscopic vortical motion. We evidence in Fig. 1.31e (top-right and bottom-left panels) that the combination of alignment ($A \neq 0$) and of repulsive interactions ($B \neq 0$ and/or $b \neq 0$) is necessary and sufficient to observe spontaneously flowing vortices.

## 3 Theory and discussion

Having identified the very ingredients necessary to account for our observations, we can now gain more detailed physical insight into the spatial structure of the vortices by constructing a minimal hydrodynamic theory. We start from Eqs. (1.96), (1.97) and (1.98), ignoring the C term in Eq. (1.98). The model can be further simplified by inspecting the experimental variations of the individual roller velocity with the local packing fraction, see the Supplementary Information. The roller speed only displays variations of 10% as $\phi(\mathbf{r})$ increases from $10^{-2}$ to $4\times10^{-2}$. These minute variations suggest ignoring the contributions of the repulsive forces in Eq. (1.96), and solely considering the interplay between the alignment and repulsion torques on the orientational dynamics of Eq. (1.97). These simplified equations of motion are coarse-grained following a conventional kinetic-theory framework reviewed in [136] to establish the equivalent to the Navier-Stokes equations for this two-dimensional active fluid. In a nutshell, the two observables we need to describe are the local area fraction $\phi$ and the local momentum field $\phi\Pi$. They are related to the first two angular moments of the one-particle distribution function $\psi(\mathbf{r},\hat{\mathbf{p}},t) = \pi a^2\langle\sum_i \delta(\mathbf{r}-\mathbf{r}_i)\delta(\hat{\mathbf{p}}-\hat{\mathbf{p}}_i)\rangle$, which evolves according to a Fokker-Plank equation derived from the conservation of $\psi$ and Eqs. (1.96) and (1.97). This equation is then recast into an infinite hierarchy of equations for the angular moments of $\psi$. The two first equations of this hierarchy, corresponding to the mass conservation equation and to the momentum dynamics, are akin to the continuous theory first introduced phenomenologically by Toner and Tu [136, 212]:

$$\partial_t\phi + v_0\nabla\cdot\left(\phi\Pi\right) = 0, \tag{1.99}$$

$$\partial_t\left(\phi\Pi\right) + v_0\nabla\cdot\left(\phi\mathbf{Q} + \frac{\phi}{2}\mathbb{I}\right) = \mathbf{F}(\phi,\Pi,\mathbf{Q}), \tag{1.100}$$

where $\mathbf{Q}$ is the usual nematic order parameter. The meaning of the first equation is straightforward, while the second calls for some clarifications. The divergence term on the left-hand side of Eq. (1.100) is a convective kinematic term associated with the self-propulsion of the particles. The

force field **F** on the right-hand side would vanish for non-interacting particles. Here, at first order in a gradient expansion, **F** is given by:

$$\mathbf{F} = -\mathrm{D}\,\phi\Pi + \alpha\phi^2(\mathbb{I} - 2\mathbf{Q})\cdot\Pi - \beta\phi(\mathbb{I} - 2\mathbf{Q})\cdot\nabla\phi. \tag{1.101}$$

This force field has a clear physical interpretation. The first term reflects the damping of the polarization by the rotational diffusion of the rollers. The second term, defined by the time rate $\alpha = (\int_{r>2a} r\mathrm{A}(r)\mathrm{d}r)/a^2$, echoes the alignment rule at the microscopic level and promotes a nonzero local polarization. The third term, involving $\beta = (\int_{r>2a} r^2\mathrm{B}(r)\mathrm{d}r)/(2a^2)$, is an anisotropic pressure reflecting the repulsive interactions between rollers at the microscopic level. Eqs. (1.99) and (1.100) are usually complemented by a dynamical equation for **Q** and a closure relation. This additional approximation, however, is not needed to demonstrate the existence of vortex patterns and to rationalize their spatial structure.

Looking for axisymmetric steady states, it readily follows from mass conservation, Eq. (1.99), that the local fields must take the simple forms: $\phi = \phi(r)$, $\Pi = \Pi_\varphi(r)\mathbf{e}_\varphi$ and $\mathbf{Q} = \mathrm{Q}(r)(\mathbf{e}_\varphi\mathbf{e}_\varphi - \mathbf{e}_r\mathbf{e}_r)$, where $\mathrm{Q}(r) > 0$. We also infer the relation $\left[-\mathrm{D} + \alpha\phi(1-2\mathrm{Q})\right]\phi\Pi_\varphi = 0$ from the projection of the momentum equation, Eq. (1.100), on the azimuthal direction. This relation tells us that the competition between rotational diffusion and local alignment results in a mean-field transition from an isotropic state with $\Pi_\varphi = 0$ to a polarized vortex state with $\Pi_\varphi \neq 0$ and $\mathrm{Q} = \frac{1}{2}\left(1 - \mathrm{D}/(\alpha\phi)\right)$. This transition occurs when $\phi$ exceeds $\phi^\star \equiv \mathrm{D}/\alpha$, the ratio of the rotational diffusivity to the alignment strength at the hydrodynamic level. In addition, the projection of Eq. (1.100) on the radial direction sets the spatial structure of the ordered phase:

$$2\frac{v_0}{r}\mathrm{Q} - \beta\,(1+2\mathrm{Q})\,\frac{\mathrm{d}\phi}{\mathrm{d}r} = 0, \tag{1.102}$$

with again $\mathrm{Q} = \frac{1}{2}\left(1 - \phi^\star/\phi\right)$ in the ordered polar phase. This equation has a clear physical meaning and expresses the balance between the centrifugal force arising from the advection of momentum along a circular trajectory and the anisotropic pressure induced by the repulsive interactions between rollers. It has an implicit solution given by

$$\frac{r}{r^\star} = \exp\left[2\Lambda\frac{\phi}{\phi^\star} + \Lambda\log\left(\frac{\phi}{\phi^\star} - 1\right)\right]. \tag{1.103}$$

$\phi(r)$ is therefore parametrized by the dimensionless number $\Lambda \equiv \phi^\star\frac{\beta}{v_0}$ reflecting the interplay between self-propulsion and repulsive interactions. Given the experimental values of the microscopic parameters, $\Lambda$ is much smaller that unity ($\Lambda \sim 0.08$). An asymptotic analysis reveals that $r^\star$ is the typical core radius of the vortex. For $r < r^\star$, the density increases slowly as $\phi \sim \phi^\star\left[1 + (r/r^\star)^{1/\Lambda}\right]$ for all $\phi_0$ and $\mathrm{R_c}$. As $r$ reaches $r^\star$, it increases significantly and then growths logarithmically as $\phi \sim v_0/\beta\log(r/r^\star)$ away from the vortex core. However, $r^\star$ is an integration constant which is solely defined via the mass conservation relation: $\pi\mathrm{R_c^2}\phi_0 = \int_0^{\mathrm{R_c}} 2\pi r\phi(r)\,\mathrm{d}r$ and therefore only depends on $\phi_0$ and $\mathrm{R_c}$. $r^\star$ does not provide any intrinsic structural scale, and the vortex patterns formed in different confinements are predicted to be self-similar in agreement with our experiments and simulations despite the simplification made in the model, Fig. 1.30e. In addition, Eq. (1.103) implies that the rollers self-organize by reducing their density at the center of the vortex down to $\phi = \phi^\star$, the mean area fraction at the onset of collective motion, again in excellent agreement with our measurements in Fig. 1.30e.

In order to characterize the orientational structure of the vortices, an additional closure relation is now required. The simplest possible choice consists in neglecting correlations of the orientational fluctuations, and therefore assuming $\mathrm{Q} = \Pi_\varphi^2/2$. This choice implies that

$$\Pi_\varphi(r) = \sqrt{1 - \phi^\star/\phi(r)}. \tag{1.104}$$

Eqs. (1.103) and (1.104) provide a very nice fit of the experimental polarization curve as shown in Fig. 1.30b, and therefore capture both the pitchfork bifurcation scenario at the onset of collective

motion and the saturation of the polarization at high packing fractions. The best fit is obtained for values of $\phi^\star$ and $\beta$ respectively five and two times larger than those deduced from the microscopic parameters. Given the number of simplifications needed to establish both the microscopic and hydrodynamic models, the agreement is very convincing. We are then left with a hydrodynamic theory with no free fitting parameter, which we use to compute the area fraction of the outer polarized ring where $\Pi_\varphi > 0.5$. The comparison with the experimental data in Fig. 1.30f is excellent.

Furthermore, Eqs. (1.103) and (1.104) predict that the rollers are on the verge of a phase separation. If the roller fraction in the vortex core were smaller ($\phi < \phi^\star$), orientational order could not be supported and an isotropic bubble would nucleate in a polar liquid. This phase separation is avoided by the self-regulation of $\phi(r = 0)$ at $\phi^\star$.

Altogether our theoretical results confirm that the vortex patterns stem from the interplay between self-propulsion, alignment, repulsion and confinement. Alignment interactions promote a global azimuthal flow. If the rollers were not confined, the population would evaporate as self-propulsion induces a centrifugal force despite the absence of inertia. Finally, the repulsive interactions prevent condensation of the population on the geometrical boundary and allow for extended vortical patterns.

We close this discussion by stressing on the generality of this scenario. Neither the nature of the repulsive couplings nor the symmetry of the interactions yielding collective motion are crucial, thereby making the above results relevant to a much broader class of experimental systems. For instance, self-propelled particles endowed with nematic alignment rules are expected to display the same large-scale phenomenology. The existence of a centrifugal force indeed does not rely on the direction of the individual trajectories. Shaken elongated rods, concentrated suspensions of bacteria, or motile biofilaments, among other possible realizations, are expected to have a similar phase behavior. Quantitative local analysis of their spatial patterns [67, 122, 145, 190, 222] would make it possible to further test and elaborate our understanding of the structure of confined active matter.

## 4 Conclusion

We have taken advantage of a unique experimental system where ensembles of self-propelled colloids with well-established interactions self-organize into macrosopic vortices when confined by circular geometric boundaries. We have identified the physical mechanism that chiefly dictates this emergent behavior. Thanks to a combination of numerical simulations and analytical theory, we have demonstrated that orientational couplings alone cannot account for collective circular motion. Repulsion between the motile individuals is necessary to balance the centrifugal flow intrinsic to any ordered active fluid and to stabilize heterogeneous yet monophasic states in a broad class of active fluids. A natural challenge is now to quantify the robustness of these spontaneously flowing states when their collective excitations are frustrated by the geometry and/or topology of the boundaries.

**Acknowledgements** We benefited from valuable discussions with Nicolas Desreumaux, Olivier Dauchot, and John Toner on related questions. This work was partly funded by the ANR program MiTra, and Institut Universitaire de France. D.S. acknowledges partial support from the Donors of the American Chemical Society Petroleum Research Fund and from NSF CAREER Grant No. CBET-1151590. K.S. was supported by the JSPS Core-to-Core Program "Non-equilibrium dynamics of soft matter and information".

**Author Contributions** A.B. and V.C. carried out the experiments and processed the data. D.D., C.S., O.C., F.P., and D.S. carried out the the numerical simulations. J.-B.C., K.S. and D.B. established the analytical model. All the authors discussed and interpreted results. D.B., J.-B.C. and D.B. wrote the manuscript. D.B. conceived the project. A.B. and J.-B.C. have equally contributed to this work.

## Methods

***Experiments*** We use fluorescent PMMA colloids (Thermo scientific G0500, 2.4 µm radius), dispersed in a 0.15 mol.L$^{-1}$ AOT/hexadecane solution. The suspension is injected in a wide microfluidic chamber made of double-sided scotch tapes. The tape is sandwiched between two ITO-coated glass slides (Solems, ITOSOL30, 80 nm thick). An additional layer of scotch tape including a hole having the desired confinement geometry is added to the upper ITO-coated slide. The holes are made with a precision plotting cutter (Graphtec robo CE 6000). The gap between the two ITO electrodes is constant over the entire chamber H = 220 µm. The electric field is applied by means of a voltage amplifier (Stanford Research Systems, PS350/5000V-25W). All the measurements were performed 5 minutes after the beginning of the rolling motion, when a steady state was reached for all the observables.

The colloids are observed with a 4X microscope objective for particle tracking, PIV and number-density measurements. High-speed movies are recorded with a CMOS camera (Basler ACE) at a frame rate of 190fps. All images are 2000×2000 8-bit pictures. The particles are detected to sub-pixel accuracy and the particle trajectories are reconstructed using a MATLAB version of a conventional tracking code [58]. The PIV analysis was performed with the mpiv MATLAB code. A block size of 44 µm was used.

***Numerical simulations*** The simulations are performed by numerically integrating the equations of motion Eqs. (1.96), and (1.97). Particle positions and rolling directions are initialized randomly inside a circular domain. Integration is done using an Euler scheme with an adaptive time step $\delta t$, and the diffusive term in the equation for the rotational dynamics is modeled as a Gaussian variable with zero mean and with variance $2\mathrm{D}/\delta t$. Steric exclusion between particles is captured by correcting particle positions after each time step so as to prevent overlaps. Bouncing off of particles at the confining boundary is captured using a phenomenological torque that reorients the particles towards the center of the disc; the form of the torque was chosen so at the reproduce the bouncing trajectories observed in the experiments.

# Supplementary Information

## A Dynamics of a single roller

At low packing fraction, $\phi_0 \ll \phi^\star$, the colloids behave as non-interacting persistent random walkers. Their motion is described by:

$$\partial_t \mathbf{r}_i = v_0 \hat{\mathbf{p}}_i = v_0(\cos\theta_i, \sin\theta_i), \tag{1.105}$$

$$\partial_t \theta_i = \xi_i(t), \tag{1.106}$$

where $\xi_i$ is a white noise with zero mean and variance $\langle \xi_i(t)\xi_i(t')\rangle = 2\mathrm{D}\delta(t-t')$. The velocity autocorrelation function decays exponentially as

$$\langle v_0\hat{\mathbf{p}}_i(t+\mathrm{T}) \cdot v_0\hat{\mathbf{p}}_i(t)\rangle = v_0^2\, \mathrm{e}^{-\mathrm{DT}}, \tag{1.107}$$

and the mean-squared displacement is given by:

$$\langle [\mathbf{r}_i(t+\mathrm{T}) - \mathbf{r}_i(t)]^2\rangle = 2\frac{v_0^2}{\mathrm{D}^2}\left(\mathrm{DT} - 1 + \mathrm{e}^{-\mathrm{DT}}\right). \tag{1.108}$$

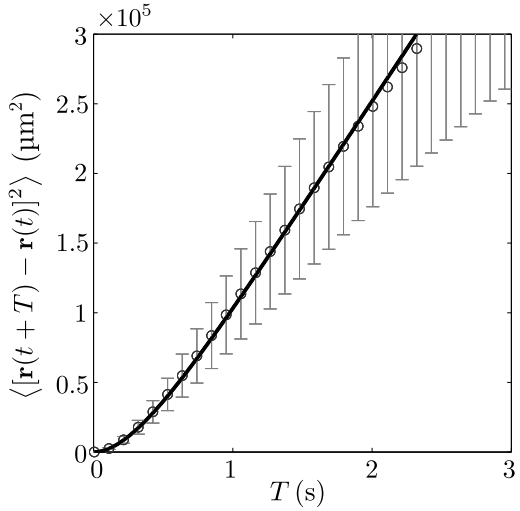


**Figure 1.32** – Mean-squared displacement of the rollers, $\langle[\mathbf{r}_i(t+\mathrm{T})-\mathbf{r}_i(t)]^2\rangle_{i,t}$ plotted as a function of the lag time T. Open symbol: experiments (error bars 1SD). Full line: theoretical prediction.

The later expressions are used to fit the experimental data, Fig. 1.29c and Supplementary Fig. 1.32 below, and provide the following values for the particle speed and diffusivity:

$$v_0 = 493 \pm 17\,\mu\mathrm{m.s}^{-1}, \tag{1.109}$$

$$\mathrm{D}^{-1} = 0.31 \pm 0.02\,\mathrm{s}. \tag{1.110}$$

# B Population of interacting rollers

## B.1 Microscopic model

In [36], we have theoretically described the microscopic dynamics of a population of colloids rolling on a conducting surface. We briefly summarize this model. A colloid powered by the Quincke1896 mechanism, when rotating close to a wall, exchanges momentum with this solid surface and translates at a speed given by

$$v_0 = \frac{a\tilde{\mu}_t}{\mu_r \tau}\sqrt{\left(\frac{\mathrm{E}_0}{\mathrm{E}_\mathrm{Q}}\right)^2 - 1}. \tag{1.111}$$

$\mathrm{E}_\mathrm{Q}$ is the critical electric field below which the particle does not rotate. The Maxwell-Wagner time $\tau$ characterizes the dynamics of the electric charges at the colloid surface, which are responsible for the Quincke1896 instability. $\mu_r$ and $\tilde{\mu}_t$ are mobility coefficients accounting for the viscous drag exerted by the liquid in the vicinity of solid wall that depend logarithmically on the distance to the solid wall [36]. In order to account for the roller-roller interactions at long distances, we have computed the electrostatic and hydrodynamic fields induced by the motion of a colloid. Assuming pairwise additive interactions, we have shown that these fields promote the alignement of the velocity of neighboring particles. Within this framework, the speed of the colloids is taken to be a constant as it relaxes to $v_0$ much faster than the typical timescale of the orientation dynamics. In addition to these far-field couplings, we model the short-distance repulsion between colloids by an effective hard-core potential. The resulting equations of motion are given by Eqs. (1.96)–(1.98)

in the main text, where the functions $A(r)$, $B(r)$, $C(r)$ are given by:

$$A(r) = A_1\left(\frac{a}{r}\right)^3\Theta(r) + A_2\left(\frac{a}{r}\right)^5\Theta(r), \tag{1.112}$$

$$B(r) = B_1\left(\frac{a}{r}\right)^4\Theta(r), \tag{1.113}$$

$$C(r) = C_1\left[2\left(\frac{a}{H}\right)\left(\frac{a}{r}\right)^2 + \left(\frac{a}{r}\right)^3\Theta(r)\right] + C_2\left(\frac{a}{r}\right)^5\Theta(r). \tag{1.114}$$

These electrostatic and hydrodynamic couplings are exponentially screened over a distance set by the channel height H (see Fig. 1.28a, main text). For sake of simplicity, we approximate the screening function $\Theta(r)$ by the step function $\Theta(r) = 1$ if $r \leq H/\pi$ and $\Theta(r) = 0$ otherwise. In addition, the coefficients of the above functional forms are given by:

$$A_1 = 3\tau^{-1}\tilde{\mu}_s, \tag{1.115}$$

$$A_2 = 9\tau^{-1}\left(\frac{\mu_\perp}{\mu_r} - 1\right)\left(\chi^\infty + \frac{1}{2}\right)\left(1 - \frac{E_Q^2}{E_0^2}\right), \tag{1.116}$$

$$B_1 = 6\tau^{-1}\left(\frac{\mu_\perp}{\mu_r} - 1\right)\sqrt{\frac{E_0^2}{E_Q^2} - 1}\left[\left(\chi^\infty + \frac{1}{2}\right)\frac{E_Q^2}{E_0^2} - \chi^\infty\right], \tag{1.117}$$

$$C_1 = A_1, \tag{1.118}$$

$$C_2 = \frac{5}{3}A_2. \tag{1.119}$$

$\mu_r$ and $\mu_\perp$ are mobility coefficients which only depend on the viscosity of the liquid and the gap $d$ between the colloid and the surface. $\chi^\infty$ depends on the dielectric permittivities $\epsilon_l$ and $\epsilon_p$ of the liquid and of the particles.

$$\chi^\infty = \frac{\epsilon_p - \epsilon_l}{\epsilon_p + 2\epsilon_l}. \tag{1.120}$$

A thorough derivation of this model is provided in the supplementary informations of [36].

## B.2 Estimation of the simulation parameters

In order to perform numerical simulations relevant to our experimental conditions, we have estimated the coefficients of the equations of motion as follows. The speed $v_0$ and the rotational diffusivity D have been deduced from the single-particle dynamics, Eqs. (1.109) and (1.110). The threshold electric field $E_Q$ is measured experimentally as the critical value at which the colloids start moving. We use typical values for the dielectric permittivities of hexadecane ($\epsilon_l = 2.2\epsilon_0$) and PMMA colloids ($\epsilon_p = 2.6\epsilon_0$) [152] to evaluate $\chi^\infty = 0.06$. The mobility coefficients are estimated. We assume the distance between a particle and the surface to be $d \sim 50\,\text{nm}$. Although this parameter is not controlled precisely, it only yields small corrections to the mobility coefficients in the limit $d \ll a$, and weakly impacts the particle dynamics. Using the expressions derived in [89, 90, 130, 148], we find $\tilde{\mu}_s = 0.30$, $\mu_\perp/\mu_r = 1.6$ and $\tilde{\mu}_t/\mu_r = 8.7 \times 10^{-2}$. Finally, the Maxwell-Wagner time $\tau$ was calculated from Eq. (1.111): $\tau = 0.29\,\text{ms}$. As a result, we obtain the following values for the microscopic coefficients:

$$A_1 = B_1 = C_1 = 0.9\,\tau^{-1}, \tag{1.121}$$

$$A_2 = 1.0\,\tau^{-1}, \tag{1.122}$$

$$C_2 = 1.7\,\tau^{-1}. \tag{1.123}$$

## C Variation of the roller speed with the packing fraction

In Supplementary Fig. 1.33, we plot the individual roller velocity $v_0$ as a function of the local area fraction $\phi$. As $\phi$ varies from $10^{-2}$ to $4 \times 10^{-2}$, $v_0$ only increases by $\sim 10\%$.

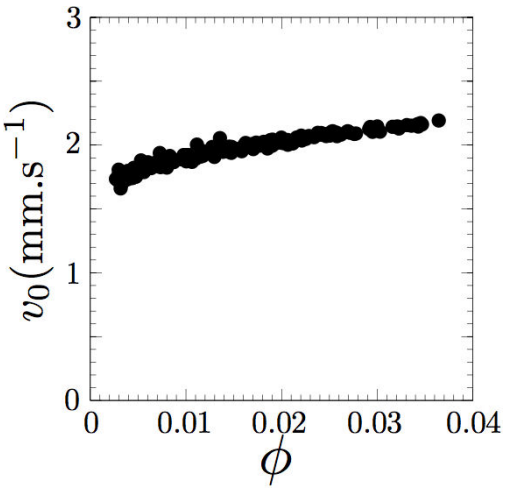


**Figure 1.33** – Variation of the roller velocity with the local area fraction. $E/E_Q = 1.4$.

# Article: *Tailoring the interactions between self-propelled bodies*

J.-B. Caussin and D. Bartolo, *Eur. Phys. J. E* **37**, 55 (2014)

We classify the interactions between self-propelled particles moving at a constant speed from symmetry considerations. We establish a systematic expansion for the two-body forces in the spirit of a multipolar expansion. This formulation makes it possible to rationalize most of the models introduced so far within a common framework. We distinguish between three classes of physical interactions: (i) potential forces, (ii) inelastic collisions and (iii) non-reciprocal interactions involving polar or nematic alignment with an induced field. This framework provides simple design rules for the modeling and the fabrication of self-propelled bodies interacting via physical interactions. A class of possible interactions that should yield new phases of active matter is highlighted.

## 1 Introduction

Active materials composed of motile bodies define a quickly-growing field of statistical and soft-matter physics [136, 216]. Over the last decades, much attention has been devoted to the individual dynamics of self-propelled particles (e.g. effective diffusion and migration in an external field), and to the collective properties of large populations (e.g. transition to collective motion, and emergence of coherent spatial patterns) [136, 175, 216].

From a theoretical perspective, the large-scale properties of active populations have been investigated for several interaction schemes at the single-particle level, see e.g. [49, 57, 95, 128, 156, 215]. In most of the models, dynamical rules such as velocity-alignment or hard-core repulsion were included without refereeing to the microscopic physics responsible for these couplings. A priori a number of alternative phenomenological rules could be considered, yet no global framework exists to elaborate and classify such interactions with overlooked symmetries.

From an experimental perspective, significant progress has been made over the last years, and a number of artificial active systems are now available, including self-propelled colloids [36, 112, 151, 154, 204], vibrating grains [68, 120, 122, 144], biofilaments [188, 190, 201]. Now that the fabrication of motile microscopic systems is a problem that has been partly solved, a natural next step is to consider the self-assembly of these autonomous units into new materials. The design of such active phases requires a deeper understanding of the interaction symmetries between their elementary units. Surprisingly, until now, the two-body interactions between self-propelled colloids and filaments have been scarcely characterized.

In this paper, we classify the symmetries of the mutual interactions between self-propelled bodies moving at a constant speed. We first decompose systematically the two-body force fields in a generalized multipole expansion which solely requires that the particles live in a homogeneous space (translational invariance). We then show how little additional information about the interaction process further simplify the form of the interactions. We consider explicitly three relevant cases: (i) Isotropic particles interacting only via potential interactions, (ii) Isotropic particles interacting via two-body inelastic collisions, and (iii) Particles of arbitrary shape that interact

via non-reciprocal interactions (*viz.* interactions that are non invariant upon Galilean transformations). We systematically exemplify our results with classical active-matter models, which we rationalize within a unified framework. We close this paper by suggesting guidelines for the design of new active materials.

## 2 Interacting self-propelled bodies: equations of motion

By definition, self-propelled particles convert stored internal energy to propel themselves in the absence of any external force [136]. We consider here the simplest framework supporting this definition: point particles moving at a *constant* speed $v_0$ in a homogeneous space. More precisely, any force acting on the particle $a$ located at $\mathbf{r}_a$ and moving at a velocity $\mathbf{v}_a = v_0\hat{\mathbf{p}}_a$ alters only its direction of motion, defined by the unit vector $\hat{\mathbf{p}}_a$. We also assume that the particles interact via pairwise-additive couplings. The equations of motion for the particle $a$ are then the Newton's equations completed by the constant velocity constraint:

$$\partial_t \mathbf{r}_a = \hat{\mathbf{p}}_a, \tag{1.124}$$

$$\partial_t \hat{\mathbf{p}}_a = (\mathbb{I} - \hat{\mathbf{p}}_a\hat{\mathbf{p}}_a)\cdot \sum_{b\neq a} \mathbf{F}_{b\to a}, \tag{1.125}$$

where $\mathbf{F}_{b\to a}$ is the force exerted by particle $b$ on particle $a$, and where we have set $v_0 = 1$. The projection operator $(\mathbb{I} - \hat{\mathbf{p}}_a\hat{\mathbf{p}}_a)$ ensures that the norm of the velocity vector $\hat{\mathbf{p}}_a$ remains constant. Eq. (1.125) implies that particles having a constant speed reorient and align along the net force that they experience. These equations, that have been extensively studied [177], can also be viewed as the asymptotic limit of a broader class of active-particle dynamics, see e.g. [101, 128, 219]. Our predictions do not strictly require the propulsion speed to be a constant, but only that some internal dissipation mechanisms causes $v_0$ to relax towards its stationary value in a time much shorter than the changes in the velocity direction. We further clarify this point and discuss the robustness of Eqs. (1.124) and (1.125) in Appendix A, by studying a specific energy-exchange model [55, 74, 128].

## 3 Interactions in homogeneous media: Translational invariance

We now establish a generic expression which classifies the interactions according to their angular symmetries. For sake of clarity, we restrict the discussion to two spatial dimensions; the generalization to a 3D system is provided in Appendix B. The force exerted by particle $b$ on particle $a$ is a priori a function of the two positions $\mathbf{r}_a$, $\mathbf{r}_b$ and orientations $\hat{\mathbf{p}}_a$, $\hat{\mathbf{p}}_b$. However, by definition, in a homogenous medium $\mathbf{F}_{a\to b}(\mathbf{r}_a, \mathbf{r}_b; \hat{\mathbf{p}}_a, \hat{\mathbf{p}}_b)$ is translationally invariant, and therefore only depend on the relative positions of the particles: $\mathbf{r}_a - \mathbf{r}_b$. We now identify 2D vectors to complex numbers, and note $\mathbf{r}_a - \mathbf{r}_b = r_{ab}\exp(i\varphi_{ab})$, where $r_{ab}$ is the interparticle distance and $\varphi_{ab}$ the relative angular position. Without any additional assumption, we Fourier transform $\mathbf{F}_{b\to a}$ with respect to $\varphi_{ab}$ and obtain:

$$\mathbf{F}_{b\to a} = \sum_{\mathrm{k}} f_{\mathrm{k}}(r_{ab}, \hat{\mathbf{p}}_a, \hat{\mathbf{p}}_b)\, \mathrm{e}^{i\left[\mathrm{k}\varphi_{ab} + \psi_{\mathrm{k}}(r_{ab}, \hat{\mathbf{p}}_a, \hat{\mathbf{p}}_b)\right]}. \tag{1.126}$$

Transforming the real and imaginary parts into polynomial series in $\cos\varphi_{ab}$ and $\sin\varphi_{ab}$, and after some elementary algebra, Eq. (1.126) is recast into a more intuitive expansion akin to a multipolar series:

$$\begin{aligned}\mathbf{F}_{b\to a} = \mathbf{f}_0 + f_1^{\mathrm{div}}\hat{\mathbf{r}}_{ab} + f_1^{\mathrm{rot}}\boldsymbol{\epsilon}\cdot\hat{\mathbf{r}}_{ab} \\ + f_{-1}\left(2\frac{\mathbf{f}_{-1}\mathbf{f}_{-1}}{f_{-1}^2} - \mathbb{I}\right)\cdot\hat{\mathbf{r}}_{ab} + \mathbf{f}_2\cdot(2\hat{\mathbf{r}}_{ab}\hat{\mathbf{r}}_{ab} - \mathbb{I}) + \dots\end{aligned} \tag{1.127}$$

$f_1^{\rm div} = f_1 \cos\psi_1$ and $f_1^{\rm rot} = -f_1 \sin\psi_1$ are scalars, $\boldsymbol{\epsilon}$ is the completely antisymmetric Levy-Civita symbol, and all the other coefficients are vectors: $\mathbf{f}_0 = f_0(\cos\psi_0, \sin\psi_0)$, $\mathbf{f}_{-1} = f_{-1}(\cos(\psi_{-1}/2), \sin(\psi_{-1}/2))$ and $\mathbf{f}_2 = f_2(\cos\psi_2, -\sin\psi_2)$. We recall that all the $\mathbf{f}_k$ depend in principles on the relative position and on the orientations of particles $a$ and $b$. The terms in Eq. (1.127) are classified according to their angular periodicity, the index k corresponds to the topological charge of the force field induced by the particle $b$: the larger k, the faster the angular variations of the field. Eq. (1.127) is already a pivotal result of this paper as it describes all the possible symmetries of the field in which a self-propelled particle reorients. In order to gain more physical insight into this formal expansion, the first modes are plotted in Fig. 1.35, and discussed below.

- The k = 0 component is a field having a constant orientation. The particle $a$ reorients along $\mathbf{F}_{a\to b}$, which is aligned with the vector $\mathbf{f}_0(r_{ab}, \hat{\mathbf{p}}_a, \hat{\mathbf{p}}_b)$ regardless of the relative positions of the particles.

- The k = 1 component in Eq. (1.127) generically corresponds to a spiral force field. To better understand its contribution, it is convenient to distinguish between its divergence and rotational components as done in Eq. (1.127) and Fig. 1.35. The first term, $f_1^{\rm div}\hat{\mathbf{r}}_{ab}$, has the symmetry of a monopolar field. This term therefore gives rise to repulsive (resp. attractive) couplings. For example, particle $a$ reorients along $\hat{\mathbf{r}}_{ab}$ if $f_1^{\rm div}(r_{ab}, \hat{\mathbf{p}}_a, \hat{\mathbf{p}}_b) > 0$. The second term, the rotational part $f_1^{\rm rot}\boldsymbol{\epsilon}\cdot\hat{\mathbf{r}}_{ab}$, breaks the bottom-top symmetry in 2D, which implies that $f_1^{\rm rot}$ is a pseudoscalar quantity. Consequently, $f_1^{\rm rot}$ is non-zero only for particles having some chiral features. In such an interaction field, a chiral particle $b$ could be forced to circle around its neighbor.

- The k = −1 component has the form of an hyperbolic elongation field with a negative topological charge. The k = 2 contribution has the dipolar symmetry, the direction of the dipole being set by the vector $\mathbf{f}_2(r_{ab}, \hat{\mathbf{p}}_a, \hat{\mathbf{p}}_b)$. Similarly, the higher-order terms of the Fourier expansion correspond to force fields having positive or negative topological charges. Note that the contributions from the k < 0 components do not correspond to conventional multipoles associated with a Laplacian field.

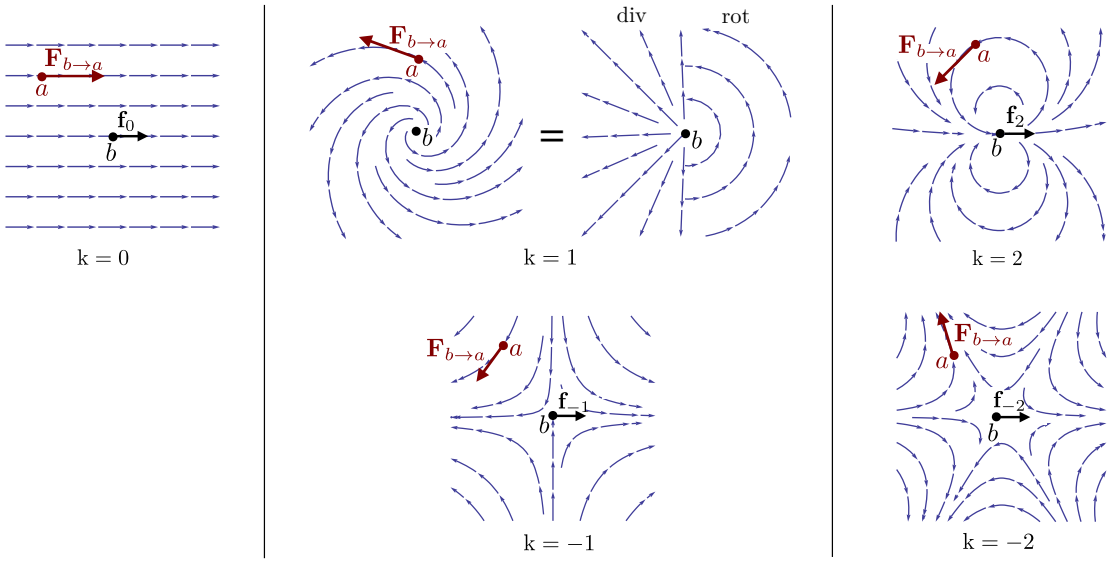


**Figure 1.34** – Sketch of the first modes of the Fourier expansion Eq. (1.127). The force exerted by particle $b$ on particle $a$ is deduced from the field $\mathbf{F}_{b\to a}(\mathbf{r}-\mathbf{r}_b, \hat{\mathbf{p}}_a, \hat{\mathbf{p}}_b)$ at the position $\mathbf{r} = \mathbf{r}_a$. For k ≠ 1, the force field breaks the rotational symmetry, its direction is set by the vector $\mathbf{f}_{\rm k}$. We recover the symmetries of a standard multipolar expansion for k > 0, while the k < 0 components have negative topological charges. Note that the spiral field k = 1 is the linear superposition of a curl-free and of a divergence-less monopolar fields.

We have classified all the possible symmetries of the fields that cause the particle reorientation. In order to fully prescribe the orientational dynamics, we now have to specify how the $\mathbf{f}_k$s relate to the particle orientations and relative distance. In order to do so, we focus on three types of interactions which encompass most of the numerical and experimental systems.

## 4 Potential interactions between isotropic particles

We first consider the simplest possible setup: isotropic particles interacting via potential interactions. $\mathbf{F}_{a\to b} = -\nabla_a U(r_{ab})$ derives from a potential $U(r_{ab})$ which only depends on the interparticle distance. Consequently, $\mathbf{F}_{a\to b}$ readily reduces to the sole curl-free part of the mode $k = 1$ in Eq. (1.127). The force field has the symmetry of a monopole, with a strength $f_1^{\text{div}}(r_{ab}) = -\partial_{r_{ab}} U(r_{ab})$, it results in attractive or repulsive couplings. Such potential interactions have been studied in a number of numerical models, see e.g. [55, 74, 80, 100, 128]. For instance, d'Orsogna *et al.* demonstrated that forces deriving from a Morse potential can lead to the emergence of a number of patterns all having an a rotational symmetry, such as vortices, rings and circular clumps [74]. We stress that potential forces cannot explicitly couple the velocities of isotropic particles. However we will show in Sect. 6, and in Appendix C, that potential forces can yield net alignment interactions between slender bodies.

## 5 Inelastic collisions between isotropic particles

We now turn to a more general situation and assume that the particles undergo physical two-body collisions, where $\mathbf{F}_{a\to b}$ could also be associated to a dissipative process. However, we still restrain here to the situation where $\mathbf{F}_{a\to b}$ is invariant upon Galilean transformations. In other words, $\mathbf{F}_{a\to b}$ is assumed to only depend on the relative position, $\mathbf{r}_{ab}$, and on the relative orientation/velocity, $\hat{\mathbf{p}}_a - \hat{\mathbf{p}}_b$. The coefficients of the Fourier series hence depend only on $\hat{\mathbf{p}}_a - \hat{\mathbf{p}}_b$, and the vector coefficients $\mathbf{f}_{k\neq 1}$ in Eq. (1.127) are all oriented along $\hat{\mathbf{p}}_a - \hat{\mathbf{p}}_b$:

$$\mathbf{f}_k = f_k(r_{ab}, |\hat{\mathbf{p}}_a - \hat{\mathbf{p}}_b|)\,(\hat{\mathbf{p}}_a - \hat{\mathbf{p}}_b). \tag{1.128}$$

It follows from Eq. (1.127) that $\mathbf{F}_{b\to a} = -\mathbf{F}_{a\to b}$. Even though the self-propulsion mechanism does not conserve momentum, see Eq. (1.124), the invariance of the forces upon Galilean transformations implies that they obey the Newton's third law. This situation typically corresponds to the model for vibrated polar disks introduced in [219]. Weber *et al.* studied numerically a system of polar grains set in motion by the vibration of a substrate and interacting via short-range inelastic collisions [68, 94, 120, 144]. They model the interactions by the spring-and-dash-pot model and assume that $\mathbf{F}_{a\to b} = -\lambda[(\hat{\mathbf{p}}_a - \hat{\mathbf{p}}_b)\cdot\hat{\mathbf{r}}_{ab}]\hat{\mathbf{r}}_{ab} + \kappa(d - r_{ab})\hat{\mathbf{r}}_{ab}$. The first term is associated with viscous friction, and the last term corresponds to elastic repulsion for $r_{ab} < d$. They observed numerically that such inelastic collisions can lead to velocity alignment interactions, thereby giving rise to a macroscopic polar order. In the classification given by Eq. (1.127), the force corresponds to a combination of the three components $k = 0$, 1 and 2, where $\mathbf{f}_0 = \mathbf{f}_2 = -(\lambda/2)(\hat{\mathbf{p}}_a - \hat{\mathbf{p}}_b)$ and $f_1^{\text{div}} = \kappa(d - r_{ab})$. Beyond this specify model which beautifully accounts for experimental results, the present framework makes it possible to provide a clear design rule for collision-induced velocity alignment at the two-particle level. The lowest-order mode of $\mathbf{F}_{a\to b}$, $\mathbf{f}_0 = f_0(r_{ab}, |\hat{\mathbf{p}}_a - \hat{\mathbf{p}}_b|)\,(\hat{\mathbf{p}}_a - \hat{\mathbf{p}}_b)$, is the only one that promotes a net polar alignment regardless of the two particles conformation provided that $f_0 < 0$ ($f_0 > 0$ would result in anti-alignement interactions). Particles interacting via $\mathbf{f}_0$ evolve according to

$$\partial_t \hat{\mathbf{p}}_a = -f_0(r_{ab}, |\hat{\mathbf{p}}_b - \hat{\mathbf{p}}_a|)\,(\mathbb{I} - \hat{\mathbf{p}}_a\hat{\mathbf{p}}_a)\cdot\hat{\mathbf{p}}_b. \tag{1.129}$$

Consequently, any other contribution to the force expansion, Eq. (1.127), would compete with this velocity-alignment rule and, in principle, could yield macroscopic states with more complex symmetries that a mere polar phase.

# 6 Nonreciprocal interactions.

We now consider forces that are not necessarily invariant upon Galilean transformations, and therefore relax the reciprocal condition. $\mathbf{F}_{a\to b}$ can now be different from $-\mathbf{F}_{b\to a}$. Prominent instances are: (i) hydrodynamic interactions between simmers [37, 185]: when swimming in a liquid, particle $b$ creates a flow field that causes particle $b$ to reorient in this flow, thereby yielding effective long-range interactions. (ii) Polar phoretic particles respond to the local variations of a scalar quantity (chemical potential [4, 154, 204], temperature [112]). They are also prone to align in the phoretic field induced by their neighbors [28, 181]. More generally, we here describe particles that reorient in a field originated from its neighbors. Note that this broader class encompasses the potential interactions that we first considered. The field in which the particle aligns would precisely correspond to the gradient of the potential.

In all that follows, we denote by $\mathbf{h}(\mathbf{r}-\mathbf{r}_b,\hat{\mathbf{p}}_b)$ the field created by particle $b$ at position $\mathbf{r}$. We assume that $\mathbf{h}$ depends on time only via the particles' conformation (this hypothesis corresponds to a zero-Peclet number approximation in the context of phoretic particles) and that it does not dependent on $\mathbf{p}_a$. This approximation is well-suited in a far-field description, since at long distance the orientation of particle $a$ does not modify the field induced by particle $b$.

We now have to specify how the particle reorients in the external field $\mathbf{h}$ to fully define the expression of $\mathbf{F}_{a\to b}$. In view of gaining more physical intuition, we first introduce a prototypical dumbbell model that can be simply solved.

## 6.1 Self-propelled dumbbells

We consider dumbbells made of two rigidly connected disks separated by a distance $\ell$, Fig. 1.35A. Looking at the motion of the dumbbell $a$, we denote by $\mathbf{R}_a^{(1)}$ and $\mathbf{R}_a^{(2)}$ the positions of the two disks. We assume that the particle propels along its main axis: $\hat{\mathbf{p}}_a = (\mathbf{R}_a^{(1)}-\mathbf{R}_a^{(2)})/\ell$. The dynamics of the dumbbell is then modeled as follows. Both disks respond linearly to the field $\mathbf{h}(\mathbf{R}-\mathbf{r}_b,\hat{\mathbf{p}}_b)$ exerted by particle $b$, where $\mathbf{R}=\mathbf{R}_a^{(j)}$, $j=1,2$. As thoroughly demonstrated in Appendix C, the equation of motion of the dumbbell orientation then reduces to:

$$\partial_t\hat{\mathbf{p}}_a = (\mathbb{I}-\hat{\mathbf{p}}_a\hat{\mathbf{p}}_a)\cdot\left[\alpha\mathbf{h}(\mathbf{r}_a-\mathbf{r}_b,\hat{\mathbf{p}}_b)+\beta(\hat{\mathbf{p}}_a\cdot\nabla)\mathbf{h}\right], \tag{1.130}$$

where $\alpha$ and $\beta$ are two constant scalar quantities. This equation correspond to Eq. (1.125) with $\mathbf{F}_{a\to b}$ given by:

$$\mathbf{F}_{a\to b} = \alpha\mathbf{h}(\mathbf{r}_a-\mathbf{r}_b,\hat{\mathbf{p}}_b)+\beta(\hat{\mathbf{p}}_a\cdot\nabla)\mathbf{h}+\mathscr{O}(\ell^2\nabla^2). \tag{1.131}$$

We also show in Appendix C that $\alpha$ can either be a positive or a negative quantity depending of the relative mobility coefficients of the two disks. Hence two different behaviors are obtained. If the two disks are *not* identical (polar dumbbell), $\alpha\neq 0$ and the force is $\mathbf{F}_{a\to b}=\alpha\mathbf{h}(\mathbf{r}_a-\mathbf{r}_b,\hat{\mathbf{p}}_b)+\mathscr{O}(\ell\nabla)$. The dumbbell aligns with, or opposite to $\mathbf{h}(\mathbf{r}_a-\mathbf{r}_b,\hat{\mathbf{p}}_b)$. Conversely, if the two disks are identical, then $\alpha=0$ and the first term in Eq. (1.130) vanishes. The force then reduces to $\mathbf{F}_{a\to b}=\beta(\hat{\mathbf{p}}_a\cdot\nabla)\mathbf{h}$, and the dumbbell aligns nematically in a direction set by the field gradient. This minimalist setup already shows that multiple field alignment rules can exist. We now go beyond this specific picture and discuss more generally the polar and nematic cases.

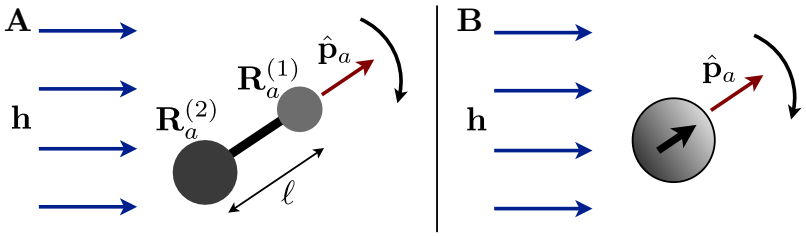


**Figure 1.35** – Polar alignment in an external field $\mathbf{h}$. **A**– An asymmetric dumbbell reorients in the field. **B**– An isotropic particle carrying a polar internal structure can also align its velocity with the field.

## 6.2 Polar alignment in an induced field

We first assume polar alignment in the direction of the field, which, regardless of the shape of the particle, translates into:

$$\mathbf{F}_{a\to b} = \alpha\,\mathbf{h}(\mathbf{r}_a - \mathbf{r}_b, \hat{\mathbf{p}}_b), \tag{1.132}$$

where $\alpha$ is here a phenomenological coefficient. The force is independent of $\hat{\mathbf{p}}_a$. As a consequence, the coefficients of the expansion in Eq. (1.127) only depend on $r_{ab}$ and $\hat{\mathbf{p}}_b$, and the scalar coefficients $f_1^{\rm div}$ and $f_1^{\rm rot}$ solely depend on the interparticle distance. In addition, the vector coefficients $\mathbf{f}_{k\neq 1}$ are necessarily oriented along $\hat{\mathbf{p}}_b$:

$$\mathbf{f}_k = f_k(r_{ab})\hat{\mathbf{p}}_b. \tag{1.133}$$

We illustrate this result with three concrete examples. (i) This situation has been considered in the context of interacting polar swimmers in confinement [37, 125], and of the motion of biofilament in plant cytoskeleton [224]. For confined swimmers, Eq. (1.127) reduces to the sole dipolar term (k = 2) which reflects the potential flow induced by any type of self-propelled object in a rigidly confined liquid film. In a different context, Kumar *et al.* have demonstrated experimentally and numerically that pointy rods lying on a shaken bed of isotropic grains experience self-propulsion and velocity alignment interactions [122]. The rods interact effectively as they align locally with the polar displacement field induced by the motion of their neighbors on top of the shaken bead layer. (ii) This type of coupling is also responsible for the emergence of flocking patterns and of spontaneously flowing phases in the ensembles of colloidal rollers introduced in [36]. The velocity of a roller aligns in the direction of the flow field induced by the surrounding motile colloids. As show in [36] (supplementary materials), within a far-field approximation, the roller-roller interaction combines the first terms of Eq. (1.127), k = 0, 1 and 2. We emphasize that the colloidal rollers have a perfectly isotropic shape, however their velocity very quickly relaxes in the direction of their dipolar electric-charge distribution. This polar internal degree of freedom is responsible for the polar-alignement rule in the external field, see Fig. 1.35B. (iii) Finally this type of coupling also encompasses the interactions used in agent-based models for collective motion, provided that they involve pairwise-additive interactions. In all these sequels of the seminal Vicsek model [215], see e.g. [25, 79, 156], the interactions exactly correspond to the first Fourier mode, $\mathbf{f}_0 = f_0(r_{ab})\hat{\mathbf{p}}_b$. On top of this velocity-alignment rule, short-range repulsion and long-range attraction have also been considered to reproduce the morphology of cohesive flocks akin to animal populations [49, 57, 92]. They are associated with the k = 1 component of the multipole expansion.

## 6.3 Nematic alignment in an induced field

In line with the previous discussion, and with Eq. (1.130), some motile particle, say $a$, can also align nematically with the field $\mathbf{h}(\mathbf{r}_a - \mathbf{r}_b, \hat{\mathbf{p}}_b)$ induced by particle $b$. This condition translates into the following generic expression for the induced force:

$$\mathbf{F}_{a\to b} = \beta\,\mathbf{N}(\mathbf{r}_a - \mathbf{r}_b, \hat{\mathbf{p}}_b)\cdot\hat{\mathbf{p}}_a, \tag{1.134}$$

were $\mathbf{N}$ is a tensor that can be constructed from the field $\mathbf{h}$ and the $\nabla$-operator, depending on the type of induced field and particle shape we are talking about. For instance, for the symmetric dumbbells $\mathbf{N}$ takes the simple form: $\mathbf{N} = \nabla\mathbf{h}$, see Eq. (1.130). More generally, when the nematic-alignment rule arises from the slenderness of the particle, the expression of the tensor $\mathbf{N}$ is given by the so-called Jeffery's equation first introduced in the context of fluid mechanics [111, 183, 184]. Eq. (1.134) implies that the force $\mathbf{F}_{b\to a}$ linearly depends on $\hat{\mathbf{p}}_a$. The amplitudes of the Fourier coefficients, $f_k$ in Eq. (1.126), therefore include a factor $\hat{\mathbf{p}}_a\cdot\hat{\mathbf{r}}_{ab}$ or $\hat{\mathbf{p}}_a\cdot\hat{\mathbf{p}}_b$, and the vectors $\mathbf{f}_{k\neq 1}$ in Eq. (1.127) are oriented along $\hat{\mathbf{p}}_b$. The k-coefficient of the classification in Eq. (1.127) takes the generic form:

$$\mathbf{f}_k = \left[f_k^{(pp)}(r_{ab})\hat{\mathbf{p}}_a\cdot\hat{\mathbf{p}}_b + f_k^{(rp)}(r_{ab})\hat{\mathbf{p}}_a\cdot\hat{\mathbf{r}}_{ab}\right]\hat{\mathbf{p}}_b. \tag{1.135}$$

An important example concerns the zeroth-order term: both the $f_0^{pp}$ and the $f_0^{rp}$ contributions promote nematic alignment between the two interacting particles $a$ and $b$ for this first lowest-order term. We are now aware of any experimental realization, where self-propelled particles would experience nematic interactions mediated by an induced field. For instance in the seminal pusher/puller model of Saintillan et al. Active swimmer align nematically in the far-field flow induced by their motion. However these hydrodynamic interactions only correspond to the k = +3 mode in Eq. (1.127), thereby yielding complex spatiotemporal fluctuations in swimmer suspensions which cannot support nematic order [183, 184].

### 6.4 Higher-order symmetries

For particles having more complex shapes, the reorientation in the field in principle involves higher symmetries than the polar or nematic modes. For instance, the force can include higher-order terms such as $\mathbf{F}_{a\to b} = \gamma \mathbf{M}(\mathbf{r}_a - \mathbf{r}_b, \hat{\mathbf{p}}_b) : \hat{\mathbf{p}}_a \hat{\mathbf{p}}_a$, where $\mathbf{M}$ is a third-rank tensor build from the field $\mathbf{h}$ and its derivatives. Following the same procedure, classifying the interactions associated with these higher-order couplings is straightforward.

## 7 Discussion

Building only on symmetry arguments, we have introduced a formal classification of all the possible interactions between self-propelled particles. This classification does not only rationalize all the previously introduced models within a unique formal framework, it also brings two unanticipated perspectives on the physics of interacting motile bodies.

Firstly, from a technical perspective, the classification defined by Eq. (1.125) makes it possible to quickly identify the salient features of the two-body dynamics, even if the interactions take a complex form. For instance, it offers a simple mean to check wether the interactions promote velocity alignment (polar or nematic). In practical terms, Eqs. (1.125) and (1.127) imply that that $\mathbf{F}_{b\to a}$ supports a net alignment of the velocities only if its zero mode does not vanish. Equivalently, a simple criteria for two-body alignment is that the angular integral of the two-body force does not vanish. From Eq. (1.126), it necessarily takes the simple form:

$$\int \mathbf{F}_{b\to a}\, \mathrm{d}\varphi_{ab} = \epsilon \hat{\mathbf{p}}_b + \epsilon' \hat{\mathbf{p}}_a \tag{1.136}$$

where the $\hat{\mathbf{p}}_a$ term does not contribute to the orientational dynamics, see Eq. (1.125). Any nonzero value for $\epsilon$ yields alignment. To distinguish between interactions that promote polar or nematic ordering, one should also look at the dependence on $\hat{\mathbf{p}}_a$ of $\epsilon$. If $\epsilon$ is unchanged as the particle $a$ changes its orientation ($\hat{\mathbf{p}}_a \to -\hat{\mathbf{p}}_a$), then $\mathbf{F}_{a\to b} \sim \hat{\mathbf{p}}_b$ and leads to polar alignment in Eq (1.125). In contrast, if the sign of $\epsilon$ changes as particle $a$ changes its orientation ($\hat{\mathbf{p}}_a \to -\hat{\mathbf{p}}_a$), then $\mathbf{F}_{a\to b}$ leads to nematic alignment in Eq (1.125).

Secondly, going back to the initial motivation of this work, the phase of an ensemble of interacting particles is set by the symmetries of the interactions at the microscopic level. Although this statement is obvious for equilibrium systems, it has been surprisingly overlooked when considering active matter. Until now, all the theoretical models and the (quantitatively characterized) experimental realizations of active matter involving physical interactions have been restricted to the k = 0, 1, 2, 3 modes of the classification (1.127). Eq. (1.127) demonstrate that there exist a number of possible interactions rules between self-propelled particles that have not been considered at all, even though they should yield novel macroscopic phases of active matter. A special attention should be devoted to the k = −1 and k = −2 modes of Eq. (1.127). All the kinetic theories of active matter confirmed that interactions with a low angular symmetry strongly contribute to the large-scale hydrodynamics of these systems. These types of interactions are therefore expected to significantly contribute to the phase behavior of unanticipated active materials.

This work was partly funded by ANR grant MITRA and by the Institut Universitaire de France.

## Appendix A. Impact of small fluctuations of the particle speed

In this section, we further extend the range of validity of the equations of motion (1.124)–(1.125). Let us consider the more general case where small fluctuations of the particle speed are allowed. Following e.g. [74, 128], we model self-propulsion by a non-linear friction force and assume the following equations of motion:

$$\partial_t \mathbf{r}_a = \mathbf{v}_a, \tag{1.137}$$

$$\partial_t \mathbf{v}_a = \frac{1}{\tau}(1-|\mathbf{v}_a|)\,\mathbf{v}_a + \sum_{b\neq a} \mathbf{F}_{b\to a} + \boldsymbol{\xi}_a(t). \tag{1.138}$$

Eq. (1.138) is a momentum conservation equation. The first term on the r.h.s. models self-propulsion. It describes the conversion of internal energy into translational motion, and accounts for dissipative friction forces. As a result, the particle speed relaxes to $|\mathbf{v}|=1$. In addition, $\sum \mathbf{F}_{b\to a}$ is the total external force acting on particle $a$. We also include here a possible noise term $\boldsymbol{\xi}_a(t)$ with zero mean and variance $\langle \boldsymbol{\xi}_a(t)\boldsymbol{\xi}_a(t')\rangle = 2\mathrm{D}\delta(t-t')\mathbb{I}$. For the sake of clarity we discard active noise, which would stem from fluctuations in the propulsion mechanism and could be easily included as well, see e.g. [177].

We focus on small fluctuations of the speed, i.e. we assume that $\tau\mathrm{D} = \mathscr{O}(\epsilon)$ and $\tau\mathrm{F}_{b\to a} = \mathscr{O}(\epsilon)$, where $\epsilon \ll 1$. It is worth noting that Eq. (1.138) is the only possible expression for the propulsion force at first order in $\epsilon$. For sake of simplicity we restrain here to particles moving in a 2D space, as the generalization to 3D is straightforward.

In order to obtain stochastic equations for the particle position and orientation, we have to integrate out the speed fluctuations. This is easily done by using polar coordinates. We introduce $\mathbf{v}_a = (1+u_a)\hat{\mathbf{p}}_a$, where $u_a = \mathscr{O}(\epsilon)$, and we describe the particle orientation by the polar angle $\theta_a$: $\hat{\mathbf{p}}_a = (\cos\theta_a, \sin\theta_a)$. Similarly, we write the force as: $\sum_b \mathbf{F}_{b\to a} \equiv \mathrm{F}_a(t)\big(\cos\phi_a(t), \sin\phi_a(t)\big)$. Eqs. (1.137)–(1.138) are recast into:

$$\partial_t \mathbf{r}_a = (1+u_a)\hat{\mathbf{p}}_a, \tag{1.139}$$

$$\tau\partial_t u_a = -u_a + \tau\mathrm{D} + \tau\mathrm{F}_a\cos(\theta-\phi_a) + \xi^u_a(t), \tag{1.140}$$

$$\tau\partial_t \theta_a = -\tau\mathrm{F}_a\sin(\theta-\phi_a) + \tau\xi^\theta_a(t) + \mathscr{O}(\epsilon^2), \tag{1.141}$$

where $\xi^u_a$ and $\xi^\theta_a$ are independent white noises with zero mean and variance $\langle \xi^u_a(t)\xi^u_a(t')\rangle = \langle \xi^\theta_a(t)\xi^\theta_a(t')\rangle = 2\mathrm{D}\delta(t-t')$. The term $\tau\mathrm{D}$ in Eq. (1.140) is a spurious drift term that classically results from the Stratonovich discretization scheme used here to define the noise terms, see e.g. [175].

Eqs. (1.140)–(1.141) involve two well separated time scales. In Eq. (1.140), the particle speed relaxes to $|\mathbf{v}|=1$ in a time $\sim\tau$. The force and noise terms only give rise to subdominant corrections. Conversely, in Eq. (1.141) the particle orientation evolves on a much longer time scale $\sim\tau/\epsilon$. Indeed, self-propulsion corresponds to a spontaneous breaking of the rotational symmetry, the orientation is not constrained to relax toward a position set by any potential. Only the external forces and noise dictate the orientational dynamics.

We now want to describe the particle dynamics on time scales much longer than $\tau$. In other words, we want to average the dynamics over the fast variations of the particle speed. Firstly, we integrate Eq. (1.140) and combine this result with Eq. (1.139), which yields

$$\begin{aligned}\partial_t \mathbf{r}_a = {}& (1+\tau\mathrm{D})\hat{\mathbf{p}}_a + \tau\xi_t(t)\,\hat{\mathbf{p}}_a \\ & + \sum_b \int \mathrm{G}(t-t')\,\tau\,[\mathbf{F}_{b\to a}(t')\cdot\hat{\mathbf{p}}_a(t')]\hat{\mathbf{p}}_a(t)\,\mathrm{d}t',\end{aligned} \tag{1.142}$$

and

$$\partial_t \theta_a = -\mathrm{F}_a\sin(\theta-\phi_a) + \xi^\theta_a(t), \tag{1.143}$$

where $\xi_t(t)$ is a colored translational noise, with zero mean and correlations defined by $\langle \xi_t(t)\xi_t(t')\rangle = (\mathrm{D}/\tau)\exp\big[-|t-t'|/\tau\big]$. The kernel G is given by $\mathrm{G}(t) = \tau^{-1}\exp[-(t)/\tau]\,\Theta(t)$, where $\Theta$ is the Heaviside step function. When considering only time variations at scales much larger than $\tau$, the time

correlations of the translational noise vanish, $\langle \xi_t(t)\xi_t(t')\rangle \sim 2\mathrm{D}\delta(t-t')$ and we recover a simple Markovian kernel $\mathrm{G}(t-t') \sim \delta(t-t')$. Coming back to vector notations for the particle orientation, the two coarse-grained equations of motion are:

$$\partial_t \mathbf{r}_a = \hat{\mathbf{p}}_a + \tau \sum_b \mathbf{F}_{b\to a}\cdot\hat{\mathbf{p}}_a\hat{\mathbf{p}}_a + \tau\xi_t(t)\,\hat{\mathbf{p}}_a, \tag{1.144}$$

$$\partial_t \hat{\mathbf{p}}_a = (\mathbb{I} - \hat{\mathbf{p}}_a\hat{\mathbf{p}}_a)\cdot\left[\sum_b \mathbf{F}_{b\to a}(t) + \boldsymbol{\xi}_a(t)\right]. \tag{1.145}$$

We recover Eq. (1.125) for the orientation dynamics. The velocity of the particle, Eq. (1.144), is the sum of the self-propulsion $\hat{\mathbf{p}}_a$ and additional advection terms due to the interactions and the noise. However, these contributions correspond to small corrections as $\tau\mathrm{F}_{b\to a}$ and $\tau\mathrm{D}$ were assumed to be of order $\epsilon$. The equations of motion that we assumed in the main text therefore correspond to the limit $\tau \to 0$ of this more general model. In other words, Eqs. (1.124) and (1.125) are valid when the relaxation of the speed towards $|\mathbf{v}| = 1$ is much faster than the modification of the particle's direction due to interactions and noise.

## Appendix B. Generalization to 3D space

The 3D generalization of Eq. (1.126) is a spherical harmonics expansion, and contains a much larger number of terms. However, most of them are discarded by the symmetries of the interactions. For potential interactions between isotropic particles, the force is radial. For Galilean-invariant interactions, the force field depends on a unique vector, $\hat{\mathbf{u}} = (\hat{\mathbf{p}}_b - \hat{\mathbf{p}}_a)/|\hat{\mathbf{p}}_b - \hat{\mathbf{p}}_a|$. Its expression is therefore invariant by rotation around the $\hat{\mathbf{u}}$-axis. For particles aligning in a field, the force field also depends on a unique vector, $\hat{\mathbf{u}} = \hat{\mathbf{p}}_b$, if the alignment rule is polar. The case of particles aligning nematically is readily inferred from the polar case by adding a factor $\hat{\mathbf{p}}_a\cdot\hat{\mathbf{p}}_b$ or $\hat{\mathbf{p}}_a\cdot\hat{\mathbf{r}}_{ab}$ in the expression of the force.

These symmetry requirements greatly simplify the spherical harmonics expansion. In an orthonormal basis $(\hat{\mathbf{x}},\hat{\mathbf{y}},\hat{\mathbf{u}})$, we find:

$$\begin{aligned}\mathbf{F}_{b\to a} = f_0\hat{\mathbf{u}} + \sum_{\mathrm{k}\geq 1}\Bigg[ f_{\mathrm{k}}\begin{vmatrix} \mathrm{Y}_{\ell,x}(\hat{\mathbf{r}}_{ab}) & \\ \mathrm{Y}_{\ell,y}(\hat{\mathbf{r}}_{ab}) & + f_{-\mathrm{k}}\\ \mathrm{Y}_{\ell,0}(\hat{\mathbf{r}}_{ab}) & \end{vmatrix}\begin{matrix} -\mathrm{Y}_{\ell,x}(\hat{\mathbf{r}}_{ab}) \\ -\mathrm{Y}_{\ell,y}(\hat{\mathbf{r}}_{ab}) \\ \mathrm{Y}_{\ell,0}(\hat{\mathbf{r}}_{ab})\end{matrix} \\ + \Omega_{\mathrm{k}}\begin{vmatrix} -\mathrm{Y}_{\ell,y}(\hat{\mathbf{r}}_{ab}) \\ \mathrm{Y}_{\ell,x}(\hat{\mathbf{r}}_{ab}) \\ 0 \end{vmatrix}\Bigg],\end{aligned} \tag{1.146}$$

where $\mathrm{Y}_{\ell,m}$ are the spherical harmonics, $\mathrm{Y}_{\ell,x} = (\mathrm{Y}_{1,-1} - \mathrm{Y}_{1,1})/2$ and $\mathrm{Y}_{\ell,y} = -(\mathrm{Y}_{1,-1} + \mathrm{Y}_{1,1})/(2i)$. In vector notations, the above equation takes a much more compact form:

$$\begin{aligned}\mathbf{F}_{b\to a} = f_0\hat{\mathbf{u}} + f_1\hat{\mathbf{r}}_{ab} + f_{-1}(2\hat{\mathbf{u}}\hat{\mathbf{u}} - \mathbb{I})\cdot\hat{\mathbf{r}}_{ab} + \Omega_1\hat{\mathbf{u}}\times\hat{\mathbf{r}}_{ab} \\ + f_2\hat{\mathbf{u}}\cdot(3\hat{\mathbf{r}}_{ij}\hat{\mathbf{r}}_{ij} - \mathbb{I}) + \ldots\end{aligned} \tag{1.147}$$

The components $f_{\mathrm{k}>0}$ correspond to a standard multipolar series, they have the symmetries of monopolar, dipolar, quadrupolar fields etc. The coefficients $f_{-1}$ and $\Omega_{\mathrm{k}}$ are associated with elongational and rotational fields, respectively.

## Appendix C. Equations of motion for a dumbbell-shaped particle

We consider particles composed of two rigidly connected disks separated by a fixed distance $\ell$. Looking at the motion of particle $a$, we denote by $\mathbf{R}_a^{(1)}$ and $\mathbf{R}_a^{(2)}$ the positions of the two disks. We assume here that the dumbbell propels along its principal axis: $\hat{\mathbf{p}}_a = (\mathbf{R}_a^{(1)} - \mathbf{R}_a^{(2)})/\ell$. The dynamics of the dumbbell is modeled as follows. We assume that the disk $j$ propels itself in the direction $\hat{\mathbf{p}}_a$

and experiences the force field $\mathbf{h}(\mathbf{R}_a^{(j)} - \mathbf{r}_b, \hat{\mathbf{p}}_b)$ exerted by particle $b$ ($j = 1$ or 2). The corresponding equations of motion are:

$$\partial_{tt}\mathbf{R}_a^{(1)} = \frac{1}{\tau_1}\left(\hat{\mathbf{p}}_a - \partial_t \mathbf{R}_a^{(1)}\right) + \mathbf{h}(\mathbf{R}_a^{(1)} - \mathbf{r}_b, \hat{\mathbf{p}}_b) + \mathbf{F}_a^{(2)\to(1)}, \tag{1.148}$$

$$\partial_{tt}\mathbf{R}_a^{(2)} = \frac{1}{\tau_2}\left(\hat{\mathbf{p}}_a - \partial_t \mathbf{R}_a^{(2)}\right) + \mathbf{h}(\mathbf{R}_a^{(2)} - \mathbf{r}_b, \hat{\mathbf{p}}_b) + \mathbf{F}_a^{(1)\to(2)}, \tag{1.149}$$

where, the first term on the r.h.s accounts for the competition between the propulsion and the drag force experienced by the two disks. The phenomenological drag coefficients $\tau_1^{-1}$ and $\tau_2^{-1}$ depend on the sizes of the disks. The internal tension forces $\mathbf{F}_a^{(2)\to(1)}$ and $\mathbf{F}_a^{(1)\to(2)}$ are Lagrange multipliers that preserve the inextensibility constraint $|\mathbf{R}_a^{(1)} - \mathbf{R}_a^{(2)}| = \ell$.

The timescales $\tau_1$ and $\tau_2$ control the relaxation of the particle speed towards $\hat{\mathbf{p}}_a$. As we did it in Appendix A, we assume that they are much faster than the evolution of the force field $\mathbf{h}$. In this overdamped limit, the dynamics of the dumbbell becomes:

$$\partial_t \mathbf{R}_a^{(1)} = \hat{\mathbf{p}}_a + \tau_1 \mathbf{h}(\mathbf{R}_a^{(1)} - \mathbf{r}_b, \hat{\mathbf{p}}_b) + \tau_1 \mathbf{F}_a^{(2)\to(1)}, \tag{1.150}$$

$$\partial_t \mathbf{R}_a^{(2)} = \hat{\mathbf{p}}_a + \tau_2 \mathbf{h}(\mathbf{R}_a^{(2)} - \mathbf{r}_b, \hat{\mathbf{p}}_b) + \tau_2 \mathbf{F}_a^{(1)\to(2)}. \tag{1.151}$$

In addition, the inextensibility condition imposes $(\partial_t \mathbf{R}_a^{(1)} - \partial_t \mathbf{R}_a^{(2)}) \cdot \hat{\mathbf{p}}_a = 0$. Introducing the center of drag of the dumbbell, $\mathbf{r}_a = (\tau_2 \mathbf{R}_a^{(1)} + \tau_1 \mathbf{R}_a^{(2)})/(\tau_1 + \tau_2)$, and assuming that the variations of the force field $\mathbf{h}(\mathbf{r} - \mathbf{r}_b, \hat{\mathbf{p}}_b)$ occur on large length scales compared to the particle size, the equations of motion are:

$$\partial_t \mathbf{r}_a = \hat{\mathbf{p}}_a + \bar{\tau}\left[2\mathbf{h}(\mathbf{r}_a - \mathbf{r}_b, \hat{\mathbf{p}}_b) + \mathbf{F}_a^{(1)\to(2)} + \mathbf{F}_a^{(2)\to(1)}\right], \tag{1.152}$$

$$\partial_t \hat{\mathbf{p}}_a = (\mathbb{I} - \hat{\mathbf{p}}_a\hat{\mathbf{p}}_a) \cdot \left[\alpha \mathbf{h}(\mathbf{r}_a - \mathbf{r}_b, \hat{\mathbf{p}}_b) + \beta(\hat{\mathbf{p}}_a \cdot \nabla)\mathbf{h}\right], \tag{1.153}$$

where $\bar{\tau} = \tau_1\tau_2/(\tau_1 + \tau_2)$, $\alpha = (\tau_1 - \tau_2)/\ell$ and $\beta = -(\tau_1^2 + \tau_2^2)/(\tau_1 + \tau_2)$. Eq. (1.152) describes the translational motion of the particle. Note that the advection terms are are subdominant in the small-$\bar{\tau}$ limit (as we explained it in Appendix A. The orientational dynamics of the dumbbell due to interactions with particle $b$ is described by Eq. (1.153). This equation is identical to Eq. (1.125) with the effective force

$$\mathbf{F}_{a\to b} = \alpha \mathbf{h}(\mathbf{r}_a - \mathbf{r}_b, \hat{\mathbf{p}}_b) + \beta(\hat{\mathbf{p}}_a \cdot \nabla)\mathbf{h} + \mathcal{O}(\ell^2\nabla^2). \tag{1.154}$$

CHAPTER 2

# Emergent spatial structures in flocking models

In the previous chapter, an important feature of the colloidal population has not been explained: at the onset of collective motion, polar bands form and propagate. As a matter of fact, this experimental observation reflects a long-standing theoretical problem. In all models of self-propelled spins interacting via short-range alignment rules, heterogeneous spatial patterns having the form of propagating bands are generically found. As a consequence, any "mean-field" theory focusing on spatially-homogeneous states fails at describing the transition to collective motion. This fundamental problem has been extensively addressed numerically in different models, and a variety of band patterns have been reported. However, no unifying theory exists to account for the shape of these spatial patterns.

In this chapter, we introduce a dynamical-system framework that rationalizes the experimental and numerical phenomenology reported so far. We show that the nonlinear excitations of hydrodynamic theories exactly correspond to the three types of patterns that were hitherto observed. We analyze their shape and their existence domain, and suggest a link with the first-order nature of the transition to collective motion.

This work was done in collaboration with A. Solon, A. Peshkov, H. Chaté, T. Dauxois, J. Tailleur and V. Vitelli.

This chapter is organized as follows.

1) In the first section, we recall the context of this work. We classify the spatial patterns reported so far and we discuss the connection with the order of the transition to collective motion.

2) We then define the hydrodynamic equations which we study. They are introduced in section 2 from simple phenomenological considerations.

3) In section 3, we summarize the dynamical-system approach that we use to analyze the nonlinear solutions of the hydrodynamic theories. This is the main part of this work. It is thoroughly explained in the article "Emergent spatial structures in flocking models: a dynamical system insight", which is reproduced p. 105.

4) Finally, we use this method to build a realistic description of the band patterns observed in numerical simulations.

# 1 Emergent polar patterns at the transition to collective motion

In this section, we introduce the problem we are interested in. We recall the previous numerical and experimental results which remain poorly understood theoretically.

## 1.1 Numerical and experimental facts

We recall that, throughout this thesis, we restrict ourselves to polar active matter. We consider populations of self-propelled particles that experience alignment couplings and display polar structures at large scale. In this class of systems, much effort has been devoted to understanding the transition to collective motion from numerical simulations of the Vicsek model. In particular, the nature of the transition has been intensely debated [1, 9, 49, 216]. Although the question remains controversial in some limits, there are clear numerical evidences that the transition is *first-order* (see the careful finite-size scaling analysis carried out by H. Chaté and coworkers [49]). For instance, hysteresis has been clearly observed close to the transition point (as we recalled it in the Introduction) [49].

The first-order nature of the transition is associated with another distinctive feature: at the onset of collective motion, the system self-organizes into spatially-heterogeneous phases. Dense polar structures form and move in a disordered gas. At a first glance, this behavior seems easy to explain: first-order transitions are known to give rise to phase separations, such as a bubble of vapor coexisting with the liquid. Yet, in active systems, the polarized regions do not reduce to spherical droplets delimited by a microscopic interface, but take more complex shapes. More precisely, a number of simulations and experiments have demonstrated that the polar patterns take the form of band-shaped swarms. These patterns are shown in Fig. 2.1 [36, 49, 91, 92, 136, 141, 175, 190, 197, 216, 219]. They consist in dense regions of aligned particles that propagate in a dilute, weakly-polarized background. The bands are invariant in the direction transverse to the propagation direction. This observation is a robust feature of polar active matter. It was reported in the vast majority of numerical models based on self-propelled particles experiencing metric alignment rules, in periodic boundary conditions. Similar structures were also found in synthetic experimental populations.

Beyond their qualitative similarity, the exact shape of the dynamical patterns is not universal. It depends on the specifics of the interaction rule at the microscopic level. More precisely, the patterns which were hitherto reported take three different forms, see Fig. 2.1.

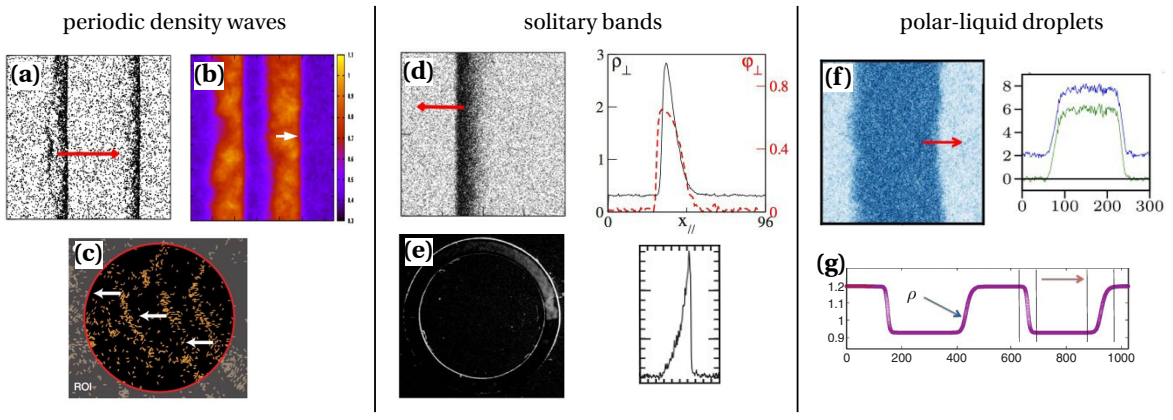


**Figure 2.1** – Band patterns in polar active matter. **(a)** Simulation of the Vicsek model; reproduced from [49]. **(b)** Simulation of a hydrodynamic theory; reproduced from [141]. **(c)** Motility assays of actin filaments; reproduced from [190]. **(d)** Simulation of the Vicsek model: a snapshot and the corresponding density (black solid line) and polarization (red dotted line) profiles; reproduced from [49]. **(e)** Colloidal rollers in a racetrack confinement and shape of the corresponding density profile; see Chapter 1. **(f)** Simulation of the active Ising model; reproduced from [197]. **(g)** Simulation of a hydrodynamic theory; reproduced from [91].

(i) *Periodic density waves*: a periodic arrangement of dense and polar structures propagates in the system [49, 92, 141, 190, 219].

(ii) *Solitary bands*: a solitonic polar structure moves in a sea of disordered particles [36, 49, 92, 175, 219]. The band is often strongly asymmetric, with a sharp front and a smooth tail.

(iii) *Polar-liquid droplets*: a droplet of polar liquid coexists with a disordered gas, the two phases being separated by thin domain walls [91, 197].

It is worth noting that, in Vicsek-like models the particles solely interact via local velocity-alignment rules. The previous results demonstrate that such interactions do not solely break the rotational symmetry, leading to polar structures. They also yield a spontaneous breaking of the *translational* symmetry: spatial patterns are formed in the absence of any attractive couplings. Elucidating this surprising behavior is a long-standing problem in active matter.

## 1.2 How to describe the transition to heterogeneous polar phases?

The conventional theoretical framework of polar active matter consists in continuum descriptions. As we already stressed it in the Introduction and in Chapter 1, the hydrodynamic theories indeed account for a phase transition between isotropic and polar states. However, it predicts that spatially-homogeneous polar phases emerge from a continuous bifurcation. Hence the observed spatial patterns cannot be explained by a simple phase-separation scenario.

A tentative hypothesis consists in investigating the role of fluctuations. In equilibrium systems, it is well known that fluctuations can make first-order a transition which is second-order at the mean field level. It is interesting to check wether a similar mechanism could explain the first-order nature of the transition to collective motion, in Vicsek-like models. There are two main scenarios of fluctuation-induced first-order phase transitions.

- Halperin, Lubensky and Ma analyzed situations in which the order parameter is coupled to a gauge field (e.g. type-I superconductors and smectic-A liquid crystals) [99]. The fluctuations of the gauge field make the transition discontinuous. Similar behaviors have been found in non-equilibrium systems, using functional-integral approaches [146]. This scenario could seem appealing in active matter, where the density field is coupled to the polarization. However, we have checked that including noise in the hydrodynamic equations, and integrating over the fluctuations of the density field, does *not* make the transition first-order. Hydrodynamic theories of active matter have no gauge structure.

- Brazowskii identified another mechanism, relevant for systems displaying a layered structure [35]. The spatial patterns arise from a linear instability of the homogeneous ordered phase. When the growth rate of the fluctuation spectrum is maximum for a finite wave-vector $q_0 \neq 0$, it has been shown that fluctuations make the transition first-order. The periodicity of the emergent pattern is then set by the most unstable wavector, $2\pi/q_0$. This scenario has been successfully applied to a number of systems (e.g. cholesteric liquid-crystals or Rayleigh-Bénard convection in the Swift-Hohenberg theory [104, 202]). Again, it could seem well-suited to understand the periodic band patterns found e.g. in the Vicsek model. However, hydrodynamic theories of active matter reveal that the most unstable wave-vector is $q_0 = 0$ (see Chapter 1, p. 35 for more details). Hence the periodicity of the structure is *not* set by any linear argument, and the Brazowskii mechanism does not hold.

Hence none of these scenarios apply to the transition to collective motion. Heterogeneous polar phases arise from a different mechanism. In this chapter, we rather analyze the non-linear solutions of hydrodynamic equations in the absence of fluctuations. This approach is justified by

previous numerical works, which showed that hydrodynamic theories support the emergence of spatial structures. Band patterns have been found from direct simulations of hydrodynamic equations in [91, 141], and solitonic solutions have been obtained numerically in [25] from a coarse-grained description of a microscopic model. Building on these observations, we analyze the shape of the propagating bands using a dynamical-system framework. We show that fluctuations are *not* required to explain the first-order nature of the transition.

## 2 A phenomenological hydrodynamic description

We now define the hydrodynamic equations which we study. Since we aim at rationalizing the various numerical and experimental observations within a unifying framework, we do not focus on a specific model. We derive phenomenological equations from simple physical arguments.

### 2.1 Generic structure of the hydrodynamic equations

We start from a simple result from kinetic theories of active matter. We consider a population of particles which propel themselves at a constant speed $v_0 = 1$. We have explained in Chapter 1 how the microscopic equations of motion can be coarse-grained. We have shown that the resulting large-scale equations couple successive hydrodynamic fields: the density $\rho(\mathbf{r}, t)$, the polarization $\mathbf{\Pi}(\mathbf{r}, t)$, the nematic-order tensor $\mathbf{Q}(r, t)$. For the sake of convenience, we also introduce the momentum field $\mathbf{W}(\mathbf{r}, t) = \rho(\mathbf{r}, t)\mathbf{\Pi}(\mathbf{r}, t)$. The evolution equations take the generic form:

$$\partial_t \rho + \nabla \cdot \mathbf{W} = 0, \tag{2.1}$$

$$\partial_t \mathbf{W} + \nabla \cdot \left( \rho \mathbf{Q} + \frac{1}{2} \rho \mathbb{I} \right) = \mathscr{F}\{\rho, \mathbf{W}, \mathbf{Q}\}. \tag{2.2}$$

Eq. (2.1) is the particle-conservation equation. The momentum equation, Eq. (2.2), involves two types of terms. First, self-propulsion results in momentum advection. This kinematic effect corresponds to the left-hand side of Eq. (2.2). Second, interactions give rise to effective forces, which are accounted for by the functional $\mathscr{F}\{\rho, \mathbf{W}, \mathbf{Q}\}$. In a population of non-interacting particles, one would find $\mathscr{F}\{\rho, \mathbf{W}, \mathbf{Q}\} = \mathbf{0}$.

Based on the numerical and experimental results, we focus on structures varying along the mean direction of motion, $x$, and invariant along the transverse $y$-direction: $\rho = \rho(x, t)$, $\mathbf{W} = W(x, t)\hat{\mathbf{x}}$, and $\mathbf{Q} = Q(x, t)(\hat{\mathbf{x}}\hat{\mathbf{x}} - \hat{\mathbf{y}}\hat{\mathbf{y}})$. Eqs. (2.1) and (2.2) reduce to:

$$\partial_t \rho + \partial_x W = 0, \tag{2.3}$$

$$\partial_t W + \partial_x \left( \rho Q + \frac{1}{2} \rho \right) = \mathscr{F}\{\rho, W, Q\}. \tag{2.4}$$

To further specify the form of the hydrodynamic equations, we now discuss the interaction term (r.h.s. of Eq. (2.4)) and the kinematic terms (l.h.s. of Eq. (2.4)) separately.

### 2.2 Interaction term: effective potential

The term $\mathscr{F}\{\rho, W, Q\}$ is responsible for the spontaneous symmetry breaking leading to polar phases. Following Toner and Tu [211, 214], we assume an expression akin to the Landau theory of phase transitions:

$$\mathscr{F} = \left( a_2 - a_4 W^2 \right) W. \tag{2.5}$$

In addition, we postulate simple density-dependences for $a_2$ and $a_4$ as follows.

- In all models based on short-ranged (metric) interaction rules, the strength of the alignment force experienced by a particle increases with the number of neighbors in the interaction radius. Hence the transition to collective motion can be reached by increasing the density. In agreement with all existing kinetic theories, close to the transition we assume a linear dependence $a_2(\rho) = \rho - \rho_c$ (in a convenient choice of units). As a consequence, Eqs. (2.2) and (2.5) predict a bifurcation from a disordered phase at $\rho < \rho_c$, with $W = 0$, to a spatially-homogeneous state with momentum $W = \sqrt{(\rho - \rho_c)/a_4}$, at $\rho > \rho_c$.

- Deep in the polar phase, $\rho \gg \rho_c$, the polarization behaves as $\Pi = W/\rho \sim \rho^{-1}\sqrt{\rho/a_4}$. We impose that it saturates to a non-zero value, $\Pi_0$, at high density. Indeed, for particles moving at a constant speed the polarization cannot be larger than 1, as $\Pi = 1$ is reached when all particles are aligned. Some models are more restrictive and impose an upper bound $\Pi_0 < 1$, as we will discuss it later. The simplest choice which ensures the saturation of the polarization is $a_4(\rho) = (\rho\Pi_0^2)^{-1}$.

In this simple approach, we restrict ourselves to alignment interactions. Note that attractive or repulsive couplings, e.g., would yield additional terms proportional to $\partial_x\rho$ (see Chapter 1) which could be treated as well.

### 2.3 Kinematic term: non-linear friction

Now that the ineraction term is fully specified, we discuss the kinematic term, $\partial_x(\rho Q + \rho/2)$. As we already noted in Chapter 1, Eqs. (2.3) and (2.4) do not define a closed set of equations. They must be complemented by an extra closure relation which links $\rho$, $W$ and $Q$.

For one-dimensional problems such as the active Ising model considered in [197], the answer is trivial: only two directions of motion are allowed ($\hat{\mathbf{x}}$ and $-\hat{\mathbf{x}}$). From the definition of the hydrodynamic fields (Chapter 1 p. 30), it is readily found that $Q = 1/2$.

In two dimensions, the problem is more complex and approximations must be done. In Chapter 1, we have established closure assumptions in two opposite limits.

(i) *Weak polarization:* most of the available kinetic theories of active matter were derived in the limit of small polarizations [25, 136]. In this regime, we consider the following form for the momentum equation[1]:

$$\partial_t W + \xi W \partial_x W = \left[ (\rho - \rho_c) - \frac{W^2}{\rho\Pi_0^2} \right] W - \lambda \partial_x \rho + D \partial_{xx} W, \tag{2.6}$$

where we have replaced the interaction term by the expression established above. The coefficients $\lambda$, $\xi$ and $D$ are independent of the density (we note that kinetic theories predict $\lambda = 1/2$, as it can can be readily seen from the limit $Q \to 0$).

(ii) *Strong polarization:* when the polarization is close to 1, we have stressed in Chapter 1 that the previous closure approximation leads to non-physical results. We have proposed another relation assuming Gaussian fluctuations around the mean direction of motion. With this ansatz, the nematic order-parameter is $Q = \Pi^4/2$ (see Chapter 1).

In that follows, we first introduce our dynamical-system approach in the weakly-polarized situation. We will then show how to build a more realistic description that interpolates between weakly- and strongly-polarized states. Before we proceed, let us make a remark on the nucleation of the band patterns.

[1] Here, we aim at introducing our approach from the simplest equations which capture the physics of flocking. Note that other terms, such as $\partial_x(W^2)$ or $(\partial_x W)(\partial_x \rho)$, can be included as well.

### 2.4 Nucleation of the band pattern

In the literature, a linear stability argument provides a first picture for the growth of band structures. As we noted it in the previous chapter, the density dependence of the coefficient $a_2$, in the alignment force Eq. (2.5), makes the homogeneous polar state unstable against finite-wavelength perturbations [91, 141]. This linear instability can be understood as follows. In dense regions, the alignment interactions increase the local polarization (first term of Eq. (2.6)). Concentrated regions get strongly-polarized and form a group of aligned particles that move coherently. When moving across the dilute background, this swarm captures even more particles which align with the coherent group, and grows.

The *nucleation* of spatial patterns is therefore well understood from a linear theory. It is based on the density-dependence of the coefficient $a_2$, which is a necessary condition for the formation of bands (consistently, in models assuming topological alignment rules, $a_2$ does not depend on the local density and bands were not observed [160]). However, the *shape* of the patterns is not understood. It is set by the non-linearities of the hydrodynamic equations and cannot be captured by a linear theory. In the next section, we therefore analyze the non-linear solutions.

## 3 Shape of the band pattern: a dynamical-system insight

We now outline the dynamical-system approach that we introduced to explain the band patterns. This section summarizes the article "Emergent spatial structures in flocking models: a dynamical system insight", which can be found p. 105. We first look for propagating solutions and specify the boundary conditions. Then we introduce the dynamical-system method. We show that the propagating solutions exactly correspond to the three types of patterns which were hitherto observed numerically and experimentally. Finally, we discuss the existence domain of the band patterns and stress that several solutions coexist, thereby making the transition to collective motion first-order.

### 3.1 Propagative solutions of hydrodynamic equations

We introduce the method using the hydrodynamic equations derived for weakly-polarized states:

$$\partial_t \rho + \partial_x W = 0, \tag{2.7}$$

$$\partial_t W + \xi W \partial_x W = \left[ (\rho - \rho_c) - \frac{W^2}{\rho \Pi_0^2} \right] W - \lambda \partial_x \rho + D \partial_{xx} W. \tag{2.8}$$

We stress Eqs. (2.7) and (2.8) are simple realizations of the generic Toner and Tu equation, which hold for any polar active system [211, 214]. Following Bertin, Droz and Grégoire [25], we look for

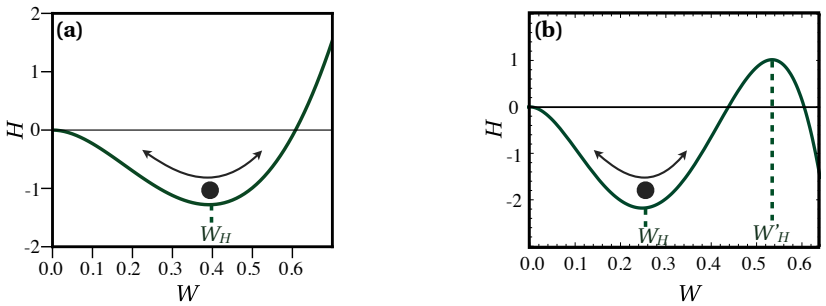


**Figure 2.2** – Effective potential H(W). Depending on the values of the parameters $\rho^\star$ and $c$, the potential can display **(a)** one or **(b)** two maxima.

propagating solutions of Eqs. (2.7) and (2.8):

$$\rho = \rho(x - ct), \tag{2.9}$$
$$W = W(x - ct), \tag{2.10}$$

where $c$ is the probation speed. With this ansatz, the mass-conservation equation (2.7) readily implies [25]:

$$\rho = \rho^\star + \frac{1}{c} W. \tag{2.11}$$

The momentum equation (2.8) is then recast into a second-order ordinary differential equation of the form:

$$D\ddot{W} + \dot{W}\frac{dF}{dW} + \frac{dH}{dW} = 0, \tag{2.12}$$

where the dot symbol denotes derivative with respect to $x - ct$. In addition, $F(W) = \left(c - \frac{\lambda}{c}\right) W - \frac{1}{2} W^2$ and H(W) is provided in the supplementary document of the article. Importantly, both F(W) and H(W) depend on $\rho^\star$ and $c$, which are two free parameters.

It is worth noting that Eq. (2.12) amounts to the equation of motion of a particle of mass D and position W. The particle experiences a non-linear friction set by F(W) and moves in a potential H(W), which is plotted in Fig. 2.2 for two sets of values of the parameters $\rho^\star$ and $c$. Following these well-established first steps, we have therefore mapped the global excitations of a population of N coupled particles onto a one-body problem.

Finally, we have to specify boundary conditions. Mass conservation implies that $\rho(x \to -\infty) = \rho(x \to +\infty)$. The propagation of a spatial structure which would not meet this requirement would increase or decrease the total particle number in the system. From Eq. (2.11), this condition readily imposes that $W(x \to -\infty) = W(x \to +\infty)$. In the mechanical picture of a particle moving in the potential H(W), the particle comes back to its initial position. It cannot get stuck or escape the potential well. Hence the mass-conservation condition strongly constrains the shapes of the functions H(W) and F(W), i.e. the values of the parameters $\rho^\star$ and $c$.

### 3.2 Dynamical-system analysis

In order to establish the shape of the propagating patterns and their existence domain in the plane $(\rho^\star, c)$, we analyze Eq. (2.12) from a dynamical-system perspective. We introduce the auxiliary variable $Z \equiv D\dot{W} + F(W)$ and recast Eq. (2.12) into the 2-dimensional dynamical system:

$$\dot{W} = \frac{1}{D}\left[Z - F(W)\right], \tag{2.13}$$
$$\dot{Z} = -\frac{dH}{dW}. \tag{2.14}$$

The solutions correspond to trajectories in the phase space (W,Z). Importantly, the patterns that fulfill the mass-conservation condition, $W(x \to -\infty) = W(x \to +\infty)$, are associated with *closed* trajectories.

The existence and the shape of closed orbits in the phase space are deduced from the stability of the fixed points of the dynamical system, by calculating their eigenvalues and eigendirections. This approach is more thoroughly explained in the article. In brief, three types of closed trajectories exist.

(i) *Periodic orbits – periodic density waves*: when varying the parameters $\rho^\star$ and $c$, the dynamical system undergoes a Hopf bifurcation. The fixed point located at the minimum of the potential H(W), denoted by $W_H$ in Fig. 2.2, becomes linearly unstable. Trajectories spiral from this unstable point to a cyclic attractor – a limit cycle, see Fig. 2.3(a). The trajectory

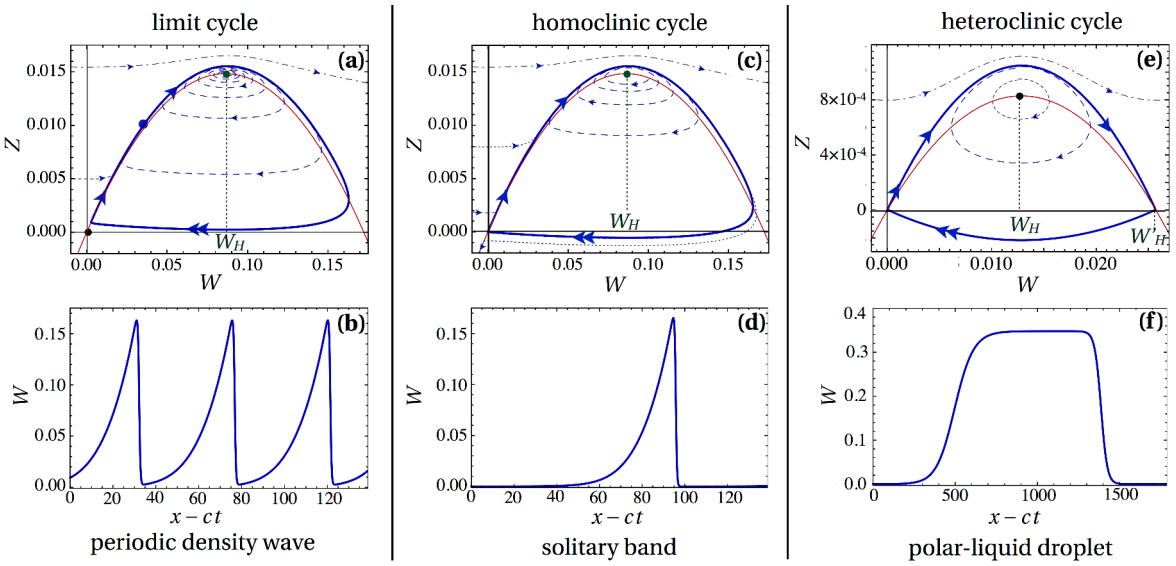


**Figure 2.3** – Numerical solutions of the dynamical system, Eqs. (2.13)–(2.14). **(a)** Trajectories of the dynamical system (2.13)–(2.14) in the phase space (W,Z) (the expressions of the hydrodynamic coefficients and the parameter values are provided in the article). The fixed points are located at the extrema of the potential H(W) and lie on the red curve Z = F(W) . Here the effective potential has only one maximum at W = 0, as sketched in Fig. 2.2(a). Solid blue line: limit cycle. **(b)** Periodic pattern of polar bands, corresponding to the limit cycle shown in **(a)**. **(c)** Homoclinic cycle: same parameters as **(a)** but for a lower value of $\rho^\star$. **(d)** Solitary band, corresponding to the homoclinic cycle shown in **(c)**. **(e)** Heteroclinic cycle . The existence of heteroclinic orbits requires that the effective potential has another maximum at $W = W'_H$, as sketched in Fig. 2.2(b). **(f)** Polar-liquid droplet, corresponding to the heteroclinic cycle shown in **(e)**.

never stops along the cycle, as it never reaches a fixed point. In real space, it therefore corresponds to a periodic crystal of parallel bands that propagate at the velocity $c$, Fig. 2.3(b). When the coefficient D is small, we have shown that the bands are strongly asymmetric. They are composed of a long exponential tail terminated by a sharp front at the head. When varying the parameters $\rho^\star$ and $c$, both the amplitude and the period of the band pattern change.

(ii) *Homoclinic cycles – solitary bands*: the dynamical system has another fixed point located at (W = 0,Z = 0), which is a saddle-point. For some values of $\rho^\star$ and $c$, the limit cycle intercepts the origin and becomes a homoclinic orbit, as exemplified in Fig. 2.3(c). Its period diverges: at the end of the cycle, the trajectory gets stuck at the saddle-point. In real space, this solution is a solitary band which cruises in a non-polarized background with density $\rho^\star$, Fig. 2.3(d).

(iii) *Heteroclinic cycles – polar liquid droplets*: for some values of the parameters $\rho^\star$ and $c$, the effective potential H(W) has a second maximum, denoted by $W'_H$ in Fig. 2.2(b). In the phase space, the dynamical system has a second saddle point. This configuration allows a third type of solution: a heteroclinic cycle that connects the two saddle points, as shown in Fig. 2.3(e). The dynamics freezes at these two fixed points. In real space, the corresponding pattern is a localized droplet of polar liquid which moves in a disordered gas, Fig. 2.3(f). The two branches of the heteroclinic cycles correspond to the domain walls which separate these two phases.

These three types of patterns exactly correspond to those observed in simulations and experiments. In addition, we emphasize that the salient features of the spatial patterns do not depend on the specific forms of the hydrodynamic coefficients, in Eq. (2.8). At the qualitative level, the dynamics in the phase space is solely set by the fixed points of the dynamical system, and by their

stability. Only the global shapes of the effective potential H(W) and of the friction curve F(W) matter. The dynamical-system framework therefore rationalizes the previous observations and provides a method to analyze the shapes of the 1D spatial excitations of any hydrodynamic theory.

### 3.3 Existence domain of the band solutions

Until now, we have identified an infinite family of band-type solutions, which is parametrized by the two free parameters $\rho^\star$ and $c$. In Fig. 2.4, we plot the domain of existence of the band patterns in the plane $(c,\rho^\star)$. Its upper limit (solid black line) corresponds to the Hopf bifurcation that yields the emergence of limit cycles. Periodic density waves are found below this line. The lower limit (dotted-dashed black line) was computed numerically by A. Solon and J. Tailleur. It corresponds to the homoclinic bifurcation at which the limit cycle collapses with the saddle point at the origin. The solitary bands are fond along this line. The heteroclinic cycle, if any, is unique: polar-liquid droplets are fond at the blue point only.

In addition, the ensemble of band patterns is restrained by the total particle number. The mean density $\rho_0$ in the system is fixed: only the band solutions that match this constraint exist. We are left with an infinite family of solutions, which is parametrized by one free parameter. As a result, the solution is not unique. For a given value of $\rho_0$, several spatial patterns may coexist. This prediction has been confirmed by numerical observations on the Vicsek model, carried out in the group of H. Chaté. For instance, Fig. 2.5 shows two simulations performed with identical values of all simulation parameters: two-band and single-band patterns can be found starting from the same initial conditions.

More importantly, band solutions can exist when the average density $\rho_0$ is smaller than the critical density $\rho_c$. Hence they also coexist with the isotropic phase at $\rho_0 \lesssim \rho_c$. This result confirms the first-order scenario for the transition to collective motion. The band patterns are a genuine, yet spatially heterogeneous, phase of active matter. They exist in a range of densities below $\rho_c$, in which the isotropic gas remains stable. This finding is consistent with the observation of hysteresis

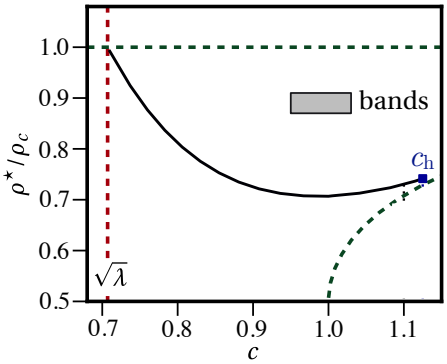


**Figure 2.4** – Band phase diagram in the plane $(c,\rho^\star)$. Non-linear bands exist only in the grey region. Solitary bands are found along the dotted-dahed line. Polar-liquid droplets are fond at the point $c = c_h$ only.

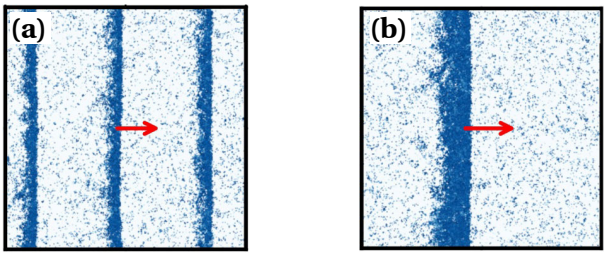


**Figure 2.5** – Numerical snapshots of the band phase in the Vicsek model. **(a)** and **(b)** were obtained with identical values of all simulation parameters, and starting from the same initial conditions (random positions and orientations).

close to the transition [49]. It is the formation of heterogeneous polarized structures which makes the transition first-order.

As a last remark, we note that a similar Hopf-bifurcation scenario was also found in a different class of systems. Giomi and Marchetti considered a model of active suspensions, in which propelled particles are advected in the flow induced by their swimming motion [88]. They demonstrated that periodic traveling waves also coexist with the isotropic phase at the onset of collective motion. In spite of notable differences in the shape of the patterns, this observation suggests that the formation of spatial structures might arise from similar mechanisms in "dry"and "wet" systems.

# 4 Band patterns in a more realistic model

In section 2, we have noticed that the hydrodynamic equations take different forms in weakly- and strongly-polarized states. Yet, the bands observed numerically and experimentally consist in strongly-polarized regions that propagate in a weakly-polarized background. Any realistic description therefore has to interpolate between these two limits.

In this section, we generalize the dynamical-system method introduced above and propose a more accurate model. We first define a dynamical system which interpolates between the weakly- and strongly-polarized regimes. We then discuss the consequences on the existence domain of the band solutions.

## 4.1 Definition of the dynamical system

Let us first recall the asymptotic limits in which the hydrodynamic equations were derived.

(i) *Weak polarization:* in the limit $W \to 0$, we have shown that the non-linear friction takes the form:

$$\frac{dF}{dW} \sim c - \frac{1}{2c}. \tag{2.15}$$

(ii) *Strong polarization:* when the polarization is close to 1, we have written the nematic order-parameter as $Q = \Pi^4/2$. From Eq. (2.4), the resulting non-linear friction is deduced as:

$$\frac{dF}{dW} \sim c - \frac{1}{2c} - 2\Pi^3 + \frac{3}{2c}\Pi^4, \tag{2.16}$$

where $\Pi = \frac{W}{\rho} = \frac{cW}{c\rho^\star + W}$. For large densities and polarizations, $W \gg c\rho^\star$, the latter expression reduces to:

$$\frac{dF}{dW} \sim c - \frac{1}{2c} - \frac{c^3}{2} + \mathcal{O}\left[\left(\frac{c\rho^\star}{W}\right)^2\right]. \tag{2.17}$$

We interpolate between these two asymptotic regimes. We assume the following expression for the friction term, which reproduces Eq. (2.15) for vanishing Ws and Eq. (2.17) when $W \gg c\rho^\star$:

$$\frac{dF}{dW} = c - \frac{1}{2c} - \frac{c^3}{2} + \frac{c^3}{2}\left(\frac{c\rho^\star}{c\rho^\star + W}\right)^2. \tag{2.18}$$

The function F(W), defined by Eq. (2.18), is plotted in Fig. 2.6. It has the same qualitative shape as the parabola that we considered previously, with a maximum at $W = W_F$.

## 4.2 Existence domain of the band-like patterns

As the shape of the functions H(W) and F(W) defined above are qualitatively unchanged, we recover patterns having the same qualitative shape as previously. Examples of numerical solutions in the phase space (W,Z) and in real space are shown in Fig. 2.7. We recover periodic crystals of asymmetric bands and solitary-band solutions. When the maximum polarization is $\Pi_0 < 1$, polar-liquid droplets can be obtained as well.

More interestingly, the modified friction term, Eq. (2.18), significantly impacts the existence domain of the band patterns. Here, we have not computed the entire domain numerically. However, we have plotted in Fig. 2.8 the Hopf-bifurcation line, defined by the condition $W_F = W_H$. Bands exist in the vicinity of this curve. Depending on the value of the maximum polarization, $\Pi_0$, two distinct behaviors are found.

(i) $\Pi_0 = 1$: in a first class of models, the polarization can be arbitrary close to one. Let us con-

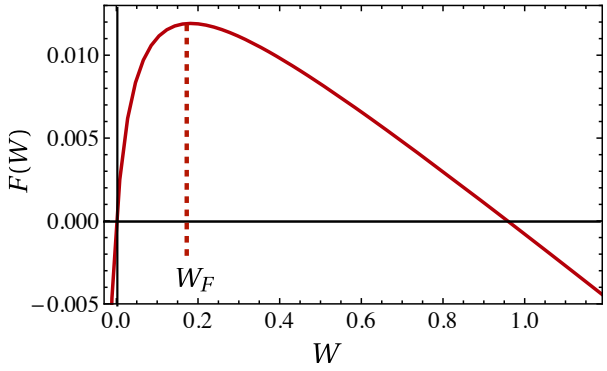


**Figure 2.6** – Friction term F(W), defined by Eq. (2.18), plotted for $\rho_c = 0.1$, $\rho^\star = 0.062$, $c = 0.9$.

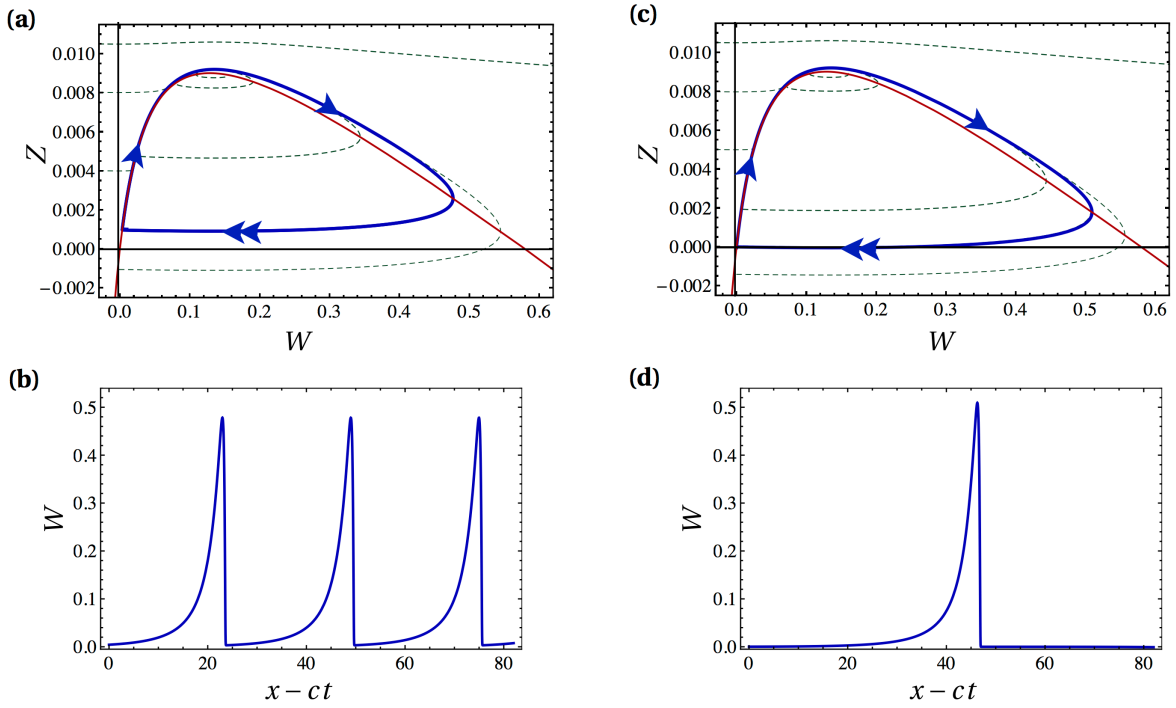


**Figure 2.7** – **(a)** Trajectories of the dynamical system in the phase space (W,Z), for $\Pi_0 = 0.88$, $\rho_c = 0.1$, $c = 0.882$. $\rho^\star$ was chosen so that $W_H - W_F \gtrsim 0$. Thick blue line: limit cycle. Thin red line: curve Z = F(W). **(b)** Periodic band pattern corresponding to the limit cycle shown in **(a)**. **(c)** Same as **(a)** for a slightly smaller value of $\rho^\star$. Thick blue line: homoclinic cycle. Thin red line: curve Z = F(W). **(d)** Solitary band corresponding to the heteroclinic cycle shown in **(c)**.

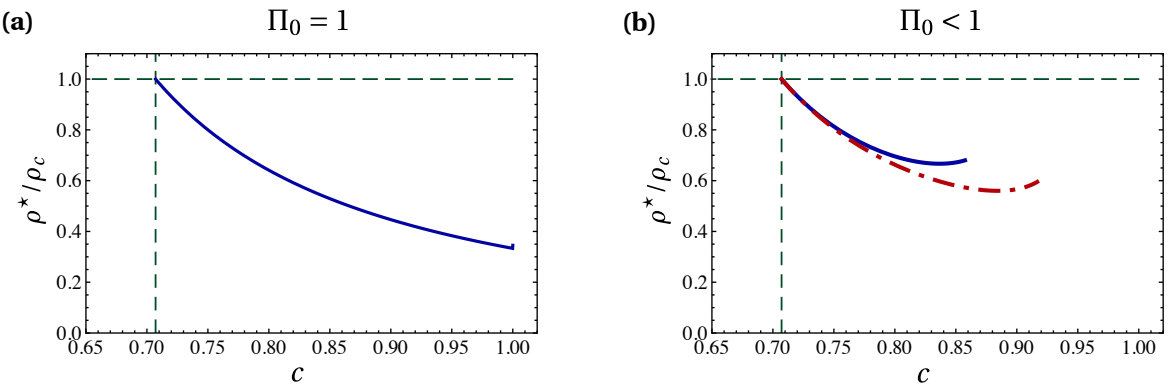


**Figure 2.8** – Hopf-bifurcation line, defined by $W_H - W_F = 0$, in the parameter space $(c, \rho^\star/\rho_c)$. Band-like solutions exist close to this line. **(a)** $\Pi_0 = 1$. **(b)** Solid blue line: $\Pi_0 = 0.8$. Red dashed line: $\Pi_0 = 0.9$.

sider e.g. the flying-XY model [79, 156]. We recall that particle $i$ interacts with all neighbors lying in a disk $\mathscr{A}_i$ of radius R. Its orientation $\theta_i$ evolves according to:

$$\partial_t \theta_i = -\frac{1}{\tau} \sum_{j \in \mathscr{A}_i} \sin(\theta_i - \theta_j) + \xi_i(t), \tag{2.19}$$

where $\xi_i(t)$ is a noise term. In the right-hand side, the first term promotes polar ordering. As alignment interactions are pairwise-additive, its amplitude is proportional to the number of neighbors in the interaction disk, which scales as $\sim \rho\pi R^2$. Increasing the local density, the strength of this alignment term can be made arbitrary large. Conversely the noise term, which destroys the polarization, does not depend on $\rho$. As a result, the polarization can be made arbitrary close to $\Pi_0 = 1$ by increasing the density.
In the existence domain of band solutions, Fig. 2.8(a), there is no solution propagating faster than the particles: $c \leq 1$. Consequently, the effective potential H(W) never displays a secondary maximum, and polar-liquid droplets do not exist. In addition, we numerically find that the amplitude of the band diverges when $c \to 1$. The latter result suggests that short-range repulsion may be required to prevent the collapse of the population and recover band-like patterns. Surprisingly, a full numerical characterization of this basic model is still lacking.

(ii) $\Pi_0 < 1$: in a second class of models, the upper-bond of the polarization is set by the noise introduced in the microscopic dynamics. Let us consider e.g. the Vicsek model, with scalar noise [25, 49, 215]. The orientation of particle $i$ is updated at each time-step $\Delta t$ according to the rule:

$$\theta_i(t + \Delta t) = \bar{\theta}_i + \xi_i(t), \tag{2.20}$$

where $\bar{\theta}_i$ is the mean orientation of the neighbors lying in the domain $\mathscr{A}_i$. Here the amplitude of the alignment term does not depend on the number of neighbors lying in the interaction radius (the interactions are not pairwise-additive). The polarization cannot be made arbitrary large by increasing the local density. Assuming a Gaussian noise with variance $\eta$, it is bounded by $\Pi_0 \sim \exp(-\eta^2/2)$. Decreasing the amplitude of the noise increases the maximum polarization allowed.
The existence domain of band solutions is plotted in Fig. 2.8(b). We find that the bands cannot propagate faster than $c_{\max} < 1$. The maximum speed increases with $\Pi_0$. In other words, $c_{\max}$ decreases for increasing noise amplitudes, in agreement with the agent-based simulations carried out in [25]. Similarly, $\rho^\star$ cannot be smaller than a value $\rho^\star_{\min}$ which increases with the noise amplitude. Recalling that $\rho^\star$ is the density of the gas phase through which a solitary band travels, this finding is also compatible with the numerical results reported

in [25]. Finally, we note that patterns propagating faster than $\Pi_0$ can be found. Hence the effective potential H(W) can display a secondary maximum, and polar-liquid droplets *a priori* exist.

The above discussion shows that minute changes in the definition of the interaction rule can dramatically alter the shape of the large-scale patterns. In the hydrodynamic equations, the structure of the band phase strongly depends on the functional forms of the coefficients. It is sensitive to the details of the microscopic model, and cannot be deduced solely from symmetry considerations.

## Conclusion and perspectives

To conclude, we have generically studied the inhomogeneous traveling solutions of hydrodynamic theories of polar active-matter. Using a dynamical-system framework, we have analyzed the shape and the existence domain of these non-linear patterns. We have shown that they exactly correspond to those hitherto observed in numerical simulations and experiments: (i) periodic density waves, (ii) solitary bands, and (iii) polar-liquid droplets cruising in an isotropic phase.

Several questions still have to be addressed to get a complete understanding of the transition to collective motion.

- This work does not explain the selection of a pattern among the possible solutions of the hydrodynamic equations. Fluctuations obviously play a key role in the patter-selection process. In order to get more insight into this problem, one should study the stability of the non-linear solutions against small perturbations. In addition, the role of the initial conditions could be further investigated: as several solution may coexist, different initial states may lead to different patterns. We note that the experiments on the roller population (Chapter 1) give a first glimpse into the band formation: starting from a disordered state, it was observed that several bands form, collide and coalesce. In the transient regime, complex collision events may favor large-amplitude/fast bands. This scenario should be studied more carefully.

- The selection of a solution also depends on the specifics of the interactions, at the microscopic level. Different microscopic models lead to different final states, although the hydrodynamic equations always keep the Toner-Tu form. Symmetry considerations at the macroscopic level are not enough to predict the shape of the final pattern. It would be interesting to identify the microscopic ingredients that qualitatively matter for the selection of a spatial structure. As a first step in this direction, A. Solon, H. Chaté and J. Tailleur have simulated the hydrodynamic equations that we studied above, assuming that the polarization field is either a scalar or a vectorial quantity [198]. In the former case (relevant e.g. for the active Ising model [197]) they found polar-liquid droplets, while the latter case (relevant e.g. for the Vicsek model) yields periodic band patterns. More work is required to fully understand the differences between all active-spin models.

- Up to now, much attention has been devoted to the transition between the isotropic state and the band phase. However, at higher densities or lower noise amplitudes, the band patterns give way to a homogeneous polar state. It would be interesting to study this second transition from heterogeneous to homogeneous polar phases.

- In a disordered phase, several solitary bands can nucleate. The interaction between these solitonic structures could be questioned.

- Finally, we come back to the population of Quincke rollers. The above theory does not account for a striking feature of the experimental patterns: it was found that the propagating

bands have no intrinsic length-scale. Their length increases linearly with the size of the system (see Chapter 1). One should study whether this property can be explained by changing the functional dependences of the hydrodynamic coefficients, in Eq. (2.8). In particular, steric repulsion between particles might impact the shape of the band by regulating the maximum density at the front.

# Article: *Emergent spatial structures in flocking models: a dynamical system insight*

J.-B. Caussin, A. Solon, A. Peshkov2012, H. Chaté, T. Dauxois, J. Tailleur, V. Vitelli and D. Bartolo, *Phys. Rev. Lett.* **112**, 148102 (2014)

We show that hydrodynamic theories of polar active matter generically possess inhomogeneous traveling solutions. We introduce a unifying dynamical-system framework to establish the shape of these intrinsically nonlinear patterns, and show that they correspond to those hitherto observed in experiments and numerical simulation: periodic density waves, and solitonic bands, or polar-liquid droplets both cruising in isotropic phases. We elucidate their respective multiplicity and mutual relations, as well as their existence domain.

Could the emergence of collective motion in fish schools, bird flocks, and insect swarms be understood within a unified physical framework? A growing stream of works has approached this provocative question following the seminal work of Vicsek *et al.*, who considered self-propelled point particles interacting solely via local velocity-alignment rules [215]. This model displays a spontaneous rotational-symmetry breaking leading to orientational order [136, 215, 216]. In addition, a number of subsequent simulations and experiments have revealed an even more surprising feature. At the onset of collective motion, despite the lack of any attractive interactions, polar active matter self-organizes in the form of band-shape swarms [25, 36, 49, 91, 92, 109, 141, 190, 197]. However, depending on the specifics of the systems, these dynamical patterns take three different forms: (i) delocalized density waves [49, 190], as exemplified in Fig. 2.9(a), (ii) solitonic structures [25, 36, 109], Fig. 2.9(b), and (iii) phase-separated states [91, 141, 197], Fig. 2.9(c). Although it is now clear that they are responsible for the first-order nature of the transition towards collective motion [92, 109, 197], no unifying theory exists to account for the origin and the variety of these band patterns.

In this letter, we convey a comprehensive description of the propagative excitations of polar active matter. Using a hydrodynamic description and dynamical system concepts, we establish the shape of these intrinsically nonlinear band structures, and show that they correspond to those observed in all the available experiments and numerical simulation, see e.g. [25, 36, 49, 91, 109, 141, 175, 190, 197, 219].

Our starting point is a hydrodynamic description of compressible polar active fluids [136, 211, 214]. Since we are chiefly interested in structures varying only along the main direction of motion, we focus here on a one-dimensional problem. The local density field $\rho(x,t)$ obeys a conservation equation which complements the equation governing the momentum field $W(x,t) = \rho(x,t)P(x,t)$, where $P(x,t) \in [0,1]$ is a polarization field. Following Toner1995,Tu1998 and Tu [211, 214] these equations read

$$\partial_t \rho + \partial_x W = 0 \tag{2.21}$$

$$\partial_t W + \xi W \partial_x W = a_2 W - a_4 W^3 - \lambda \partial_x \rho + D \partial_{xx} W \tag{2.22}$$

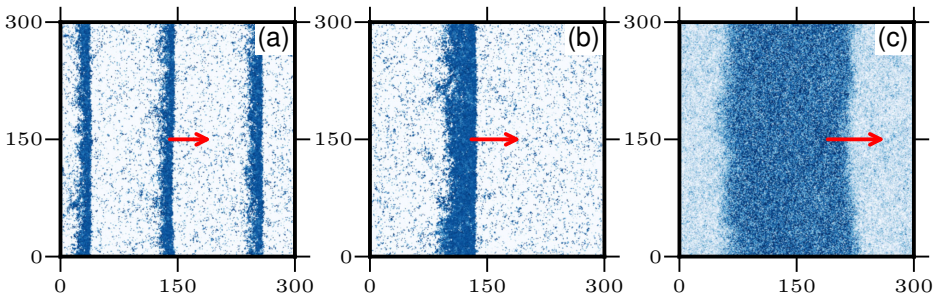


**Figure 2.9** – Band patterns observed in agent-based simulations. **(a)** Smectic arrangement of polar bands in the Vicsek model with vectorial noise [49]. Speed $v = 0.5$, noise intensity $\eta = 0.6$ and density $\rho = 1.1$. **(b)** A solitary band observed for the same model and same parameters as in (a). **(c)** Polar-liquid droplet in an isotropic phase observed in the active Ising model [197], with inverse temperature $\beta = 6$, density $\rho = 5$, hopping rate $D = 1$, and bias $\epsilon = 0.9$. More simulation details can be found in the Supplementary Information.

where all the coefficients *a priori* depend both on $\rho$ and $W^2$. These phenomenological equations were introduced to account for a continuous mean-field transition from a homogeneous isotropic state with $\rho = \rho_0$ and $P = 0$ when $a_2 < 0$, to a homogeneous polarized state with $P = \rho_0^{-1}\sqrt{a_2/a_4}$ when $a_2 > 0$. In addition, the $\lambda$ term reflects the pressure gradient induced by density heterogenities. $\xi$ and $D$ are two transport coefficients associated respectively with the advection and the diffusion of the local order parameter. Following [25], we now look for propagating solutions of Eqs. (2.21) and (2.22): $\rho = \rho(x - ct)$ and $W = W(x - ct)$, where $c$ is the propagation speed [25, 141]. This ansatz reduces Eq. (2.21) to an algebraic relation:

$$\rho = \rho^\star + \frac{1}{c}W \tag{2.23}$$

When a band moves in an isotropic gas, see e.g. Fig. 2.9(b), the constant $\rho^\star$ corresponds to the gas density. Inserting the latter expression in Eq. (2.22) leads to a second order ordinary differential equation:

$$D\ddot{W} + \dot{W}\frac{dF}{dW} + \frac{dH}{dW} = 0, \tag{2.24}$$

where $H(W)$ is defined via $dH/dW = a_2 W - a_4 W^3$, $F(W) = \left(c - \frac{\lambda}{c}\right)W - \frac{1}{2}\xi W^2$, and the dot symbol denotes derivative with respect to $\tau \equiv x - ct$. Therefore, the band-pattern problem is recast into a dynamical system framework: establishing the shape of the bands amounts to describing the motion of a particle of mass $D$ and position $W$ in a potential $H(W)$, and experiencing a nonlinear friction $F(W)$, see Fig. 2.10(a). Note that the particle gains (resp. losses) energy when $F'(W) < 0$ (resp. $F'(W) > 0$).

Mass conservation in the original problem, Eq. (2.21), constrains the boundary conditions of Eq. (2.24) as $W(x \to -\infty) = W(x \to +\infty)$. Given this simple observation, without any further calculation, we can anticipate all the possible band patterns: the solutions of Eq. (2.24) correspond to closed trajectories in the $(W, \dot{W})$ plane. Therefore they necessarily belong to one of the three following classes: (i) periodic orbits, (ii) homoclinic cycles (the trajectory includes one saddle point), or (iii) heteroclinic cycles (the trajectory includes two saddle points). Back in real space, as exemplified in Fig. 2.11, these trajectories respectively correspond to three possible propagating patterns $W(x - ct)$: (i) a smectic phase composed of ordered bands ($W$ varies periodically with $x - ct$), (ii) a localized solitary wave, the length of which being set by the "time" taken to explore the homoclinic cycle, (iii) a polar-liquid droplet separated by domain walls from an isotropic gaseous phase, the fraction of polar liquid being given by the ratio between the waiting times at the two saddle points. These three patterns exactly correspond to those *hitherto* observed in model experiments, and in numerical simulations at the onset of collective motion.

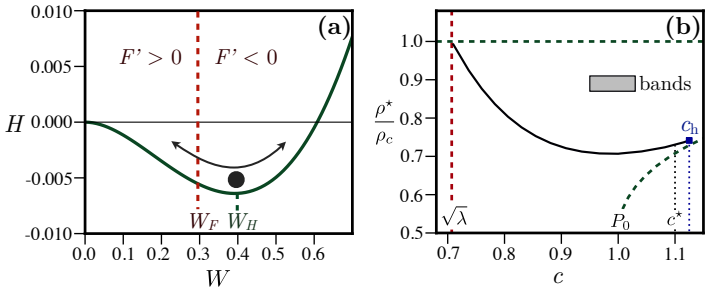


**Figure 2.10** – **(a)** Sketch of the motion of an oscillating point particle in the effective potential H(W) for $P_0 = 1$, $\rho_c = 1$, $\lambda = 0.5$, $\xi = 1$, $c = 0.9$ and $\rho^\star = 0.7$. The system looses or gains energy H when $F'(W) > 0$ or $F'(W) < 0$. **(b)** Band phase diagram for the same parameters. Non-linear bands exist only in the grey region. The dashed lines correspond the the conditions $W_H > 0$, and $W_F > 0$. For $c < c^*$, the black full line corresponds to the supercritical Hopf-bifurcation. Polar-liquid droplets states are observed only at $c = c_h$.

Motivated by this pivotal observation, we now turn to the study of equation (2.24). For sake of clarity we henceforth specify the functional dependence of the phenomenological coefficients in Eq. (2.22). As the density is a control parameter of the transition to collective motion for all models based on short-range alignment interactions, $a_2(\rho)$ has to change sign at a finite density $\rho_c$ [136, 216]. Different systems may result in different functions $a_2(\rho)$. We choose a simple linear dependence $a_2 = \rho - \rho_c$ which is consistent, close to $\rho_c$, with all existing kinetic theories [13, 25, 36, 79, 197]. In addition, having e.g. the original Vicsek model in mind, we want to capture the saturation of the average polarization of a homogeneous polar state of density $\rho = \rho_0$, when $\rho_0 \gg \rho_c$, at a non-zero value $P_0$. In agent-based models, $P_0$ is set by the noise amplitude. Here, since $P \sim \rho_0^{-1}[(\rho_0 - \rho_c)/a_4]^{1/2}$, the simplest possible choice yielding the correction saturation is $a_4(\rho) = (\rho P_0^2)^{-1}$. This choice simplifies the equations studied numerically in [141]. In all that follows, $\xi$, $\lambda$ and D are kept constant.

Now that Eqs. (2.21)-(2.22) have been fully defined, we can obtain their propagative solutions explicitly by solving Eq. (2.24). We stress that the two functions H(W) and F(W) are parametrized by two independent parameters: $\rho^\star$ and $c$, which specify the shape of the bands. Their explicit form are provided in the Supplementary Information and H is plotted in Fig. 2.10(a) for a given set of parameters. The existence of closed trajectories in the $(W, \dot{W})$ plane requires that the system has at least one fixed point [5]. Hence, keeping in mind that Eq. (2.24) describes the motion of a massive particle in a potential, we look for trajectories that display at least one oscillation. This obviously requires: (i) that H has a local minimum at a finite value $W_H > 0$ (and thus a local maximum at $W = 0$), and (ii) that the friction $F'(W)$ changes sign at a finite $W_F > 0$ so that the particle do not fall to and remains stuck at $W_H$ where H is minimum. It is straightforward to show that the former condition implies $\rho^\star < \rho_c$, and the latter $c > \sqrt{\lambda}$. In order to establish the shape of the periodic trajectories of the dynamical system, and in turn the shape of the bands, we need to go beyond this simple picture. We introduce the auxiliary variable $Z \equiv D\dot{W} + F(W)$ and recast Eq. (2.24) into the 2-dimensional dynamical system:

$$\dot{W} = \frac{1}{D}[Z - F(W)] \tag{2.25}$$

$$\dot{Z} = -\frac{dH}{dW} \tag{2.26}$$

This change of variable greatly simplifies the investigation of the fixed points of the dynamical system now defined by Eqs (2.25)-(2.26) [200]. It has at least two fixed points: $(0,0)$ and $(W_H, F(W_H))$. A conventional linear stability analysis shows that $(0,0)$ is always a saddle point. Conversely the second fixed point $(W_H, F(W_H))$ calls for a more careful discussion. It undergoes a Hopf-bifurcation as $W_H - W_F$ changes sign, as can be seen on the eigenvalues of the Jacobian matrices (see Supplementary Information). This bifurcation, which we will thoroughly characterize elsewhere, is supercritical (resp. subcritical) if $c < c^*$ (resp. $c > c^*$), where the critical velocity $c^*$ is defined

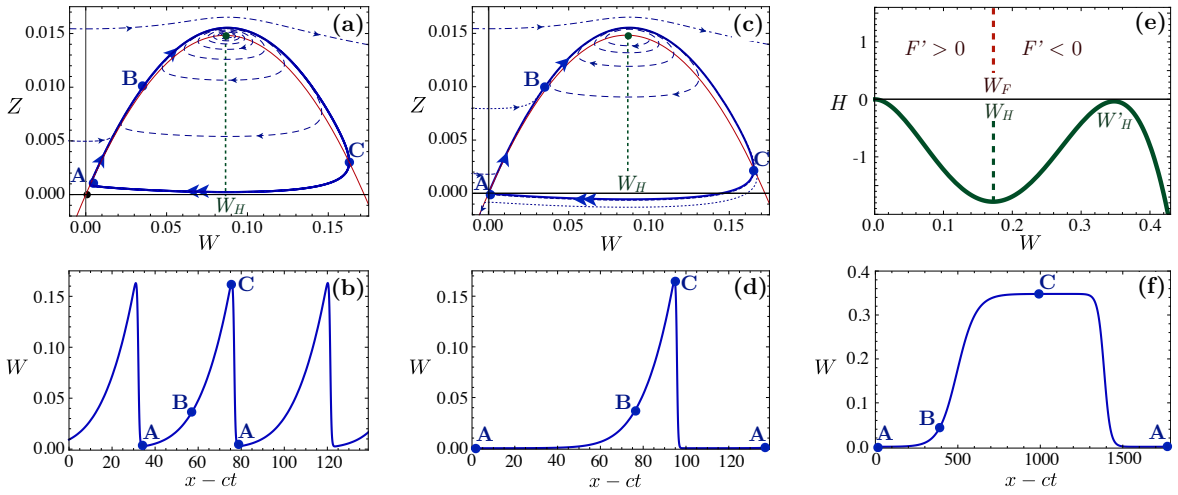


**Figure 2.11** – **(a)** Dashed lines: dynamical system trajectories, for $P_0 = 1$, $\rho_c = 0.1$, $\lambda = 0.5$, $\xi = 4$, $D = 0.1$, $c = 0.9$. $\rho^\star$ was chosen such that $W_H \gtrsim W_F$. Thick line: stable limit cycle. Thin line: $Z = F(W)$ curve. **(b)** Polar smectic corresponding to the limit cycle shown in **(a)**. **(c)** Homoclinic orbit; same parameters as in **(a)** but for a lower value of $\rho^\star$. **(d)** Solitonic band corresponding to the limit cycle shown in **(c)**. **(e)** H(W), full line, plotted for $P_0 = 1$, $\rho_c = 1$, $\lambda = 1$, $\xi = 10$ and $D = 50$. The dashed lines show the positions of $W_F$ and $W_H$. The values of $c$ and $\rho^\star$ give rise to an heteroclinic cycle (see Supplementary Information). **(f)** Polar-liquid droplet for the same values of the parameters as in **(e)**, see also the Supplementary Information.

implicitly by $H'''(W_H) = 0$. Both the bifurcation line and $c^*$ can be computed analytically and are shown in Fig. 2.10(a). More importantly, regardless of its sub- or super-critical nature the Hopf bifurcation results in an unstable spiral trajectory which can lead the system towards a cyclic attractor. We now describe how these limit cycles are explored in the (W,Z) plane, and relate these nonlinear trajectories to the morphologies of the band patterns.

*Polar smectic phase/periodic orbits.* To gain more quantitative insight, we consider large-amplitude cycles in the limit of small D [2]. For small W, Eq. (2.25) implies that the system quickly relaxes towards the curve $Z = F(W)$ in a time $\sim D^{-1}$. Close to the origin, the dynamics is controlled by the linear properties of the saddle point (0,0), which defines two well-separated scales. It can be easily shown that the stable direction is nearly horizontal, it is associated with a fast relaxation at the rate $\tau_-^{-1} \sim D^{-1}(c - \lambda/c)$. Conversely, the unstable direction is nearly tangent to the curve $Z = F(W)$, and corresponds, again in the small-D limit, to a much slower growth at the rate $\tau_+^{-1} \sim (\rho_c - \rho^\star)/(c - \lambda/c)$. The shape of large-amplitude cycles immediately follows from this discussion and from the parabolic shape of F(W). Let us start from the left of the cycle, point A in Fig. 2.11(a), close to the origin. We call $W_{min}$ the abscissa of this point, which is the minimum value of W in the cycle. As noted above, the trajectory first remains near the parabola $Z = F(W)$. If A is close enough to the origin, this part of the cycle is explored slowly, in a time $\sim \tau_+$. Then the trajectory approaches the unstable point $(W_H, F(W_H))$. It therefore leaves the parabola and starts spiraling, at a point labeled B in Fig. 2.11(a) (B is here defined as the point where the trajectory deviates from the $Z = F(W)$ curve by 5%). It finally crosses the parabola again, at point C, and $\dot{W}$ changes sign, see Eq. (2.25). W then decreases and the system quickly goes back to point A in a time typically set by $\sim \tau_-$. To further check this picture we have numerically computed the phase portraits of Eqs. (2.25) and (2.26), Fig. 2.11(a) (dotted lines). The typical periodic orbit shown in Fig. 2.11(a) (full line) is in excellent agreement with the scenario described above. From this analysis, we infer the shape of the steadily propagating band pattern $W(x - ct)$. As anticipated, periodic orbits correspond to a polar smectic phase composed of equally-spaced bands, in qualitative agreement with the experimental pictures reported in [190], and Fig. 2.9(a). The numerical shape

[2] More precisely, we consider $D \ll \frac{(c^2-\lambda)^2}{4c^2(\rho_c-\rho^\star)}$.

of a smectic pattern is shown in Fig. 2.11(b). It is composed of strongly asymmetric excitations, which reflects the time-scale separation in the underlying dynamical system close to the origin; the large-amplitude bands are composed of a long exponential tail, and of a sharp front at the head. Note that we describe here the propagation of large-amplitude excitations in a polarized environment. However the minimum polarization in the regions separating the bands, $W_{min}$, can be vanishingly small. In this limit the period of the crystalline structure would diverge logarithmically as $\tau_+ \log(W_F/W_{min})$.

*Solitary bands/Homoclinic cycles.* In the limiting case where the minimal value of W goes to 0 ($W_{min} = 0$), point A then corresponds to the saddle located at the origin. Consequently the orbits followed by the dynamical system become homoclinic. As exemplified in Fig. 2.11(c), they are not periodic anymore, as the trajectory remains stuck at $(0,0)$. In real space, the associated pattern is a solitary wave emerging out of a disordered gas, Fig. 2.11(d). We stress that the existence of solitonic structures at the onset of collective motion is one of the more robust observations made in agent-based simulations [25, 49, 109], see Fig. 2.9(b).

*Polar liquid droplets/Heteroclinic cycles.* Until now, we have restricted our analysis to the case where the dynamical system only probes the first two extrema of H. However, looking for high-speed solutions ($c > P_0$), H displays an additional extremum at $W'_H > W_H$, see Fig. 2.11(e). $(W'_H, F(W'_H))$ is a second saddle point. Therefore heteroclinic cycles are found when A is located at the origin and C at the second saddle. The cycles are not periodic as the dynamics freezes both at A and C. In real space, the corresponding structure, $W(x-ct)$, is a localized domain, a polar-liquid droplet, traveling in a disordered gas, whose length is given by the residence at point C, Fig. 2.11(f). This phase-separation pattern corresponds to the one numerically observed in the active spin model, Fig. 2.9(c), and in a generalization of the 2D Toner1995,Tu1998 and Tu model [91, 197]. In the small $P_0$ limit, the shapes of the asymmetric domain walls bounding the polar-liquid droplets can be computed exactly (see Supplementary Information).

Several comments are in order. Firstly, we emphasize that the salient features of the swarming patterns do not depend on the specific functional forms of the hydrodynamic coefficients in Eq. (2.22). The limit-cycle solutions solely require the existence of a Hopf bifurcation, and the dynamics along this cycle is chiefly controlled by the stability of the other fixed points. Therefore, at a qualitative level, only the global shapes of the effective potential H(W) and the friction curve F(W) matter. For instance, we shall stress that a hydrodynamic theory where $a_4 = \text{cst}$ in Eq. (2.22) would yield non-linear patterns qualitatively identical to those shown in Fig. 2.9 (not shown). Only the sign reversal of $a_2(\rho)$ at $\rho_c$ was necessary to observe band patterns, in agreement with [160].

Secondly, we emphasize that travelling band can exist when the average density $\rho_0$ is smaller than $\rho_c$, though the linear stability of Eqs. (1) and (2) predicts that no small-amplitude wave can propagate [136]. The fundamental propagative excitations of polar active matter are intrinsically nonlinear below $\rho_c$.

Thirdly, we come back to the status of the solutions described above. Until now we have identified an infinite family of band-type solutions, located in the vicinity of the Hopf-bifurcation line in the $(c, \rho^\star)$ plane, grey region in Fig. 2.10(b). The boundaries of this region are found by looking for non-degenerate solutions satisfying $W > 0$, and its extent is an increasing function of the diffusivity D. The domain of existence of the bands collapses on the Hopf-bifurcation line in the limit $D \to 0$. The homoclinic cycles, corresponding to solitary waves, are constraint to include one saddle point. Therefore they define a one-parameter ensemble of band-type solutions. This ensemble corresponds to the lower boundary of the phase diagram, Fig. 2.10(b) (dashed-dotted line), and is established by taking the infinite-period limit. The heteroclinic solution, polar-liquid droplet, is constrained by the existence of two saddles along a cycle. Therefore, if any, the heteroclinic cycle is unique. It is a limiting case of the one-parameter homoclinic family, point $c_h$ in Fig. 2.10(b).

Finally, we discuss the pattern-selection problem. The ensemble of band-type solutions described above is actually restrained by the mass-conservation law. The mean density $\rho_0$ in the system is fixed, therefore only band shapes compatible with this value exist. However, we are a priori left with an infinite family of solutions, which is parametrized by one free parameter. Hence, we predict that, for a given value of $\rho_0$, several solutions propagating at different speeds may coexist. This conjecture is again supported by numerical evidences. In Fig. 2.9 the three-band and single-band patterns correspond to identical values of all the simulation parameters. The full resolution of the challenging pattern-selection problem obviously goes beyond the scope of this letter. However, a tentative picture for the nucleation of stationary swarms from a disordered state can be attempted from Eq. (2.22). The emergence of sharp fronts is natural since the l.h.s. of (2.22) has the form of Burgers equation, which supports rarefaction shocks [221]. A density fluctuation above $\rho_c$ grows and polarizes via the generic coupling between density and order embodied in the $\rho$-dependence of $a_2$ in Eq. (2.22). When these two competing effects balance each other, the density at the top of the shock is pinned, and a constant-shape asymmetric band steadily propagates. In the transient regime, we therefore expect several bands to form and collide, until the system reaches one of the possible steady states. This mechanism might favor large-amplitude/fast bands via coalescence events, in agreement with the experiments reported in [36].

To close this letter we comment on the role of fluctuations on the transition towards collective motion [216]. Eq. (2.22) predicts a second-order transition for homogeneous systems. Here, we have evidenced that stationary polarized excitations (solitary bands, and polar-liquid droplets) can coexist with a homogeneous isotropic phase, which in turn confirms the first order scenario evidenced in numerical simulations [49, 92]. This coexistence does not rely on any fluctuation-induced mechanism, unlike all the conventional equilibrium scenarios making first order a mean-field second-order transition (e.g. Brazowskii1975 [35] and Halperin-Lubensky-Ma [99]). However, beyond the mean-field deterministic picture, fluctuations are very likely to play a major role in the stability, the selection, and the ordering of the band patterns. These difficult but crucial problems are the topic for future work.

We thank J. Toner for valuable comments and suggestions. DB acknowledges support from Institut Universitaire de France, and ANR project MiTra. HC, AP, AS, and JT thank the Max Planck Institute for the Physics of Complex Systems, Dresden, for providing the framework of the Advanced Study Group “Statistical Physics of Collective Motion” within which part of this work was performed.

# Supplementary Information

## A Microscopic models

Figure 1 of the main text shows typical examples of inhomogeneous structures found in polar flocking models. Fig. 2.9(a) and 2.9(b) stem from a Vicsek model with vectorial noise [49] while Fig. 2.9(c) comes from an active Ising model [197]. We recall below the definition of these models, while more details can be found in the original publications [49, 197].

### A.1 Vicsek model

N point-like particles are moving off-lattice in 2d at constant speed $v_0$. At each time step, the direction along which each particle moves is updated in parallel, according to the rule

$$\theta_i(t+1) = \arg\left(\sum_{j\in\mathscr{S}_i} \mathbf{v_j}(t) + \eta\mathscr{N}_i\xi\right) \tag{2.27}$$

where $\theta_i$ is the angle made by the velocity $\mathbf{v_i}$ of the $i^{\text{th}}$ particle and, say the $x$-axis. The sum runs on particles in $\mathscr{S}_i$, the neighborhood of $i$ of radius $r_0$. $\mathscr{N}_i$ is the number of particles in $\mathscr{S}_i$ and $\xi$ is a random unit vector with no angular correlation. This equation defines so-called vectorial noise version of the Vicsek model [49, 215].

### A.2 Active Ising model

N particles carrying a spin $\pm1$ move and interact on a 2d lattice, an arbitrary number of particles being allowed on each site. The particles can hop to any adjacent sites or flip theirs spins according to Monte-Carlo rates. The spin-flipping results from an on-site ferromagnetic interaction, a particle reverses its spin S on site $i$ at rate

$$\mathrm{W}(\mathrm{S}\to-\mathrm{S}) = \exp\left(-\beta\mathrm{S}\frac{m_i}{\rho_i}\right) \tag{2.28}$$

where $m_i$ and $\rho_i$ are the magnetization and the number of particles on site $i$ and $\beta$ plays the role of an inverse temperature. The "self-propulsion" of the particles stems from a bias on the hopping direction: particle $k$ hop to the left (resp. right) with rates $\mathrm{D}(1+\varepsilon\mathrm{S}_k)$ (resp. $\mathrm{D}(1-\varepsilon\mathrm{S}_k)$) and to the top and bottom with rate D. This sets an effective self-propulsion at speed $2\mathrm{D}\varepsilon\mathrm{S}_k$ in the horizontal direction.

## B Expressions of H and F

Using the functional dependences of $a_2(\rho)$ and $a_4(\rho)$ that we introduced in the main text, we find the following expressions for the friction F and the potential H:

$$\mathrm{F}(\mathrm{W}) = \left(c-\lambda c^{-1}\right)\mathrm{W} - \frac{1}{2}\xi\mathrm{W}^2, \tag{2.29}$$

$$\frac{\mathrm{dH}}{\mathrm{dW}} = \left[-(\rho_c-\rho^\star) + \frac{\mathrm{W}}{c} - \frac{c\mathrm{W}^2}{\mathrm{P}_0^2(c\rho^\star+\mathrm{W})}\right]\mathrm{W}. \tag{2.30}$$

The latter equation can be integrated over W and yields

$$\begin{aligned}\mathrm{H}(\mathrm{W}) = &-\frac{1}{2}(\rho_c-\rho^\star)\mathrm{W}^2 + \frac{1}{3c}\mathrm{W}^3 - \frac{c^3\rho^{*2}}{\mathrm{P}_0^2}\mathrm{W} + \frac{c^2\rho^*}{2\mathrm{P}_0^2}\mathrm{W}^2 \\ &- \frac{c}{3\mathrm{P}_0^2}\mathrm{W}^3 + \frac{c^4\rho^{*3}}{\mathrm{P}_0^2}\log\left(1+\frac{\mathrm{W}}{c\rho^\star}\right).\end{aligned} \tag{2.31}$$

## C Eigenvalues of the Jacobian matrix

The eigenvalues of the Jacobian matrix evaluated at the fixed point $(W_H, F(W_H))$ are plotted in Fig. 2.12. The signs of their real and imaginary parts are only set by the difference $W_H - W_F$, hence a Hopf bifurcation occurs at $W_H = W_F$.

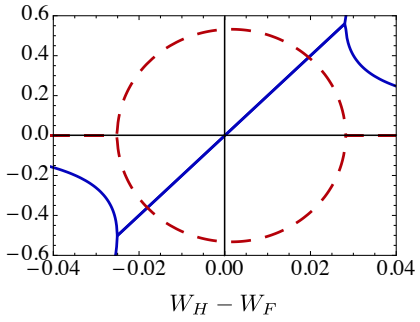


**Figure 2.12** – Eigenvalues of the Jacobian matrix at the fixed point $(W_H, F(W_H))$, as a function of $W_H - W_F$. The curves were plotted for fixed $c = 0.9$ by varying $\rho^\star$. Blue solid line: real part. Red dashed line: imaginary part.

## D Polar liquid domains/Heteroclinic cycles

We compute analytically the shape of the heteroclinic orbits, *i.e.* the boundary between a polar-liquid droplet and the surrounding isotropic gas, in the limit of small $P_0$. Since the magnetization scale is set by $P_0$, when $P_0 \to 0$, $W \ll \rho^*$ so that the Hamiltonian reduces to

$$\frac{dH}{dW} = \left[ -(\rho_c - \rho^*) + \frac{W}{c} - \frac{W^2}{P_0^2 \rho^*} \right] W \tag{2.32}$$

Note that this cubic expression becomes exact if we assume the coefficient $a_4$ to be independent of $\rho$ and $W^2$, in the hydrodynamic equations (Eq. (2) main text). With this potential, solutions can be found using the Ansatz

$$W_\pm(x - ct) = \frac{W'_H}{2} \left[ 1 + \tanh\left( \Lambda_\pm (x - ct) \right) \right], \tag{2.33}$$

which yields excellent agreement with the numerical solution of the ODE, see Fig. 2.13. For a given set of parameters, only one heteroclinic cycle is found in the $(\rho^*, c)$ plane and indeed, inserting

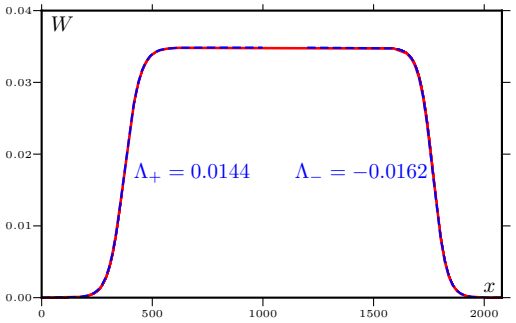


**Figure 2.13** – Heteroclinic orbit obtained by numerical integration (plain red line) and fit with Ansatz (2.33) (dashed blue lines). Fitting parameters are the width of the front $\Lambda_\pm$ and the position of the front. Parameters: $P_0 = 0.1$, $\rho_c = 1$, $\xi = 10$, $\lambda = 0.01$, $D = 50$, $c = 0.218$, $\rho^* = 0.9502$.

Eq. (2.33) in the ODE with the potential given by Eq. (2.32) we obtain a unique solution ($\rho^*$, $c$) given by

$$c = \frac{1}{3\sqrt{2}}\sqrt{\tilde{P}_0 + 9\lambda + \sqrt{72P_0^2\lambda + (9\lambda + \tilde{P}_0^2)^2}} \tag{2.34}$$

$$\rho^* = \frac{9c^2\rho_c}{9c^2 + 2P_0^2} \tag{2.35}$$

$$W_H' = \frac{2P_0^2\rho^\star}{3c} \tag{2.36}$$

$$\Lambda_\pm = \frac{(c - \frac{\lambda}{c})}{4D}\left(-1 \pm \sqrt{1 + \frac{4D(\rho_c - \rho^*)}{(c - \frac{\lambda}{c})^2}}\right) \tag{2.37}$$

where $\tilde{P}_0 = P_0^2(3\xi\rho_c - 2)$.

Table 2.1 compares the five parameters $c$, $\rho^\star$, $W_H'$, $\Lambda_+$ and $\Lambda_-$ found analytically to the best fit. The agreement is excellent.

| | Numerical | Analytical |
|---|---|---|
| c | 0.218 | 0.2041 |
| $\rho^*$ | 0.9502 | 0.949 |
| $W_H'$ | 0.0348 | 0.0310 |
| $\Lambda_+$ | 0.0144 | 0.0152 |
| $\Lambda_-$ | -0.0162 | -0.0167 |

Table 2.1 – Comparison between numerical and analytical values obtained in the limit $P_0 \to 0$. Parameters: $P_0 = 0.1$, $\rho_c = 1$, $\xi = 10$, $\lambda = 0.01$, $D = 50$. Numerically, $\Lambda_\pm$ are obtained by fitting the profile with Ansatz (2.33).

We thank J. Toner for a careful reading of the supplementary document and for suggesting the compact formula shown in Eq. (2.36).

CHAPTER 3

# Geometry of interacting trajectories in a flock

In the previous chapters, we have followed the standard framework of active matter: the population of motile individuals is viewed as an active fluid, described by smoothly-varying hydrodynamic fields [136]. This approach is well-suited for studying the phase behavior of the system. It has proven successful in elucidating the polar patterns that were observed in experiments and simulations. However, it is not sufficient to fully account for the dynamics of the active particles: by definition, the hydrodynamic equations do not retain all information on the individual motion at small time- and length-scales. In this chapter, we therefore focus on a complementary description of active populations. Rather than studying the collective patterns at large scale, we study the *individual* dynamics at all scales. This approach may be useful for practical issues. In contrast with the Quincke rollers, in the vast majority of systems the microscopic dynamics cannot be modeled *a priori*. This situation includes all animal populations, in which behavioral rules must be inferred from experimental measurements, see e.g. [46, 132]. In order to build a microscopic model, one needs quantitative observables that can be measured on actual flocks. Eulerian hydrodynamic descriptions, based on coarse-grained quantities, are obviously not sufficient to unambiguously build and test models at the individual level.

Here, we adopt a *Lagrangian* approach. Combining numerical and analytical results, we characterize the trajectories of interacting bodies using geometrical quantities. We introduce observables that probe the individual motion and the mixing dynamics within a flock, and we study their statistics in paradigmatic flocking models.

This chapter is divided in two parts.

First, we geometrically describe the individual motion. Building on an analogy with semi-flexible polymers at equilibrium, we analyze the curvature and the writhe of three-dimensional trajectories. The results are described p. 122 and followings.

Second, we turn to the relative motion of the individuals. We define a measure of the mixing within a compact flock, which we quantify as the winding of the braid formed by the particle trajectories. This approach is introduced in the article “Braiding a flock: winding statistics of interacting flying spins", which can be found p. 134.

Before entering the details, we begin with a very short summary of the main ideas and results.

## 1 Why is a geometric approach relevant?

Let us first consider the paradigmatic flocking models in a geometric perspective. N particles, located at positions $\mathbf{r}_i$ ($i = 1, ..., N$) in three-dimensional space, propel themselves along directions $\hat{\mathbf{t}}_i$ at a constant speed $v_0$. Their equations of motion, in three spatial dimensions, take the form:

$$\frac{\mathrm{d}}{\mathrm{d}t}\mathbf{r}_i = v_0\hat{\mathbf{t}}_i, \tag{3.1}$$

$$\frac{\mathrm{d}}{\mathrm{d}t}\hat{\mathbf{t}}_i = \mathbf{T}_i\left(\{\mathbf{r}_j, \hat{\mathbf{t}}_j\}\right) + \boldsymbol{\xi}_i. \tag{3.2}$$

Eq. (3.2) describes the rotation of the particle orientation. $\hat{\mathbf{t}}_i$ diffuses on the unit sphere due to the Gaussian rotational noise $\boldsymbol{\xi}_i \perp \hat{\mathbf{t}}_i$, with zero mean and variance $\langle \boldsymbol{\xi}_i(t)\boldsymbol{\xi}_i(t')\rangle = 2D\,\delta(t-t')\mathbb{I}$. The interactions with the neighbors take the form of an effective torque, $\mathbf{T}_i\left(\{\mathbf{r}_j, \hat{\mathbf{t}}_j\}\right)$, which changes the particle direction.

As the particles move at constant speed, time exactly corresponds to the curvilinear coordinate of the trajectories, $s = v_0 t$. The trajectory of particle $i$ in real space, $\{\mathbf{r}_i(t)\}$, is deduced from the path $\{\hat{\mathbf{t}}_i(s)\}$ followed by its direction on the unit sphere. By definition, $\hat{\mathbf{t}}_i(s)$ is the unit tangent vector of the trajectory. Its rotation along the curve, $\frac{\mathrm{d}}{\mathrm{d}s}\hat{\mathbf{t}}_i = \kappa_i\hat{\mathbf{n}}_i$, defines the curvature $\kappa_i$ and the normal vector $\hat{\mathbf{n}}_i$ in the Frénet frame. As a result, Eq. (3.2) can be rewritten in a geometric form:

$$v_0\,\kappa_i\hat{\mathbf{n}}_i = \mathbf{T}_i\left(\{\mathbf{r}_j, \hat{\mathbf{t}}_j\}_j\right) + \boldsymbol{\xi}_i. \tag{3.3}$$

Remarkably, the dynamics of interacting flying spins reduces to a purely geometric problem. Eq. (3.3) relates the local curvature of the $i^{\text{th}}$ trajectory to the positions and tangent vectors of the neighboring trajectories. The population of self-propelled particles can be seen as a bundle of interacting curves. In the following, we therefore use geometric quantities to characterize the shape and the entanglement of the trajectories.

## 2 Geometric description of the individual dynamics

In the first part of this chapter, p. 122 and followings, we characterize the shape of active-particle trajectories. This approach is based on the following observation: in the canonical framework of polar active matter, which consists in polar alignment interactions, the particle trajectories are equivalent to semi-flexible polymers at equilibrium. The analogy is easily understood for non-interacting particles, $\mathbf{T}_i = \mathbf{0}$ (disordered phase akin to Fig. 3.1(a)). Eq. (3.2) readily shows that the tangent vector $\hat{\mathbf{t}}_i$ diffuses on the unit sphere. The direction of motion decorrelates over a typical time $D^{-1}$, i.e. over a typical distance $\ell_p \sim v_0 D^{-1}$. The resulting trajectory exactly corresponds to a polymer chain having a persistence length $\ell_p$, which arises from the interplay between a finite bending modulus and thermal fluctuations [180, 186]. We extend this analogy to particles experiencing alignment interactions, in strongly polarized phases (Fig. 3.1(b)). Assuming Vicsek-like alignment rules for $\mathbf{T}_i$, in a mean-field description, we show that the alignment torques induced by the neighbors translate to a stretching force applied to the equivalent polymer. We then exploit this analogy to characterize the trajectories. We describe the non-equilibrium motion of active particles with the tools commonly used to study polymers. We consider two geometric quantities: (i) the curvature, which measures the in-plane bending of the trajectory; (ii) the writhe, which measures the integrated torsion of the trajectory out of its plane of curvature [21, 135, 178]. Combining analytical and numerical results, we show how these quantities probe the individual dynamics.

In particular, we show that the typical curvature reflects the collective organization of the system into polar phases. More precisely, the curvature statistics depends on the time resolution $\delta t$ at which the trajectory is observed ($\delta t$ sets the short-time cut-off required to interpret the white noise $\boldsymbol{\xi}(t)$). Fig. 3.1(d) shows the mean curvature plotted versus the coarse-graining time $\delta t$, for

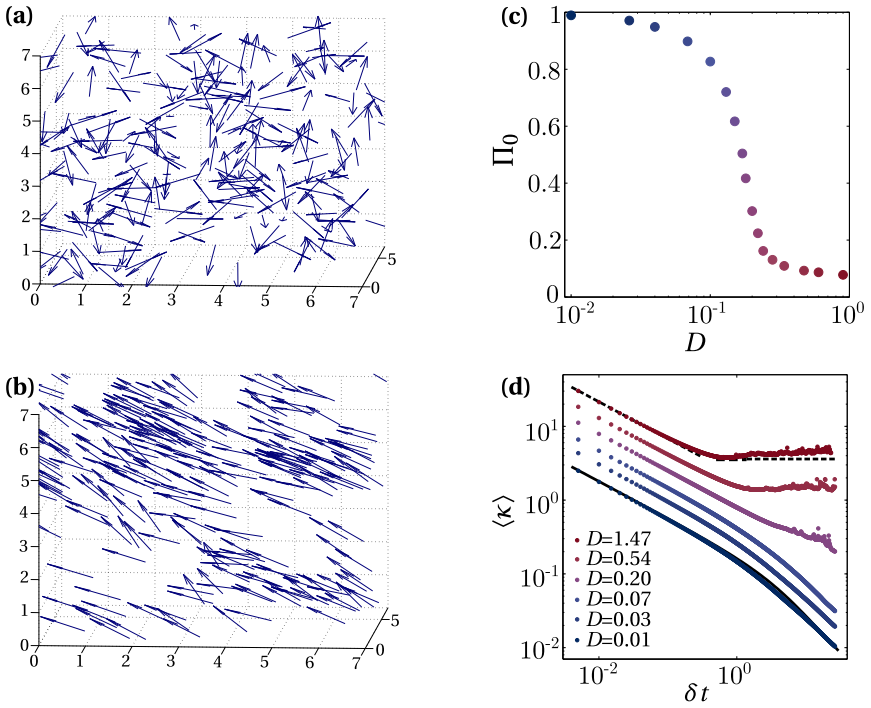


**Figure 3.1** – Simulation of the model Eqs. (3.1)–(3.2), with Vicsek-like alignment interactions (250 particle in a periodic box of length 7). **(a)** Instantaneous positions and orientations of the particles in the isotropic phase, D = 1.47. **(b)** Same as **(a)** in the polar phase, D = 0.01. **(c)** Mean polarization, $\Pi_0$, plotted versus the amplitude of the noise. **(d)** Mean curvature of the trajectories, plotted versus the time resolution at which the trajectory is observed. The different colors correspond to different noise amplitudes. Dots: numerical data. Dashed black line: theoretical prediction for non-interacting particles (D = 1.47). Solid black line: theoretical prediction for strongly-polarized states (D = 0.01).

different noise amplitudes. The numerical results are in good quantitative agreement with the analytical predictions established from the polymer analogy (black lines). For long $\delta t$s, isotropic and polar phases display markedly different behaviors. The transition to collective motion, Fig. 3.1(c), has a clear signature on the curvature of the particle trajectories. Finally, we discuss the robustness of the results to the form of the interactions. We study a more complex numerical model which reproduces compact flocks akin to animal groups in the wild [49, 57, 92]. Alignment interactions are associated with attractive and repulsive couplings. We show that the curvature statistics bear the signature of the microscopic dynamics at all time scales.

## 3 Geometric description of the mixing dynamics

In the second part of this chapter, we go beyond the mean-field description considered below. Focusing on compact polar flocks akin to Fig. 3.2(a), we study the relative motion of the particles within the group in a geometric perspective. More precisely, we quantify the mixing dynamics. As they move, the individuals continuously exchange their position: their trajectories are not parallel but form a braid of tangled curves. In this approach, the mixing within the flock is measured by the entanglement between the trajectories.

In order to build a more quantitative description, we introduce a measure of the entanglement of the trajectories in a convenient representation [34, 161, 205]. As we are interested in the internal dynamics of the group, irrespective of its global motion, we follow the particle displacements in a frame which is parallel-transported with the flock. When individuals exchange their positions, they trajectories cross each other, as depicted in Fig. 3.2(b). By counting the crossings, we calculate the winding of the braid formed by the trajectories, W(T). This quantity gives the averaged number

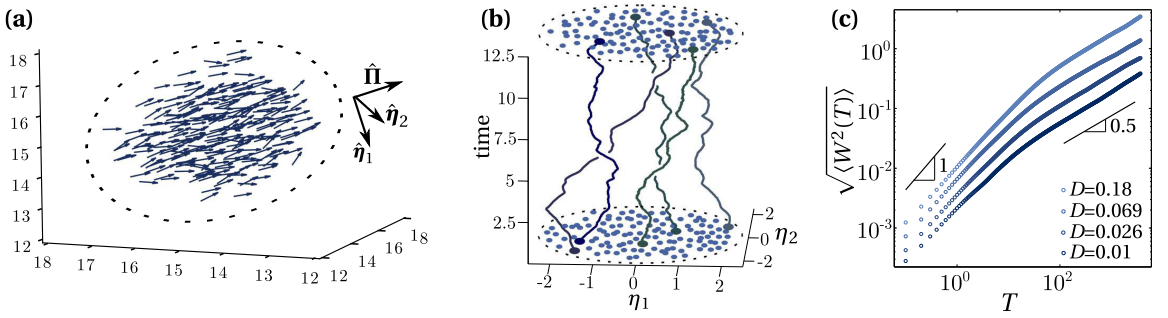


**Figure 3.2** – **(a)** The positions of the particles are followed in the frame $(\hat{\boldsymbol{\eta}}_1, \hat{\boldsymbol{\eta}}_2, \hat{\boldsymbol{\Pi}})$ which is parallel-transported with the flock. **(b)** Braid of entangled trajectories. When particles exchange their relative positions in the flock, their trajectories cross each other. **(c)** Standard deviation of the winding of the braid, plotted versus time.

of turns made by an arbitrary particle around an other one, during a time T.

We investigate the statistics of the winding numerically, and show that it displays two main features.

(i) In Fig. 3.2(c), we plot the standard deviation $\sqrt{\langle \mathrm{W}^2(\mathrm{T})\rangle}$ versus time. It displays a crossover between a ballistic regime at short times, where $\sqrt{\langle \mathrm{W}^2(\mathrm{T})\rangle} \propto \mathrm{T}$, and a diffusive growth at long times, where $\sqrt{\langle \mathrm{W}^2(\mathrm{T})\rangle} \propto \sqrt{\mathrm{T}}$.

(ii) Studying the correlations of the trajectory crossings, we show that the winding statistics results from correlated particle displacements at the entire-flock scale.

We finally identify the origin of these numerical findings. The formation of a polar flock corresponds to a spontaneous breaking of the rotational symmetry. It therefore gives rise to a soft orientational mode, consisting in a global rotation of the flock around its direction of motion, which twists the trajectories at the entire-flock scale. We show that this coherent rotation chiefly rules the winding statistics at long times. As the existence of a soft rotation mode is generic to all the flying-spin models [26], we expect our results to be qualitatively robust to the detailed form of the interactions.

All these results are detailed in the article “Braiding a flock: winding statistics of interacting flying spins", p. 134.

## Conclusion and perspectives

In this chapter, we have focused on the geometry of the paradigmatic active-matter models. Combining analytical and numerical approaches, we have characterized the particle trajectories and their entanglement in three-dimensional flocks.

Coming back to an experimental perspective, this approach provides observables which could be measured in real systems. It may be useful to further test the relevance of the standard active-matter models to the description of actual flocks. More specifically, the following questions could be addressed.

- In all models, the emergence of polar flocks arises from a spontaneous breaking of the rotational symmetry. All spatial directions are *a priori* equivalent. However, animal flocks often respond to external perturbations and fields that explicitly break the rotational symmetry. For instance, it was observed in bird flocks that the vertical axis (defined by gravity) has a specific status [43]; the group mostly follows horizontal directions. The direction of motion

is also influenced by the presence of food, predators or by seasonal migration. This explicit breaking of space isotropy may cause discrepancies between actual flocks and theoretical models. In particular, the soft orientational mode, which chiefly rules the winding of the trajectories, may be suppressed by external fields. The impact of constant fields on the dynamics could be investigated both theoretically and experimentally.

- In a similar perspective, it was observed that bird flocks change their direction of motion by performing sudden collective turns [6, 8]. In our approach, these events create numerous crossings between the individual trajectories, in response to external perturbations. It would be interesting to study how external fluctuations impact the geometry of the individual trajectories.

- We restricted ourselves to particles moving at constant speed. One could study how fluctuations of the propulsion speed change the geometry of the trajectories [26, 142]. For instance, a flocking model was recently proposed to account for the inertia of the individuals [7, 8, 46], and could be considered in a similar geometric perspective.

- The dynamics of active particles moving in disordered media has raised growing interest in the past years [53, 54, 166]. For instance, it was numerically and experimentally found that self-propelled particles can be trapped by obstacles, leading to subdiffusive behaviors (see [54], and recent experimental results obtained by N. Desreumaux and V. Chikkadi on the Quincke rollers [143]). The curvature of the trajectories might be an efficient tool to quantify the trapping of the particles and the radius of their orbits.

# Trajectories of aligning self-propelled particles: geometric characterization

Here, we describe the dynamics of interacting self-propelled particles. Combining analytical and numerical approaches, we characterize their trajectories in three spatial dimensions. We show that the paradigmatic framework of active matter – particles moving at a constant speed and undergoing alignment interactions – can be mapped onto a well-studied equilibrium problem: the individual trajectories are analogous to semi-flexible polymer chains. Building on this analogy, we characterize the writhe and the curvature of active-particle trajectories. We show that this Lagrangian description probes the collective organization of the population into polar phases. It makes is possible to directly measure the different time-scales of the dynamics by varying the time resolution at which the trajectories are observed.

We proceed as follows. In the first section, we establish the analogy between particle trajectories and polymer chains, in both isotropic and strongly-polarized phases. We then exploit this result, in section 2, to deduce the statistics of the writhe fluctuations. Section 3 is devoted to the curvature of the trajectories. We show that the transition to collective motion has a clear signature on the typical curvature. Finally, we compare the analytical expressions to numerical results, in section 4. We validate the theoretical predictions and discuss their robustness to different interaction rules. We emphasize that analyzing the typical trajectory of one individual makes it possible to finely probe the global organization of the flock.

## 1 Active-particle trajectories as semi-flexible polymers

We start from the paradigmatic models of flocking [216]. N persistent random walkers ($\mathbf{r}_i(t)$, $i = 1 \dots \mathrm{N}$) propel at a constant speed $v_0$ along a direction $\hat{\mathbf{t}}_i$. Their equations of motion, in three spatial dimensions, take the form:

$$\frac{\mathrm{d}}{\mathrm{d}t}\mathbf{r}_i = v_0 \hat{\mathbf{t}}_i, \tag{3.4}$$

$$\frac{\mathrm{d}}{\mathrm{d}t}\hat{\mathbf{t}}_i = \mathbf{T}_i\left(\{\mathbf{r}_j, \hat{\mathbf{t}}_j\}\right) + \boldsymbol{\xi}_i. \tag{3.5}$$

The particle orientation, $\hat{\mathbf{t}}_i$, diffuses on the unit sphere due to the Gaussian rotational noise $\boldsymbol{\xi}_i \perp \hat{\mathbf{t}}_i$, with zero mean and variance $\langle \boldsymbol{\xi}_i(t)\boldsymbol{\xi}_i(t')\rangle = 2\mathrm{D}\,\delta(t-t')\mathbb{I}$. The interactions with the neighbors take the form of an effective torque, $\mathbf{T}_i\left(\{\mathbf{r}_j, \hat{\mathbf{t}}_j\}\right)$, which rotates the particle direction. We consider two limiting cases: non-interacting bodies ($\mathbf{T}_i = \mathbf{0}$), and particles experiencing Vicsek-like alignment torques leading to polar organization. In both situations, we show that the non-equilibrium dynamics of a particle can be mapped onto an equilibrium problem: the trajectories correspond to the conformations of semi-flexible polymer chains.

### 1.1 Free particles – isotropic phase

We first consider the simple case of non-interacting particles: $\mathbf{T}_i = \mathbf{0}$. This limit is also relevant when the interaction term, in Eq. (3.5), has a very small amplitude compared to the rotational noise. The particles behave as persistent random walkers moving at constant speed. Their orientation vectors $\hat{\mathbf{t}}_i$ diffuse on the unit sphere and decorrelate over a typical time $\mathrm{D}^{-1}$. In other words, the direction of motion remains correlated over a persistence length $\sim v_0/\mathrm{D}$ along a trajectory. A similar geometry is found for semi-flexible polymer chains, which also display a persistence length set by the competition between the bending modulus and thermal noise. Let us draw the analogy explicitly. As the particle moves at constant speed, its trajectory in real space, $\{\mathbf{r}_i(t)\}$, is equivalent to the path followed by its orientation on the unit sphere, $\{\hat{\mathbf{t}}_i(t)\}$. The probability of this path is deduced from Eq. (3.5). It is given by [2]:

$$\mathrm{P}\left[\hat{\mathbf{t}}_i(t)\right] = \frac{1}{\mathrm{Z}} \exp\left[-\frac{1}{4\mathrm{D}}\int \mathrm{d}t \left(\frac{\mathrm{d}\hat{\mathbf{t}}_i}{\mathrm{d}t}\right)^2\right], \tag{3.6}$$

where Z is a normalization constant. To make the connection with semi-flexible polymers, we introduce the curvilinear coordinate along the trajectory, $s = v_0 t$. Eq. (3.6) corresponds to the distribution of the conformations of a worm-like polymer chain at equilibrium [180, 186]. The equivalent polymer has a bending modulus K and is described by the Hamiltonian $\mathscr{H} = \frac{1}{2}\mathrm{K}\int \mathrm{d}s \left(\mathrm{d}\hat{\mathbf{t}}_i/\mathrm{d}s\right)^2$. From Eq. (3.6), we readily identify the persistence length of the polymer at temperature T with the persistence length of the particle trajectory: $\mathrm{K}/(k_\mathrm{B}\mathrm{T}) \equiv v_0/(2\mathrm{D})$. The constant-speed constraint, Eq. (3.4), translates into a local inextensibility condition for the polymer [116].

### 1.2 Aligning particles – strongly polarized phase

We now extend the previous analogy to populations of particles experiencing alignment interactions. We show that, in a mean-field approach, the trajectory of a particle is analogous to a polymer stretched by a constant force. Following the paradigmatic Vicsek model, we assume that particle $i$ aligns its direction of motion along the mean orientation of its neighbors. Assuming that it interacts with the $\mathrm{N}_i^\mathrm{A}$ particles lying in the sphere $\mathscr{A}_i$ of radius $\mathrm{R}_\mathrm{A}$, it experiences the torque:

$$\mathbf{T}_i = \left(\mathbb{I} - \hat{\mathbf{t}}_i\hat{\mathbf{t}}_i\right)\cdot\frac{1}{\tau}\frac{1}{\mathrm{N}_i^\mathrm{A}}\sum_{j\in\mathscr{A}_i}\hat{\mathbf{t}}_j, \tag{3.7}$$

where $\tau$ is the typical alignment time. The projection operator $\left(\mathbb{I} - \hat{\mathbf{t}}_i\hat{\mathbf{t}}_i\right)$ ensures that $\hat{\mathbf{t}}_i$ rotates while keeping a unit norm, in Eq. (3.5). Below a critical value of the noise amplitude, this variant of the Vicsek model gives rise to polar states, in which the particle directions are aligned. The polar organization is described by the global polarization vector, $\mathbf{\Pi}_0 = \frac{1}{\mathrm{N}}\sum_i \hat{\mathbf{t}}_i$.

We use a mean-field approach to describe the strongly-polarized phase. In the alignment torque, Eq. (3.7), we approximate the local average over the neighbors by the overall polarization: $\frac{1}{\mathrm{N}_i^\mathrm{A}}\sum_{j\in\mathscr{A}_i}\hat{\mathbf{t}}_j \sim \mathbf{\Pi}_0$. This crude ansatz is certainly not valid in dilute or spatially-heterogeneous systems. However, at high densities and deep in the polar phase, when the average orientation of the neighbors remains very close to $\Pi_0 \sim 1$, it simply states that the particle continuously experiences a strong alignment force. Eq. (3.5) then reduces to:

$$\frac{\mathrm{d}}{\mathrm{d}t}\hat{\mathbf{t}}_i = \left(\mathbb{I} - \hat{\mathbf{t}}_i\hat{\mathbf{t}}_i\right)\cdot\frac{1}{\tau}\mathbf{\Pi}_0 + \boldsymbol{\xi}_i. \tag{3.8}$$

Deep in the polar phase, the orientation of particle $i$ remains very close to the mean direction of motion $\hat{\mathbf{\Pi}}_0$. Denoting by $\boldsymbol{\eta}_i(t)$ the transverse orientational fluctuations, the direction of motion is set by the unit vector $\hat{\mathbf{t}}_i(t) = \sqrt{1-\eta_i^2(t)}\,\hat{\mathbf{\Pi}}_0 + \boldsymbol{\eta}_i(t)$. In the limit of small fluctuations, we obtain:

$$\hat{\mathbf{t}}_i(t) = \left(1 - \frac{\eta_i^2(t)}{2}\right)\hat{\mathbf{\Pi}}_0 + \boldsymbol{\eta}_i(t) + \mathscr{O}\left(\eta_i^4\right), \tag{3.9}$$

where the unit vector $\hat{\mathbf{\Pi}}_0 \equiv \mathbf{\Pi}_0/\Pi_0$ gives the mean direction of motion. Inserting this expression in the evolution equation (3.8), we arrive at:

$$\frac{\mathrm{d}}{\mathrm{d}t}\boldsymbol{\eta}_i = -\frac{\Pi_0}{\tau}\boldsymbol{\eta}_i + \boldsymbol{\xi}_i + \mathscr{O}\left(\eta_i^3\right). \tag{3.10}$$

The latter equation corresponds to the well-known Ornstein-Uhlenbeck process. In the direction transverse to $\hat{\mathbf{\Pi}}_0$, the particle orientation fluctuates in a harmonic effective potential, the strength of which is set by the magnitude of mean polarization, $\Pi_0$.

We now map this dynamics onto an equivalent polymer problem. To do so, we consider the probability of a trajectory $\boldsymbol{\eta}_i(t)$, as we did it for free particles. It is given by the following Onsager-Machlup functional, derived from the Langevin equation (3.10) [2]:

$$\mathrm{P}\left[\boldsymbol{\eta}_i(t)\right] \propto \exp\left[-\frac{1}{4\mathrm{D}}\int \mathrm{d}t\left(\frac{\mathrm{d}\boldsymbol{\eta}_i}{\mathrm{d}t} + \frac{\Pi_0}{\tau}\boldsymbol{\eta}_i\right)^2\right]. \tag{3.11}$$

Expanding the square in the integral, we note that the cross-term is a time derivative: $2(\Pi_0/\tau)\frac{\mathrm{d}\boldsymbol{\eta}_i}{\mathrm{d}t}\cdot\boldsymbol{\eta}_i = \frac{\mathrm{d}}{\mathrm{d}t}\left[(\Pi_0/\tau)\eta_i^2\right]$. It only contributes to the normalization factor. Up to this trivial gauge transformation, we obtain:

$$\mathrm{P}\left[\boldsymbol{\eta}_i(t)\right] \propto \exp\left[-\frac{1}{4\mathrm{D}}\int \mathrm{d}t\left(\frac{\mathrm{d}\boldsymbol{\eta}_i}{\mathrm{d}t}\right)^2 - \frac{\Pi_0^2}{4\mathrm{D}\tau^2}\int \mathrm{d}t\,\boldsymbol{\eta}_i^2\right]. \tag{3.12}$$

Introducing the curvilinear coordinate $s = v_0 t$, we rewrite this equation as a thermal distribution: $\mathrm{P}\left[\boldsymbol{\eta}_i(t)\right] \propto \exp\left[-\mathscr{H}/(k_\mathrm{B}\mathrm{T})\right]$. The corresponding Hamiltonian has the form: $\mathscr{H} = \frac{1}{2}\mathrm{K}\int \mathrm{d}s\,(\mathrm{d}\boldsymbol{\eta}_i/\mathrm{d}s)^2 + \frac{1}{2}\mathrm{F}\int \mathrm{d}s\,\boldsymbol{\eta}_i^2$, where $\mathrm{K}/(k_\mathrm{B}\mathrm{T}) \equiv v_0/(2\mathrm{D})$ and $\mathrm{F}/(k_\mathrm{B}\mathrm{T}) \equiv \Pi_0^2/(2\mathrm{D}v_0\tau^2)$. This formal identification has a clear physical interpretation in polymer physics. The first term of the Hamiltonian corresponds to a bending energy, as we discussed it previously. In the paraxial approximation, Eq. (3.9), the last term can be rewritten as: $\frac{1}{2}\mathrm{F}\int \mathrm{d}s\,\boldsymbol{\eta}_i^2 = \mathrm{F}\int \mathrm{d}s\,\left(1 - \hat{\mathbf{\Pi}}_0\cdot\hat{\mathbf{t}}_i\right)$. Recalling that $\hat{\mathbf{t}}_i = \frac{\mathrm{d}}{\mathrm{d}s}\mathbf{r}_i$, it takes the equivalent form: $\frac{1}{2}\mathrm{F}\int \mathrm{d}s\,\boldsymbol{\eta}_i^2 = -\mathrm{F}\hat{\mathbf{\Pi}}_0\cdot\int \mathrm{d}\mathbf{r}_i + \mathrm{cte}$. Hence it corresponds to the potential energy induced by a stretching force $\mathrm{F}\hat{\mathbf{\Pi}}_0$, applied at the extremity of the polymer (see e.g. [33, 116, 137]). In the polymer analogy, the mean-field alignment torque translates into a constant stretching force.

In the following, we exploit the analogy with polymers at equilibrium to characterize the dynamics of aligning self-propelled particles. We aim at relating the geometry of the individual trajectories to the global state of the system. How does a single trajectory provide information on the collective organization of the population?

## 2 Writhe of the trajectories

The geometry of a curve is usually described by two properties: the curvature quantifies its local bending, and the torsion accounts for its three-dimensional twisting behavior. We use a similar framework to characterize the particle trajectories. Let us first study the torsion properties. The local torsion of a curve is usually given by the rotation of the binormal vector, in the Frénet-Serret frame. This definition requires that the curve has at least two derivatives. This is not the case for the trajectories resulting from Eqs. (3.4)–(3.5), which are not regular enough for the torsion to be well-defined [170]. Bulding on the analogy with polymers, we rather consider an integral quantity which also quantifies the three-dimensional winding of the trajectory: its writhe [33, 78, 135, 178].

Let us first recall the definition of the writhe, following [135]. We consider a 3D curve of length L such that the initial and final tangent vectors are identical: $\hat{\mathbf{t}}(s=0) = \hat{\mathbf{t}}(s=\mathrm{L})$, see Fig. 3.5(a). At the beginning of the curve, we choose two arbitrary vectors $\hat{\mathbf{u}}_1(0)$ and $\hat{\mathbf{u}}_2(0)$, tangent to $\hat{\mathbf{t}}(0)$, which

define an orthonormal basis. We then study the parallel transport of this frame along the path. Due to the writhing of the curve in 3D space, the final frame $\left(\hat{\mathbf{u}}_1(\mathrm{L}), \hat{\mathbf{u}}_2(\mathrm{L}), \hat{\mathbf{t}}(\mathrm{L})\right)$ has rotated with respect to $\left(\hat{\mathbf{u}}_1(0), \hat{\mathbf{u}}_2(0), \hat{\mathbf{t}}(0)\right)$ by an angle $\phi(\mathrm{L})$. The writhe of the curve is the number of turns made by the parallel-transported frame around the tangent vector $\hat{\mathbf{t}}(0) = \hat{\mathbf{t}}(\mathrm{L})$: it is defined by $\mathrm{Wr}(\mathrm{L}) \equiv \phi(\mathrm{L})/(2\pi)$. In order to extend this definition to arbitrary curves and compute the writhe numerically, it is convenient to introduce an equivalent representation. In Fig. 3.5(b), we sketch the path followed by the tangent vector $\hat{\mathbf{t}}(s)$ on the unit sphere, between $s = 0$ and $s = \mathrm{L}$. The angle $\phi(\mathrm{L})$ exactly corresponds to the area enclosed by this path on the sphere. This definition is the Fuller expression of the writhe [178]. It can be generalized to arbitrary curves, $\hat{\mathbf{t}}(s = 0) \neq \hat{\mathbf{t}}(s = \mathrm{L})$, by closing the associated path on the sphere by a geodesic (this simple choice ensures that planar curves have no writhe) [21, 135].

The writhe of worm-like polymer chains has been characterized in the literature. Using the analogy established in section 1, we directly transpose these available results to the trajectories of self-propelled particles. We again consider the two limits of non-interacting particles (isotropic phases) and strongly-polarized states.

***Free trajectories*** In the isotropic phase, the trajectories are equivalent to free polymer chains of length $v_0\mathrm{T}$, where T denotes the observation time. As positive and negative writhing are equally probable, the writhe distribution has no mean: $\langle \mathrm{Wr}(\mathrm{T}) \rangle = 0$. Theoretical expressions for the variance $\left\langle \mathrm{Wr}^2(\mathrm{T}) \right\rangle$ have been obtained in two asymptotic regimes.
(i) For short observation times compared to the persistence time, $\mathrm{T} \ll \mathrm{D}^{-1}$, the variance growth quadratically with time: $\left\langle \mathrm{Wr}^2(\mathrm{T}) \right\rangle = (\mathrm{DT})^2/12$.
(ii) For long observation times, $\mathrm{T} \gg \mathrm{D}^{-1}$, continuous models lead to a logarithmic divergence of the variance $\left\langle \mathrm{Wr}^2(\mathrm{T}) \right\rangle$ [32, 33, 135]. This behavior arises from the Fuller definition of the writhe, which is singular when $\hat{\mathbf{t}}(s) = -\hat{\mathbf{t}}(0)$ (see [135, 178]). In practice, this divergence is regularized by the discretization of the curve, and results in a diffusive behavior [135, 178]:

$$\left\langle \mathrm{Wr}^2(\mathrm{T}) \right\rangle \propto \mathrm{DT}. \tag{3.13}$$

***Trajectories in polar phases*** The writhe of stretched polymers has been studied by Sinha [195]. Transposing the result to the particle trajectories in strongly-polarized phases, the probability dis-

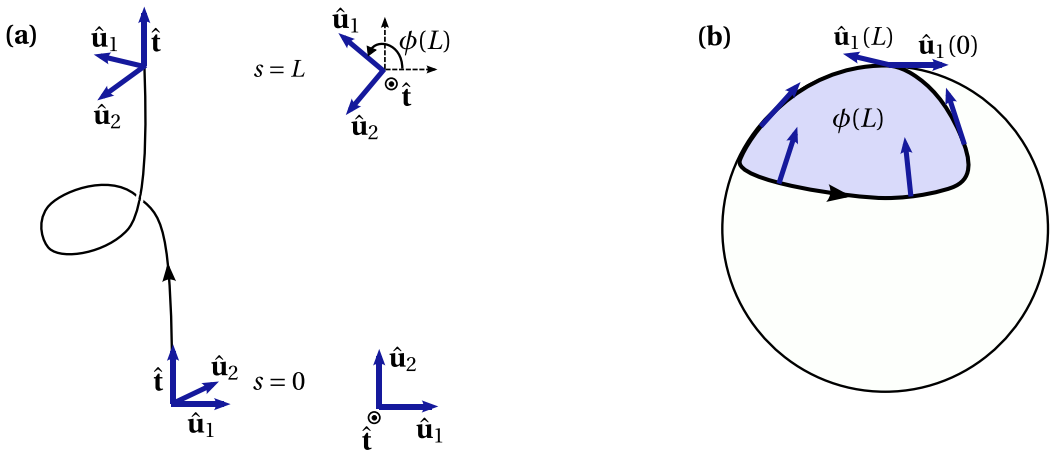


**Figure 3.3** – Definition of the writhe. **(a)** Rotation of the parallel-transported frame $\left(\hat{\mathbf{u}}_1(s), \hat{\mathbf{u}}_2(s), \hat{\mathbf{t}}(s)\right)$ along a writhing curve. When $\hat{\mathbf{t}}(s = 0) = \hat{\mathbf{t}}(s = \mathrm{L})$, the rotation angle $\phi(\mathrm{L})$ around the tangent vector is well-defined. **(b)** The rotation angle $\phi(\mathrm{L})$ corresponds to the area enclosed by the path $\hat{\mathbf{t}}(s)$ on the unit sphere. The blue arrows show the parallel transport of $\hat{\mathbf{u}}_1(s)$.

tribution of the writhe is:

$$P\left(Wr(T)\right) = \mathcal{N} \exp\left[-\frac{T\Pi_0}{\tau}\sqrt{1+\frac{4\pi^2}{D^2T^2}Wr^2}\right] \tag{3.14}$$

(where $\mathcal{N}$ is a normalization factor). For $T \ll D^{-1}$, the variance is [178]:

$$\left\langle Wr^2(T)\right\rangle = \frac{D\tau}{4\pi^2\Pi_0}DT. \tag{3.15}$$

We finally compare the results obtained for free particles and for trajectories in polar phases. At long observation times, the variance of the writhe grows linearly in both cases: $\left\langle Wr^2(T)\right\rangle \propto T$. In conclusion, the global organization of the population into polar states does not alter the diffusive behavior of the writhe fluctuations. It only impacts their growth rate at the quantitative level: the writhe is strongly reduced in the polar phase, where $D\tau/\Pi_0 \ll 1$. The writhe is therefore unlikely to be a useful quantity to probe the organization of a flock from the inspection of a single-particle trajectory. Conversely, we show in the next section that the curvature of a trajectory is a powerful measure of the collective dynamics.

## 3 Curvature of the trajectories

In order to find a geometric quantity which would qualitatively reflect the collective organization into polar phases, we now turn to the in-plane bending of the trajectories. We study the statistics of the curvature, which is defined from the rotation of the unit tangent vector as:

$$\kappa = \left|\frac{d\hat{\mathbf{t}}}{ds}\right|, \tag{3.16}$$

where $s = v_0 t$ is the curvilinear coordinate. The statistics of the curvature is set by Eq. (3.5). In this continuous-time model, it can be readily seen that the variance $\langle\kappa^2(t)\rangle$ diverges in the continuous-time limit, since $\langle\boldsymbol{\xi}_i(t)\cdot\boldsymbol{\xi}_i(t)\rangle = 4D\,\delta(0)$. Having tracking observations in mind, we introduce a coarse-graining time $\delta t$ to interpret the white noise and regularize the curvature distribution. In other words, the individual trajectory is observed at a finite time resolution $\delta t$.

### 3.1 Free trajectories

We first focus on non-interacting particles. We again take advantage of the analogy with polymers at equilibrium and recall the result obtained for free semi-flexible chains. Rappaport *et al.* studied a worm-like chain made of segments of length $\delta s$, with bending modulus K [171]. In three spatial dimensions, the curvature follows the following Rayleigh distribution:

$$P(\kappa|\delta s) = \frac{\kappa}{\kappa_0^2}\exp\left(-\frac{\kappa^2}{2\kappa_0^2}\right), \tag{3.17}$$

where $\kappa_0^2 = k_B T/(K\delta s)$. Here, the transposition to active-particle trajectories less direct. Indeed, the trajectories are not discretized as segments of fixed *length*. The motion is observed at a finite *time* resolution. We therefore have to make the link between $\delta s$, in Eq. (3.17), and the coarse-graining time $\delta t$. Two different behaviors are obtained depending on the value of $\delta t$ with respect to the persistence time $D^{-1}$.

***Fine time resolution:*** $\delta t \ll D^{-1}$ When the coarse-graining time is much smaller than the persistence time of the dynamics, we have $\delta s = v_0\delta t$. The curvature follows the Rayleigh distribution given by Eq. (3.17). Its mean value is $\langle\kappa\rangle = \sqrt{\pi/2}\,\kappa_0$. Using the polymer analogy, we readily obtain: $\langle\kappa\rangle = \sqrt{\pi D/\left(v_0^2\,\delta t\right)}$. Note that, given the peaked shape of the curvature distribution, the mean curvature is close to the typical curvature measured on an arbitrary trajectory.

***Coarse time resolution:*** $\delta t \gg D^{-1}$ We also consider the case of long coarse-graining times. Although this limit results in a loss of information about the particle dynamics, we will see that it effectively characterizes the degree of organization of the population. As $\delta t \gg D^{-1}$, the persistence in the particle dynamics cannot be observed. The apparent trajectory corresponds to a 3D uncorrelated random walk. The distance $\delta s$ traveled during the coarse-graining time $\delta t$ follows a Maxwell distribution: $P(\delta s) = \left(4\pi D_{\text{eff}}^3 \delta t^3\right)^{-1/2} \delta s^2 \exp\left[-\delta s^2/(4D_{\text{eff}}\delta t)\right]$, where the diffusion coefficient is deduced from the equations of motion: $D_{\text{eff}} = v_0^2/(6D)$ (see e.g. [157, 175]). The probability of the curvature is then obtained from the polymer analogy, Eq. (3.17):

$$P(\kappa|\delta t) = \int d\delta s \, P(\kappa|\delta s) \, P(\delta s). \tag{3.18}$$

The mean curvature is funally deduced as $\langle\kappa\rangle = \int d\kappa \, \kappa P(\kappa;\delta t)$. After a straightforward calculation of the integrals, we find: $\langle\kappa\rangle = \sqrt{6}D/v_0$.

Summarizing the previous results, the mean curvature of the trajectory depends on the coarse-graining time $\delta t$ as follows:

$$\langle\kappa\rangle \sim \begin{cases} \sqrt{\dfrac{\pi D}{v_0^2 \delta t}} & \text{if } \delta t \ll D^{-1}, \quad (3.19) \\ \sqrt{6}\dfrac{D}{v_0} & \text{if } \delta t \gg D^{-1}. \quad (3.20) \end{cases}$$

When $\delta t \ll D^{-1}$, $\langle\kappa\rangle$ decreases upon increasing the coarse-graining time, as $\langle\kappa\rangle \propto \delta t^{-1/2}$. This result can be understood as follows. Short time resolutions make it possible to observe the roughness of the trajectory at small length scales: large curvature can be measured. Averaging over longer times $\delta t$ smoothes the trajectory, and thus reduces its mean curvature. Conversely, when $\delta t \gg D^{-1}$ we obtain a very different behavior. $\langle\kappa\rangle$ becomes independent of the coarse-graining time, and is solely set by the persistence length of the trajectory.

## 3.2 Trajectories in polar phases

We now turn to particles in strongly-polarized phases. Their trajectories are analogous to stretched polymers. In the paraxial approximation, Eq. (3.9), the curvature reduces to $\kappa = v_0^{-1}\left|d\boldsymbol{\eta}/dt\right|$. As previously, we introduce the coarse-graining time $\delta t$ to regularize the curvature distribution. More precisely, the curvature of the coarse-grained trajectory is:

$$\kappa(t) = v_0^{-1}\left|\int dt' \, G_{\delta t}(t-t') \frac{d\boldsymbol{\eta}}{dt}(t')\right|, \tag{3.21}$$

where $G_{\delta t}$ is the coarse-graining kernel. We choose, e.g., the rectangle function: $G_{\delta t}(t) = (\delta t)^{-1}$ for $t \in [-\delta t/2, \delta t/2]$, and $G_{\delta t}(t) = 0$ otherwise.

In order to calculate the probability distribution of the curvature, we decompose $\boldsymbol{\eta} = \eta_1 \hat{\mathbf{e}}_1 + \eta_2 \hat{\mathbf{e}}_2$, where $\hat{\mathbf{e}}_1$ and $\hat{\mathbf{e}}_2$ are orthogonal unit vectors transverse to the mean direction of motion $\hat{\mathbf{\Pi}}_0$. Defining the algebraic curvatures

$$\kappa_a(t) = v_0^{-1} \int dt' \, G_{\delta t}(t-t') \frac{d\eta_a}{dt}(t') \tag{3.22}$$

for $a = 1$ or 2, we find

$$\kappa = \sqrt{\kappa_1^2 + \kappa_2^2}. \tag{3.23}$$

We first establish the probability distribution of the components $\kappa_a$ ($a = 1$ or 2). It is given by the following functional integral:

$$P(\kappa_a|\delta t) \propto \int \mathscr{D}\boldsymbol{\eta}(t) \, \delta\left(\int dt' G_{-\delta t}(t') \frac{d\eta_a}{dt}(t') - v_0\kappa\right) P\left[\boldsymbol{\eta}(t)\right], \tag{3.24}$$

where the probability of the trajectory $P\left[\boldsymbol{\eta}(t)\right]$ follows Eq. (3.12). Replacing the Dirac function by its integral expression and introducing the Fourier components $\boldsymbol{\eta}_\omega = \int \mathrm{d}t\, \boldsymbol{\eta}(t) e^{i\omega t}$, we arrive at:

$$P(\kappa_a|\delta t) \propto \int \mathscr{D}\boldsymbol{\eta}_\omega \int \mathrm{d}\lambda\, \exp\left[ i\lambda \left( \int \frac{\mathrm{d}\omega}{2\pi} G_{\delta t,\omega}\, i\omega \eta_{a,\omega} - v_0 \kappa \right) \right] \exp\left[ -\frac{1}{4D} \int \frac{\mathrm{d}\omega}{2\pi} \left( \omega^2 + \frac{\Pi_0^2}{\tau^2} \right) |\boldsymbol{\eta}_\omega|^2 \right]. \tag{3.25}$$

The integrals over the Lagrange multiplier $\lambda$ and over the polymer conformations $\boldsymbol{\eta}_\omega$ are Gaussian integrals, which can be easily evaluated. This straightforward calculation leads to:

$$P(\kappa_a|\delta t) = \frac{\sqrt{2}}{\kappa_0\sqrt{\pi}} \exp\left( -\frac{\kappa_a^2}{2\kappa_0^2} \right), \tag{3.26}$$

where

$$\kappa_0^2 = \frac{1}{\ell_p} \int \frac{\mathrm{d}\omega}{2\pi} \frac{(\omega\tau/\Pi_0)^2}{1+(\omega\tau/\Pi_0)^2} |G_{\delta t,\omega}|^2. \tag{3.27}$$

Taking for $G_{\delta t}$ the rectangle function specified above, the latter expression reduces to:

$$\kappa_0^2 = \frac{2D}{v_0^2\,\delta t} \frac{\tau}{\Pi_0 \delta t} \left( 1 - e^{-\Pi_0 \delta t/\tau} \right). \tag{3.28}$$

The curvature statistics is finally deduced from Eqs. (3.23) and (3.26). It again follows a Rayleigh distribution:

$$P(\kappa|\delta s) = \frac{\kappa}{\kappa_0^2} \exp\left( -\frac{\kappa^2}{2\kappa_0^2} \right), \tag{3.29}$$

As a result, the curvature distribution has the same shape as for free particles. The alignment interactions solely impact its expectation value:

$$\langle\kappa\rangle = \sqrt{\frac{\pi D}{v_0^2\,\delta t} \frac{\tau}{\Pi_0 \delta t} \left( 1 - e^{-\Pi_0 \delta t/\tau} \right)}. \tag{3.30}$$

Upon varying the coarse-graining time, the mean curvature therefore displays a crossover between two regimes:

$$\langle\kappa\rangle \sim \begin{cases} \sqrt{\dfrac{\pi D}{v_0^2\,\delta t}} & \text{if } \delta t \ll \tau, \qquad (3.31) \\ \dfrac{1}{v_0 \delta t} \sqrt{\dfrac{\pi D \tau}{\Pi_0}} & \text{if } \delta t \gg \tau. \qquad (3.32) \end{cases}$$

When $\delta t$ is much shorter than the typical alignment time $\tau$, we recover the expression obtained for non-interacting particles. The alignment dynamics is not probed at this time-scale, it reduces to a slow bending of the trajectory which does not impact its local roughness. The curvature becomes sensitive to the alignment interactions when $\delta t$ reaches the typical reorientation time. When $\delta t \gg \tau$, we end up with a different scaling: $\langle\kappa\rangle \propto \delta t^{-1}$.

Comparing the latter results to those obtained for free particles, we find that the curvature bears the signature of the collective organization into polar phases. The typical curvature measured from individual trajectories displays very different behaviors at long $\delta t$s, in these two limits. In isotropic phases, $\langle\kappa\rangle$ becomes independent of the coarse-graining time at large $\delta t$s. By contrast, in strongly-polarized states, it decreases as $\langle\kappa\rangle \propto \delta t^{-1}$ for $\delta t \gg \tau$. Upon decreasing the noise amplitude, the transition to collective motion is reflected by a crossover between these two regimes. The transition can be clearly identified by analyzing a typical trajectory.

# 4 Numerical validation and robustness of the results

## 4.1 Numerical models

In this last section, we confront the analytical predictions derived above to numerical results. We simulate two agent-based models.

***Alignment only*** First, we check numerically our theoretical expressions. We solve the equations of motion (3.4) and (3.5) with the alignment torque given by Eq. (3.7), using a forward Euler scheme. N = 250 particles move at the speed $v_0 = 1$ and align with their neighbors, in a cubic box of length 7 with periodic boundaries. The interaction range is $R_A = 1$, and the typical alignment time is set to $\tau = 1$. Upon decreasing the noise amplitude, this generalization of the Vicsek model displays a transition to polar states, as demonstrated by the growth of the averaged polarization $\Pi_0$, see Figs. 3.4(a) and 3.4(b). In such small systems, the transition is a continuous crossover and band patterns are not observed [49].

***Compact flocks*** Second, we go beyond this reference framework and test the robustness of our results to more complex dynamics. We simulate a more elaborate model, in which the alignment interactions are entangled with attractive and repulsive couplings. We focus on equations of motion that produce compact swarms, akin to the bird flocks or fish schools observed in the wild. Following [27, 49, 57, 92, 172], we add attractive interactions at long distance to prevent the evaporation of the swarm and ensure its cohesion. We also assume short-range repulsion to avoid collisions between individuals. In the equations of motion (3.4) and (3.5), the interactions are now

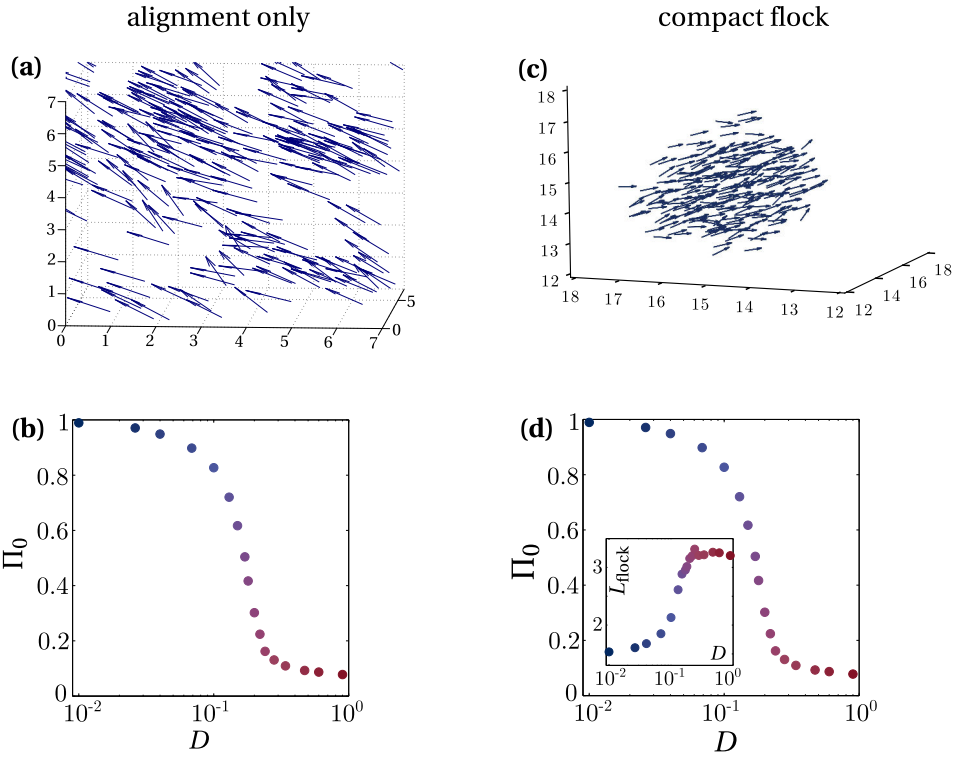


**Figure 3.4** – **(a)** Numerical simulation of the model Eqs. (3.4)–(3.5), with the Vicsek-like alignment torque (3.7). Example of polar phase obtained in a 3D periodic box (250 particles, D = 0.01). **(b)** Mean polarization plotted versus the variance of the noise, in the same model. **(c)** Compact flocks produced by the model (3.33) (250 particles, D = 0.02). **(d)** Mean polarization plotted versus the noise amplitude, in compact flocks. Inset: typical size of the flock plotted versus the noise amplitude.

described by the effective torque:

$$\mathbf{T}_i = \left(\mathbb{I} - \hat{\mathbf{t}}_i \hat{\mathbf{t}}_i\right) \cdot \frac{1}{\tau} \left[ \frac{1}{\mathrm{N}_i^{\mathrm{A}}} \sum_{j \in \mathscr{A}_i} \hat{\mathbf{t}}_j + \frac{1}{\mathrm{N}_i^{\mathrm{B}}} \sum_{j \in \mathscr{B}_i} f(r_{ij}) \hat{\mathbf{r}}_{ij} \right], \tag{3.33}$$

where $\mathbf{r}_{ij} \equiv \mathbf{r}_i - \mathbf{r}_j$. We recover the alignment interactions introduced in the previous model, Eq. (3.5), within the sphere $\mathscr{A}_i$ of radius $\mathrm{R_A} = 1$. The additional term describes the attractive and repulsive couplings with the $\mathrm{N}_i^{\mathrm{B}}$ neighbors lying in the sphere $\mathscr{B}_i$ of radius $\mathrm{R_B} = 5$ [57]. These interactions are attractive above a distance $2r_c$ and repulsive for $r_c \leq r_{ij} < 2r_c$, with a divergent amplitude at the hard-core radius $r_{ij} = r_c$ [49, 92]. We take $f(r_{ij}) = 1 - \left[r_c/(r_{ij} - r_c)\right]^5$ with $r_c = 0.4$. An example of polar flock is shown in Fig. 3.4(c). Due to the alignment interactions, the latter equations of motion yield a transition between isotropic and polar states, as shown by the increase of the mean polarization $\Pi_0$ upon decreasing the noise amplitude, Fig. 3.4(d). In addition, the population condenses into coherent flocks due to the long-distance attraction. This behavior is quantified by the typical size of the group, $\mathrm{L_{flock}} \equiv \left[\mathrm{N}^{-1} \sum_i (\mathbf{r}_i - \bar{\mathbf{r}})^2\right]^{1/2}$, which sharply decreases when D is reduced below the transition to polar order, Fig. 3.4(d) inset.

We measure numerically the writhe and the curvature of the trajectories in these two models, and compare to the analytical expressions.

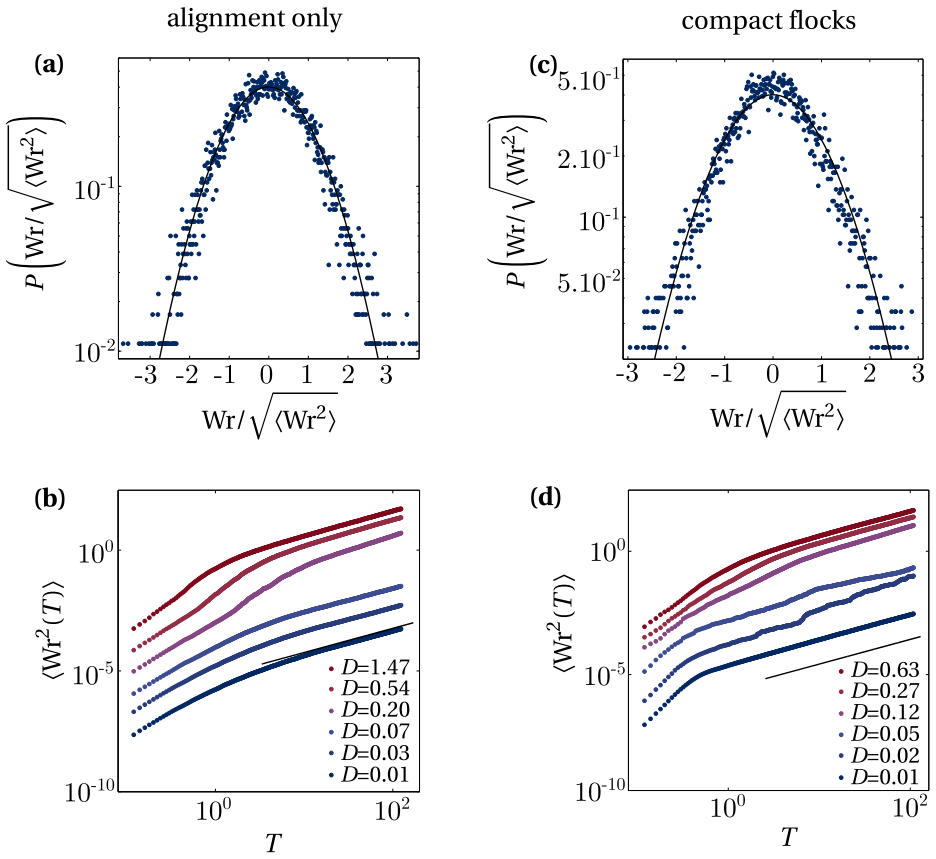


**Figure 3.5** – Writhe statistics. **(a)** Reduced probability distribution of the writhe, deep in the polar phase, obtained for alignment interactions only (D = 0.01, $\Pi_0 = 0.98$, T = 2.5). **(b)** Variance of the writhe plotted versus the observation time T, for different noise amplitudes. Black line: theoretical prediction for strongly polarized phases (D = 0.01, $\Pi_0 = 0.98$, no free parameter). **(c)** Same as **(a)** for the second numerical model, leading to compact flocks (D = 0.01, T = 2.5). Black line: theoretical distribution, Eq. (3.14), established in the absence of attraction/repulsion. **(d)** Same as **(b)** for compact flocks. Black line: theoretical prediction in the absence of attraction/repulsion, Eq. (3.15), deep in the polar phase (D = 0.01, $\Pi_0 = 0.99$).

## 4.2 Writhe of the trajectories

***Alignment only*** We first consider the reference model, including alignment interactions only, Eq. (3.7). In Fig. 3.5(a), we plot the normalized distribution of the writhe deep in the polar phase. Its shape is well reproduced by the analytical expression, Eq. (3.14). The variance of the writhe fluctuations are shown in Fig. 3.5(b) versus the observation time T, for different noise amplitudes. We find the expected diffusive scaling at long times, $\langle \mathrm{Wr}^2(\mathrm{T})\rangle \propto \mathrm{T}$. In strongly-polarized phases, we also check that the growth rate is in quantitative agreement with Eq. (3.15) (blue bottom curve).

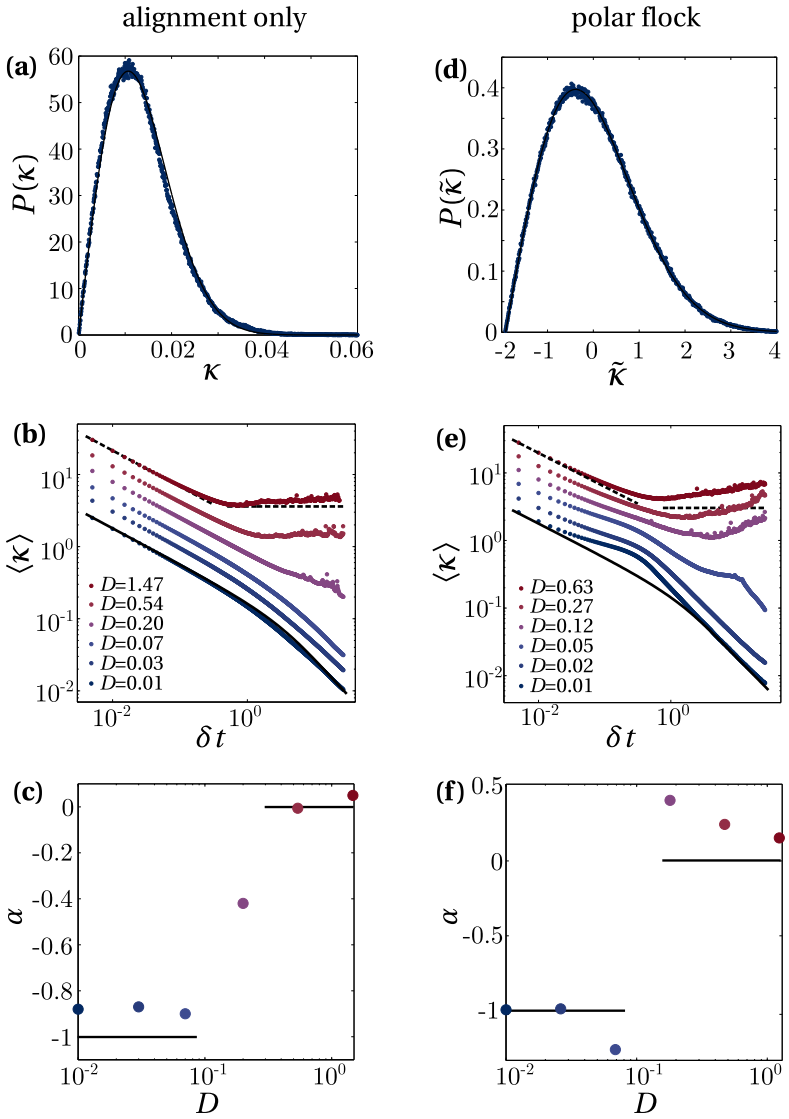


**Figure 3.6** – Curvature statistics. **(a)** Probability distribution of the curvature in the polar phase, obtained with alignment interactions only (D = 0.01, $\delta t = 10^3$). Blue dots: numerical results. Superimposed black line: theoretical curve. **(b)** Mean curvature of the trajectories plotted versus the coarse-graining time $\delta t$, for different noise amplitudes. Polar phases are obtained for $\mathrm{D} < \mathrm{D}_c \approx 0.2$. Dashed black line: theoretical predictions for the isotropic state (D = 1.47). Solid black line: theoretical prediction for the strongly-polarized phase (D = 0.01). **(c)** In the long-$\delta t$ limit, the mean curvature behaves as $\langle \kappa \rangle \propto \delta t^{\alpha}$. The exponent $\alpha$ is plotted versus the noise amplitude. Black lines: theoretical predictions for isotropic ($\alpha = 0$) and strongly-polarized ($\alpha = -1$) phases. **(d)** Probability distribution of the reduced curvature, $\tilde{\kappa} = (\kappa - \langle \kappa \rangle)/\sqrt{\langle \kappa^2 \rangle}$, in compact polar flocks (D = 0.01, $\delta t = 0.025$). Black line: Rayleigh distribution. **(e)** Same as **(b)** for compact flocks. The black lines are the theoretical predictions obtained in the absence of attraction/repulsion (dashed lines: D = 0.63, solid line: D = 0.01). **(f)** Same as **(c)** for compact flocks.

***Compact flocks*** Having validated the theoretical expressions, we test their robustness to the addition of attractive and repulsive interactions, Eq. (3.33). The statistics of the writhe is shown in Figs. 3.5(c) and 3.5(d). We recover the same shape for the probability distribution, and the same diffusive behavior at long observation times, $\langle \mathrm{Wr}^2(\mathrm{T}) \rangle \propto \mathrm{T}$. The detailed form of the interactions only impacts the writhe statistics at the quantitative level.

### 4.3 Curvature of the trajectories

***Alignment only*** As we did it above, we first check the analytical predictions in the reference model, Eq. (3.7). We coarse-grained the trajectories by averaging the particle positions over a time $\delta t$. A typical probability distribution is plotted in Fig. 3.6(a) (blue dots), and displays excellent agreement with the Rayleigh distribution Eq. (3.17), with no free parameter (black line). Fig. 3.6(b) shows the mean curvature as a function of the coarse-graining time. The numerical results are again in quantitative agreement with the theory. In addition, they confirm that the curvature bears a clear signature of the transition to collective motion. The emergence of polar order is attested by the dependence of the mean curvature in the coarse-graining time, $\langle \kappa \rangle \propto \delta t^{\alpha}$. We measure the scaling exponent $\alpha$ on the numerical data and plot it as a function of D, in Fig. 3.6(c). As expected, the transition to collective motion is associated with a crossover from $\alpha \approx 0$ in isotropic states (high noise), to $\alpha \approx -1$ in polar phases (low noise). Note that our results do not display exactly the exponent $\alpha = -1$ expected in polar phases, which suggests that the asymptotic regime $\delta t \gg \tau$ was not fully reached within our simulation time.

On a practical perspective, this approach may also provide a powerful tool to measure the alignment time $\tau$ from experimental data. This quantity cannot be readily deduced from macroscopic measurements in a steady state, as the large-scale observables systematically combine the different time-scales of the dynamics. For instance, the global polarization results from the competition between the alignment and diffusion times. Conversely, evaluating the mean curvature for different coarse-graining times provides a direct measurement of the relaxation time $\tau$. Experimentally, this procedure can be easily implemented by making successive time averaged on the data. It makes it possible to directly test the model at the single-particle level, irrespective of any coarse-graining approximation.

***Compact flocks*** We finally compare these results, obtained for particles moving in periodic space, to the model defined by Eq. (3.33). The trajectories are now confined within a compact flock. The probability distribution of the curvature, Fig. 3.6(d), is very well described by the Rayleigh distribution (3.17). Its shape is therefore robust to the introduction of alignment and repulsion in the model. This is not the case for the mean curvature $\langle \kappa \rangle$, which is plotted as a function of $\delta t$ in Fig. 3.6(e). Let us consider the limits of isotropic and strongly-polarized states, and compare the numerical results (colored dots) to the analytical predictions obtained for alignment interactions only (black lines).

(i) In isotropic flocks (e.g. D = 0.63), we observe a crossover between two regimes when $\delta t$ reaches the persistence time $\mathrm{D}^{-1}$, in agreement with Eqs. (3.19)–(3.20). However, the mean curvature does not plateau to a constant values at large $\delta t$s, but slightly increases with the coarse-graining time. This behavior results from the confinement of the particles inside a finite-size flock, due to the long-distance attraction. Let us denote by $\tau_{\mathrm{flock}}$ the typical time needed for a particle to move from the center to the edge of the flock. When $\delta t \gg \tau_{\mathrm{flock}}$, the particle explores the entire volume of the flock during the coarse-graining time. Its averaged position therefore remains very close to the center of mass of the flock: the apparent trajectory is confined in a small domain, the size of which decreases when increasing $\delta t$. The typical radius of curvature, $\langle \kappa \rangle^{-1}$, therefore decreases upon increasing $\delta t$.

(ii) In strongly-polarized flocks (e.g. D = 0.01), we recover the behavior of non-interacting particles at small $\delta t$s, as expected from Eq. (3.31). When the trajectory is observed at small time-scales compared to the typical interaction times, the interactions have no impact on the local

curvature. Upon increasing $\delta t$, the numerical results deviate from the reference model (alignment only). The overshoot visible in Fig. 3.6(e) may result from the repulsion between the particles: when $\delta t$ reaches the typical collision time, the curvature becomes sensitive to the short-range collisions which deviate the particle trajectories and therefore increase their roughness. Upon further increasing the coarse-graining times, this collisional dynamics is averaged out and the curvature probes the alignment couplings. We therefore recover the theoretical prediction, Eq. (3.32). Note that a different behavior is expected at larger coarse-graining times, when $\delta t$ reaches the typical diffusion time inside the flock $\tau_{\text{flock}}$. We do not explore this regime here, as the long-time mixing will be studied in the paper reproduced p. 134.

The previous results again prove that the curvature reflects the global organization of the population. The mean curvature, plotted as a function of $\delta t$, is a signature of the microscopic dynamics. Varying the coarse-graining time makes it possible to probe the particle motion at all time-scales. It may be useful to directly test a microscopic model against experimental data, and quantitatively measure the typical time-scales involved. Of particular interest is the long-$\delta t$ behavior, which quantifies the emergence of polar order. The scaling exponent of $\langle\kappa\rangle$ versus $\delta t$, which is plotted in Fig. 3.6(f) as a function of the noise amplitude, looks discontinuous at the transition to collective motion. More theoretical work is required to go beyond these heuristic interpretations, and quantitatively understand how the confinement within polar flocks impacts the curvature statistics.

## 5 Conclusion

In summary, we have characterized the trajectories of interacting self-propelled particles using geometric quantities. Building on the analogy with semi-flexible polymers, we have described the statistics of their writhe and curvature. In particular, we have shown that measuring the mean curvature from a typical trajectory makes it possible to probe the collective dynamics of the population at different time-scales.

We finally mention two possible extensions to this work. First, in real flocks the speed of the individuals also fluctuates [26]. The trajectories would then correspond to extensible polymer chains. The introduction of a compression modulus in the equivalent polymer problem may strongly impact the curvature and the writhe statistics. Second, experimental setups now make it possible to track the individual positions in animal populations, such as bird flocks or midge swarms [7]. Studying the trajectories may be useful to build behavioral models which reproduce the individual dynamics. For instance, recent experimental evidences suggest that midge swarms may be poised closed to a critical point [7, 10, 44]. The curvature of the trajectories might provide another tool to test the proximity of a transition in such systems.

# Article: *Braiding a flock: winding statistics of interacting flying spins*

J.-B. Caussin and D. Bartolo, submitted to *Phys. Rev. Lett.* (2015)

When animal groups move coherently in the form of a flock, their trajectories are not all parallel, the individuals exchange their position in the group. In this Letter we introduce a measure of this mixing dynamics, which we quantify as the winding of the braid formed from the particle trajectories. Building on a paradigmatic flocking model we numerically and theoretically explain the winding statistics, and show that it is predominantly set by the global twist of the trajectories as a consequence of a spontaneous symmetry breaking.

The collective behaviors observed in animal groups have attracted much attention in the biology, the mathematics and the physics communities over the last 20 years. Quantitative data analysis have established that the salient traits of collective motion are very well captured by the dynamics of flying spins: persistent random walkers endowed with interactions akin to ferromagnetic couplings between their velocities [40, 44, 132, 136, 155, 216]. This framework has been extensively exploited to rationalize structural and dynamical properties starting from the emergence of directed motion, to rapid (orientational) information transfer, see [8, 27, 45, 92, 132, 215] and references therein. However, beyond these spectacular results, the internal dynamics of a flock, the relative motion of the individuals, remains scarcely investigated both experimentally and theoretically yet it is known to display non-trivial anomalous behaviors [43, 211, 214].

In this Letter, we theoretically describe the mixing statistics of an archetypal flying-spin model. We first stress the intrinsic geometrical nature of the dynamics of particles in a flock and map this problem to the braiding statistics of their trajectories. We evidence the nontrivial statistics of the winding between pairs of motile-particle trajectories, which is a robust measure of their entanglement. This quantity displays spatial correlations at the population scale. We single out the reason for the nontrivial statistics and show that the spontaneous breaking of a rotational symmetry causes the global twist of the flock to chiefly rule the long-time winding fluctuations.

***Flocking geometry.*** We begin with a simple remark on the geometry of flying-spin models. Let us first recall the paradigmatic agent-based model of flocking, see e.g. [27, 92, 132, 216]. N persistent random walkers, $\mathbf{r}_i(t)$, $i = 1 \dots \mathrm{N}$, propel at a constant speed $v_0 = 1$ along a direction $\hat{\mathbf{t}}_i$ which diffuses on the unit sphere. Time therefore corresponds to the curvilinear coordinate of the trajectories. The rotation of the unit tangent vector, $\dot{\hat{\mathbf{t}}}_i = \kappa_i \hat{\mathbf{n}}_i$, defines the curvature $\kappa_i$ and the normal vector $\hat{\mathbf{n}}_i$ in the Frénet frame. The coupled equations of motion of the particles take the generic form:

$$\kappa_i \hat{\mathbf{n}}_i = (\mathbb{I} - \hat{\mathbf{t}}_i \hat{\mathbf{t}}_i) \cdot \mathbf{F}_i(\{\mathbf{r}_j, \hat{\mathbf{t}}_j\}_j) + \boldsymbol{\xi}_i(t), \tag{3.34}$$

where $\boldsymbol{\xi}_i \perp \hat{\mathbf{t}}_i$ is the rotational noise. The $\mathbf{F}_i$s describe the interactions between the self-propelled particles, they *a priori* depend both on the position and orientation of the particles. The projection operator $(\mathbb{I} - \hat{\mathbf{t}}_i \hat{\mathbf{t}}_i)$ ensures that $\hat{\mathbf{n}}_i \perp \hat{\mathbf{t}}_i$. Remarkably, Eq. (3.34) relates the curvature of the trajectory to the positions and tangent vectors of the neighboring trajectories. Hence the dynamics of the

population reduces to a geometrical problem: the flock can be seen as a bundle of interacting curves. In this framework, the relative motion of the individuals is inferred from the entanglement of their trajectories, which we characterize in this paper.

We use a standard (metric) form of $\mathbf{F}_i$ to account for the flocking dynamics:

$$\mathbf{F}_i = \frac{1}{\tau \mathrm{N}_i^{\mathrm{A}}} \sum_{j\in\mathscr{A}_i} \hat{\mathbf{t}}_j + \frac{1}{\tau \mathrm{N}_i^{\mathrm{B}}} \sum_{j\in\mathscr{B}_i} f(r_{ij})\,\hat{\mathbf{r}}_{ij}, \tag{3.35}$$

where $\tau$ is a relaxation time, which we henceforth set to $\tau = 1$, and $\mathbf{r}_{ij} \equiv \mathbf{r}_i - \mathbf{r}_j$. The first term in Eq. (3.35) is the ferromagnetic term which promotes alignment with the mean direction of the $\mathrm{N}_i^{\mathrm{A}}$ neighbors lying in the sphere $\mathscr{A}_i$ of radius $\mathrm{R_A} = 1$. The second term is introduced to yield compact flocks, and corresponds to attractive and repulsive interactions within the sphere $\mathscr{B}_i$ of radius $\mathrm{R_B} = 5$ [57]. Following [49, 92], we assume that these interactions are attractive above a distance $2r_c$, and repulsive when $r_c \le r_{ij} < 2r_c$ with a divergent amplitude at $r_{ij} = r_c$. Here, we take $f(r_{ij}) = 1 - [r_c/(r_{ij} - r_c)]^5$ with $r_c = 0.4$. Rotational diffusion is accounted for by the uncorrelated Gaussian white noises $\boldsymbol{\xi}_i$ of variance 2D. Eqs. (3.34) and (3.35) are first solved numerically using an explicit Euler scheme. Below a critical noise amplitude $\mathrm{D}_c \sim 0.2$, the rotational symmetry of the particle orientation is spontaneously broken. A compact polar flock forms and moves along $\boldsymbol{\Pi}(t) = \langle \hat{\mathbf{t}}_i(t) \rangle_i$ as exemplified in Fig. 3.7(a). Decreasing D below $\mathrm{D}_c$ the magnitude of the polarization $\boldsymbol{\Pi}$ increases.

***Quantifying the entanglement of the trajectories.*** Inspired by Lagrangian mixing in fluids, we now introduce a quantity which quantifies the entanglement of the trajectories [34, 161, 164, 205]. Let us first define a convenient representation of the relative motion of the individuals irrespective of the global motion of the flock. We consider a frame $(\mathrm{G}(t), \hat{\boldsymbol{\eta}}_1(t), \hat{\boldsymbol{\eta}}_2(t), \hat{\boldsymbol{\Pi}}(t))$, shown in Fig. 3.7(a). The origin is the center of mass $\mathrm{G}(t)$ of the flock, and the axis are parallel transported along the trajectory of G. We then project the $\mathbf{r}_i$s on the plane $(\hat{\boldsymbol{\eta}}_1(t), \hat{\boldsymbol{\eta}}_2(t))$, see Fig. 3.7(b). If the flock were undergoing a rigid-body motion, the projected positions would be stationary. In order to quantify the deviations from this trivial behavior, we choose a reference axis, say $\hat{\boldsymbol{\eta}}_1$, and observe the relative positions of the particles along this line. As the group is rotationally invariant around $\hat{\boldsymbol{\Pi}}$, all directions of observation are equivalent. The mixing in the flock results in particle exchanges along $\hat{\boldsymbol{\eta}}_1$. We keep track of these crossings over time, and of the relative positions in the orthogonal direction $\hat{\boldsymbol{\eta}}_2$. We assign an index $\epsilon = \pm 1$ to each crossing, as depicted in Figs. 3.7(b), 3.7(c). Considering two particles $i$ and $j$, we then define their *pair winding number*, $w_{ij}(\mathrm{T})$, as the linking number between their world lines. $w_{ij}(\mathrm{T})$ is the half algebraic sum of the crossing indexes involving particles $i$ and $j$, between time $t_0$ and $t_0 + \mathrm{T}$. This quantity has a clear meaning: it counts the number of turns of particle $i$ around $j$ (or, equivalently, of $j$ around $i$) , since a clockwise (resp. counter-clockwise) turn results in two negative (resp. positive) crossings. We finally average over the pairs and define the *total winding* between $t_0$ and $t_0 + \mathrm{T}$, which is our measure of the entan-

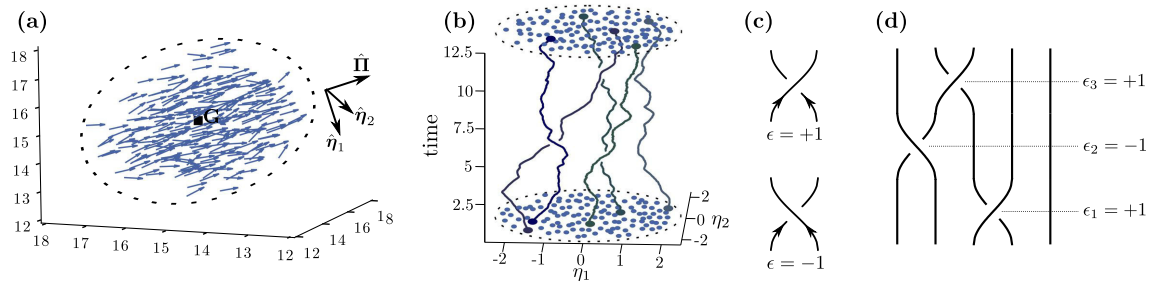


**Figure 3.7** – **(a)** Instantaneous positions and orientations of the particles in a compact polar flock (250 particles), and definition of the parallel-transported frame $(\hat{\boldsymbol{\eta}}_1, \hat{\boldsymbol{\eta}}_2, \hat{\boldsymbol{\Pi}})$. $\mathrm{D} = 2.6 \times 10^{-2}$. **(b)** World lines of 5 particles in a polar flock. $\mathrm{D} = 2.6 \times 10^{-2}$. **(c)** Definition of the crossing signs. **(d)** Braid diagram associated to the world lines drawn in Fig. 3.7(b).

glement of the world lines:

$$\mathrm{W(T)} = \frac{1}{\mathcal{N}_p} \sum_{(i,j)} w_{ij}(\mathrm{T}), \tag{3.36}$$

where $\mathcal{N}_p = \mathrm{N(N-1)/2}$ is the number of pairs. Importantly, W(T) does not depend on the distance between the particles, only the signs of the crossings and the times at which they occur matter. Therefore the world lines define a *braid* that can be drawn in the form of a normalized braid diagram, Fig. 3.7(d) [205]. Denoting by $\epsilon_a$ the sign of the $a^{\text{th}}$ crossing, we turn the sum over the pairs into a topological invariant of the braid: $\mathrm{W(T)} = (2/\mathcal{N}_p)\sum_a \epsilon_a$. Practically we use the Artin representation of the braid word [34, 81, 205] and the *braidlab* library [206] to compute both the pair and the total winding numbers. The topological nature of W(T) makes it a very robust measure of the flock mixing. We now carefully investigate its statistics.

***Winding statistics.*** The normalized distributions of W(T) are plotted in Fig. 3.8(a) for different values of the noise amplitude. For all the trajectory lengths, the total winding follows a Gaussian statistics with zero mean since the flock has no intrinsic chirality: clockwise and counterclockwise windings are equally probable. The winding distribution is fully characterized by its standard deviation $\langle \mathrm{W}^2(\mathrm{T})\rangle^{\frac{1}{2}}$, where the brackets denote the average over different initial conditions. The winding fluctuations increase linearly with the curvilinear length of the trajectories at short times: $\langle \mathrm{W}^2(\mathrm{T})\rangle^{\frac{1}{2}} \propto \mathrm{T}$, and crosses over to a diffusive regime where $\langle \mathrm{W}^2(\mathrm{T})\rangle^{\frac{1}{2}} \propto \mathrm{T}^{\frac{1}{2}}$ at long times, Fig. 3.8(b). These first results would naively suggest a simple scenario. If the crossing events were uncorrelated the Gaussian statistics would readily stem from the central limit theorem as W(T) is the average of the crossing signs. In addition, the variance of W(T) would obviously grow in a diffusive manner. However, this appealing explanation is inconsistent with a deeper analysis of the data. Let us carefully study the correlations between the pair windings, which are quantified

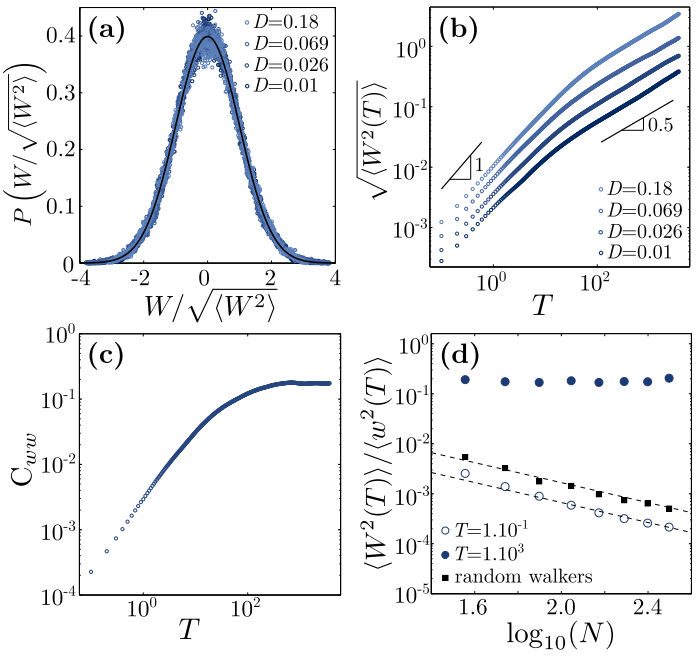


**Figure 3.8** – **(a)** Probability distribution of the total winding W(T), normalized by its standard deviation (T = $10^3$). The different noise amplitudes correspond to different polarizations of the flock, ranging from 0.45 (D = 0.18) to 0.99 (D = 0.01). Solid line: Gaussian distribution. **(b)** Standard deviation of the total winding, $\sqrt{\langle \mathrm{W}^2(\mathrm{T})\rangle}$, as a function of time T, for different noise amplitudes (log scale). **(c)** Correlation function, defined by Eq. (3.37), as a function of T. **(d)** Variance of the total winding normalized by the variance of the pair winding, plotted versus the particle number (log scale). Open circles: T = $10^{-1}$. Filled circles: T = $10^3$. Black squares: random walkers confined in a circular box of radius 20, diffusivity: 10. Time step: 0.1. Dashed lines: slope −1.

by:

$$\mathrm{C}_{ww}(\mathrm{T}) = \frac{1}{\mathcal{N}_p(\mathcal{N}_p-1)} \sum_{(i,j)} \sum_{(k,l)\neq(i,j)} \frac{\langle w_{ij}(t)\, w_{kl}(\mathrm{T})\rangle}{\langle w^2(\mathrm{T})\rangle}, \tag{3.37}$$

where $\langle w^2(t)\rangle = \mathcal{N}_p^{-1}\sum_{(i,j)}\langle w_{ij}^2(\mathrm{T})\rangle$ is the variance of the pair windings. Given this definition, $\mathrm{C}_{ww}(\mathrm{T}) = 0$ for uncorrelated $w_{ij}$s, and $\mathrm{C}_{ww}(\mathrm{T}) = 1$ when the pair windings are fully correlated. Unexpectedly, we find that the correlation between the pair windings does not vanish at long times. Conversely, it increases and plateaus at a finite value, Fig. 3.8(c), thereby ruling out the simple scenario sketched above. In order to check that this unexpected behavior is not a finite-size artifact, we first note that $\mathrm{C}_{ww}(\mathrm{T}) \sim \langle \mathrm{W}^2(\mathrm{T})\rangle / \langle w^2(\mathrm{T})\rangle$ in the large-$\mathcal{N}_p$ limit and plot the ratio $\langle \mathrm{W}^2(\mathrm{T})\rangle / \langle w^2(\mathrm{T})\rangle$ for flocks of different sizes N, in Fig. 3.8(d). Whereas short trajectories have indeed winding correlations $\mathrm{C}_{ww}(\mathrm{T})$ that decay with the system size, as 1/N, the winding correlations of the long trajectories do not display any significant variations with N when increasing the particle number by a factor of ~ 8. In order to gain more insight into these tho opposite behaviors, we computed the same quantity for the wordlines of independent 2D random walkers confined in a circular box. $\mathrm{C}_{ww}$ follows the same 1/N nontrivial scaling observed for short flocking trajectories. We shall note that the finite time step of our numerical scheme regularizes the winding statistics of the random walkers and makes it possible to define its variance [19]. This second set of observations confirms that the saturation of $\mathrm{C}_{ww}(\mathrm{T})$ at long time originates from extended correlations of the crossing events.

***A twist in the statistics.*** We now elucidate the physical mechanism responsible for the winding correlations. We first note that a global instantaneous rotation of the flock around $\hat{\mathbf{\Pi}}$ would result in a fully correlated pair winding. We therefore separate the associated global trajectory twist from

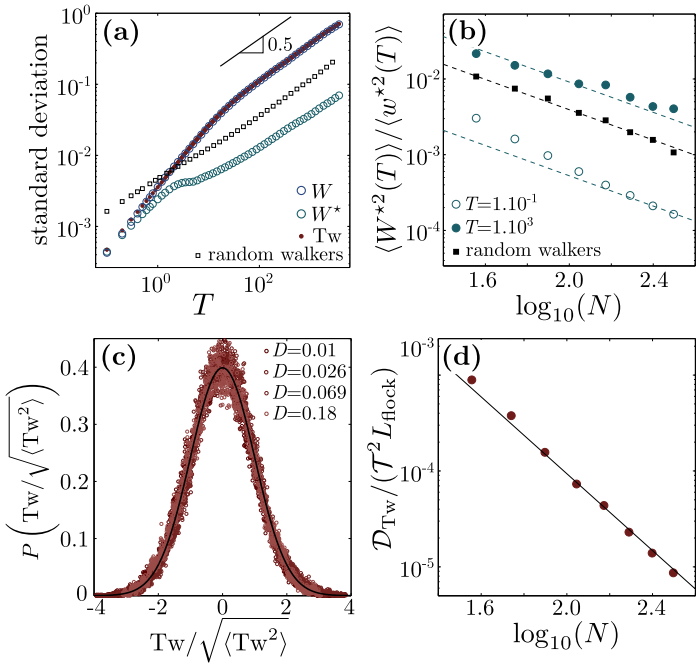


**Figure 3.9** – **(a)** Standard deviation of the total winding, $\sqrt{\langle \mathrm{W}^2(\mathrm{T})\rangle}$ (blue open circles), $\sqrt{\langle \mathrm{W}^{\star 2}(\mathrm{T})\rangle}$ (green open circles) and $\sqrt{\langle \mathrm{Tw}^2(\mathrm{T})\rangle}$ (red filled circles), as a function of T. Black squares: total winding of confined random walkers, same parameters as in Fig. 2. **(b)** Variance of the total winding normalized by the variance of the pair winding computed in the twisting frame for different particle numbers (log scale). Open circles: $\mathrm{T} = 10^{-1}$. Filled circles: $\mathrm{T} = 10^3$. Black squares: confined random walkers. Dashed lines: slope −1. **(c)** Probability distribution of the twist, normalized by its standard deviation ($\mathrm{T} = 10^3$). Solid line: normal distribution. **(d)** The normalized twist diffusivity: $\mathscr{D}_{\mathrm{Tw}}/(\mathscr{T}^2 \mathrm{L}_{\mathrm{flock}})$ decays quadratically with N (log scale). Solid line: slope −2.

the total winding. Denoting by $\boldsymbol{\eta}_i$ the position of particle $i$ projected in the observation plane $(\mathrm{G}, \hat{\boldsymbol{\eta}}_1, \hat{\boldsymbol{\eta}}_2)$, the instantaneous rotation rate of the flock is:

$$\Omega = \frac{1}{\mathrm{N}} \sum_i \frac{1}{\eta_i^2} (\boldsymbol{\eta}_i \times \dot{\boldsymbol{\eta}}_i) \cdot \hat{\boldsymbol{\Pi}}. \tag{3.38}$$

Integrating over time, we define the global twist that is the number of turns of the flock around $\hat{\boldsymbol{\Pi}}$:

$$\mathrm{Tw}(\mathrm{T}) = \frac{1}{2\pi} \int_{t_0}^{t_0+\mathrm{T}} \mathrm{d}t\, \Omega(t). \tag{3.39}$$

We finally define the winding of the untwisted trajectories in the frame $(\mathrm{G}, \hat{\boldsymbol{\eta}}_1^\star, \hat{\boldsymbol{\eta}}_2^\star)$, obtained by rotating the parallel-transported frame $(\mathrm{G}, \hat{\boldsymbol{\eta}}_1, \hat{\boldsymbol{\eta}}_2)$ by an angle $2\pi \times \mathrm{Tw}$:

$$\mathrm{W}^\star = \mathrm{W} - \mathrm{Tw}. \tag{3.40}$$

Hence $\mathrm{W}^\star = \mathcal{N}_p^{-1} \sum_{(i,j)} w_{ij}^\star$, where $w_{ij}^\star = w_{ij} - \mathrm{Tw}$ is the winding between particles $i$ and $j$ in this rotating frame. Within the braid picture, $\mathrm{W}^\star$ is found by factorizing out the global twist of the braid word [65, 66, 196].

In Fig. 3.9(a), we plot the standard deviation of W, Tw and $\mathrm{W}^\star$ versus T.The twist contribution dominates the total winding at long times and $\langle \mathrm{W}^2 \rangle \sim \langle \mathrm{Tw}^2 \rangle$. This numerical fact is better understood by noting that the winding in the rotating frame qualitatively follows the behavior displayed by confined random walkers. Above the relaxation time $\tau = 1$ introduced in Eq. (3.35), $\mathrm{W}^\star(\mathrm{T})$ follows the same diffusive evolution: $\langle \mathrm{W}^{\star 2}(\mathrm{T}) \rangle \propto \mathrm{T}$ [93]. More importantly, we also find the same $1/\mathrm{N}$ asymptotic scaling for $\mathrm{C}_{w^\star w^\star} \sim \langle \mathrm{W}^{\star 2}(\mathrm{T}) \rangle / \langle w^{\star 2}(\mathrm{T}) \rangle$ showing that the spatial correlations of the displacements are short-ranged *at all times*, Fig. 3.9(b). This result contrasts with the behavior of the total winding in the parallel-transported frame where $\mathrm{C}_{ww} \sim \langle \mathrm{W}^2(\mathrm{T}) \rangle / \langle w^2(\mathrm{T}) \rangle$ hardly depends on N at long times, Fig. 3.8(d). We can therefore propose the following scenario : the long-range spatial correlations in the flock arise from the global rotation of the flock, hence from the global twist of the trajectories.

***Hydrodynamic description of the trajectories' twist.*** The very origin of the global rotation of the flock roots from the spontaneous breaking of the rotational symmetry of particle velocities. This symmetry breaking gives rise to a soft orientational mode [26] which twists the trajectories in the parallel-transported frame at the entire-flock scale. We now lay out a more quantitative explanation by switching to an hydrodynamic description of the flock viewed as a active-fluid drop. We use the conventional hydrodynamic framework first introduced phenomenologically by Toner and Tu [211, 214] and later derived from microscopic theories [23, 25, 79, 136]. The fluid density and velocity fields are $\rho(\mathbf{r}, t)$ and $\mathbf{v}(\mathbf{r}, t)$. We focus on strongly polarized flocks in which all particles follow the same average direction. The momentum equation linearized around the homogeneously polarized state takes the simple form [136, 212]:

$$\partial_t(\rho\mathbf{v}) + \lambda(\hat{\boldsymbol{\Pi}} \cdot \nabla)\rho\mathbf{v} = -\nabla \mathrm{P}(\rho) + \Gamma \nabla^2(\rho\mathbf{v}) + \mathbf{f}, \tag{3.41}$$

where P is the local pressure, and $\mathbf{f}(\mathbf{r}, t)$ is a Gaussian white noise with correlation $\langle f_\alpha(\mathbf{r}, t) f_\beta(\mathbf{r}', t') \rangle = 2\tilde{D}\, \delta(\mathbf{r} - \mathbf{r}')\delta(t - t')\delta_{\alpha\beta}$. In this continuous limit, the global rotation rate, Eq. (3.38), is given by:

$$\Omega = \frac{1}{\mathrm{N}} \int \mathrm{d}^3\mathbf{r}\, \frac{1}{\eta^2} (\boldsymbol{\eta} \times \rho\mathbf{v}) \cdot \hat{\boldsymbol{\Pi}}. \tag{3.42}$$

Two comments are in order. Firstly, deep in the polarized phase, the linearity of Eq. (3.41) implies that the momentum fluctuations are Gaussian. After space and time integration, Eqs. (3.42) and (3.39) imply that the twist also follows a normal distribution, in agreement with our numerical findings reported in Fig. 3.9(c). Secondly, the damping of velocity fluctuations is set by the diffusive term $\Gamma\nabla^2(\rho\mathbf{v})$, in Eq. (3.41) (see [136, 212] for more details). Hence the Fourier mode

with wave-vector $\mathbf{q}$ decays in a time $\sim (\Gamma q^2)^{-1}$. While small-wavelength perturbations are quickly damped, the large-scale fluctuations that occur at the size of the flock, $q \sim 1/\mathrm{L_{flock}}$, remain correlated over a time $\mathscr{T} \sim \mathrm{L_{flock}^2}/\Gamma$. This observation explains the time behavior of the trajectories' twist fluctuations. At short times, $\mathrm{T} < \mathscr{T}$, the small-$q$ fluctuations result in finite time correlations in the rotation rate $\Omega$. Consequently, the twist fluctuations persist and undergo a "balistic" growth: $\langle \mathrm{Tw}^2(\mathrm{T})\rangle \propto \mathrm{T}^2$. At long times, $\mathrm{T} > \mathscr{T}$, all the Fourier modes have been relaxed, the correlations vanish, and one recovers the observed diffusive behavior for the trajectory-twist: $\langle \mathrm{Tw}^2(\mathrm{T})\rangle \sim \mathscr{D}_{\mathrm{Tw}}\mathrm{T}$.

We further check this analysis, by studying how the diffusion coefficient $\mathscr{D}_{\mathrm{Tw}}$ depends on the size of the flock. The temporal correlations of the rotation rate are computed from Eq. (3.41) and (3.42). In the long-time limit, $|t-t'| \gg \mathscr{T}$, we have $\langle \Omega(t)\Omega(t')\rangle \sim \mathscr{D}_{\mathrm{Tw}}\delta(t-t')$, where the effective diffusivity scales as $\mathscr{D}_{\mathrm{Tw}} \propto \tilde{\mathrm{D}}\mathscr{T}^2\mathrm{L_{flock}N}^{-2}$. This quantitative prediction is in excellent agreement with our numerical data, shown in Fig. 3.9(d). In addition, introducing the mean density $\rho_0$ of the flock, we find $\mathscr{D}_{\mathrm{Tw}} \propto \rho_0^{-5/3}\mathrm{N}^{-1/3}$. Assuming that $\rho_0$ weakly depends on N, the variance of the twist is predicted to decay very slowly with the flock size as $\mathrm{N}^{-1/3}$. This scaling confirms that the ratio between the twist and the local winding fluctuations ($\langle \mathrm{W}^{\star 2}\rangle / \langle w^{\star 2}\rangle \sim \mathrm{N}^{-1}$) diverges with the flock size. Given our limited range of flock sizes, the $-\frac{1}{3}$ scaling law could not be quantitatively checked. Nonetheless this weak decay is again consistent with the minute variations reported in Fig. 3.8(d). These analytical predictions unambiguously confirm that the soft rotational mode which results in the global twist of the trajectories chiefly rules the winding statistics and hence the mixing of the self-propelled particles at long times. The prominence of the twist fluctuations is expected to be qualitatively robust to the detailed form of the interactions; it solely relies on the existence of a soft rotation mode which is generic to all the flying spin models.

We close with Letter from a potential experimental perspective. In most of the situations, in the wild, external perturbations and fields (e.g. gravity [43]) explicitly break the rotational symmetry. Measuring the winding statistics should be an effective mean to probe the response of the flock to these external bias which are difficult to quantify otherwise.

We acknowledge support from Institut Universitaire de France and ANR project MiTra.

# Perspectives and open questions

In this thesis, the collective dynamics of aligning self-propelled particles has been studied from different angles: microscopic description of an experimental system, connection with the hydrodynamics of polar active matter, spatial patterns at large scale, geometry of individual trajectories. We have already summarized the main results and mentioned related open questions at the end of the previous chapters. To close this manuscript, let us finish with a few more general perspectives.

- A number of questions arise from kinetic theories. In this thesis, we have solely used these methods as a tool to coarse-grain the microscopic dynamics of the colloidal rollers. In particular, we did not pay much attention to the spatial correlations between particles, following all the previous works on active matter. Yet, this question is crucial to understanding the microscopic origin of the giant density fluctuations, found in polar phases. Rather than studying the correlations *a posteriori*, from the fluctuating hydrodynamics of the population, one could try to trace back the anomalous large-scale fluctuations from the correlations between the particle positions.

- In this thesis, we have studied different steady states of the hydrodynamics of active matter: homogeneous polar liquid, band patterns, heterogeneous vortex. As we already stressed it several times, the selection of a pattern among these various solutions is not understood. This complex problem involves the boundary conditions, the detailed form of the interactions, and depends on the initial condition. The formation and the stability of the spatial patterns of active matter should be further investigated in the future.

- Over the past years, a number of numerical works have studied more complex dynamics than the simple Vicsek model, by adding e.g. attractive and repulsive couplings [50, 55, 57, 92, 128, 140], inertia for the moving particles [6, 8, 46, 225], or assuming a density-dependent propulsion speed [79]. The large-scale phenomenology turns out to be dramatically altered by these changes. Even slight modifications of the interaction rule (e.g. short-ranged vs. metric-free couplings) impact the spatial patterns [123, 160, 198]. However, apart from the Vicsek model, thorough numerical characterizations are still lacking. To better understand the differences between these closely-related models, it may be enlightening to systematically compare the different implementations of the Vicsek ideas. For instance, how do pairwise-additive interactions (such as in the "flying-XY model" [79, 156]) change the phenomenology? What is the impact of the particle inertia? How do different boundary conditions alter the structure of the polar states?

- By definition, polar phases emerge from a spontaneous breaking of the rotational symmetry. Consistently, the theoretical models rely on the hypothesis that all directions of space are equivalent. We discussed in Chapter 3 the consequence of this assumption on the coherent rotation of polar flocks. However, Cavagna *et al.* showed that diffusion in starling flocks is anisotropic: it is minimal along the mean direction of motion *and* along the vertical direction [43]. The latter anisotropy is not expected from the available models. It would

be interesting to build theories which would account e.g. for the gravity field, and study the impact of this explicit breaking of the rotational symmetry.

- Another interesting question is the shape of compact flocks. In the wild, the coherent motion of animal populations usually takes the form of cohesive groups. This behavior has never been clearly seen in any synthetic experiment: when observed, polar structures systematically cruise in a disordered sea of particles that spans the entire box. As a matter of fact, it has been shown numerically that cohesive polar groups arise from a subtle interplay between alignment, repulsion and attraction [57]. However, the shape of these coherent flocks has never been rationalized theoretically. In addition to the emergence of polar order, it would be challenging to understand the formation of an interface separating the flock from the external medium, as well as its fluctuations and response to external perturbations. Can we describe the flock as a droplet of active liquid, having an effective surface tension?

- Recent works have studied numerically the dynamics of active particles in disordered media. In ensembles of non-interacting particles, it was shown that a random distribution of repulsive obstacles can lead to sub-diffusive dynamics. In populations of aligning particles, it can destroy polar order [53, 54]. Consistent quantitative observations have been made very recently by N. Desreumaux and V. Chikkadi on the colloidal rollers [143]. These first numerical and experimental results open interesting perspectives for theoretical works.

The previous questions could probably motivate future works in the same spirit as this thesis, connecting theoretical, numerical and experimental approaches. I hope that new interesting results will be obtained in these directions.

APPENDIX

# Non-equilibrium dynamics of confined suspensions

In this appendix, I reproduce two articles devoted to the hydrodynamics of confined particle-ladden fluids. When modeling the experimental system of colloidal rollers, in Chapter 1, we have found that the hydrodynamic couplings between the particles have a long-ranged component. It impacts the large-scale structure of the polar phase by destroying the giant density fluctuations. As a matter of fact, this long-ranged dipolar interaction is not specific to the population of Quincke rollers. It exists in all confined suspensions, when particles move between two rigid walls in a thin layer of liquid. This situation encompasses two classes of systems. (i) A first class consists in the transport of *passive* particles driven in thin channels or in semi-rigid films, e.g. colloid deposition on solid surfaces [63, 64], protein motion in lipid membranes [77] or droplet-base microfluidics [15, 162, 191] (see Fig. A.1(a)). Due to the friction with the confining walls, the particle moves slower than the surrounding liquid and cause distortions of the uniform advection flow. (ii) A second situation corresponds to *active* suspensions composed of self-propelled particles, e.g. active droplets moving in microfluidic channels [209] or bacteria swimming in nanometer-thin films [61, 227] (see Fig. A.1(b)). The motion of the particles again induces a flow in the liquid. Although the transport mechanisms are very different at the single-particle level, these two classes of confined suspensions display large-scale dynamical patterns such as propagating density heterogeneities [17] and coherent clusters [227], shown in Fig. A.1. Here, we investigate the impact of hydrodynamic interactions on the large-scale organization of these systems. We address the collective dynamics of non-brownian particles under rigid confinement, in both passive and active suspensions.

At large scale compared to the confinement width, the hydrodynamics of thin films of vis-

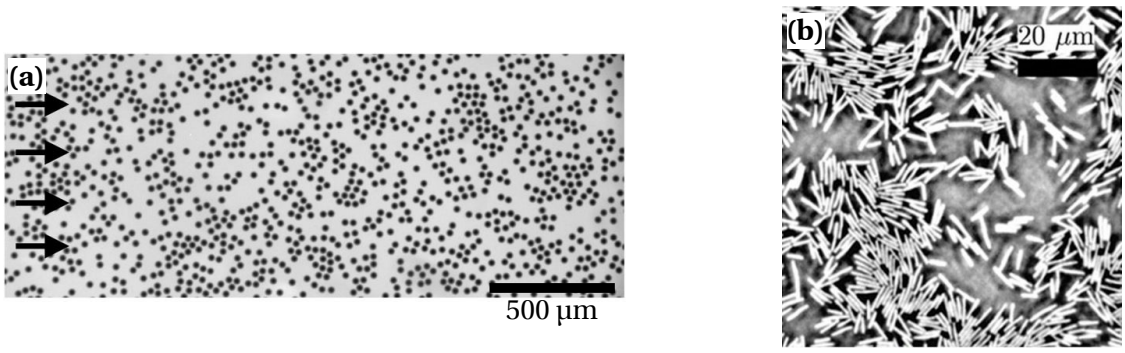


**Figure A.1** – Two examples of confined suspensions. **(a)** Droplets transported by an external flow in a microfluidic channel. Density waves freely propagate. **(b)** Colony of bacteria *bacillus subtilis* swimming in a thin film of liquid. The bacteria form coherent clusters (reproduced from [227]).

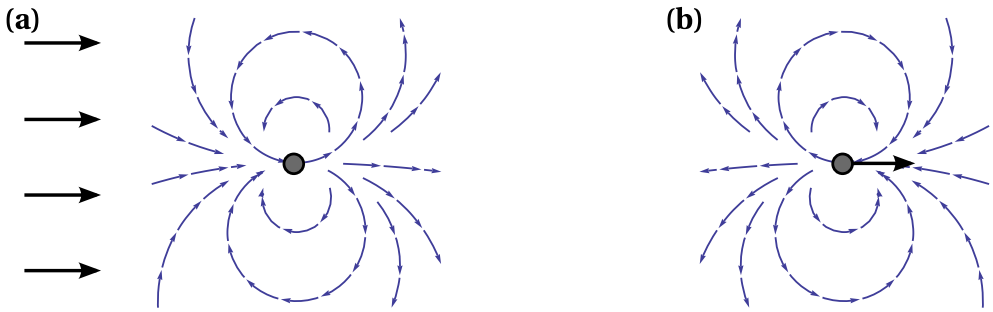


**Figure A.2** – Disturbance flow field induced a long distance by a particle, in quasi-bidimensional confinement. **(a)** Passive particle driven by a uniform external flow. **(b)** Active particle moving in the fluid.

cous fluids reduces to a Laplacian problem. The two-dimensional flow field is potential: $\mathbf{v}(\mathbf{r},t) = -\nabla\Phi(\mathbf{r},t)$. The incompressibility condition, $\nabla\cdot\mathbf{v} = 0$, readily translates into $\Delta\Phi = 0$. The latter equation, which is satisfied everywhere in the fluid, does not hold inside the solid particles: boundary conditions are imposed at their surface. The resulting flow is calculated by considering fictive source-singularities located at the particle positions: $\Delta\Phi = \mathrm{S}(\mathbf{r},t)$, where the source distribution $\mathrm{S}(\mathbf{r},t)$ is zero outside of the particles. In the far field, the flow induced by a particle is deduced from a multipolar expansion of $\mathrm{S}(\mathbf{r},t)$. As mass conservation forbids source monopoles, the lowest-order multipole is a source-sink dipole [59, 77]. It is the dominant contribution at long distance. A particle located at $\mathbf{r} = 0$ induces a dipolar disturbance flow:

$$\mathbf{v}(\mathbf{r}) = \frac{\boldsymbol{\sigma}}{2\pi r^2}\cdot(2\hat{\mathbf{r}}\hat{\mathbf{r}} - \mathbb{I})\,, \tag{A.1}$$

where the dipole strength is proportional to the particle speed with respect to the fluid. The streamlines are sketched in Fig. A.2.

Importantly, the previous argument does not depend on the detailed transport mechanism at the particle level. This result contrasts with unconfined fluids: in 3D suspensions of self-propelled particles, the far-field flow has a different symmetry, and its sign depends on the propulsion mode (the extensile or contractile nature of the swimmer) [14, 183, 185]. Conversely, under rigid confinement, the flow induced by the stress distribution at the surface of the particle is screened by the rigid walls, which are momentum reservoirs. The remaining unscreened flow solely arises from mass conservation, due to the displacement of a finite-size object. As a result, the far-field flows induced by passive and active particles have the same dipolar symmetry and the same $r^{-2}$ decay, Eq. (A.1) and Fig. A.2. These two situations can therefore be studied within a similar theoretical framework. Using a simple kinetic theory, we investigate the dynamics of particles coupled by long-ranged dipolar interactions.

In suspensions of passive suspensions cruising in a quasi-bidimensional channel, we find that density excitations freely propagate in all directions, even though the particles are neither affected by potential force nor by inertia, Fig. A.1(a). The dispersion relation is shaped by the combination of the long-ranged hydrodynamic interactions and local excluded volume effects. This works combines theory and experiments, carried out by Nicolas Desreumaux and Raphaël Jeanneret. It was done in collaboration with Eric Lauga. The results are explained in the article “Hydrodynamic fluctuations in confined particle-laden fluids”, reproduced p. 149.

In active suspensions, the hydrodynamic interactions between confined swimmers solely depend on their shape. Unlike in 3D suspensions, the particles reorient in uniform flows due to friction with the confining walls. By studying the large-scale dynamics of isotropic populations, we find that hydrodynamic interactions can promote the formation of coherent structures. This work was done with Tommaso Brotto and Eric Lauga. It is detailed in the article “Hydrodynamic of confined active fluids”, see p. 156.

# Article: *Hydrodynamic fluctuations in confined particle-laden fluids*

N. Desreumaux, J.-B. Caussin, R. Jeanneret, E. Lauga and D. Bartolo, *Phys. Rev. Lett.* **111**, 118301 (2013)

We address the collective dynamics of non-Brownian particles cruising in a confined microfluidic geometry and provide a comprehensive characterization of their spatiotemporal density fluctuations. We show that density excitations freely propagate at all scales, and in all directions even though the particles are neither affected by potential forces nor by inertia. We introduce a kinetic theory which quantitatively accounts for our experimental findings, demonstrating that the fluctuation spectrum of this non-equilibrium system is shaped by the combination of truly long-range hydrodynamic interactions and local collisions. We also demonstrate that the free propagation of density waves is a generic phenomenon which should be observed in a much broader range of hydrodynamic systems.

Understanding the collective dynamics of non-Brownian particles in viscous fluids is a long-standing challenge in fluid mechanics. For example, many features of sedimentation in a quiescent fluid are still poorly understood. Rather than falling along straight lines, as an isolated particle does, sedimenting particles experience swirling motion correlated over large finite distance, the physical origin of which has been under debate for more than 30 years [96, 167]. The conceptual complexity of this collective dynamics contrasts with the formal simplicity of the (linear) Stokes equation that rules low-Reynolds-number flows. Immersed bodies generically affect both the momentum and the mass transfers of the fluid, even when not driven by external fields. As a result, long-range interactions arise between the particles due to the interplay between the local velocity of the fluid and the motion of the particles. They vanish only for uniform flows, for which the particles would be all advected at the same speed as the fluid, irrespective of their spatial distribution. Such a condition is never achieved when the fluid is confined by rigid walls or obstacles. Friction with the bounding walls causes strong distortions of the flow field, inducing effective interactions between the particles [31, 59, 70, 77]. As it turns out the transport of particle-laden fluid through rigidly confined geometries is is involved in a number of industrial and natural processes, including filtration [107], colloid deposition on solid surfaces [63, 64], droplet-based microfluidics [15, 191], Propel2005 micro-flows [162], protein motion in lipid membranes [77], bacteria swarming [227, 228]. Understanding the particle transport in confined films is a necessary first step toward the description of particle traffic in more complex geometries such as ordered, or random porous networks. Recently, pioneering experiments probed the propagation of density heterogeneities in bidimensional emulsions and droplet streams [16, 17]. Focusing on a semi-local quantity, the droplet density averaged over the channel width, Beatus2009 et al revealed the propagation of longitudinal Burgers shocks, resulting from the linear variation of the droplet speed with the local density [17]. However, this observation does not account for the complexity of the structural [179], and spatiotemporal fluctuations observed at all scales in rigidly confined particle-laden fluids, regardless of their specific geometry, composition, and driving mechanism,

see e.g. [17, 47, 179, 209, 227].

Here we combine advanced microfluidic experiments and kinetic theory to shed light on the collective dynamics of particles advected in shallow microchannels. We first characterize their density fluctuations. We show that they freely propagate, at all scales and in all directions, in a dispersive manner. We then quantitatively demonstrate how the interplay of hydrodynamic and steric interactions shape the fluctuation spectrum of this many-body non-equilibrium system. Finally, we show how bidimensional microfluidic emulsions can be effectively used as a proxy to probe collective effects in a much broader range of hydrodynamic systems including diffusiophoretic suspensions, foams, or emulsions, cruising through porous media, and confined sedimentation.

We developed a model microfluidic experiment which made it possible to track the individual positions of hundred of thousands of identical droplets interacting hydrodynamically in a shallow channel. Briefly, the system consists of a monodisperse oil-in-water emulsion flowing in a shallow microchannel. The length and width of the channel, $L \times W = 5\,\mathrm{cm} \times 5\,\mathrm{mm}$, are much larger than its height, $h = 27 \pm 0.1\,\mu\mathrm{m}$, which compares with the droplet diameter, see Fig. A.3. The emulsion is therefore confined in a quasi-2D geometry. The droplets are formed at a conventional flow-focusing junction followed by a dilution module. The fluid flow-rates are imposed by high-precision syringe pumps. Etched-glass microchips ensure that the channel dimensions are unaffected by the flow conditions. In addition, the geometry of the junction, and the range of flow rates, are chosen so-that the formation of the droplet was unaffected by the dilution flow. Therefore we accurately controlled both the droplet radius, $R_d$, and the average area fraction, $\phi$, occupied by the emulsion. We report here results obtained for $R_d = 16.7 \pm 0.3\,\mu\mathrm{m}$ ($R_d/h = 0.62$), and $0.21 < \phi < 0.56$. Varying the droplet sizes up to $R_d \sim 2h$ does not qualitatively change our measurements. The droplets are visualized using fluorescence imaging. For each experiment we tracked $\sim 10^5$ particle trajectories in a region close to the center of the main channel, Fig. A.3B.

In the absence of droplets, the fluid flow would be uniform along the $x$-direction in the observation region. This is evidenced by the linear trajectories followed by isolated droplets cruising along the channel. Conversely, even at the smallest surface fraction, when an emulsion flows, the droplets undergo large transverse and longitudinal fluctuations in their motion. These fluctuations lead to the formation of particle clusters at all scales. These clusters are clearly seen to travel at a speed that is different from the mean droplet velocity. Density bands transverse to the flow are faster than the longitudinal ones. However, these clusters are transient structures, they form and break apart in a continuous fashion. Our purpose is to elucidate the physical mechanisms responsible for this complex and fluctuating dynamics. To quantify the spatiotemporal fluctuations of the droplet density field $\rho(\mathbf{r}, t)$, where $\mathbf{r} = (x, y)$, we measure its power spectrum. Introducing the Fourier transform of the local density, $\rho_{\mathbf{q},\omega'} = \frac{1}{2\pi}\int \rho(\mathbf{r}, t) e^{i(\mathbf{q}\cdot\mathbf{r} - \omega' t)} \mathrm{d}\mathbf{r}\,\mathrm{d}t$, the power spectrum is defined as $|\tilde{\rho}_{\mathbf{q},\omega'}|^2$, where $\tilde{\rho}(\mathbf{r}, t) \equiv \rho(\mathbf{r}, t) - \langle \rho(\mathbf{r}, t) \rangle$. Practically, $\rho$ is computed from the particle positions as $\rho(\mathbf{r}, t) \equiv \sum_i \mathcal{G}(\mathbf{r} - \mathbf{r}_i(t))$, where $\mathbf{r}_i(t)$ is the position of the $i^{\mathrm{th}}$ droplet, and where $\mathcal{G}$ is a Gaussian shape function.

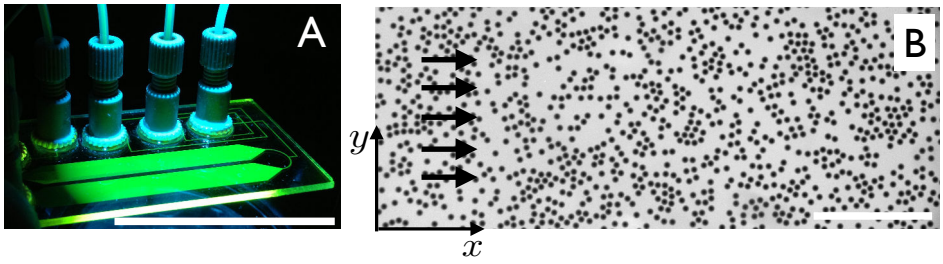


**Figure A.3** – **A**– Picture of the microfluidic setup. During the experiments one of these two 5-cm long channels was continuously fed with monodisperse droplets. Scale bar: 5 cm. **B**– Typical snapshot of an experimental movie. The black arrows indicate the direction of the flow. Scale bar: 500 µm.

In Fig. A.4A, we show a cut of a typical power spectrum in the $(\omega', q_x)$ plane. This example corresponds to $\phi = 0.39$, and to $q_y R_d = 0.2$. Several important comments are in order: (i) The power spectrum is localized in the Fourier space, which is the hallmark of propagative dynamics for the density fluctuations, as first noted in [17] for the specific case of the $y$-averaged density mode ($q_y = 0$). We stress that compression modes propagate even though the droplets do not interact via potential forces, and even though their inertia is negligible compared to the viscous friction at this scale. These "sound" modes originate only from the hydrodynamic coupling between the advected particles; (ii) The curve on which the spectrum is peaked corresponds to the dispersion curve of the density waves. It deviates markedly from a straight line at moderate wavelengths. The hydrodynamic interactions do not merely renormalize the mean advection speed but cause the density fluctuations to propagate in a dispersive fashion; (iii) The global shape of the spectrum is conserved for every area fraction, and more surprisingly for every wave vector $q_y$ provided that the wavelength remains larger than the particle size (see below).

In all that follows, we discard the trivial non-dispersive contribution due to the advection at the mean droplet velocity $\langle \mathbf{v}_d \rangle$. We focus on the density fluctuations in the frame moving at $\langle \mathbf{v}_d \rangle$, and introduce the reduced pulsation $\omega \equiv \omega' - \langle v_d \rangle q_x$. Experiments done at different area fractions, and thus at different continuous phase velocities due to dilution, are compared by normalizing the wave vectors by $R_d^{-1}$, and the pulsations by $v_F/R_d$, where $v_F$ is the velocity of the continuous phase imposed by the seringee pumps. Fig. A.4B shows a typical dispersion relation: $\omega = \omega(q_x, q_y)$, obtained for $\phi = 0.39$. The spectrum is symmetric along the $q_y$ direction as expected from the symmetry of the system. Furthermore, density fluctuations propagate in all directions except in the one strictly transverse to the flow ($q_x = 0$). In addition, the dispersion curve displays an axial

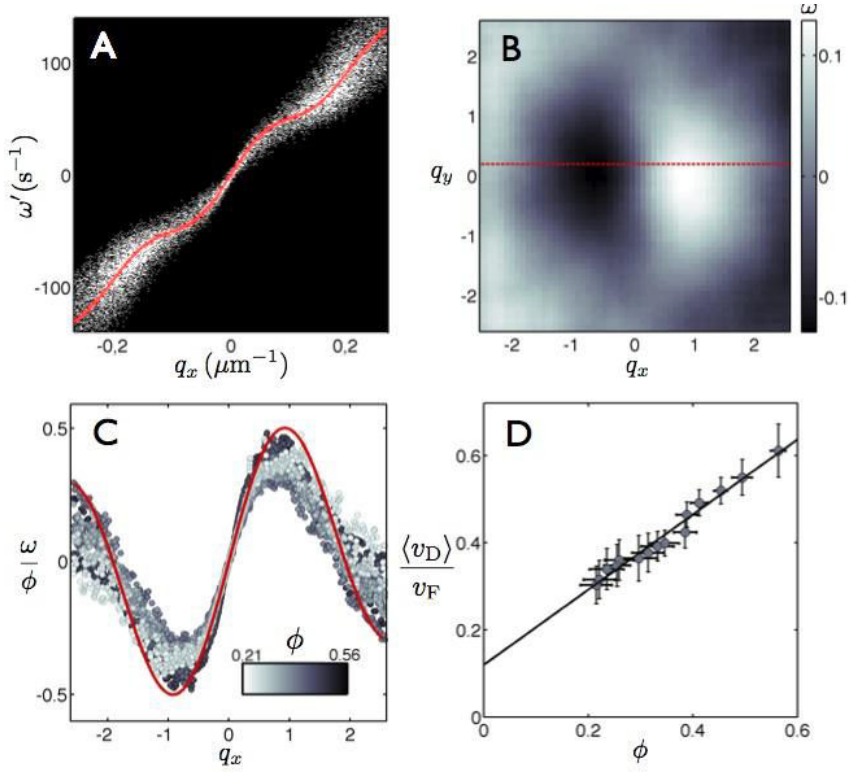


**Figure A.4** – **A**– Grayscale power spectrum of the density fluctuations plotted in the $(q_x, \omega')$ plane for $q_y = 0.2/R_d$, $\phi = 0.39$, and $v_F = 1\,mm/s$. Solid line: theoretical prediction for the location of the dispersion curve. **B**– Experimental dispersion curve $\omega(q_x, q_y)$, $\phi = 0.39$. Recall that units are chosen so that $R_d = 1$, and $v_F = 1$. The dotted line indicates the $q_y$ value corresponding to the power spectrum shown in A. **C**– Renormalized dispersion relations in the moving frame, $q_y = 0$. Circles: experimental data, solid line: theoretical prediction, Eq. (A.7), with no adjustable parameter. **D**– Variations of the mean droplet velocity with $\phi$. Circles: experimental data. Solid line: best linear fit. The error bars account for statistical fluctuations, and correspond to the standard deviation.

symmetry with respect to the $q_y$-axis. It is worth noting that the sign of the associated phase velocity changes as $q_x$ increases. The long wavelength excitations propagate downstream, while the short wavelength excitations propagate upstream.

In Fig. A.4C, we show that once renormalized by $\phi$, the dispersion relations corresponding to 12 different area fractions collapse on a single master curve. This noticeable collapse is not specific to the purely longitudinal waves and occurs for all the possible $q_y$ values. Our systematic rescaling demonstrate that a unique set of physical mechanisms dictates the collective motion of the droplets, at all scales, regardless of the droplet density.

We now propose a theoretical model which quantitatively accounts for our experimental findings. The instantaneous configuration of the emulsion is fully determined by the positions of N identical axisymmetric particles: $\mathbf{r}_i(t)$, $i = 1 \ldots N$. The dynamics of an isolated particle has proven to be correctly captured by a constant mobility coefficient, $\mu$, defined as $\dot{\mathbf{r}}_i(t) \equiv \mu \mathbf{v}(\mathbf{r}_i, t)$ where $\mathbf{v}(\mathbf{r}, t)$ is the in-plane fluid velocity field averaged over the channel height in the absence of the particle $i$ [16, 17]. In our quasi-2D geometry, the fluid flow is potential and derives from the local pressure field, $\mathbf{v} = -G\nabla P$, where $G = h^2/12\eta$, $\eta$ being the viscosity of the aqueous phase; $\mathbf{v}(\mathbf{r}, t)$ is then fully determined when considering the incompressibility condition, and the no-flux boundary conditions through the sidewalls of the channel as well. In a particle-free channel, the velocity field would be uniform, $\mathbf{v} = v_F \hat{\mathbf{x}}$. The particles are not passive tracers ($\mu < 1$), therefore their relative motion with respect to the fluid results in a dipolar disturbance of the surrounding flow [59, 77]. The potential dipolar perturbation, $\mathbf{v}^{dip}(\mathbf{r}, \mathbf{r}_i(t))$, induced at the position $\mathbf{r}$ by a particle located at $\mathbf{r}_i(t)$ is defined by the modified incompressibility relation

$$\nabla \cdot \mathbf{v}^{dip}(\mathbf{r}, \mathbf{r}_i(t)) = \sigma \partial_x \delta(\mathbf{r} - \mathbf{r}_i(t)), \tag{A.2}$$

where $\sigma$ is the dipole strength ($\sigma > 0$). In order to establish the equations of motion of the N particles, we now assume the dipolar disturbances to be pairwise additive. This yields $\dot{\mathbf{r}}_i(t) = \mu v_F \hat{\mathbf{x}} + \mu \sum_{j \neq i} \mathbf{v}^{dip}(\mathbf{r}_i(t), \mathbf{r}_j(t))$. We now move from these N coupled equations to an hydrodynamic description for the particle density field $\rho(\mathbf{r}, t)$. $\rho(\mathbf{r}, t)$ obeys the conservation equation

$$\partial_t \rho(\mathbf{r}, t) + \nabla \cdot \mathbf{j}(\mathbf{r}, t) = 0. \tag{A.3}$$

In order to relate the local particle current $\mathbf{j}(\mathbf{r}, \mathbf{t})$ to the local structure of the suspension, we used a conventional kinetic theory framework [139, 173]

$$\mathbf{j}(\mathbf{r}, t) = \mu \rho(\mathbf{r}, t) \mathbf{v}_F + \mu \int d\mathbf{r}' \mathbf{v}^{dip}(\mathbf{r}, \mathbf{r}') \rho^{(2)}(\mathbf{r}, \mathbf{r}', t), \tag{A.4}$$

where $\rho^{(2)}(\mathbf{r}, \mathbf{r}', t)$ is the two-point distribution function. We now assume that the particle positions decorrelate over a distance as small as one particle diameter. In addition to this mean-field approximation, we also explicitly account for the steric repulsion between the particles via the following closure relation for Eq. (A.4)

$$\rho^{(2)}(\mathbf{r}, \mathbf{r}') = \begin{cases} 0 & \text{if} \quad |\mathbf{r} - \mathbf{r}'| < 2R_d, \\ \rho(\mathbf{r})\rho(\mathbf{r}') & \text{if} \quad |\mathbf{r} - \mathbf{r}'| \geq 2R_d, \end{cases} \tag{A.5}$$

where $R_d$ is the radius of a particle. Eqs. (A.4) and (A.5) define the equations of motion for the particle-density field. In principle, the effective extent of the excluded volume could be larger that the particle radius due to short-range intermolecular repulsions, and lubrication forces. However no measurable difference with the actual droplet radius could be observed in our experiments. We now focus on the dynamics of small density fluctuations, $\tilde{\rho}(\mathbf{r}, t)$, around an homogeneous state: $\tilde{\rho}(\mathbf{r}, t) \equiv \rho(\mathbf{r}, t) - \rho_0$, where $\rho_0 = \langle \rho(\mathbf{r}, t) \rangle = \phi/(\pi R_d^2)$. As done in our experiments, we work in the frame moving at the mean droplet velocity $\langle \mathbf{v}_d \rangle = \mu v_F \hat{\mathbf{x}} + \mu \rho_0 \int_{|\mathbf{r}-\mathbf{r}'| \geq 2R_d} \mathbf{v}^{dip}(\mathbf{r}, \mathbf{r}') \, d\mathbf{r}'$. At leading order in $\tilde{\rho}$, and combining Eqs. (A.4) and (A.5), the current functional that captures both the

hydrodynamic interactions (long-range) and the contact interactions (short-range) remains non-local: $\tilde{\mathbf{j}}(\mathbf{r},t) \equiv \mu\rho_0 \int_{|\mathbf{r}-\mathbf{r}'|\geq 2R_d} \mathbf{v}^{\mathrm{dip}}(\mathbf{r},\mathbf{r}')\tilde{\rho}(\mathbf{r}',t)\,d\mathbf{r}'$. However, using Eq. (A.2) and focusing on particles far from the sidewalls, then $\nabla\cdot\tilde{\mathbf{j}}$ takes a simple local form

$$\nabla\cdot\tilde{\mathbf{j}}(\mathbf{r},t) = -\frac{\mu\rho_0\sigma}{4\pi R_d}\int_0^{2\pi}\tilde{\rho}(\mathbf{r}-2R_d\hat{\mathbf{r}}')\cos\theta' d\theta', \tag{A.6}$$

where, since $R_d \ll W$, we have used the expression of the dipolar perturbation corresponding to an unbounded domain [59], $\mathbf{v}^{\mathrm{dip}}(\mathbf{r},\mathbf{r}+2R_d\hat{\mathbf{r}}')\cdot\hat{\mathbf{r}}' = -(\sigma\cos\theta')/8\pi R_d^2$, with $\hat{\mathbf{r}}' \equiv \cos\theta'\hat{\mathbf{x}} + \sin\theta'\hat{\mathbf{y}}$ . We now look for plane wave solutions $\tilde{\rho}(\mathbf{r},t) = \sum_{\mathbf{q}}\tilde{\rho}_{\mathbf{q}}\exp(i\omega t - i\mathbf{q}\cdot\mathbf{r})$ of Eq. (A.3). After some elementary algebra we infer their dispersion relation, which is our main theoretical result

$$\omega = (\mu\sigma\rho_0)q_x\frac{J_1(2qR_d)}{2qR_d}, \tag{A.7}$$

where $J_1$ is the first Bessel function. As $\omega$ is real, this relation implies that density waves freely propagate in the channel in qualitative agreement with our experimental observations. It is worth noting that since $\nabla\cdot\tilde{\mathbf{j}}$ is a local quantity, the form of the dispersion relation is generic, and does *not* depend on the channel size, and geometry. In addition, the linear variations of $\omega$ with $\rho_0$ explain the collapse of the normalized dispersion relations on a single master curve over the entire range of wave vectors (Fig. A.4C). We now move to a quantitative comparison between our theoretical predictions and our experimental measurements. Eq. (A.7) is fully determined by two physical parameters: the droplet radius $R_d$, and $\mu\sigma\rho_0$ that quantifies the strength of the hydrodynamic couplings. In order to determine this latter parameter, we exploit another specific feature of the hydrodynamic interactions. Due to their symmetry, the sum of all the dipolar perturbations would leave the mean droplet velocity unchanged in an isotropic and homogeneous system. However, in anisotropic-channel geometries, $\langle\mathbf{v}_d\rangle$ increases linearly with the mean density irrespective of the channel size [15]. At $0^{\mathrm{th}}$ order in $\tilde{\rho}$, $\langle\mathbf{v}_d\rangle = \mu v_F\hat{\mathbf{x}} + \frac{1}{2}(\mu\sigma\rho_0)\hat{\mathbf{x}}$. Importantly this relation provides a direct means to measure independently the last unknown parameter of our theory. The linear increase of the measured value of $\langle v_D\rangle$ with $\rho_0$ appears clearly in Fig. A.4D. The strength of the hydrodynamic coupling ($\mu\sigma\rho_0$) can thus be inferred from a linear fit (see Fig. A.4D). We superimposed our theoretical predictions for the dispersion relation, Eq. (A.7), both in the laboratory frame and in the frame moving at $\langle\mathbf{v}_d\rangle$ in Figs. A.4A and A.4C. We find that the agreement between the theory and the experiments is excellent over a wide range of wave vectors, and of area fractions. Without any free fitting parameters, our model quantitatively captures the dispersive nature of the density fluctuations observed in the flowing emulsions.

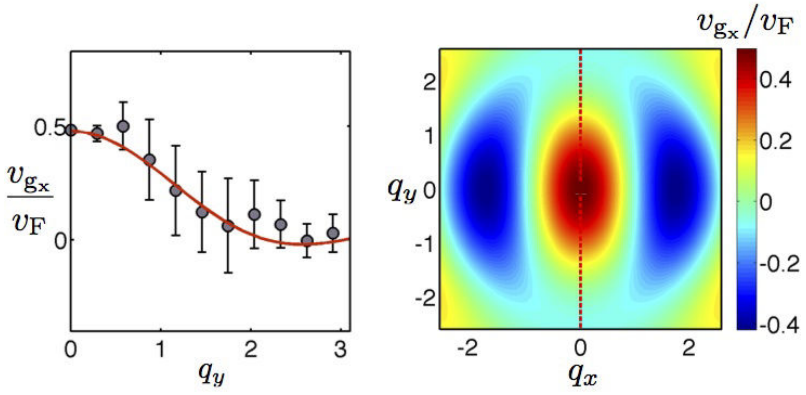


**Figure A.5** – **A**– $v_{g_x}$ plotted versus $q_y$ at $q_x = 0$. Circles: experimental data for $\phi = 0.56$. Solid line: Theoretical prediction with no adjustable parameter deduced from Eq. (A.7). The error bars correspond to a 95% confidence interval in the measurement of $v_{g_x}$ from the slope of the dispersion curve. **B**– Theoretical prediction for the variations of the group velocity, $v_{g_x}$ with the wave vector components. Dotted line: $q_x = 0$. The variations of $v_{g_x}$ along this direction are shown in A.

To gain additional physical insight into the propagation of the density waves, it is worth looking at the small-$q$ expansion of Eq. (A.7): $\omega = \frac{1}{2}\mu\sigma\rho_0 q_x[1-\frac{1}{2}(q\mathrm{R_d})^2]+\mathcal{O}\left((q\mathrm{R_d})^4\right)$. At leading order, this relation is non-dispersive (linear) whatever the direction of propagation. The phase velocity scales linearly with the magnitude of the dipolar coupling $\sigma$. In addition, it does not depend explicitly on $\mathrm{R}_d$, which implies that the small-$q$ excitations propagate only due to the long-range hydrodynamic interactions between the particles. Conversely, the dispersive term in $\omega(\mathbf{q})$ explicitly depends on the particle radius. At high $q$, the propagation of the density waves is set by the combination of the excluded volume interactions and the angular symmetry of the hydrodynamic couplings.

To introduce our last quantitative results, we recall that one of the most striking feature observed in the flowing emulsions is the propagation of vertical density bands which propagate at a significantly faster speed than the mean droplet flow. An homogeneous vertical band spanning the entire width of the channel corresponds to the linear superposition of plane waves associated with $q_y = 0$, and with $q_x$'s distributed around $q_x = 0$. In the frame moving at $\langle \mathbf{v}_\mathrm{d} \rangle$, their speed is given by the $x$-component of the group velocity $v_{\mathrm{g}_x}(q_x, q_y) = \partial\omega/\partial q_x$ evaluated at $q = 0$. In Fig. A.5A, we plot the experimental values of $v_{\mathrm{g}_x}(0, q_y)$, which we measured from the slope at the origin of the dispersion curves (as the ones shown in Fig. A.4C). Again the agreement with the theoretical curve deduced from Eq. (A.7) is excellent. This plot reveals that the density bands extended across the entire channel width are the fastest and propagate at velocities 1.5 higher that the mean droplet flow, thereby making them highly visible on the experimental movies. To go beyond this observation, we used Eq. (A.7), to plot the magnitude of $v_{\mathrm{g}_x}(q_x, q_y)$ for all $q$s, Fig. A.5B. $v_{\mathrm{g}_x}$ displays non-monotonic variations with both $q_x$, and $q_y$ and changes its sign at high $q$s. In the frame moving at $\langle \mathbf{v}_\mathrm{d} \rangle$, and for $q\mathrm{R}_d \ll 1$, $v_{\mathrm{g}_x}$ is positive. The wave packets propagate faster than the mean flow due to the hydrodynamic interactions that shape the dispersion curve in the long-wavelength limit. In contrast, the excluded volume interactions between the droplets result in the opposite effect: at high $q$ the density-wave packets propagate upstream ($v_{\mathrm{g}_x} < 0$, for $q\mathrm{R}_d > 1$).

As a last theoretical comment we note that the kinetic theory framework that we introduced is not restricted to dipolar interactions. It could be used without additional complexity to address the density fluctuations in unbounded sedimenting suspensions. Strong qualitative differences are expected due to the loss of fore-aft symmetry for Stokeslets-type hydrodynamic interactions [96].

To close this letter we further stress on the relevance of our results to a much broader range of physical systems. Two ingredients dictate the collective behavior of the confined emulsions: (i) the hydrodynamic interactions between the particles derive from a potential, and have dipolar symmetry, (ii) the particles have a finite size. As it turns out these two features are shared by a number of very distinct hydrodynamic systems. A first class of example concern the transport of particles in porous media. Regardless of the spatial dimension (2D or 3D), the fluid flow in a porous network is a potential flow at scales larger than the typical pore size. In addition, it has been recently shown that when particles locally obstruct the porous network they induce a dipolar perturbation to the velocity field [47]. Therefore, the dispersive propagation of density excitations is expected to be found in particle filters, blood, micro-vessels, soils, etc. It is also worth noting that the dipolar couplings found in Hele-Shaw and in networks geometries are not restricted to particles advected by the surrounding fluid. Sedimenting particles, rising bubbles and even self-propelled particles would move faster than the host fluid, thereby inducing a dipolar perturbation in the far field as well. The same collective phenomenology would be found except that the speed of the density waves should have the opposite signs, and that the mean particle velocity should decay with the volume fraction. As a last example, we point that particles diffusiophoretically transported by an homogeneous solute gradient [150] should also display a very similar propagative dynamics, as they also induce a weak far field disturbance that has a dipolar symmetry [3]. This last example makes it clear that confinement is not a requirement to observe the propagation of dispersive waves. The model microfluidic experiment that we characterized and described in a quantitative fashion should be seen as a proxy to probe generic collective effects in particle-laden fluids driven out of equilibrium.

We acknowledge stimulating interactions with C. Savoie and M. Guérard. We thank D. Saintillan and T. Beatus2009 for valuable comments and discussions, and Bertrand Levaché for help with the experiments. We also acknowledge funding from the National Science Foundation (grant to CBET-0746285 to EL).

# Article: *Hydrodynamics of confined active fluids*

T. Brotto, J.-B. Caussin, E. Lauga and D. Bartolo, *Phys. Rev. Lett.* **110**, 038101 (2013)

We theoretically describe the dynamics of swimmer populations confined in thin liquid films. We first demonstrate that hydrodynamic interactions between confined swimmers only depend on their shape and are independent of their specific swimming mechanism. We also show that due to friction with the walls, confined swimmers do not reorient due to flow gradients but the flow field itself. We then quantify the consequences of these microscopic interaction rules on the large-scale hydrodynamics of isotropic populations. We investigate in details their stability and the resulting phase behavior, highlighting the differences with conventional active, three-dimensional suspensions. Two classes of polar swimmers are distinguished depending on their geometrical polarity. The first class gives rise to coherent directed motion at all scales whereas for the second class we predict the spontaneous formation of coherent clusters (swarms).

Soft materials composed of motile particles have seen a surge of interest over the last couple of years. They encompass auto-phoretic colloids [204], self-propelled droplets [209], and vibrated grains [68, 119]. This interest was triggered by their fascinating structural and transport properties akin to the one found in biological systems such as bacterial suspensions, migrating cells, and cytoskeletal extracts (see Ref. [136] and references therein). These so-called active fluids are ensembles of self-driven particles capable of propelling themselves in the absence of any external actuation [41, 136, 168, 212, 216]. From a theoretical perspective, these systems are commonly separated into two classes depending on the way they exchange momentum with their surroundings [136, 168, 212]. "Dry" systems, typically walkers, or crawlers, achieve locomotion by transferring momentum to a rigid substrate, and interact via short range contact interactions. In contrast "wet" systems, typically suspensions of swimmers, conserve momentum, and the particles interact at finite distance via long-range hydrodynamic interactions. A number of experimentally relevant situations involve monolayers of active particles living in confined fluid films, and thus belong to both classes – e.g. bacteria swimming on the surface of a cell-culture gel, or active colloids and droplets moving in microfluidic channels [61, 209, 228].

In this Letter, we describe the phase behavior of active fluids confined in two-dimensional (2D) geometries. In order to do so, we first revisit the description of hydrodynamic interactions under confinement. We demonstrate that the far-field flow induced by a swimmer does not depend on the specifics of its swimming mechanism. The notions of pushers and pullers for instance, prevalent in three dimensions (3D), are not relevant in thin films [182, 183]. In addition, on the basis of a prototypal microscopic model, we show that due to friction with the walls, confined polar swimmers are not only prone to align along the local elongation axis but with the flow field itself. We then exploit these new interactions rules in 2D to address the large-scale dynamics of confined populations of swimmers. We establish a novel set of hydrodynamic equations for confined active films, which qualitatively differ from the modified Leslie-Eriksen equations for active liquid crystals [136]. An investigation of the resulting phase behavior leads to the distinction

between two classes of polar swimmers depending on their geometrical polarity. The first class (large-head), gives rise to the emergence of coherent particle motion along the same direction at all scales whereas for the second class (large-tail), we predict the spontaneous formation of coherent clusters (swarms).

Let us consider an ensemble of self-propelled particles confined in a thin film of a Newtonian liquid. We address strongly confined geometries where the particle height is comparable to the film thickness, $h$, see Fig. A.6 (left). At scales larger than $h$, the fluid flow is characterized by the projection of the $z$-averaged velocity field in the $(x, y)$ plane. Far from a swimmer, the projected flow field $\mathbf{u}(\mathbf{r}, t)$ is potential

$$\mathbf{u}(\mathbf{r}) = -\mathrm{G}\nabla\Pi(\mathbf{r}), \tag{A.8}$$

where $\Pi(\mathbf{r})$ is the pressure at $\mathbf{r} = (x, y)$. The Darcy factor G scales as $\mathrm{G} \sim h^2/\eta$ [97].

How does confinement affect hydrodynamic interactions between swimmers? In unbounded fluids, the flow induced by a swimmer depends on the microscopic details of the propulsion mechanism [75, 76, 124]. In the far-field, this flow is often well approximated by a force-dipole singularity, with a $\sim 1/r^2$ spatial decay, and as such has been used in most theoretical models [14, 127, 183]. This description results in the distinction between so-called pushers (or extensile swimmers), and pullers (or contractile swimmers). They corresponds to *force*-dipoles having opposite signs, and displaying different large scale dynamics [14, 127, 183]. When confined by solid walls, these flows are screened algebraically and decay as $\sim 1/r^3$, while retaining their angular symmetry. This screening of hydrodynamic interactions was shown to suppress generic instabilities which are the hallmark of isotropic pusher suspensions [136].

As it turns out, however, the two main consequences of confinement has actually been overlooked so far. Any multipolar stress distribution on the surface of the swimmer actually yields only subdominant contributions to the flow in the far field. For any particle transport mechanism (swimming, driving, advection) the far-field flow induced by a particle moving in a confined fluid has instead the symmetry of a potential *source*-dipole and decays as $\sim 1/r^2$ [16, 47, 129]. The distinction between pushers and pullers is thus irrelevant under confinement. Irrespective of the propulsion mechanism, the flow induced by a swimmer located at $\mathbf{r} = \mathbf{r}(t)$ is defined by Eq. (A.8) and by a modified incompressibility relation

$$\nabla \cdot \mathbf{u}(\mathbf{r}) = -\boldsymbol{\sigma} \cdot \nabla\delta(\mathbf{r} - \mathbf{r}(t)), \tag{A.9}$$

where the dipole strength is $\boldsymbol{\sigma} \equiv \sigma\left[\dot{\mathbf{r}}(t) - \mathbf{u}^{(0)}(\mathbf{r}(t))\right]$ where $\mathbf{u}^{(0)}$ is the velocity field in absence of the particle, and $\sigma$ scales as the square of the particle size (for a disk-shape particle, $\sigma$ is twice the particle area) [16]. The dipolar solution, $\mathbf{u}^{\mathrm{d}}(\mathbf{r}|\mathbf{r}(t), \boldsymbol{\sigma})$, of Eqs. (A.8)-(A.9) is given, for a particle located at the origin, by

$$\mathbf{u}^{\mathrm{d}}(\mathbf{r}|\mathbf{0}, \boldsymbol{\sigma}) = \frac{1}{2\pi|\mathbf{r}|^2}\,(2\hat{\mathbf{r}}\hat{\mathbf{r}} - \mathbb{I}) \cdot \boldsymbol{\sigma}, \tag{A.10}$$

with $\hat{\mathbf{r}} \equiv \mathbf{r}/|\mathbf{r}|$ and $\mathbb{I}$ the identity tensor [16, 129]. This framework has proven to accurately describe the interactions between confined advected droplets even in concentrated systems [17, 18, 47,

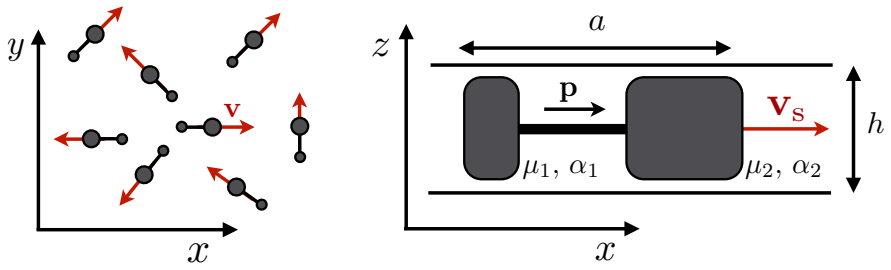


**Figure A.6** – Left: Sketch of a confined suspension of active particles swimming freely in the $(x, y)$ plane. Right: Close-up on a single polar swimmer (see text for notation). The active particles are confined between two walls in the $z$-direction.

48]. Importantly, the angular symmetry of $\mathbf{u}^{\mathrm{d}}$ is different from the one of a force dipole: it is a polar flow field displaying the same angular dependence as that of a force *monopole* under confinement [129] despite the swimmers being self-driven. The reason for this apparent paradox lies in the continuous momentum exchange with the confining walls, via the shear flow in the thin films that lubricate the swimmer-wall contacts, see Fig. A.6.

The second important difference with 3D suspensions concerns hydrodynamic interactions between swimmers. In order to account for these interactions, we first establish the equations of motion of an isolated swimmer in a arbitrary fluid flow. We focus on swimming bodies with polar shapes, as is the case for most motile cells. For a swimmer at position $\mathbf{r}(t)$ we denote $\mathbf{p}(t)$ its orientation ($|\mathbf{p}|^2 = 1$) and $v_{\mathrm{s}}$ the magnitude of its swimming velocity along $\mathbf{p}$. From symmetry considerations and at leading order in $|\nabla\mathbf{u}|$, the equations of motion of a polar swimmer for $\{\mathbf{r}(t), \mathbf{p}(t)\}$ take the generic form

$$\dot{\mathrm{R}}_\alpha = v_{\mathrm{s}} p_\alpha + \mu_\perp(\delta_{\alpha\beta} - p_\alpha p_\beta)u_\beta + \mu_\parallel(p_\alpha p_\beta)u_\beta, \tag{A.11}$$

$$\dot{p}_\alpha = \nu(\delta_{\alpha\beta} - p_\alpha p_\beta)u_\beta + \nu'(\delta_{\alpha\beta} - p_\alpha p_\beta)(\nabla_\gamma u_\beta)p_\gamma, \tag{A.12}$$

where $\mu_\perp$ (resp. $\mu_\parallel$) is a transverse (resp. longitudinal) mobility coefficient and $\nu$ and $\nu'$ are two rotational mobility coefficients. In unbounded fluids, we have $\nu = 0$ and $\mu_\perp = \mu_\parallel = 1$, and Eq. (A.12) then corresponds to Jeffrey's equation commonly used to quantify the orientation of anisotropic particles with the flow-elongation axis [124, 183]. Conversely, confined suspensions offer the possibility of having a nonzero value for $\nu$. Instead of reorienting due to flow gradients, swimmers can reorient because of the flow itself, a new type of orientational dynamics which has not been considered so far.

To provide insight into the conditions for nonzero values of $\nu$, we derive the above equations of motion for a prototypal microscopic model (dumbbell). We show how the lubricated friction with the walls induce both anisotropic mobility ($\mu_\perp \neq \mu_\parallel$) and a direct coupling between the flow velocity and the particle orientation ($\nu \neq 0$). Consider a rigid-dumbbell swimmer, composed of two disks of radius $b_1$ (resp. $b_2$) located at $\mathbf{r}_1$ (resp. $\mathbf{r}_2$), and connected by a frictionless rigid rod of length $a \gg \{b_1, b_2\}$ (see Fig. A.6, right). The lubrication forces between a disk-shape particle and the solid walls hinder its advection by the fluid. Passive disks would be transported at a velocity $\dot{\mathbf{r}}_i(t) = \mu_i \mathbf{u}(\mathbf{r}_i)$ ($i = 1,2$), where the mobility coefficient $\mu_i$ is comprised between 0 (fixed obstacle) and 1 (passive tracer). We also introduce the drag coefficients $\alpha_i$: when a disk is pulled by an external force $\mathbf{F}$ in a quiescent fluid, it moves at a velocity $\dot{\mathbf{r}}_i(t) = \alpha_i \mathbf{F}$. Let us now assume that the two disks would propel at a velocity $v_{\mathrm{s}}^{(0)}\mathbf{p}$ when alone, and let us compute the swimming speed and mobility coefficients from Eqs. (A.11)-(A.12) for the dummbell. The displacement of each disk results from the competition between (i) self-propulsion, (ii) the advection by the external flow $\mathbf{u}^{(0)}$, (iii) the advection of the disk $i$ by the dipolar perturbation induced by the motion of the disk $j$, $\mathbf{u}^{\mathrm{d}}(\mathbf{r}_i|\mathbf{r}_j, \boldsymbol{\sigma}_j)$, and (iv) the inextensibility constraint, $\mathbf{r}_2 - \mathbf{r}_1 = a\mathbf{p}$. At leading order in $b_i/a$, these contributions yield the following equations of motion for the "head" ($i = 2$) and the "tail" ($i = 1$) of the swimmer:

$$\dot{\mathbf{r}}_1 = v_{\mathrm{s}}^{(0)}\mathbf{p} + \mu_1[\mathbf{u}^{(0)}(\mathbf{r}_1) + \mathbf{u}^{\mathrm{d}}(\mathbf{r}_1|\mathbf{r}_2, \boldsymbol{\sigma}_2)] + \alpha_1 \mathbf{T}, \tag{A.13}$$

$$\dot{\mathbf{r}}_2 = v_{\mathrm{s}}^{(0)}\mathbf{p} + \mu_2[\mathbf{u}^{(0)}(\mathbf{r}_2) + \mathbf{u}^{\mathrm{d}}(\mathbf{r}_2|\mathbf{r}_1, \boldsymbol{\sigma}_1)] - \alpha_2 \mathbf{T}, \tag{A.14}$$

where the tension $\mathbf{T}$ ensures the inextensibility condition, $\mathbf{p}\cdot(\dot{\mathbf{r}}_2 - \dot{\mathbf{r}}_1) = 0$. Defining the center of drag of the swimmer as $\mathbf{r} \equiv (\alpha_1\mathbf{r}_2 + \alpha_2\mathbf{r}_1)/(\alpha_1 + \alpha_2)$, Eqs. (A.13)-(A.14) are readily recast into the form of Eqs. (A.11)-(A.12) with a dumbbell velocity and mobility coefficients given at leading order by $v_{\mathrm{s}} = v_{\mathrm{s}}^{(0)} + \mathcal{O}((b_i/a)^2)$, $\mu_\perp = \alpha_2\mu_1(1-\gamma_2) + \alpha_1\mu_2(1-\gamma_1)$, $\mu_\parallel = \alpha_2\mu_1(1+\gamma_2) + \alpha_1\mu_2(1+\gamma_1)$ and $\nu = [(\mu_2+\mu_1\gamma_2) - (\mu_1+\mu_2\gamma_1)]/a$, where $\gamma_i \equiv b_i^2(\mu_i - 1)/a^2$. We first see that the translational mobility coefficients, $\mu_{\perp,\parallel}$ depend only on the anisotropy of the swimmer, and are independent of its geometrical polarity (they remain unchanged upon a $1 \leftrightarrow 2$ permutation). In addition, as $\mu_\parallel < \mu_\perp$, a non-swimming dumbbell making a finite angle with a uniform flow field would drift at a finite angle from the flow direction. We also obtain that indeed $\nu \neq 0$ for polar swimmers. Since the $\mu_i$'s are

decreasing functions of the particle radius, $\nu$ is negative for large-head swimmers ($b_2 > b_1$), and positive otherwise. From Eq. (A.12) we thus get that in a uniform flow large-head swimmers would reorient against the flow and propel upstream. In contrast, large-tail swimmers ($b_1 > b_2$) would swim downstream. For apolar swimmers, $\nu$ vanishes and the orientation of a symmetric dumbbell evolves according to the Jeffrey's orbits, Eq. (A.12), where $\nu = 0$ and $\nu' = a[\mu_2(1+\gamma_1)+\mu_1(1+\gamma_2)]/2$. Note that since $\mathbf{u}$ is irrotational, the orientation of an isotropic swimmer made of a single disk is not coupled to the background flow. In the rest of the paper we discard the conventional $\nu'$ contribution to the orientational dynamics. It only yields short-wavelength corrections to the large-scale description of polar-swimmers suspensions described below.

We now turn to the dynamics of a dilute population of interacting swimmers in a quiescent fluid. We introduce the one-point probability distribution function, $\Psi(\mathbf{r},\mathbf{p},t)$ for swimmers with orientation $\mathbf{p}$ at position $\mathbf{r}$ and time $t$. The dynamics of the active particles is defined by Eqs (A.11)-(A.12), with the fluid velocity field, $\mathbf{u}(\mathbf{r},t)$, resulting from the linear superposition of force dipoles induced by each swimmer, $\mathbf{u}(\mathbf{r},t) = \int \mathrm{d}\mathbf{p}\mathrm{d}\mathbf{r}'\,\Psi(\mathbf{r}',\mathbf{p},t)\mathbf{u}^{\mathrm{d}}(\mathbf{r}|\mathbf{r}',\boldsymbol{\sigma}')$, where $\boldsymbol{\sigma}' = \sigma v_{\mathrm{s}}\mathbf{p}$. Assuming, that swimmers are subject to translational and rotational diffusion, $\Psi(\mathbf{r},\mathbf{p},t)$ obeys the continuity equation

$$\partial_t\Psi = -\nabla\cdot(\Psi\dot{\mathbf{r}}) - \nabla_{\mathbf{p}}\cdot(\Psi\dot{\mathbf{p}}) + \mathrm{D}\nabla^2\Psi + \mathrm{D}_r\nabla^2_{\mathbf{p}}\Psi, \tag{A.15}$$

where $\dot{\mathbf{r}}$ and $\dot{\mathbf{p}}$ are defined by Eqs. (A.11)-(A.12), D and $\mathrm{D}_r$ are the translational and the rotational diffusion coefficients respectively, and $\nabla_{\mathbf{p}}$ stands for the gradient on the unitary circle. For simplicity, we neglect the translational diffusion. Specifically, anticipating on our results, we assume $\mathrm{D} \ll v_{\mathrm{s}}^2/\mathrm{D}_{\mathrm{R}}$, which is true for most biological and artificial micro-size swimmers. Note that for homogeneous suspensions, and due to the symmetry of the dipolar coupling, the sum of all hydrodynamic interactions vanishes: when $\nabla\Psi(\mathbf{r},\mathbf{p},t) = 0$, we have $\int \mathrm{d}\mathbf{r}'\,\mathbf{u}^{\mathrm{d}}(\mathbf{r}|\mathbf{r}',\boldsymbol{\sigma}') = 0$, and thus from Eqs. (A.11)-(A.12) it follows that $\dot{\mathbf{p}} = \mathbf{0}$, and $\nabla\cdot\dot{\mathbf{r}} = 0$. The dynamics of an homogeneous population, from Eq. (A.15), reduces thus to the orientational diffusion of an isolated swimmer, and homogeneous phases relax toward an isotropic state over a time $\sim \mathrm{D}_{\mathrm{R}}^{-1}$.

We now investigate the dynamic response of the homogeneous and isotropic phase to spatial fluctuations of the concentration and orientation of the active particles. The phase behavior is described in term of (i) the concentration field, $c(\mathbf{r},t) \equiv \int\Psi(\mathbf{r},\mathbf{p},t)\mathrm{d}\mathbf{p}$, (ii) the local polarization, $\mathbf{p}(\mathbf{r},t) \equiv \frac{1}{c}\int\mathbf{p}\Psi(\mathbf{r},\mathbf{p},t)\mathrm{d}\mathbf{p}$, and (iii) the local nematic-orientation tensor, $\mathbf{Q}(\mathbf{r},t) \equiv \frac{1}{c}\int(\mathbf{pp}-\frac{1}{2}\mathbf{I})\Psi(\mathbf{r},\mathbf{p},t)\mathrm{d}\mathbf{p}$. To establish their equation of motion, we need to add a closure relation to Eq. (A.15). As we focus on deviations from isotropic and homogeneous states, we expand $\Psi$ linearly in its three first moments [14, 127]

$$\Psi(\mathbf{x},\mathbf{p},t) = \frac{1}{2\pi}c\left(1+2p_\alpha\mathrm{P}_\alpha+4p_\alpha p_\beta\mathrm{Q}_{\alpha\beta}\right), \tag{A.16}$$

where the numerical coefficients are chosen so that $c$, $\mathbf{p}$, and $\mathbf{Q}$ are defined in a self-consistent fashion. Defining $\bar{\mu} \equiv \frac{1}{2}(\mu_\parallel+\mu_\perp)$, and $\tilde{\mu} \equiv (\mu_\parallel-\mu_\perp)$, and after some elementary but tedious algebra, the three nonlinear equations of motion are inferred from Eqs. (A.15)-(A.16) as

$$\partial_t c = -\nabla_\alpha\left[v_{\mathrm{s}}c\mathrm{P}_\alpha + \bar{\mu}cu_\alpha + \tilde{\mu}c\mathrm{Q}_{\alpha\beta}u_\beta\right], \tag{A.17}$$

$$\partial_t(c\mathrm{P}_\alpha) = \frac{\nu}{2}u_\alpha c - \nu c u_\beta\mathrm{Q}_{\beta\alpha} - \mathrm{D}_{\mathrm{R}}c\mathrm{P}_\alpha - \nabla_\beta\mathscr{I}_{\beta\alpha}, \tag{A.18}$$

$$\partial_t(c\mathrm{Q}_{\alpha\beta}) = \frac{\nu}{2}cu_\gamma(2\delta_{\gamma(\alpha}\mathrm{P}_{\beta)} - \delta_{\alpha\beta}\mathrm{P}_\gamma) - 4\mathrm{D}_{\mathrm{R}}c\mathrm{Q}_{\alpha\beta} - \nabla_\gamma\mathscr{J}_{\gamma\alpha\beta}, \tag{A.19}$$

where the (potential) fluid velocity satisfies

$$\partial_\alpha u_\alpha = -\sigma v_{\mathrm{s}}\partial_\alpha(c\mathrm{P}_\alpha), \tag{A.20}$$

and where the expressions for the fluxes $\mathscr{I}$ and $\mathscr{J}$ are given in Supplementary Information.

Equations (A.17)-(A.20) fully describe the dynamics of the isotropic phase. We investigate their linear stability with respect to plane-wave excitations of the form $(\delta c, \delta\mathbf{p}, \delta\mathbf{Q})\exp(i\mathbf{k}\cdot\mathbf{r} - i\omega t)$,

with $\mathbf{k} = k\hat{\mathbf{x}}$. At linear order, we can integrate Eq. (A.20) for the fluid velocity, and recast the equations of motion into a set of two uncoupled linear systems having the form $\partial_t(\delta \mathrm{P}_y, \delta \mathrm{Q}_{xy}) = \mathrm{M}_{\mathrm{bend}}(\delta \mathrm{P}_y, \delta \mathrm{Q}_{xy})$ and $\partial_t(\delta c, \delta \mathrm{P}_x, \delta \mathrm{Q}_{xx}) = \mathrm{M}_{\mathrm{splay}}(\delta c, \delta \mathrm{P}_x, \delta \mathrm{Q}_{xx})$. The first system couples the transverse-polarization and the bend modes only. These modes are stable for all $k$, they correspond to damped sound-waves. The associated dispersion relation is deduced from the eigenvalues of $\mathrm{M}_{\mathrm{bend}}$ as $i\omega = \frac{1}{2}(5\mathrm{D_R} \pm i\sqrt{-9\mathrm{D_R}^2 + (k v_s/2)^2})$. In contrast, long-range hydrodynamic interactions between swimmers can destabilize the concentration ($c$), the longitudinal polarization ($\mathrm{P}_x$) and the splay modes ($\mathrm{Q}_{xx}$). To convey an intuitive description of this instability we introduce the two governing dimensionless numbers. First, $\mathrm{Pe} \equiv \nu c_0 \sigma v_s/(2\mathrm{D_R})$ is a Peclet number comparing the rotational-diffusion rate $\mathrm{D_R}$ to the rate of rotation of a polar swimmer induced by a source dipole of magnitude $\sigma c_0 v_s$ ($c_0$ being to the average concentration); large-tail swimmers (resp. large-head swimmers) correspond to $\mathrm{Pe} > 0$ (resp. $\mathrm{Pe} < 0$). The second dimensionless number, $\mathrm{H} \equiv (\bar{\mu}\sigma c_0 v_s)/v_s$, compares the swimming speed, $v_s$, to the advection velocity induced by a source dipole of magnitude $\sigma c_0 v_s$. In the long-wave-length limit ($k \to 0$), the eigenfrequencies associated with the stability matrix $\mathrm{M}_{\mathrm{splay}}$ then take the form

$$\omega_c = -i\frac{v_s^2}{2\mathrm{D_R}}\left(\frac{1-\mathrm{H}}{1+\mathrm{Pe}}\right)k^2, \tag{A.21}$$

$$\omega_{\mathrm{P}} = -i\mathrm{D_R}(1+\mathrm{Pe}) + \mathcal{O}(k^2), \tag{A.22}$$

$$\omega_{\mathrm{Q}} = -4i\mathrm{D_R} + \mathcal{O}(k^2). \tag{A.23}$$

At $0^{\mathrm{th}}$ order in $k$, the total number of swimmers being a conserved quantity we have $\omega_c = 0$, and $\mathrm{M}_{\mathrm{splay}}$ has only two non-trivial eigenvalues. Whereas rotational diffusion always stabilizes the nematic orientation ($-i\omega_{\mathrm{Q}} < 0$), hydrodynamic interactions can in fact destabilize the isotropic state. From Eq. (A.22), we see that large-head swimmers with $\mathrm{Pe} < -1$ experience a generic instability: fluctuations of the local polarization are amplified when the rotation induced by the hydrodynamic couplings overcome the diffusional relaxation of $\mathrm{P}_x$ (see Fig. A.7).

Several comments are in order. First, although the growth rate of the instability does not dependent on $k$, the total polarization ($k = 0$) is *not* unstable. As discussed above, the sum of all the hydrodynamic interactions cancels in this limit and no global directed flow can emerge spontaneously from an isotropic suspension. The instability shows however that groups of particles swimming coherently along the same direction form at all scales. Second, the generic nature of the instability is specific to the dipolar symmetry of the hydrodynamic interactions, and the polar shape of the particles, and can be intuitively rationalized as follows. From Eq. (A.20) we see that any finite wave-length perturbation of $\mathrm{P}_x$ along $x$ results in a fluid flow in the opposite direction, with amplitude $\sim \sigma c_0 v_s \delta \mathrm{P}_x$. Polar swimmers align with, or against, the local flow direction depending on their polarity. Large-head swimmers align along $-\mathbf{u}$, thereby increasing the initial perturbation of $\mathbf{p}$ and destabilizing the isotropic state. Conversely, large-tail swimmers align in

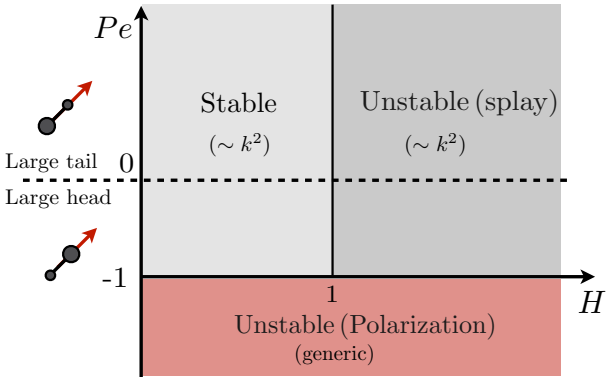


**Figure A.7** – Stability diagram of a nearly isotropic and homogeneous population of polar swimmers; $\mathrm{Pe} < 0$ (resp. $\mathrm{Pe} > 0$) refers to large-head swimmers (resp. large-tail swimmers).

the opposite direction and the local polarization relaxes to zero. As the reorientation rate of the swimmers is set by the magnitude of the velocity only (and not by the local strain-rate tensor), the growth (or relaxation) rate of the polarization is independent of the wave vector.

This novel generic instability is qualitatively different from the one observed in unbounded suspensions of pushers which, in contrast, is suppressed by confinement [136]. They differ in both the physical mechanisms at work and the structure of the unstable modes (bend versus splay modes). The only similarity is that in both systems the generic instability is a genuine collective effect due to the long-range nature of hydrodynamic interactions.

To investigate the stability of the active film when $\mathrm{Pe} > -1$, we need to consider the eigenfrequencies , and the eigenmodes of $\mathrm{M}_{\mathrm{splay}}$ up to $\mathrm{O}(k^2)$. From Eq. (A.21) we see that the combination of self-propulsion and rotational diffusion yields an effective diffusive dynamics of the suspension scaling as $\omega_c \sim (v_s^2/\mathrm{D_R})k^2$, as could have been anticipated from the single swimmer problem [105]. However, hydrodynamic interactions result in a renormalization of this single-swimmer effect. These interactions control both the magnitude and the sign of the effective translational diffusion. In the regions ($\mathrm{Pe} > -1$, $\mathrm{H} > 1$) and ($\mathrm{Pe} < -1$, $\mathrm{H} < 1$), the effective diffusivity is negative and thus slowly destabilizes the isotropic phase (Fig. A.7). The associated eigenmodes are now complex superpositions of $c$, $\mathrm{P}_x$, and $\mathrm{Q}_{xx}$, and thus clusters of aligned particles form and propel in a coherent fashion (swarms), from a homogeneous film. Notably, both large-head ($-1 < \mathrm{Pe} < 0$) and large-tail ($\mathrm{Pe} > 0$) swimmers are prone to this second splay-destabilization mechanism. In the other regions of Fig. A.7, the effective diffusivity is positive and concentration fluctuations are stable.

In summary we revisited the theoretical description of confined populations of microswimmers. We showed that active particles interact hydrodynamically in generic manner, which is independent of the microscopic details of their propulsion mechanism and that, depending on their polarity: they may reorient in flows instead of solely flow gradients. Focusing on polar swimmers, we then constructed a large scale hydrodynamic theory from a minimal microscopic model (dummbells). Our analysis showed that the macroscopic orientational dynamics is very different from the modified Leslie-Eriksen model of active liquid crystals due to a difference in the symmetry of the microscopic coupling between confined polar particles and the fluid flow. It results in a novel phase behavior for active films and, in particular, spontaneous large-scale directed motion and swarming can emerge out of isotropic populations of confined swimmers.

This work was funded in part by the NSF (grant 0746285 to E.L.), Paris Emergence research program (D. B.), and CNano Idf (D. B.). We thank Aparna Baskaran, Olivier Dauchot and David Saintillan fro valuable discussions.

# Supplementary Information

Using Ricci-calculus notation, the expression of the fluxes $\mathscr{I}$ and $\mathscr{J}$ are:

$$\mathscr{I}_{\beta\alpha} = \frac{1}{4}\left[\tilde{\mu} c \mathrm{P}_\gamma u_\gamma \delta_{\alpha\beta} + (4\bar{\mu} - \tilde{\mu}) c \mathrm{P}_\alpha u_\beta + \tilde{\mu} c \mathrm{P}_\beta u_\alpha + 4\nu c v_s (\mathrm{Q}_{\alpha\beta} + \frac{\delta_{\alpha\beta}}{2})\right], \tag{A.24}$$

$$\begin{aligned}\mathscr{J}_{\gamma\alpha\beta} = {} & \frac{v_s c}{2}[\delta_{\gamma(\alpha}\mathrm{P}_{\beta)} - \frac{\delta_{\alpha\beta}}{2}\mathrm{P}_\gamma] - \frac{\tilde{\mu} c}{4}[6u_\gamma \delta_{\alpha\beta} - u_{(\alpha}\delta_{\beta)\gamma}] + 2\bar{\mu} u_\gamma c \mathrm{Q}_{\alpha\beta} \\ & + \frac{1}{6}\tilde{\mu} c\left[-4u_\gamma \mathrm{Q}_{\alpha\beta} - 5u_\delta \mathrm{Q}_{\delta\gamma}\delta_{\alpha\beta} + 2u_\delta \mathrm{Q}_{\delta(\alpha}\delta_{\beta)\gamma} + 2u_{(\alpha}\mathrm{Q}_{\beta)\gamma}\right].\end{aligned} \tag{A.25}$$

# References


[1] M. Aldana, H. Larralde, and B. Vázquez, "On the emergence of collective order in swarming systems: a recent debate", Int. J. Mod. Phys. B **23**, 3661–3685 (2009) (cit. on pp. 4, 5, 92).

[2] A. Altland and B. Simons, *Condensed matter field theory* (Cambridge University Press, 2010) (cit. on pp. 123, 124).

[3] J. L. Anderson, "Colloid transport by interfacial forces", Annu. Rev. Fluid Mech. **21**, 61 (1989) (cit. on p. 154).

[4] I. S. Aranson, "Collective behavior in out-of-equilibrium colloidal suspensions", C. R. Phys. **14**, 518–527 (2013) (cit. on p. 83).

[5] V. Arnold, *Ordinary Differential Equations*, edited by M. MIT Press, Cambridge (1980) (cit. on p. 107).

[6] A. Attanasi, A. Cavagna, L. D. Castello, I. Giardina, A. Jelic, S. Melillo, L. Parisi, O. Pohl, E. Shen, and M. Viale, "Emergence of collective changes in travel direction of starling flocks from individual birds fluctuation", arXiv:1410.3330 (2014) (cit. on pp. 10, 121, 143).

[7] A. Attanasi, A. Cavagna, L. D. Castello, I. Giardina, S. Melillo, L. Parisi, O. Pohl, B. Rossaro, E. Shen, E. Silvestri, and M. Viale, "Finite-Size Scaling as a Way to Probe Near-Criticality in Natural Swarms", Phys. Rev. Lett. **238102**, 1–5 (2014) (cit. on pp. 10, 121, 133).

[8] A. Attanasi, A. Cavagna, L. Del Castello, I. Giardina, T. S. Grigera, A. Jelić, S. Melillo, L. Parisi, O. Pohl, E. Shen, and M. Viale, "Information transfer and behavioural inertia in starling flocks", Nature Physics **10**, 691–696 (2014) (cit. on pp. 10, 121, 134, 143).

[9] G. Baglietto and E. Albano, "Nature of the order-disorder transition in the Vicsek model for the collective motion of self-propelled particles", Phys. Rev. E **80**, 050103 (2009) (cit. on pp. 4, 5, 92).

[10] M. Ballerini, N. Cabibbo, R. Candelier, A. Cavagna, E. Cisbani, I. Giardina, V. Lecomte, a. Orlandi, G. Parisi, A. Procaccini, M. Viale, and V. Zdravkovic, "Interaction ruling animal collective behavior depends on topological rather than metric distance: evidence from a field study.", Proc. Natl. Acad. Sci. USA **105**, 1232–1237 (2008) (cit. on pp. 10, 133).

[11] A. Baskaran and M. Marchetti, "Enhanced Diffusion and Ordering of Self-Propelled Rods", Phys. Rev. Lett. **101**, 268101 (2008) (cit. on pp. 8, 12, 30).

[12] A. Baskaran and M. C. Marchetti, "Nonequilibrium statistical mechanics of self-propelled hard rods", J. Stat. Mech. – Theo. Exp. **2010**, P04019 (2010) (cit. on pp. 8, 30, 32, 33).

[13] A. Baskaran and M. C. Marchetti, "Hydrodynamics of self-propelled hard rods", Phys. Rev. E **77**, 011920 (2008) (cit. on pp. 8, 12, 17, 30, 33, 58, 107).

[14] A. Baskaran and M. C. Marchetti, "Statistical mechanics and hydrodynamics of bacterial suspensions.", Proc. Natl. Acad. Sci. USA **106**, 15567–72 (2009) (cit. on pp. 148, 157, 159).

[15] T. Beatus, R. Bar-Ziv, and T. Tlusty, "The physics of 2D microfluidic droplet ensembles", Phys. Rep. **516**, 103 (2012) (cit. on pp. 147, 149, 153).

[16] T. Beatus, T. Tlusty, and R. Bar-Ziv, "Phonons in a one-dimensional microfluidic crystal", Nat. Phys. **2**, 743 (2006) (cit. on pp. 149, 152, 157).

[17]T. Beatus, T. Tlusty, and R. Bar-Ziv, "Burgers shock waves and sound in a 2D microfluidic droplets ensemble", Phys. Rev. Lett. **103**, 114502 (2009) (cit. on pp. 147, 149–152, 157).

[18]T. Beatus, R. Bar-Ziv, and T. Tlusty, "Anomalous microfluidic phonons induced by the interplay of hydrodynamic screening and incompressibility", Phys. Rev. Lett. **99**, 124502 (2007) (cit. on p. 157).

[19]C. Bélisle and J. Faraway, "Winding angle and maximum winding angle of the two-dimensional random walk", J. Appl. Probab. (1991) (cit. on p. 137).

[20]A. Berdahl, C. J. Torney, C. C. Ioannou, J. J. Faria, and I. Couzin, "Emergent sensing of complex environments by mobile animal groups", Science **339**, 574 (2013) (cit. on p. 66).

[21]M. A. Berger and C. Prior, "The writhe of open and closed curves", J. Phys. A – Math. and Gen. **39**, 8321–8348 (2006) (cit. on pp. 118, 125).

[22]A. P. Berke, L. Turner, B. H. C., and E. Lauga, "Hydrodynamic attraction of swimming microorganisms by surfaces", Phys. Rev. Lett. **101**, 038102 (2008) (cit. on p. 68).

[23]E. Bertin, M. Droz, and G. Grégoire, "Boltzmann and hydrodynamic description for self-propelled particles", Phys. Rev. E **74**, 022101 (2006) (cit. on pp. 8, 9, 30, 138).

[24]E. Bertin, H. Chaté, and F. Ginelli, "Mesoscopic theory for fluctuating active nematics", arXiv: 1305.0772 (2013) (cit. on pp. 8, 30).

[25]E. Bertin, M. Droz, and G. Grégoire, "Hydrodynamic equations for self-propelled particles: microscopic derivation and stability analysis", J. Phys. A – Math. Theo. **42**, 445001 (2009) (cit. on pp. 3, 8, 9, 30, 32, 33, 35, 46, 47, 58, 61, 84, 94–97, 102, 103, 105–107, 109, 138).

[26]W. Bialek, A. Cavagna, I. Giardina, T. Mora, O. Pohl, E. Silvestri, M. Viale, and A. M. Walczak, "Social interactions dominate speed control in poising natural flocks near criticality.", Proc. Natl. Acad. Sci. USA **111** (2014) (cit. on pp. 10, 11, 120, 121, 133, 138).

[27]W. Bialek, A. Cavagna, I. Giardina, T. Mora, E. Silvestri, M. Viale, and A. M. Walczak, "Statistical mechanics for natural flocks of birds.", Proc. Natl. Acad. Sci. USA **109**, 4786–91 (2012) (cit. on pp. 10, 11, 129, 134).

[28]T. Bickel, G. Zecua, and A. Würger, "Polarization of active Janus particles", arXiv:1401.7833 (2014) (cit. on p. 83).

[29]J. R. Blake and A. T. Chwang, "Fundamental singularities of viscous flow", J. Eng. Math. **8**, 23–29 (1974) (cit. on pp. 26, 54).

[30]C. Blanch-Mercader and J. Casademunt, "Spontaneous motility of actin lamellar fragments", Phys. Rev. Lett. **110**, 078102 (2013) (cit. on p. 2).

[31]J. Blawzdziewicz and E. Wajnryb, "An analysis of the far-field response to external forcing of a suspension in the Stokes flow in a parallel-wall channel", Phys. Fluids **20**, 093303 (2008) (cit. on p. 149).

[32]C. Bouchiat and M. Mézard, "Elasticity Model of a Supercoiled DNA Molecule", Phys. Rev. Lett. **80**, 1556–1559 (1998) (cit. on p. 125).

[33]C. Bouchiat and M. Mézard, "Elastic rod model of a supercoiled DNA molecule", Eur. Phys. J. E **2**, 377 (2000) (cit. on pp. 124, 125).

[34]P. Boyland, M. Stremler, and H. Aref, "Topological fluid mechanics of point vortex motions", **175**, 69–95 (2003) (cit. on pp. 119, 135, 136).

[35]S. Brazovskii, "Phase transition of an isotropic system to a nonuniform state", Zh. Eksp. Teor. Fiz, 85–89 (1975) (cit. on pp. 9, 93, 110).

[36]A. Bricard, J.-B. Caussin, N. Desreumaux, O. Dauchot, and D. Bartolo, "Emergence of macroscopic directed motion in populations of motile colloids", Nature **503**, 95–98 (2013) (cit. on pp. 6, 66–72, 76, 77, 79, 84, 92, 93, 105, 107, 110).

[37]T. Brotto, J.-B. Caussin, E. Lauga, and D. Bartolo, "Hydrodynamics of Confined Active Fluids", Phys. Rev. Lett. **110**, 038101 (2013) (cit. on pp. 47, 58, 62, 65, 83, 84).

[38]J. Buhl, D. J. T. Sumpter, I. D. Couzin, J. J. Hale, E. Despland, E. R. Miller, and S. J. Simpson, "From disorder to order in marching locusts.", Science (New York, N.Y.) **312**, 1402–6 (2006) (cit. on pp. 6, 10, 43).

[39]I. Buttinoni, J. Bialké, F. Kümmel, H. Löwen, C. Bechinger, and T. Speck, "Dynamical Clustering and Phase Separation in Suspensions of Self-Propelled Colloidal Particles", Phys. Rev. Lett. **110**, 238301 (2013) (cit. on p. 2).

[40]D. S. Calovi, U. Lopez, S. Ngo, C. Sire, H. Chaté, and G. Theraulaz, "Swarming, schooling, milling: Phase diagram of a data-driven fish school model", New J. Phys. **16** (2014) (cit. on pp. 11, 134).

[41]M. E. Cates, "Diffusive transport without detailed balance in motile bacteria: does microbiology need statistical physics?", Rep. Prog. Phys. **75**, 042601 (2012) (cit. on p. 156).

[42]J.-B. Caussin and D. Bartolo, "Tailoring the interaction between self-propelled bodies", Eur. Phys. J. E **37**, 55 (2014) (cit. on p. 70).

[43]A. Cavagna, S. M. Duarte Queirós, I. Giardina, F. Stefanini, and M. Viale, "Diffusion of individual birds in starling flocks.", Proc. Bio. Sci. **280**, 20122484 (2013) (cit. on pp. 9, 120, 134, 139, 143).

[44]A. Cavagna and I. Giardina, "Bird flocks as condensed matter", Annu. Rev. Condens. Matter Phys. **5**, 183 (2014) (cit. on pp. 66, 133, 134).

[45]A. Cavagna, A. Cimarelli, I. Giardina, G. Parisi, R. Santagati, F. Stefanini, and M. Viale, "Scale-free correlations in starling flocks.", Proc. Natl. Acad. Sci. USA **107**, 11865–70 (2010) (cit. on p. 134).

[46]A. Cavagna, L. Del Castello, I. Giardina, T. Grigera, A. Jelic, S. Melillo, T. Mora, L. Parisi, E. Silvestri, M. Viale, and A. M. Walczak, "Flocking and turning: a new model for self-organized collective motion", 16 (2014) (cit. on pp. 10, 117, 121, 143).

[47]N. Champagne, R. Vasseur, A. Montourcy, and D. Bartolo, "Traffic jams and intermittent flows in microfluidic networks", Phys. Rev. Lett. **105**, 044502 (2010) (cit. on pp. 150, 154, 157).

[48]N. Champagne, E. Lauga, and D. Bartolo, "Stability and non-linear response of 1D microfluidic-particle streams", Soft Matter **7**, 11082–11085 (2011) (cit. on p. 157).

[49]H. Chaté, F. Ginelli, G. Grégoire, F. Peruani, and F. Raynaud, "Modeling collective motion: variations on the Vicsek model", Eur. Phys. J. B **64**, 451–456 (2008) (cit. on pp. 4–6, 9, 42, 79, 84, 92, 93, 100, 102, 105, 106, 109–111, 119, 129, 130, 135).

[50]H. Chaté, F. Ginelli, G. Grégoire, F. Peruani, and F. Raynaud, "Modeling collective motion: variations on the Vicsek model", Sur. Phys. J. B **64**, 451–456 (2008) (cit. on pp. 10, 13, 143).

[51]H. Chaté, F. Ginelli, and F. Raynaud, "Collective motion of self-propelled particles interacting without cohesion", Phys. Rev. E **77**, 046113 (2008) (cit. on p. 46).

[52]Y. J. Chen, Y. Nagamine, and K. Yoshikawa, "Self-propelled motion of a droplet induced by Marangoni-driven spreading", Phys. Rev. E **80**, 1–7 (2009) (cit. on p. 2).

[53]O. Chepizhko, E. G. Altmann, and F. Peruani, "Optimal noise maximizes collective motion in heterogeneous media", Phys. Rev. Lett. **110**, 238101 (2013) (cit. on pp. 121, 144).

[54]O. Chepizhko and F. Peruani, "Diffusion, Subdiffusion, and Trapping of Active Particles in Heterogeneous Media", Phys. Rev. Lett. **111**, 160604 (2013) (cit. on pp. 32, 121, 144).

[55]Y.-l. Chuang, M. R. D'Orsogna, D. Marthaler, A. L. Bertozzi, and L. S. Chayes, "State transitions and the continuum limit for a 2D interacting, self-propelled particle system", Physica D **232**, 33–47 (2007) (cit. on pp. 13, 30, 80, 82, 143).

[56]A. T. Chwang and T. Wu, "Hydromechanics of low-Reynolds-number flow. Part 2. Singularity method for Stokes flows", J. Fluid Mech. **67**, 787–815 (1975) (cit. on p. 26).

[57] I. D. Couzin, J. Krause, R. James, G. D. Ruxton, and N. R. Franks, "Collective Memory and Spatial Sorting in Animal Groups", J. Theor. Bio. **218**, 1–11 (2002) (cit. on pp. 10, 13, 79, 84, 119, 129, 130, 135, 143, 144).

[58] J. C. Crocker and G. Grier, "Methods of digital video microscopy for colloidal studies", J. Colloid Interface Sci. **179**, 298 (1996) (cit. on pp. 48, 75).

[59] B. X. Cui, H. Diamant, B. H. Lin, and S. A. Rice, "Hydrodynamic interaction in quasi-two-dimensional suspensions", Phys. Rev. Lett. **92**, 258301 (2004) (cit. on pp. 148, 149, 152, 153).

[60] A. Czirók, E. Ben-Jacob, I. Cohen, and T. Vicsek, "Formation of complex bacterial colonies via self-generated vortices", Phys. Rev. E **54**, 1791 (1996) (cit. on p. 66).

[61] N. C. Darnton, L. Turner, S. Rojevsky, and H. C. Berg, "Dynamics of Bacterial Swarming", Biophys. J. **98**, 2082–2090 (2010) (cit. on pp. 147, 156).

[62] D. Das and D. Saintillan, "Electrohydrodynamic interaction of spherical particles under Quincke rotation", Phys. Rev. E **87**, 043014 (2013) (cit. on pp. 18, 53).

[63] R. D. Deegan, O. Bakajin, T. F. Dupont, G. Huber, S. R. Nagel, and T. A. Witten, "Capillary flow as the cause of ring stains from dried liquid drops", Nature **389**, 827 (1997) (cit. on pp. 147, 149).

[64] R. D. Deegan, O. Bakajin, T. F. Dupont, G. Huber, S. R. Nagel, and T. A. Witten, "Contact line deposits in an evaporating drop", Phys. Rev. E **62**, 765 (2000) (cit. on pp. 147, 149).

[65] P. Dehornoy, "Braid-based cryptography", Contemporary Mathematics **360**, 5 (2004) (cit. on p. 138).

[66] P. Dehornoy, "Efficient solutions to the braid isotopy problem", Discrete Appl. Math. **156**, 3091 (2008) (cit. on p. 138).

[67] J. Deseigne, S. Léonard, O. Dauchot, and H. Chaté, "Vibrated polar disks: spontaneous motion, binary collisions, and collective dynamics", Soft Matter **8**, 5629 (2012) (cit. on pp. 66, 68, 74).

[68] J. Deseigne, O. Dauchot, and H. Chaté, "Collective Motion of Vibrated Polar Disks", Phys. Rev. Lett. **105**, 098001 (2010) (cit. on pp. 2, 6, 7, 12, 17, 43, 46, 79, 82, 156).

[69] N. Desreumaux, J.-B. Caussin, R. Jeanneret, E. Lauga, and D. Bartolo, "Hydrodynamic Fluctuations in Confined Particle-Laden Fluids", Phys. Rev. Lett. **111**, 118301 (2013) (cit. on pp. 57, 58).

[70] R. Di Leonardo, E. Cammarota, G. Bolognesi, H. Schafer, and M. Steinhart, "Three-dimensional to two-dimensional crossover in the hydrodynamic interactions between micron-scale rods", Phys. Rev. Lett. **107**, 044501 (2011) (cit. on p. 149).

[71] M. Doi and S. Edwards, *The Theory of Polymer Dynamics*, edited by O. Clarendon Press (1986) (cit. on pp. 33, 36).

[72] Y. Dolinsky and T. Elperin, "Dipole interaction of the Quincke rotating particles", Phys. Rev. E **85**, 026608 (2012) (cit. on p. 18).

[73] C. Dombrowski, L. H. Cisneros, S. Chatkaew, R. E. Goldstein, and J. O. Kessler, "Self-Concentration and Large-Scale Coherence in Bacterial Dynamics", Phys. Rev. Lett. **93**, 098103 (2004) (cit. on pp. 2, 43, 46).

[74] M. D'Orsogna, Y.-l. Chuang, A. L. Bertozzi, and L. S. Chayes, "Self-propelled particles with soft-core interactions: patterns, stability, and collapse", Phys. Rev. Lett. **96**, 104302 (2006) (cit. on pp. 28, 30, 80, 82, 86).

[75] K. Drescher, J. Dunkel, L. Cisneros, S. Ganguly, and R. E. Goldstein, "Fluid dynamics and noise in bacterial cell–cell and cell–surface scattering", Proc. Natl. Acad. Sci. USA **108**, 10940 (2011) (cit. on p. 157).

[76] K. Drescher, R. Goldstein, N. Michel, M. Polin, and I. Tuval, "Direct Measurement of the Flow Field around Swimming Microorganisms", Phys. Rev. Lett. **105** (2010) (cit. on p. 157).

[77] E. Evans and E. Sackmann, "Translational and rotational drag coefficients for a disk moving in a liquid membrane associated with a rigid substrate", J. Fluid Mech. **194**, 553 (1988) (cit. on pp. 147–149, 152).

[78] B. Fain, J. Rudnick, and S. Östlund, "Conformations of linear DNA", Phys. Rev. E **55**, 7364–7368 (1997) (cit. on p. 124).

[79] F. Farrell, M. C. Marchetti, D. Marenduzzo, and J. Tailleur, "Pattern formation in self-propelled particles with density-dependent motility", Phys. Rev. Lett. **108**, 1–5 (2012) (cit. on pp. 5, 6, 8, 9, 26, 30, 47, 56, 58, 84, 102, 107, 138, 143).

[80] E. Ferrante, A. Turgut, M. Dorigo, and C. Huepe, "Elasticity-based mechanism for the collective motion of self-propelled particles with spring-like interactions: A model system for natural and artificial swarms", Phys. Rev. Lett. **268302**, 1–5 (2013) (cit. on p. 82).

[81] M. Finn and J.-L. Thiffeault, "Topological optimization of rod-stirring devices", SIAM Rev. **53**, 723 (2011) (cit. on p. 136).

[82] J. Gautrais, F. Ginelli, R. Fournier, S. Blanco, M. Soria, H. Chaté, and G. Theraulaz, "Deciphering interactions in moving animal groups", Plos Comput. Bio. **8**, 1002678 (2012) (cit. on p. 66).

[83] F. Ginelli and H. Chaté, "Relevance of metric-free interactions in flocking phenomena", Phys. Rev. Lett. **105**, 1–4 (2010) (cit. on p. 5).

[84] L. Giomi, N. Hawley-Weld, and L. Mahadevan, "Swarming, swirling and stasis in sequestered bristle-bots", Proc. Roy. Soc. A – Math. Phys. **469**, 20120637–20120637 (2013) (cit. on pp. 11, 66, 68).

[85] L. Giomi, "The geometry and topology of turbulence in active nematics", 10 (2014) (cit. on p. 8).

[86] L. Giomi, M. J. Bowick, X. Ma, and M. C. Marchetti, "Defect annihilation and proliferation in active Nematics", Phys. Rev. Lett. **110**, 1–5 (2013) (cit. on p. 8).

[87] L. Giomi and A. DeSimone, "Spontaneous Division and Motility in Active Nematic Droplets", Phys. Rev. Lett. **112**, 147802 (2014) (cit. on p. 8).

[88] L. Giomi and M. C. Marchetti, "Polar patterns in active fluids", Soft Matter **8**, 129 (2012) (cit. on pp. 9, 100).

[89] A. J. Goldman, R. G. Cox, and H. Brenner, "Slow viscous motion of a sphere parallel to a plane wall – I Motion through a quiescent fluid", Chem. Eng. Sci. **22**, 637 (1967) (cit. on pp. 20, 51, 59, 77).

[90] A. J. Goldman, R. G. Cox, and H. Brenner, "Slow viscous motion of a sphere parallel to a plane wall – II Couette flow", Chem. Eng. Sci. **22**, 653 (1967) (cit. on pp. 20, 51, 53, 59, 77).

[91] A. Gopinath, M. F. Hagan, M. C. Marchetti, and A. Baskaran, "Dynamical self-regulation in self-propelled particle flows", Phys. Rev. E **85**, 061903 (2012) (cit. on pp. 9, 92–94, 96, 105, 109).

[92] G. Grégoire and H. Chaté, "Onset of Collective and Cohesive Motion", Phys. Rev. Lett. **92**, 025702 (2004) (cit. on pp. 5, 6, 13, 43, 66, 71, 84, 92, 93, 105, 110, 119, 129, 130, 134, 135, 143).

[93] A. Grosberg and H. Frisch, "Winding angle distribution for planar random walk, polymer ring entangled with an obstacle, and all that: Spitzer–Edwards–Prager–Frisch model revisited", J. Phys. A: Math. Gen. **36**, 8955 (2003) (cit. on p. 138).

[94] D. Grossman, I. S. Aranson, and E. Ben Jacob, "Emergence of agent swarm migration and vortex formation through inelastic collisions", New J. Phys. **10**, 023036 (2008) (cit. on pp. 12, 66, 82).

[95] R. Großmann, L. Schimansky-Geier, and P. Romanczuk, "Self-propelled particles with selective attraction–repulsion interaction: from microscopic dynamics to coarse-grained theories", New J. Phys. **15**, 085014 (2013) (cit. on pp. 13, 79).

[96] E. Guazzelli and J. Hinch, "Fluctuations and instability in sedimentation", Annu. Rev. Fluid Mech. **43**, 97 (2011) (cit. on pp. 149, 154).

[97] É. Guyon, J.-P. Hulin, L. Petit, and M. C. D., *Physical Hydrodynamics* (Oxford University Press, 2001) (cit. on p. 157).

[98] W. W. Hackborn, "Asymmetric Stokes flow between parallel planes due to a rotlet", J. Fluid Mech. **218**, 531 (2006) (cit. on pp. 26, 47, 55).

[99] B. Halperin, T. Lubensky, and S.-K. Ma, "First-Order Phase Transitions in Superconductors and Smectic-A Liquid Crystals", Phys. Rev. Lett. **32**, 292–295 (1974) (cit. on pp. 93, 110).

[100] T. Hanke, C. A. Weber, and E. Frey, "Understanding collective dynamics of soft active colloids by binary scattering", Phys. Rev. E **88**, 052309 (2013) (cit. on p. 82).

[101] S. Henkes, Y. Fily, and M. C. Marchetti, "Active jamming: Self-propelled soft particles at high density", Phys. Rev. E **84**, 040301 (2011) (cit. on p. 80).

[102] S. Herminghaus, C. C. Maass, C. Krüger, S. Thutupalli, L. Goehring, and C. Bahr, "Interfacial mechanisms in active emulsions.", Soft matter, 7008–7022 (2014) (cit. on p. 2).

[103] E. J. Hinch and L. G. Leal, "Constitutive equations in suspension mechanics. Part 2. Approximate forms for a suspension of rigid particles affected by Brownian rotations", J. Fluid Mech. **76**, 187 (1975) (cit. on pp. 33, 58).

[104] P. C. Hohenberg and J. B. Swift, "Metastability in fluctuation-driven first-order transitions: Nucleation of lamellar phases", Phys. Rev. E **52**, 1828–1845 (1995) (cit. on pp. 9, 93).

[105] J. R. Howse, R. A. L. Jones, A. J. Ryan, T. Gough, R. Vafabakhsh, and R. Golestanian, "Self-Motile Colloidal Particles: From Directed Propulsion to Random Walk", Phys. Rev. Lett. **99**, 8–11 (2007) (cit. on pp. 2, 161).

[106] H.-F. Huang, M. Zahn, and E. Lemaire, "Negative electrorheological responses of micro-polar fluids in the finite spin viscosity small spin velocity limit", J. Electrostat. **69**, 442 (2011) (cit. on p. 18).

[107] J.-P. Hulin, A.-M. Cazabat, E. Guyon, and F. F. Carmona, *Hydrodynamics of Dispersed Media*, edited by N. Y. Elsevier (1990) (cit. on p. 149).

[108] T. Ihle, "Kinetic theory of flocking: Derivation of hydrodynamic equations", Phys. Rev. E **83**, 030901 (2011) (cit. on pp. 8, 30).

[109] T. Ihle, "Invasion-wave-induced first-order phase transition in systems of active particles", Phys. Rev. E **88**, 040303 (2013) (cit. on pp. 9, 42, 105, 109).

[110] Z. Izri, M. N. V. D. Linden, and O. Dauchot, "Self-Propulsion of Pure Water Droplets by Spontaneous Marangoni-Stress-Driven Motion", **248302**, 1–5 (2014) (cit. on p. 2).

[111] G. B. Jeffery, "The Motion of Ellipsoidal Particles Immersed in a Viscous Fluid", Proc. Roy. Soc. A– Math. Phys. **102**, 161–179 (1922) (cit. on p. 84).

[112] H.-R. Jiang, N. Yoshinaga, and M. Sano, "Active Motion of a Janus Particle by Self-Thermophoresis in a Defocused Laser Beam", Phys. Rev. Lett. **105**, 268302 (2010) (cit. on pp. 2, 79, 83).

[113] J. F. Joanny, F. Jülicher, K. Kruse, and J. Prost, "Hydrodynamic theory for multi-component active polar gels", New J. Phys. **9** (2007) (cit. on p. 8).

[114] Y. Katz, K. Tunstrøm, C. C. Ioannou, C. Huepe, and I. D. Couzin, "Inferring the structure and dynamics of interactions in schooling fish.", Proc. Natl. Acad. Sci. USA **108**, 18720–5 (2011) (cit. on p. 11).

[115] F. C. Keber, E. Loiseau, T. Sanchez, S. J. DeCamp, L. Giomi, M. J. Bowick, M. C. Marchetti, Z. Dogic, and a. R. Bausch, "Topology and dynamics of active nematic vesicles", Science **345**, 1135–1139 (2014) (cit. on pp. 2, 66).

[116] J. Kierfeld, O. Niamploy, V. Sayakanit, and R. Lipowsky, "Stretching of semiflexible polymers with elastic bonds.", Sur. Phys. J. E **14**, 17–34 (2004) (cit. on pp. 123, 124).

[117] K. Kruse, J. Joanny, F. Jülicher, J. Prost, and K. Sekimoto, "Asters, Vortices, and Rotating Spirals in Active Gels of Polar Filaments", Phys. Rev. Lett. **92**, 1–4 (2004) (cit. on p. 8).

[118]K. Kruse, J. Joanny, F. Jülicher, J. Prost, and K. Sekimoto, "Generic theory of active polar gels: a paradigm for cytoskeletal dynamics.", Eur. Phys. J. E **16**, 5–16 (2005) (cit. on p. 8).

[119]A. Kudrolli, "Concentration Dependent Diffusion of Self-Propelled Rods", Phys. Rev. Lett. **104**, 088001 (2010) (cit. on p. 156).

[120]A. Kudrolli, G. Lumay, D. Volfson, and L. Tsimring, "Swarming and Swirling in Self-Propelled Polar Granular Rods", Phys. Rev. Lett. **100**, 058001 (2008) (cit. on pp. 2, 12, 43, 66, 68, 79, 82).

[121]A. Kumar, A. Maitra, M. Sumit, S. Ramaswamy, and G. V. Shivashankar, "Actomyosin contractility rotates the cell nucleus", Sci. Rep. **4**, 3781 (2013) (cit. on p. 2).

[122]N. Kumar, H. Soni, S. Ramaswamy, and A. K. Sood, "Flocking at a distance in active granular matter", Nat. Comm., 4688 (2014) (cit. on pp. 2, 6, 12, 66, 74, 79, 84).

[123]K.-D. N. T. Lam, M. Schindler, and O. Dauchot, "Homogeneous phases of polar active liquids", (2014) (cit. on p. 143).

[124]E. Lauga and T. Powers, "The hydrodynamics of swimming microorganisms", Rep. Prog. Phys. **72**, 096601 (2009) (cit. on pp. 157, 158).

[125]A. Lefauve and D. Saintillan, "Globally aligned states and hydrodynamic traffic jams in confined suspensions of active asymmetric particles", Phys. Rev. E **89**, 021002 (2014) (cit. on p. 84).

[126]E. Lemaire, L. Lobry, N. Pannacci, and F. Peters, "Viscosity of an electro-rheological suspension with internal rotations", Journal of Rheology **52**, 769 (2008) (cit. on p. 18).

[127]M. Leoni and T. Liverpool, "Swimmers in Thin Films: From Swarming to Hydrodynamic Instabilities", Phys. Rev. Lett. **105**, 238102 (2010) (cit. on pp. 157, 159).

[128]H. Levine, W.-J. Rappel, and I. Cohen, "Self-organization in systems of self-propelled particles", Phys. Rev. E **63**, 017101 (2000) (cit. on pp. 13, 28, 30, 79, 80, 82, 86, 143).

[129]N. Liron and S. Mochon, "Stokes flow for a Stokeslet between two parallel flat plates", J. Eng. Math. **10**, 287–303 (1976) (cit. on pp. 157, 158).

[130]Q. Liu and A. Prosperetti, "Wall effects on a rotating sphere", J. Fluid Mech. **657**, 1–21 (2010) (cit. on pp. 20, 51, 59, 77).

[131]T. B. Liverpool and M. C. Marchetti, "Organization and instabilities of entangled active polar filaments", 1–4 (2002) (cit. on p. 8).

[132]U. Lopez, J. Gautrais, I. D. Couzin, and G. Theraulaz, "From behavioural analyses to models of collective motion in fish schools", Interface Focus **2**, 693–707 (2012) (cit. on pp. 10, 11, 117, 134).

[133]E. Lushi, H. Wioland, and R. E. Goldstein, "Fluid flows created by swimming bacteria drive self-organization in confined suspensions", Proc. Natl. Acad. Sci. USA **111**, 9733 (2014) (cit. on p. 66).

[134]M. Mabrouk and C. McInnes, "Nonlinear stability of vortex formation in swarms of interacting particles", Phys. Rev. E **78**, 012903 (2008) (cit. on p. 13).

[135]A. Maggs, "Writhing geometry at finite temperature: Random walks and geometric phases for stiff polymers", J. Chem. Phys. (2001) (cit. on pp. 118, 124, 125).

[136]M. C. Marchetti, J.-F. Joanny, S. Ramaswamy, T. B. Liverpool, J. Prost, M. Rao, and R. A. Simha, "Hydrodynamics of soft active matter", Reviews of Modern Physics **85**, 1143–1189 (2013) (cit. on pp. 1, 6, 8, 9, 17, 23, 35, 37, 43, 46, 47, 60, 63, 64, 66, 72, 79, 80, 92, 95, 105, 107, 109, 117, 134, 138, 156, 157, 161).

[137]J. F. Marko and E. D. Siggia, "Stretching DNA", Macromolecules **28**, 8759–8770 (1995) (cit. on p. 124).

[138]J. R. Melcher and G. I. Taylor, "Electrohydrodynamics: a review of the role of interfacial shear stresses", Annual Review of Fluid Mechanics **1**, 111–146 (1969) (cit. on pp. 18, 43, 49, 67).

[139]A. M. Menzel, "Collective motion of binary self-propelled particle mixtures", Phys. Rev. E **85**, 021912 (2012) (cit. on pp. 8, 30, 57, 152).

[140] A. M. Menzel and H. Löwen, "Traveling and Resting Crystals in Active Systems", Phys. Rev. Lett. **110**, 055702 (2013) (cit. on pp. 13, 143).

[141] S. Mishra, A. Baskaran, and M. C. Marchetti, "Fluctuations and pattern formation in self-propelled particles", Phys. Rev. E **81**, 061916 (2010) (cit. on pp. 9, 92–94, 96, 105–107).

[142] S. Mishra, K. Tunstrøm, I. D. Couzin, and C. Huepe, "Collective dynamics of self-propelled particles with variable speed", Phys. Rev. E **86**, 011901 (2012) (cit. on p. 121).

[143] N. Desreumaux, *Émulsions microfluidiques et rouleurs colloïdaux : effets collectifs en matière molle forcée hors-équilibre* (PhD. thesis, Université Pierre et Marie Curie, 2015) (cit. on pp. 121, 144).

[144] V. Narayan, S. Ramaswamy, and N. Menon, "Long-lived giant number fluctuations in a swarming granular nematic.", Science **317**, 105–8 (2007) (cit. on pp. 2, 6, 79, 82).

[145] F. Nédélec, T. Surrey, A. C. Maggs, and S. Leibler, "Self-organization of microtubules and motors", Nature **389**, 305 (1997) (cit. on pp. 66, 74).

[146] K. Oerding and F. Wijland, "Fluctuation-induced first-order transition in a nonequilibrium steady state", J. Stat. Phys. **99**, 1365–1395 (2000) (cit. on p. 93).

[147] O. J. O'Loan and M. R. Evans, "Alternating steady state in one-dimensional flocking", J. Phys. A – Math. Gen. **32**, L99–L105 (1999) (cit. on pp. 5, 46).

[148] M. E. O'Neill and K. Stewartson, "On the slow motion of a sphere parallel to a nearby plane wall", J. Fluid Mech. **27**, 705 (2006) (cit. on pp. 20, 51, 59, 77).

[149] J. Palacci, S. Sacanna, S.-H. Kim, G.-R. Yi, D. J. Pine, and P. M. Chaikin, "Light Activated Self-Propelled Colloids", arXiv: 1410.7278 (2014) (cit. on p. 2).

[150] J. Palacci, C. Cottin-Bizonne, C. Ybert, and L. Bocquet, "Sedimentation and effective temperature of active colloidal suspensions", Phys. Rev. Lett. **105**, 1–4 (2010) (cit. on pp. 2, 154).

[151] J. Palacci, S. Sacanna, A. P. Steinberg, D. J. Pine, and P. M. Chaikin, "Living crystals of light-activated colloidal surfers.", Science **339**, 936–40 (2013) (cit. on pp. 2, 7, 43, 79).

[152] N. Pannacci, E. Lemaire, and L. Lobry, "DC conductivity of a suspension of insulating particles with internal rotation.", Sur. Phys. J. E **28**, 411–7 (2009) (cit. on pp. 18, 77).

[153] N. Pannacci, L. Lobry, and E. Lemaire, "How Insulating Particles Increase the Conductivity of a Suspension", Phys. Rev. Lett. **99**, 094503 (2007) (cit. on pp. 18, 49, 51, 52, 59, 67).

[154] W. F. Paxton, S. Sundararajan, T. E. Mallouk, and A. Sen, "Chemical locomotion.", Angewandte Chemie (International ed. in English) **45**, 5420–9 (2006) (cit. on pp. 79, 83).

[155] D. J. G. Pearce and M. S. Turner, "Density regulation in strictly metric-free swarms", New J. Phys. **16**, 082002 (2014) (cit. on p. 134).

[156] F. Peruani, A. Deutsch, and M. Bär, "A mean-field theory for self-propelled particles interacting by velocity alignment mechanisms", Eur. Phys. J. Spec. Top. **157**, 111–122 (2008) (cit. on pp. 5, 6, 26, 79, 84, 102, 143).

[157] F. Peruani and L. Morelli, "Self-Propelled Particles with Fluctuating Speed and Direction of Motion in Two Dimensions", Phys. Rev. Lett. **99**, 010602 (2007) (cit. on p. 127).

[158] A. Peshkov, I. S. Aranson, E. Bertin, H. Chaté, and F. Ginelli, "Nonlinear Field Equations for Aligning Self-Propelled Rods", Phys. Rev. Lett. **109**, 268701 (2012) (cit. on pp. 8, 30).

[159] A. Peshkov, E. Bertin, and F. Ginelli, "Boltzmann-Ginzburg-Landau approach for continuous descriptions of generic Vicsek-like models arXiv : 1404 . 3275v1 [ cond-mat . stat-mech ] 12 Apr 2014", arXiv: 1404.3275 (cit. on pp. 8, 30).

[160] A. Peshkov, S. Ngo, E. Bertin, H. Chaté, and F. Ginelli, "Continuous Theory of Active Matter Systems with Metric-Free Interactions", Phys. Rev. Lett. **109**, 098101 (2012) (cit. on pp. 5, 8, 30, 33, 58, 96, 109, 143).

[161] P. Pieranski, S. Clausen, G. Helgesen, and A. Skjeltorp, "Braids Plaited by Magnetic Holes.", Phys. Rev. Lett. **77**, 1620–1623 (1996) (cit. on pp. 119, 135).

[162] A. S. Popel and P. C. Johnson, "Microcirculation and hemorheology", Annu. Rev. Fluid Mech. **37**, 43 (2005) (cit. on pp. 147, 149).

[163] J. Prost, F. Jülicher, and J.-f. Joanny, "Active gel physics", **11** (2015) (cit. on p. 8).

[164] J. G. Puckett, F. Lechenault, K. E. Daniels, and J.-L. Thiffeault, "Trajectory entanglement in dense granular materials", J. Stat. Mech. – Theo. Exp. **2012**, P06008 (2012) (cit. on p. 135).

[165] G. Quincke, "Ueber Rotationen im constanten electrischen Felde", Ann. Phys. Chem. **59**, 417 (1896) (cit. on pp. 18, 43, 67).

[166] D. Quint and A. Gopinathan, "Swarming in disordered environments", arXiv: 1302.6564 (2013) (cit. on p. 121).

[167] S. Ramaswamy, "Issues in the statistical mechanics of steady sedimentation", Adv. Phys. **50**, 297 (2001) (cit. on p. 149).

[168] S. Ramaswamy, "The mechanics and statistics of active matter", Annual Review of Condens. Matter Phys., 323–345 (2010) (cit. on pp. 2, 156).

[169] S. Ramaswamy, R. A. Simha, and J. Toner, "Active nematics on a substrate: Giant number fluctuations and long-time tails", Europhysics Letters (EPL) **62**, 196–202 (2003) (cit. on pp. 6, 8).

[170] S. M. Rappaport and Y. Rabin, "Differential geometry of polymer models: worm-like chains, ribbons and Fourier knots", J. Phys. A – Math. Theo. **40**, 4455–4466 (2007) (cit. on p. 124).

[171] S. M. Rappaport, S. Medalion, and Y. Rabin, "Curvature Distribution of Worm-like Chains in Two and Three Dimensions", 1–8 (2008) (cit. on p. 126).

[172] C. W. Reynolds, "Flocks, herds and schools: A distributed behavioral model", ACM SIGGRAPH Computer Graphics **21**, 25–34 (1987) (cit. on pp. 10, 129).

[173] H. Risken, *The Fokker-Planck Equation: Methods of Solution and Applications*, edited by B. Springer Verlag (1996) (cit. on pp. 31, 57, 152).

[174] W. D. Ristenpart, P. Jiang, M. a. Slowik, C. Punckt, D. a. Saville, and I. a. Aksay, "Electrohydrodynamic flow and colloidal patterning near inhomogeneities on electrodes.", Langmuir **24**, 12172–80 (2008) (cit. on p. 28).

[175] P. Romanczuk, M. Bär, W. Ebeling, B. Lindner, and L. Schimansky-Geier, "Active Brownian particles", Eur. Phys. J. – Spec. Top. **202**, 1–162 (2012) (cit. on pp. 6, 79, 86, 92, 93, 105, 127).

[176] P. Romanczuk, I. Couzin, and L. Schimansky-Geier, "Collective Motion due to Individual Escape and Pursuit Response", Phys. Rev. Lett. **102**, 010602 (2009) (cit. on p. 13).

[177] P. Romanczuk and L. Schimansky-Geier, "Brownian Motion with Active Fluctuations", Phys. Rev. Lett. **106**, 230601 (2011) (cit. on pp. 80, 86).

[178] V. Rossetto and A. C. Maggs, "Writhing geometry of open DNA", J. Chem. Phys. **118**, 9864 (2003) (cit. on pp. 118, 124–126).

[179] F. Rouyer, D. Lhuillier, J. Martin, and D. Salin, "Structure, density, and velocity fluctuations in quasi-two-dimensional non-Brownian suspensions of spheres", Phys. Fluids **12**, 958 (2000) (cit. on pp. 149, 150).

[180] M. Rubinstein and R. Colby, *Polymer physics* (Oxford University Press, 2003) (cit. on pp. 118, 123).

[181] S. Saha, R. Golestanian, and S. Ramaswamy, "Clusters, asters and collective oscillations in chemotactic colloids", arXiv preprint arXiv:1309.4947, 1–25 (2013) (cit. on p. 83).

[182] D. Saintillan and M. J. Shelley, "Orientational order and instabilities in suspensions of self-locomoting rods", Phys. Rev. Lett. **99**, 058102 (2007) (cit. on p. 156).

[183] D. Saintillan and M. J. Shelley, "Instabilities and pattern formation in active particle suspensions: kinetic theory and continuum simulations", Phys. Rev. Lett. **100**, 178103 (2008) (cit. on pp. 37, 63, 64, 84, 85, 148, 156–158).

[184] D. Saintillan and M. J. Shelley, "Instabilities, pattern formation, and mixing in active suspensions", Physics of Fluids **20**, 123304 (2008) (cit. on pp. 36, 37, 63, 64, 84, 85).

[185] D. Saintillan and M. J. Shelley, "Active suspensions and their nonlinear models", Comptes Rendus Physique **14**, 497–517 (2013) (cit. on pp. 83, 148).

[186] N. Saito, K. Takahashi, and Y. Yunoki, "The statistical mechanical theory of stiff chains", J. Phys. Soc. Japan **22**, 219–226 (1967) (cit. on pp. 118, 123).

[187] G. Salbreux, J. Prost, and J.-F. Joanny, "Shape oscillations of non-adhering fibroblast cells", Phys. Rev. Lett. **103**, 058102 (2009) (cit. on p. 2).

[188] T. Sanchez, D. T. N. Chen, S. J. DeCamp, M. Heymann, and Z. Dogic, "Spontaneous motion in hierarchically assembled active matter", Nature **491**, 431–434 (2012) (cit. on pp. 2, 43, 46, 79).

[189] V. Schaller and A. R. Bausch, "Topological defects and density fluctuations in collectively moving systems", Proc. Natl. Acad. Sci. USA **110**, 4488–4493 (2013) (cit. on pp. 6, 11, 47, 65).

[190] V. Schaller, C. A. Weber, C. Semmrich, E. Frey, and A. R. Bausch, "Polar patterns of driven filaments.", Nature **467**, 73–7 (2010) (cit. on pp. 2, 6, 11, 17, 43, 45, 46, 66, 74, 79, 92, 93, 105, 108).

[191] R. Seemann, M. Brinkmann, T. Pfohl, and S. Herminghaus, "Droplet based microfluidics", Rep. Prog. Phys. **75**, 016601 (2012) (cit. on pp. 147, 149).

[192] X.-Q. Shi and Y.-Q. Ma, "Topological structure dynamics revealing collective evolution in active nematics.", Nature communications **4**, 3013 (2013) (cit. on p. 8).

[193] J. L. Silverberg, M. Bierbaum, J. P. Sethna, and I. Cohen, "Collective motion of humans in mosh and circle pits at heavy metal concerts", Phys. Rev. Lett. **110**, 228701 (2013) (cit. on p. 66).

[194] A. R. Simha and S. Ramaswamy, "Hydrodynamic fluctuations and instabilities in ordered suspensions of self-propelled particles", Phys. Rev. Lett. **89**, 058101 (2002) (cit. on pp. 43, 46).

[195] S. Sinha, "Writhe distribution of stretched polymers", Phys. Rev. E **70**, 011801 (2004) (cit. on p. 125).

[196] A. T. Skjeltorp, S. Clausen, and G. Helgesen, "Application of braid statistics to particle dynamics", Physica A **274**, 267 (1999) (cit. on p. 138).

[197] A. P. Solon and J. Tailleur, "Revisiting the Flocking Transition Using Active Spins", Phys. Rev. Lett. **111**, 078101 (2013) (cit. on pp. 5, 6, 92, 93, 95, 103, 105–107, 109, 110).

[198] A. P. Solon, H. Chat, H. Chaté, and J. Tailleur, "From Phase to Micro-Phase Separation in Flocking Models: The Essential Role of Non-Equilibrium Fluctuations", arXiv: 1406.6088 (2014) (cit. on pp. 4, 6, 103, 143).

[199] S. E. Spagnolie and E. Lauga, "Hydrodynamics of self-propulsion near a boundary: predictions and accuracy of far-field approximations", J. Fluid Mech. **700**, 105–147 (2012) (cit. on p. 26).

[200] S. Strogatz, *Nonlinear Dynamics and Chaos*, edited by N. Y. Addison-Wesley (1994) (cit. on p. 107).

[201] Y. Sumino, K. H. Nagai, Y. Shitaka, D. Tanaka, K. Yoshikawa, H. Chaté, and K. Oiwa, "Large-scale vortex lattice emerging from collectively moving microtubules.", Nature **483**, 448–52 (2012) (cit. on pp. 2, 43, 79).

[202] J. B. Swift and P. C. Hohenberg, "Hydrodynamic fluctuations at the convective instability", Phys. Rev. A **15**, 319–328 (1977) (cit. on pp. 9, 93).

[203] D. Takagi, J. Palacci, A. Braunschweig, M. Shelley, and J. Zhang, "Hydrodynamic capture of microswimmers into sphere-bound orbits", Soft Matter **10**, 1784 (2014) (cit. on p. 68).

[204] I. Theurkauff, C. Cottin-Bizonne, J. Palacci, C. Ybert, and L. Bocquet, "Dynamic Clustering in Active Colloidal Suspensions with Chemical Signaling", Phys. Rev. Lett. **108**, 268303 (2012) (cit. on pp. 2, 43, 79, 83, 156).

[205] J.-L. Thiffeault, "Braids of entangled particle trajectories", Chaos **20**, 017516 (2010) (cit. on pp. 119, 135, 136).

[206] J.-L. Thiffeault and M. Busidic, "Braidlab: a software package for braids and loops", arXiv:1410.0849 (2014) (cit. on p. 136).

[207] F. Thüroff, C. A. Weber, and E. Frey, "Critical Assessment of the Boltzmann Approach to Active Systems", Phys. Rev. Lett. **111**, 190601 (2013) (cit. on pp. 8, 30).

[208] F. Thüroff, C. A. Weber, and E. Frey, "Numerical Treatment of the Boltzmann Equation for Self-Propelled Particle Systems", Phys. Rev. X **4**, 041030 (2014) (cit. on pp. 8, 30).

[209] S. Thutupalli, R. Seemann, and S. Herminghaus, "Swarming behavior of simple model squirmers", New J. Phys. **13**, 073021 (2011) (cit. on pp. 2, 147, 150, 156).

[210] S. Thutupalli and S. Herminghaus, "Tuning active emulsion dynamics via surfactants and topology", Eur. Phys. J. E **36** (2013) (cit. on p. 2).

[211] J. Toner and Y. Tu, "Long-Range Order in a Two-Dimensional Dynamical XY Model: How Birds Fly Together", Phys. Rev. Lett. **75**, 4326–4329 (1995) (cit. on pp. 7–9, 23, 34, 37, 40, 66, 94, 96, 105, 134, 138).

[212] J. Toner, Y. Tu, and S. Ramaswamy, "Hydrodynamics and phases of flocks", Ann. Phys. **318**, 170–244 (2005) (cit. on pp. 8, 23, 37, 43, 46, 47, 64, 66, 72, 138, 156).

[213] T. Toyota, N. Maru, M. M. Hanczyc, T. Ikegami, and T. Sugawara, "Self-propelled oil droplets consuming "Fuel" surfactant", J. Am. Chem. Soc. **131**, 5012–5013 (2009) (cit. on p. 2).

[214] Y. Tu, J. Toner, and M. Ulm, "Sound Waves and the Absence of Galilean Invariance in Flocks", Phys. Rev. Lett. **80**, 4819–4822 (1998) (cit. on pp. 6–8, 34, 40, 94, 96, 105, 134, 138).

[215] T. Vicsek, A. Czirók, E. Ben-Jacob, I. Cohen, and O. Shochet, "Novel Type of Phase Transition in a System of Self-Driven Particles", Phys. Rev. Lett. **75**, 1226–1229 (1995) (cit. on pp. 3, 5, 43, 66, 79, 84, 102, 105, 111, 134).

[216] T. Vicsek and A. Zafeiris, "Collective motion", Phys. Rep. **517**, 71–140 (2012) (cit. on pp. 1, 4, 17, 43, 66, 79, 92, 105, 107, 110, 122, 134, 156).

[217] I. D. Vladescu, E. J. Marsden, J. Schwarz-Linek, V. A. Martinez, J. Arlt, A. N. Morozov, D. Marenduzzo, M. E. Cates, and W. C. K. Poon, "Filling an emulsion drop with motile bacteria", Phys. Rev. Lett. **113**, 268101 (2013) (cit. on pp. 66, 68).

[218] Wanderlass, http://www.wanderlass.com/wow-philippines/dive-pescador-moalboal.html (cit. on p. 1).

[219] C. A. Weber, T. Hanke, J. Deseigne, S. Léonard, O. Dauchot, E. Frey, and H. Chaté, "Long-Range Ordering of Vibrated Polar Disks", Phys. Rev. Lett. **110**, 208001 (2013) (cit. on pp. 6, 12, 30, 80, 82, 92, 93, 105).

[220] H. H. Wensink, J. Dunkel, S. Heidenreich, K. Drescher, R. E. Goldstein, H. Löwen, and J. Yeomans, "Meso-scale turbulence in living fluids", Annu. Rev. Fluid Mech. **109**, 14308 (2012) (cit. on p. 66).

[221] G. Whitham, *Linear and Nonlinear Waves*, edited by N. Y. John Wiley & Sons (1974) (cit. on p. 110).

[222] H. Wioland, F. G. Woodhouse, J. Dunkel, J. O. Kessler, and R. E. Goldstein, "Confinement Stabilizes a Bacterial Suspension into a Spiral Vortex", Phys. Rev. Lett. **110**, 268102 (2013) (cit. on pp. 8, 43, 66, 74).

[223] F. G. Woodhouse and R. E. Goldstein, "Spontaneous Circulation of Confined Active Suspensions", Phys. Rev. Lett. **109**, 168105 (2012) (cit. on pp. 2, 8, 36, 40, 58).

[224] F. G. Woodhouse and R. E. Goldstein, "Cytoplasmic streaming in plant cells emerges naturally by microfilament self-organization.", Proc. Natl. Acad. Sci. USA **110**, 14132–7 (2013) (cit. on p. 84).

[225] X. Yang and M. C. Marchetti, "Hydrodynamics of Turning Flocks", 1–5 (2014) (cit. on pp. 66, 143).

[226] S. R. Yeh, M. Seul, and B. I. Shraiman, "Assembly of ordered colloidal aggregates by electric field induced fluid flow", Nature **386**, 57 (1997) (cit. on p. 68).

[227] H. P. Zhang, A. Be'er, E.-L. Florin, and H. L. Swinney, "Collective motion and density fluctuations in bacterial colonies.", Proc. Natl. Acad. Sci. USA **107**, 13626–30 (2010) (cit. on pp. 2, 7, 43, 46, 147, 149, 150).

[228] R. Zhang, L. Turner, and H. C. Berg, "The upper surface of an Escherichia coli swarm is stationary.", Proc. Natl. Acad. Sci. USA **107**, 288–90 (2010) (cit. on pp. 149, 156).

**Resumé**

L'émergence de mouvements cohérents à grande échelle a été abondamment observée dans les populations animales (nuées d'oiseaux, bancs de poissons, essaims de bactéries...) et plus récemment au sein de systèmes artificiels. De tels ensembles d'individus auto-propulsés, susceptibles d'aligner leurs vitesses, présentent des propriétés physiques singulières. Cette thèse théorique étudie divers aspects de ces systèmes actifs polaires.

Dans un premier temps, nous avons modélisé une population de colloïdes auto-propulsés. En étroite association avec les travaux expérimentaux, nous avons décrit la dynamique du niveau individuel à l'échelle macroscopique. Les résultats théoriques expliquent l'émergence et la structure de motifs cohérents : (i) transition vers le mouvement collectif, (ii) propagation de structures spatiales polarisées, (iii) amortissement des fluctuations de densité dans un liquide polaire, (iv) vortex hétérogène dans des géométries confinées.

D'un point de vue plus fondamental, nous avons ensuite étudié les excitations non linéaires qui se propagent dans les systèmes actifs polaires. L'analyse des théories hydrodynamiques de la matière active, à l'aide d'outils issus des systèmes dynamiques, a permis de rationaliser les observations expérimentales et numériques reportées jusqu'ici.

Enfin, nous avons proposé une approche complémentaire pour caractériser les populations actives. Associant étude numérique et résultats analytiques, nous avons étudié les propriétés géométriques des trajectoires individuelles, ainsi que leur enchevêtrement au sein de groupes tridimensionnels. Ces observables pourraient permettre de sonder efficacement la dynamique de populations animales.

**Abstract**

The emergence of coherent motion at large scale has been widely observed in animal populations (bird flocks, fish schools, bacterial swarms...) and more recently in artificial systems. Such ensembles of self-propelled individuals, capable of aligning their velocities, are commonly referred to as polar active materials. They display unique physical properties, which we investigate in this theoretical thesis.

We first describe a population of self-propelled colloids. In strong connection with the experiments, we model the dynamics from the individual level to the macroscopic scale. The theoretical results account for the emergence and the structure of coherent patterns: (i) transition to collective motion, (ii) propagation of polar spatial structures, (iii) damping of density fluctuations in a polar liquid, (iv) heterogeneous vortex in confined geometries.

We then follow a more formal perspective, and study the non-linear excitations which propagate in polar active systems. We analyze the hydrodynamic theories of active matter using a dynamical-system framework. This approach makes it possible to rationalize the experimental and numerical observations reported so far.

Finally, we propose a complementary approach to characterize active populations. Combining numerical and analytical results, we study the geometric properties of the individual trajectories and their entanglement within three-dimensional flocks. We suggest that these observables should provide powerful tools to describe animal flocks in the wild.

Laboratoire de Physique
École Normale Supérieure de Lyon
46, allée d'Italie
69007 Lyon

École doctorale de Physique et Astrophysique de Lyon
4, rue Enrico Fermi
69622 Villeurbanne Cedex